Investigation of Nanostructured Thin Films on Surface Acoustic Wave and Conductometric Transducers for Gas Sensing Applications

A thesis submitted in fulfilment of the requirements for

the degree of Doctor of Philosophy

Rashidah Arsat

BSc. (Electrical and Electronic Engineering), University of Science Malaysia, Malaysia

MSc (Telecommunications), Loughbourough University, UK

School of Electrical and Computer Engineering

RMIT University, Melbourne, Australia

March, 2009

Author's Declaration

I certify that except where due acknowledgement has been made, the work is that of the author alone; the work has not been submitted previously, in whole or in part, to qualify for any other academic award; the content of the thesis is the result of work which has been carried out since the official commencement date of the approved research program; any editorial work, paid or unpaid, carried out by a third party acknowledged; and, ethics procedures and guidelines have been followed.

_____

Rashidah Arsat

March, 2009

Contents

List of Figures

List of Tables

Acknowledgments

First and foremost, I would like to thank my supervisors Prof. Wojtek Wlodarski and Assoc. Prof. Kourosh Kalantar-zadeh for making my PhD program a truly fruitful experience. Their encouragement, unquestionable patience and invaluable assistance enabled me to experience a great deal in such a small amount of time.

I wish to thank to my colleagues Ms. Mahnaz Shafiei, Mr. Micheal Breedon, Mr Chen Zhang, Mr. Mohd. Hanif Yaacob, Mr. Jerry Yu, Mr Laith Al-Mashat and Mr. Rick Zaideng for their help and providing a friendly and energetic environment for conducting research. I would like to pass my special thanks to Dr. Abu Z. Sadek, Dr. Sasikaran Kandasamy, Dr. Alexandru Fachete, Dr. Glenn Matthews, Dr. David Powell, Dr. Samuel Ippolito, Dr Adrian Trinchi, Dr. Zuraini Dahari, Mr. Hasan Qasim, Mr. Sharath Sriram, Ms. Madhu Baskaran, Mr. Vijay Sivan, Ms. Pantea, Dr. Rosmiwati Mohd Mokhtar, Dr Wai Chee Yau, Mr. Muhammad-Bagher Rahmani, Ms Lilin Li and Ms Joy Tan for their friendship, support and encouragement.

My thanks extend to the academic and administrative members of the School of Electrical and Computer Engineering at RMIT University for their help. I am especially grateful to the technical and MMTC staff of the school, Mr. Paul Jones, Mr Chow, Ms ChiPin Wu, Mr. Tristan for their assistance during my experiments.

My gratitude goes to Dr Xiaofeng Yu from Chinese Academic of Sciences, Shanghai for his help and assistance during my electropolymerization experiments. A special thanks to Dr. Xiuli He from Chinese Academic of Science, Beijing for making me realize the beauty of electrospinning and her help during the experiments. I also would like to take this opportunity to thank several people, without whom part of this research would not be possible. I am very grateful to Prof. Richard Kaner and Mr. Scott Gilje of the Department of Chemistry and Biochemistry, UCLA, Los Angeles for the great graphene synthesis. Special thanks also to Prof Koo Shin of the Department of Applied Chemistry, Sejong

University, Seoul, Korea for his extensive assistance in polyaniline/diamond composite synthesis.

Additionally, I would like to thank Dr. Johan du Plesis, Mr. Phil Francis and all microscopists of the Department of Applied Physics, RMIT University for their input and help in organising the material characterizations. Also thanks to Mr Frank Antolasic of the Department of Chemistry, RMIT University and Dr. Paul Spizziri of School of Physics, University of Melbourne for their help in XRD and Raman characterization, respectively.

I thank the Ministry of Higher Education (Malaysia) and University of Technology Malaysia (Malaysia) for awarding me the PhD scholarship and providing me travel support to enable me to present a paper at the international conference EACCS 2007, Singapore.

My special thanks to Mrs Norhaida Talib and her family for their help in babysitting my son while I was at university.

I also would like to take this opportunity to express my sincerest love to my husband; Mohd Kherold Nazi, my son; Muhd Aqib Addin for their love, support and patience. I thank my parents, Mr. Arsat Hayati and Mrs Amarenu Parkasi, parent-in-law: Mr. Jamal and Mrs Sewah, and my sister and brothers for their encouragement and support.

Rashidah Arsat

Abstract

In this thesis, the author proposed and developed nanostructured materials based Surface Acoustic Wave (SAW) and conductometric transducers for gas sensing applications. The device fabrication, nanostructured materials synthesis and characterization, as well as their gas sensing performance have been undertaken. The investigated structures are based on two structures: lithium niobate ($LiNbO_3$) and lithium tantalate ($LiTaO_3$). These two substrates were chosen for their high electromechanical coupling coefficient. The conductometric structure is based on langasite (LGS) substrate. LGS was selected because it does not exhibit any phase transition up to its melting point (1470 °C). Four types of nanostructured materials were investigated as gas sensing layers, they are: polyaniline, polyvinylpyrrolidone (PVP), graphene and antimony oxide (Sb_2O_3). The developed nanostructured materials based sensors have high surface to volume ratio, resulting in high sensitivity towards different gas species.

Several synthesis methods were conducted to deposit nanostructured materials on the whole area of SAW based and conductometric transducers. Electropolymerization method was used to synthesize and deposit polyaniline nanofibers on 36 ° YX $LiTaO_3$ and 64 ° YX $LiNbO_3$ SAW substrates. By varying several parameters during electropolymerization, the effect on gas sensing properties were investigated. The author also extended her research to successfully develop polyaniline/inorganic nanocomposites based SAW structures for room temperature gas sensing applications. Via electrospinning method, PVP fibres and its composites were successfully deposited on 36 ° YX $LiTaO_3$ SAW transducers. Again in this method, the author varied several parameters of electrospinning such as distance and concentration, and investigated the effect on gas sensing performance. Graphene-like nano-sheets were synthesized on 36 ° YX $LiTaO_3$ SAW devices. This material was synthesized by spin-coating graphite oxide (GO) on the substrate and then exposing the GO to hydrazine to reduce it to graphene. X-ray photoelectron spectroscopy (XPS) and Raman characterizations showed that the reduced GO was not an ideal graphene. This information was required to understand the properties of the deposited graphene and link its properties to the gas sensing properties. Thermal evaporation method was used to grow Sb_2O_3 nanostructures on LGS conductometric transducers. Using this method, different nanoscale structures such as nanorods and lobe-like

shapes were found on the gold interdigitated transducers (IDTs) and LGS substrate. The gas sensing performance of the deposited nanostructured Sb_2O_3 based LGS conductometric sensors was investigated at elevated temperatures. The gas sensing performance of the investigated nanostructured materials/SAW and conductometric structures provide a way for further investigation to future commerciallization of these types of sensors.

Chapter 1

Introduction

The purposes of this chapter is to provide a general overview and introduction for the research presented in this PhD thesis. This chapter addresses the research motivations, objectives, the author's achievements and thesis organisation.

1.1 Motivation

A sensor can be defined as a device that provides a "usable output in response to a specific measurand" [1]. The basic structure of a gas sensor is shown in Fig. 1.1.

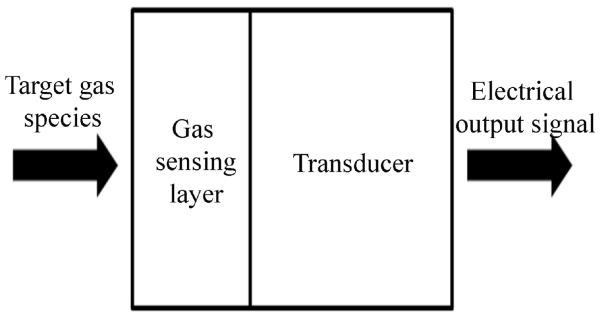

Figure 1.1: Schematic diagram of a basic gas sensor.

A gas sensor is a device incorporating a gas sensitive element (i.e: thin film) either intimately connected to or integrated within a transducer. The usual aim is to produce an electronic output signal which is proportional to the gas concentration. In recent years, the development of gas sensors has become increasingly important. Sensors are used in applications ranging from medical diagnostic and health care, defense and security, automotive and industrial manufacturing as well as environmental monitoring. Regardless of the associated applications, all sensors have the same objective which are to provide stable and accurate monitoring of the target gas.

The aim of this PhD project is to develop novel, highly sensitive gas sensors. Generally, sensors have to be exposed directly to the environment for the interaction with a target gas. This means that the sensor can also be exposed to corrosive or contamination species, which can deteroriate and interfere with the performance of the sensors. Great efforts have been made to investigate the important aspects of sensors; sensitivity, selectivity, stability and reproducibility [2]. To meet these demands, many research programs into new sensors have been conducted based on various principles and materials. It includes the efforts to enhance the performance of traditional devices using nanotechnology. Recent advances in nanotechnology has provided the opportunity to obtain more efficient performance from gas sensors compared to polycrystalline based gas sensors. Nanostructured materials offer more surface to volume ratio to interact with gas species. Because of the size effects, nanostructured materials often exhibit superior physical properties and are of great interest for sensor applications [3]. In addition, electrical, mechanical, optical, and magnetic properties of the nanostructured materials have been observed to change and can be tuned much more in comparison to the bulk form of the same material.

Recent development in the designing and sythesizing nanostructured materials have attracted much attention as these nanoscale materials hold great promise for development novel gas sensors. This includes metal oxide nanostructures [4-6], conducting and non-conducting polymer nanostructures [7-9], and carbon nanotubes [10-11]. It has been established that the sensitivity of metal oxide and conducting polymers based gas sensors depends on the grain size [12-13]. Both reports show that the entire thickness of the sensitive layer can be affected by the reactions with the gas analyte. The porosity of nanostructures

also facilitates rapid diffusion of gases in and out of these micro- or nanoporosities materials, hence increase the reaction rate resulting in faster sensor response and recovery. Besides, nanostructures increase the effective number of sites available for reactions with target molecules as most of the atoms are surface or near surface atoms.

The author's focus in this PhD research is to develop highly sensitive nanostructured material based surface acoustic wave (SAW) and conductometric gas sensors. Based on the critical literature review, which will be presented in chapter 2, the author made an informed desicion to develop novel electropolymerized dedoped polyaniline nanofibers, polyaniline/diamond and polyaniline/MWNTs nanocomposite, electrospun PVP fibers, graphene nano-sheets, and Sb_2O_3 nanostructures based SAW and conductometric sensors. The developed sensors were tested by exposure to hydrogen (H_2), nitrogen dioxide (NO_2) and carbon monoxide (CO). Based on the obtained sensing performances, the gas sensing mechanisms were discussed. This PhD research has led to many novel outcomes and contributions to the body of knowledge in the field of nanostructured materials based gas sensors. The outcomes and author achievements are listed in section 1.3 of this chapter.

1.1.1 Gas Sensors Applications

Gas sensors are increasingly needed for various activities and applications in environmental monitoring, process control as well as domestic and industrial health and safety. These applications require precise real time measurements for controlling and monitoring to increase productivity, keep environmental pollution within limits as well as maintain health and safety. The absence of sensors for the aforemention purposes can greatly hinder evaluation of the effectiveness of environmental policies and also can cause difficulty in improving industrial processes. For example, the haze episodes in Southeast Asia in 1983, 1984, 1991, 1994 and 1997 that imposed threats to the environmental management [14]. The awareness to prevent this environmental threat to re-occur and to ensure that pollution is not beyond the safety limits shows the importance of gas sensors. Furthermore, the use of flammable gas species such as CH_4, LPG and H_2 in domestic houses, the toxic or bad-smelling gases such as H_2S and NH_3 used in industrial processes [15] and the need for sensing volatile gases in food industries

reveal that gas sensors are vitally important in everyday life.

The needs for gas sensors are enormous. In recent years, the interest has grown from awareness in climate change and global warming to the chemical warfare threat. The use of chemical weapons against civilians during war is an absolute real threat. The Halabja poison gas attack occurred in 1988 during the Iran-Iraq war has confirmed this horrible reality [16]. Thousands of people died during the attack. The consequences of the attack continues in the years after the attacks due to the horrific complications, deseases and birth defects. The attack involved multiple chemical agents that are highly dangerous because of its colourless, odourless and toxicity. Therefore, the fast and accurate sensing of these gases are essential to protect human beings and animals.

Gas sensors are also important for controlling industrial health and safety, domestic and environmental monitoring as well as vehicle emissions. The use of H_2 as synthetic fuel for transportation industry, NH_3 in industrial refrigeration applications, the emission of CO from the burning of wood or charcoal at home and other applications have grown the demand in gas sensing. Each application places various requirements on the sensor and sensing sytems. However, the aims remain the same; to achieve accurate and stable monitoring of the analyte in the range of parts per millions (ppm) to parts per billion (ppb) concentrations [17].

During the research, the author investigates three different gases: H_2, NO_2 and CO. These gases are known to be able to affect the environment and human health if over exposure occur. By employing the nanostructured materials on the proposed SAW and conductometric devices, the author investigated the gas sensing performance for different gas concentrations.

In each specific applications, stringent requirements are demanded from the sensing system, especially for the sensor itself. The objective is to achieve accurate and stable monitoring of the analyte under consideration. The human physiological and environmental effects as well as the sensing applications of the abovemention gases are highlighted in the following subsections.

Hydrogen (H_2)

Hydrogen, which is a colourless and odourless gas is one of the most important reducing gases. This gas has attracted public attention as a clean fuel energy

resources after world facing oil crisis in 1973 [18]. Since then, interest in H_2 gas sensing has enjoyed a skyrocketing popularity, as hydrogen has been touted as a panacea for clean energy production. It is highly flammable and explodes in air at concentrations as low as 4% [19]. Furthermore, H_2 has a low ignition energy, posing a significant risk of deflagration. H_2 sensing also finds important applications in aerospace, chemical refining and biomedical systems [20-21].

Nitrogen Dioxide (NO_2)

Nitrogen dioxide (NO_2) is well known for its role in acid rain generation, as the primary cause of photochemical smog, as a respiratory irritant and concerningly as an olfactory paralysis agent [22-24]. Typically NO_2 is generated during the combustion cycle of internal combustion engines. However other sources of NO_2 include manufacturing industries, food processing, electricity generation from coal-fired power stations, petrol, and metal refining. Concentration of NO_2 as low as 4ppm is known to paralyse the olfactory system preventing the conscious detection of increasing NO_2 levels. As such, the detection of NO_2 at low concentration is of vital importance to minimize exposure in confined spaces and industrial environments [14,22-24].

Carbon Monoxide (CO)

Carbon monoxide is colourless, tasteless, odourless, and highly toxic gas. It is a product of the incomplete combustion of carbon-containing compound, notably in internal combustion engine [25]. Production of CO from automobile and industrial emission may contribute to the greenhouse effect and global warming. From the public health perspective, exposure towards CO is the most common type of fatal poisoning in many countries [26-27]. Exposed to CO as low as 667ppm can cause body's haemoglobin ineffective in delivering oxygen, resulting some body parts do not receive oxygen [28]. Besides, exposure to this gas also can cause severe effects on fetus of a pregnant woman. Hence, it is important to control the emission of CO with stringent legal limits and also develop procedures for continously monitoring this gas in ambient and industrial atmosphere.

1.1.2 Transducers

The information about gas concentration is converted into a form of energy which can be measured using a transducer. Choosing the right transducing platform is highly important in obtaining the desired sensing performance. Integrating transducers with nanomaterials for sensing applications can enhance their performance. This subsequently leads to increase sensitivity towards gas species.

In this research, the author used two type of transduction platforms; conductometric and SAW based. Conductometric transducers are the most common type of platforms. It involves a cheap and convenient process of fabrication. This device can measure changes occured by the analyte gas by generating changes in resistance.

In SAW transducers, metal thin film interdigitated transducers (IDTs) are fabricated on a piezoelectric substrate which act as electrical input and output ports. They are widely used as resonators, delay lines and electronic filters. Similar to conductometric transducers, SAW transducers can respond to the conductivity change when the whole area of the device are coated with sensing layer. In addition to that, a SAW sensor can also respond to mass changes and viscoelastic effects. All these interactions contribute to the change in propagation of surface waves, thereby producing a shift in the resonant frequency of the SAW sensor.

1.1.3 Nanotechnology Enabled Gas Sensors

Nanotechnology is the term used for covering the design, fabrication and utilization of functional structures with at least one characteristic dimension ranging in nanometers. In this range, the physical, chemical and biological properties are unique and can be significantly altered. The object may display their own unique properties when characteristic structural features are intermediate in between isolated atoms and bulk microscopic materials. These properties usually differ from those displayed by either atomic scale or bulk materials [29]. It is also demonstrated that the nanostructured materials possess enhanced performance properties compared to bulk materials when they are used in similar applications [30]. Ultimately this can lead to new technological opportunities as well as new

challenges such as to explore nanodevice concepts and improve techniques for the investigation of nanostructures.

Nanotechnology has a great impact in sensor technology. It offers unique advantages to the sensor design by manipulating/incorporating/fabricating/arranging materials at the molecular level, where sensing events occur [31]. Therefore, the technology is enabling the development of small, low cost and highly efficient sensors, with broad applications.

Improvement in sensitivity is the major attraction for developing nanotechnology enabled gas sensors. Nanostructured materials have a higher surface to volume ratio in comparison with polycrystalline material based thin film devices. This surface enable the detection of molecular event more effectively, thus maximising the sensor output signal [32]. By tuning the morphological and structural properties of nanomaterials, better sensitivity and selectivity can be obtained. In addition, nanostructures minimize the time taken for a measurand to diffuse into and out of the volume [33]. This definitely improves the time taken for a sensor to raise an alarm therefore preventing a potential disaster.

Attaining the benefits from nanotechnology to augment sensor performances are challenging. Sensor manufacturers encounter difficulties in synthesizing nanostructures, reading and understanding reliable responses as well as controlling nanostructures behaviour from nano to macro scales. Although numerous nanostructured materials have already been reported in literature to be used as sensing layers, there still more new materials and properties that can be discovered in order to fill in the gap of nanotechnology.

For this research, the author investigated the gas sensing applications of four different materials, which are conducting and non-conducting polymers, graphene and metal oxide. By employing nanostructured sensing layers, various aspects in gas sensing performance such as the device's sensitivity, repeatability, operational temperature and the sensing mechanism are explored.

Polyaniline Based Gas Sensors

Conducting polymers have received increasing interest since they were found in 1970s [34]. The active research on conducting polymers has led to wide applications such as in sensors [35], power sources, rechargeable batteries [36] and

electrochromic devices [37]. Among the family of conducting polymers, polyaniline is one of the most widely studied materials for gas sensing applications. This is due to its low fabrication cost, room temperature operation, facile synthesis and rich chemistry for structural modification [38-39]. Most reports indicate that polyaniline nanostructures outperform conventional polyaniline for gas sensing applications [40]. Nanostructured polyaniline, with a diameter of less than 100 nm possess porous structures when deposited as thin films and therefore provide much larger surface to volume ratio [41]. In contrast, agglomeration usually occurs in traditional polyaniline. As a result, nanostructured polyaniline allows easy diffusion of gas molecules into and out of the film and lead to a rapid diffusion of the molecules into the material. All the abovemention advantages of polyaniline has motivated the author to integrate this material with SAW transducers. Consequently the author investigated the gas sensing performance of polyaniline as well as it composites.

Polyvinylpyrrolidone (PVP) Based Gas Sensors

Generally, non-conducting polymers are defined as the polymers with high resistivity [42]. The production of such polymeric materials has grown rapidly in the past 50 years [43]. The versatility of this type of materials has developed lots of interests in polymer research and development. Although non-conducting polymers are also useful for a variety of chemical sensor types, the use of PVP as a sensing layer has been rarely reported. Usually, the non-conducting polymer PVP acts as an essential auxiliary, but not as an active material itself. The ability of thin film PVP based QCM sensors [44] and PVP/ZnO composite based sensor [45] to sense gas molecules have attracted the author of this thesis to explore the potential of nanoscale structure of PVP as gas sensing layers compared to the conventional PVP thin film.

Graphene Based Gas Sensors

Carbon is an interesting element due to its capability to form variety of allotropes which are 3D diamond and graphite, 1D carbon nanotubes and 0D fullerenes [46]. All of the carbon allotropes have been actively investigated and have shown remarkable behaviour in sensing applications [47-49].

Graphene has been the most theoretically studied allotrope of carbon for more than 60 years [46] after the first free-standing form of graphene is obtained

[50]. Its unusual properties such as ballistic electronic transport at room temperature and metal-like properties have caught the attention of many researchers to study this material. Additionally, this monoatomically thick material offers large surface area making it well-suited for gas sensing application. These therefore attracted the author to exploit graphene as a sensing layer for SAW based sensors. The employed graphene/SAW sensor provided better understanding in the graphene sensing mechanism towards H_2, NO_2 and CO gases.

Antimony Oxide Based Gas Sensors

Among all the materials, metal oxides are the most widely applied materials for gas sensing applications. Nanostructured metal oxides in the form of nanoparticles, nanorods, nanowires and nanobelts provide great opportunity to enhance the response of sensors. This is due to the fact that a sensor performance is directly related to the porosity, granularity, and ratio of surface to volume of the sensing materials. Investigation in synthesizing nanostructured Sb_2O_3 are also established, however, lack of literature are found in applying the nanostructured Sb_2O_3 thin films as sensing layer for gas sensing applications. The nanostructured Sb_2O_3 forms a porous structure when deposited as thin films. Their nanoscale dimensions and large surface to volume ratio allows quick diffusion of gases in and out of the structure. This results in higher sensitivity and faster sensor's response and recovery compared to the polycrystalline thin film Sb_2O_3. Besides, the large interaction zone results in large modulation of electrical properties upon exposure to gas analytes [51]. This therefore has attracted the author to study the sensing performance of Sb_2O_3 based sensors.

1.2 Objectives

The aim of this research program is to develop SAW and conductometric gas sensors with various nanostructured sensing materials. It is understood that nanostructured materials have high surface to volume ratio, which is a fundamental aspect for gas sensing. Different methods were employed to develop the sensors. Nanostructured material based sensors have a potential to improve sensitivity compared to the polycrystalline gas sensors. To investigate the feasibility of the proposed sensors, this research had the following objectives:

- To synthesize polyaniline nanofibers via electropolymerization technique and develop novel dedoped polyaniline nanofibers based SAW gas sensors. Detailed investigation of the developed sensors' performance based on doping, dedoping, variation of thickness of polyaniline nanofibers thin films, variation of acids concentrations and variation of doping acids were performed.

- To synthesize PVP nanofibers via electrospinning method and develop novel SAW sensors based on this material. The developed sensor performances were investigated and compared for different PVP concentrations.

- To develop novel graphene nano-sheets based SAW gas sensors to detect H_2, NO_2 and CO gases. The sensors performances (frequency shift, stability and repeatability) were investigated at different operating temperatures.

- To synthesize Sb_2O_3 via thermal evaporation method, and develop Sb_2O_3 nanorods based langasite (LGS) conductometric transducers. Sensitivity of the developed sensors were investigated as a function of their operating temperature.

- To synthesize novel nanocomposites of polyaniline/MWNTs and polyaniline/diamond. The developed sensors performance were investigated and compared for room temperature operation.

- Characterization of these novel nanostructured materials were conducted to find out morphologies, dimensions, and compositions of the materials.

- To explain the gas sensing mechanisms of all the above-mentioned novel devices.

The author chose 36° YX $LiTaO_3$ and 64° YX $LiNbO_3$ substrates as a base for the developed novel nanostructured materials/SAW sensors as these piezoelectric materials have high electromechanical coupling co-efficient. To develop nanomaterial based conductometric sensors, the author used LGS substrate with titanium/nickel/gold metallization IDTs. The LGS was chosen because this substrate does not exhibit any phase transition up to its melting point (1470 °C).

The thin film of nanostructured materials were characterized using techniques such as scanning electron microscopy (SEM), atomic force microscopy (AFM), X-Ray diffraction microscopy (XRD) etc. The material characterizations combined with the gas sensing experimental results assisted the fundamental understanding of the sensing mechanisms.

1.3 Outcomes and Author's Achievements

This thesis describes the work undertaken by the author during her PhD program. The major outcomes of this research program can be summarized below:

1. Polyaniline Based SAW and Conductometric Gas Sensors

- Novel dedoped polyaniline nanofibers based $LiTaO_3$ SAW sensors were successfully fabricated via electropolymerization method. To the best of author's knowledge, this was the first investigation on the effect of different electropolymerized polyaniline nanofiber thin film thicknesses for gas sensing. The diameter of the electropolymerized polyaniline nanofibers were observed in the range of 40 – 50 nm. The author found that the polyaniline nanofibers/SAW sensors with the thin film thickness of $\sim$3.5 μm exhibited the highest frequency shift upon exposure towards 1% H_2 concentration.

- To the best of author's knowledge, the author was the first who investigated the effect of different acid concentrations in electrolyte on the doping and depositing of polyaniline for gas sensing applications. Five different acid concentrations were prepared for depositing polyaniline nanofibers on SAW devices and exposed to different H_2 concentrations. Electropolymerized (1.0M HCl) polyaniline nanofibers based SAW sensor showed the largest frequency shift towards 1% H_2.

- The author electropolymerized polyaniline nanofibers using two different acid dopants in electrolyte. The comparison of morphology and the gas sensing performance for both doped polyaniline were conducted. Both HCl doped and HNO_3 doped polyaniline showed almost similar average thickness of nanofibers. However, nanofibers for HCl doped polyaniline were in better order than that of HNO_3 doped polyaniline, which contribute to the

high frequency shift and baseline stability of the gas sensing performance towards different concentrations of H_2 gas. This study provides valuable information for other researchers to investigate the gas sensing performance of polyaniline polymerized in different type of acids.

- Novel dedoped polyaniline nanofibers/MWNTs nanocomposite/$LiTaO_3$ SAW sensors were fabricated using electropolymerization method. It was observed that the polyaniline/MWNTs had more compact fibres structure than the polyaniline itself, which could be the result of the small frequency shift of 4.3 kHz towards 1% H_2.

- Novel polyaniline nanofibers and diamond nanocomposite were chemically synthesized and dropcasted on SAW transducers. The developed sensors were exposed to different concentrations of H_2 gas. To the author's best knowledge, the developed nanocomposite/SAW devices were investigated for gas sensing applications for the first time and are presented in this thesis.

2. PVP Based SAW Gas Gensors

- Novel electrospun PVP fibers based $LiTaO_3$ SAW sensors were successfully fabricated and exposed to different concentrations of H_2 gas. To the author's best knowledge, the PVP/SAW gas sensing results were investigated and are presented for the first time in this thesis.

- To the best of author's knowledge, no reports were found on the investigations the link of PVP morphology with the gas sensing performance. The author presented the effect of PVP concentrations on morphology with gas sensing performance in this thesis.

3. Graphene Based SAW Gas Sensors

- Graphene layers were synthesized via chemically reduced graphite oxide methods. The synthesized graphene layers were spin-coated on SAW transducers. The novel graphene nano-sheets based SAW sensors were successfully fabricated and tested towards H_2, NO_2 and CO gases. To the author's best knowledge, the developed sensors were investigated for gas sensing applications for the first time in this research.

4. Sb_2O_3 Based Conductometric Gas Sensors

- Novel Sb_2O_3 nanorods and other non-uniform nanostructures were synthesized via thermal evaporation method. The author investigated the optimization of the operational temperature and substrate to obtain the Sb_2O_3 nanostructures. The investigation of the synthesized nanostructure is presented in this thesis.

- The nanostructured Sb_2O_3 were deposited on LGS conductometric transducer. The novel Sb_2O_3 nanorods/LGS conductometric sensors were exposed to different H_2 gas concentrations and investigated at different operating temperatures.

The following papers have been published in refereed journals as well as international conference proceedings by the author based on the work undertaken in this study. Most of the material presented in these papers has been incorporated into this thesis.

- **R. Arsat**, J. Tan, W. Wlodarski and K. Kalantar-zadeh, " Hydrogen gas sensor based on Sb_xO_y nanostructures with a langasite substrate," *Sensor Letters*, vol. 4, pp. 419-425, 2006.

- **R. Arsat**, J. Tan, A. Z. Sadek, K. Shin, D. S. Ahn, C. S. Yoon, K. Kalantar-zadeh and W. Wlodarski, "Camphor sulfonic acid doped polyaniline/diamond nanofibers based ZnO/64° YX $LiNbO_3$ surface acoustic wave H_2 gas sensor," *Sensor Letters*, vol. 6, pp. 947-950, 2008.

- **R. Arsat**, M. Breedon, M. Shafiei, P. G Spizziri, K. Kalantar-zadeh, S. Gilje, R. B. Kaner and W. Wlodarski, "Graphene-like nano-sheets for surface acoustic wave gas sensor applications," *Chemical Physics Letter*, 467, pp. 344-347, 2009.

- **R. Arsat**, X. F. Yu, Y. X. Li, W. Wlodarski and K. Kalantar-zadeh, "Hydrogen gas sensor based on highly ordered polyaniline nanofibers," *Sensors and Actuators B: Chemical*, 2009, 137, pp. 529-532, 2009

- H. Qasim, A. Z. Sadek, **R. Arsat**, W. Wlodarski, I. Belski, R. B. Kaner and K. Kalantar-zadeh, "Optical and conductivity dependence on doping

concentrations of polyaniline nanofibers," in *Proc. Device and Process Technologies for Microelectronics, MEMS, Photonics, and Nanotechnology*, SPIE, Canberra, Australia, 6800, pp. 680012, 2007

- **R. Arsat**, X. F Yu, Y. X. Li, K. Kalantar-zadeh and W. Wlodarski, "Hydrogen gas sensor based on highly ordered polyaniline nanofibers," in *The 12th International Meeting on Chemical Sensors (IMCS)* Ohio, USA, 2008.

- **R. Arsat**, M. Breedon, M. Shafiei, K. Kalantar-zadeh, S. Gilje, R. B. Kaner and W. Wlodarski, "Graphene-like nano-sheets based $LiTaO_3$ surface acoustic wave NO_2 gas sensor," *Eurosensors XXII,* Dresden, Germany, pp. 1132-1135, 2008

- **R. Arsat**, M. Breedon, M. Shafiei, K. Kalantar-zadeh, S. Gilje, R. B. Kaner and W. Wlodarski, " Graphene-like nano-sheets/36 ° $LiTaO_3$ surface acoustic wave hydrogen gas sensor," *The Seventh IEEE Conference on Sensors (IEEE Sensors),* Lecce, Italy, pp. 188-191, 2008.

The author's work has been presented both personally and on her behalf at several international conferences, with the author being fortunate enough to attend the following:

- 7th East Asian Conference on Chemical Sensors, Singapore, December 3-5, 2007.

- 2008 International Conference on Nanoscience and Nanotechnology, Melbourne, Victoria, Australia, February 25-29, 2008.

1.4 Thesis Organisation

The objective of this thesis is to investigate the nanostructured materials in the form of thin films for gas sensing applications. The thesis is primarily devoted to this topic, and is divided as follow;

- Chapter 2 presents the critical literature review on nanostructured polyaniline and its composites, PVP, graphene, and Sb_2O_3 for gas sensing applications. The gas sensing mechanisms of the aforementioned nanostructured materials are also presented in this chapter.

- Chapter 3 discusses in details the SAW transducers and theory behind this device response.

- Chapter 4 outlines the fabrication methods employed to develop transducers used in this research. The author also presents the SAW and conductometric transducers design parameters in this chapter.

- Chapter 5 describes nanostructured material synthesis with particular emphasis on electropolymerization, electrospinning, spin-coating and thermal evaporating deposition techniques.

- Chapter 6 presents the instruments (SEM, XRD, AFM etc) used for the characterization of the nanostructured materials that have been synthesized via methods described in previous chapter. The results obtained from the characterization of nanostructured polyaniline, PVP, graphene, and Sb_2O_3 thin films are presented in this chapter.

- Chapter 7 focuses on the gas sensing performance of the developed nanostructured material based sensors. The four channels computer control gas calibration system that was used for testing the sensors is also described here.

- Chapter 8 concludes the thesis, and suggests the possible future works.

Chapter 2

Research Rationale

2.1 Introduction

Chapter 1 outlined the motivation, objectives and outcomes of this research, as well as some fundamental aspects of nanotechnology, nanostructured materials, and nanotechnology enabled gas sensors. The author also presented the overall organisation of this thesis.

As it is mention previously, the author has investigated the gas sensing performance of four different materials: polyaniline (with and without inorganic nanoparticles), PVP, graphene, and Sb_2O_3. Each of these materials show different properties. Therefore different gas sensing performance are obtained.

Apart from the introduction, this chapter is divided into three main sections. In section 2.2, the author presents the literature review of all four nanostructured materials. Section 2.3 presents their gas sensing performance. Section 2.4 provides the summary of this chapter.

2.2 Review on Nanostructured Materials Used in This Project

In recent years, the blooming development of nanotechnology has attracted many researchers to investigate nanostructured materials for their outstanding properties. An ability to control and tailor nanostructures make it possible to exploit

new physical and chemical properties. Nanostructured materials can be classified into different categories depending on the number of dimensions that are nano-sized such as zero dimensional (quantum dots), one-dimensional (nanofibers, nanorods) and two-dimensional (nano-films). Some of the reasons why these nanoscale structures become very interesting for gas sensing applications are as follow [52-53];

1. They have very large surface to volume ratio, which makes them ideal for use in reacting systems.

2. It is possible for nanoscale design of materials to vary their bulk properties.

3. Nanomaterials can be made functionalized to act as biosensors for DNA or proteins.

4. In nanometre scales, most of the atoms are surface or near surface atoms. This significantly increasing the effective number of sites available for reactions with target molecules.

5. Depletion layer depth or Debye length becomes one of the predominant factor at small grain sizes. It is a measure of field penetration in to the bulk. For most nanostructures the value is comparable to their diameter or width. Under such conditions, the surface chemical processes strongly influence their electronic, electrochemical and electromechanical properties.

In the following section, detail reviews of nanostructured materials that have been used for gas sensing applications throughout this research will be given.

2.2.1 Polyaniline Nanostructures Based Gas Sensors

Polyaniline has received increasing interest since its electric conductivity was found by McDiarmid et al. [54]. Besides, it is also due to its room temperature operation, low fabrication cost, facile synthesis and rich chemistry for structural modification [38-39]. Polyaniline is a unique conjugated polymer and its conductivity can be tailored to a specific application through an acid-base doping process. Studies have shown that polyaniline has three main oxidation states,

which can be seen by noting the color changes ranging from transparent leucoemeraldine, and yellow/green emeraldine to blue/black pernigraniline [37,55]. Emeraldine salt is the most conducting form of polyaniline [56]. When the polymer is doped with acid, an electrically conductive polyaniline is formed which is known as emeraldine salt. At this state, the imine nitrogen is protonated on the polymer backbone and the charge carriers are induced. It appears in green colour and has a characteristic absorbance at around 430 and 800 nm [57]. When the emeraldine salt is treated with a base (eg: NaOH), the colour changes from green to blue with characteristic absorbance peaks centered at 300 and 600 nm. This dedoped form of polyaniline which is known as emeraldine base, has a lower electrical conductivity compared to the emeraldine salt. This emeraldine base can be converted back to salt form upon treatment with acid (eg: HCl) [56]. Conductivity of polyaniline depends on its ability to transport charge carriers along the polymer backbone and for the carriers to hop between the polymer chains. This principle enables polyaniline to be used as a sensitive layer for gas sensing applications.

Conventionally, polyaniline sensing layer is made of compact thin films. Polyaniline gas sensors based on the resistance changes in thin film structures have been studied by a number of researchers [35,58-60]. Agbor et al. [35] have deposited polyaniline thin film using several different methods which are spin-coating, evaporation and Langmuir-Blodgett (LB) techniques. They observed that both spin-coated and LB polyaniline thin films appeared blue on glass substrates, indicating that emeraldine base are formed. For evaporation polyaniline thin film, the colour only changes from colourless to blue after prolonged exposure to air/moisture. The polyaniline thin film/chemiresistors were tested towards NO_x, H_2S, SO_2, CO and CH_4. However, these three types of chemiresistors do not show any response towards CO and CH_4. Via self-assembly method, Li et al. [58] fabricated polyaniline ultrathin films based on doping-induced deposition effect of emeraldine base. The films were deposited onto silicon, quartz and alumina substrates with printed silver electrodes and exposed to NO_2 and NH_3. NO_2 caused an increase in the conductivity of the polyaniline thin film which is contradictory to the results obtained by Agbor et al. [35]. This may be caused by the different protonation states of the used polyaniline. The NH_3-sensing mechanism is based on the dedoping of polyaniline by basic NH_3, since the conductivity is strongly dependent on the doping level. Xie et al. [59] have

investigated the sensing performance of ultra-thin film polyaniline based conductometric sensors towards NO_2. They prepared various numbers of layers of pure polyaniline film, as well as composite of polyaniline and polystyrene-sulfonic acid (PSSA) via LB and self-assembly (SA) methods. From the gas sensing results, polyaniline prepared by LB technique exhibits good sensitivity, whereas the one prepared via SA method shows faster recovery. Recently, Shrivas et al. [60] have exposed spin-coated polyaniline thin film/electro-chemical sensors towards NH_3 gas. They found that the resistance of the film decreases with the increase in concentration of NH_3 at known volume. The adsorption of NH_3 affects the swell and uniformity of the films which can be controlled by the molecular volume of the vapour.

Nanostructured polyaniline possess large surface area per unit mass. These nano-scale structures permit easier addition of surface functionality and interaction compared to traditional polyaniline which is highly agglomerated. When deposited as a thin film, polyaniline nanostructures form porous structure, hence have higher surface to volume ratio [41] and larger penetration depth [61] than the traditional thin film polyaniline. There have been several reports on improving polyaniline based sensors sensitivity by depositing polyaniline nanostructured form as a sensing layer [12]. As a result, most literature reports on polyaniline nanostructures indicate that nanostructured outperforms conventional polyaniline for sensing applications [13,40,62]. Compared to the conventional polyaniline, the porous structure of polyaniline nanofibers film allows gas molecules diffused easily into and out of the film, therefore lead to rapid diffusion of gas molecules.

This research concentrates on the synthesis of nanostructured polyaniline on SAW transducers. To date, several methods have been employed for the synthesis of polyaniline nanostructures. Most popular polyaniline synthesis technique is via chemical polymerization, where an oxidant is required to be added to an acid aqueous mixture of aniline monomer to initiate the polymerization [63-66]. The synthesized polyaniline is then spin-coated [65] or drop-casted [67-69] onto respective transducers to be used as sensors. The latter is the most used method for depositing polyaniline on SAW transducers [67-71] followed by airbrush method [72].

Via the abovementioned method, polyaniline nanofibers in bulk quantity are

successfully polymerized [73]. By drop-casting polyaniline nanofibers onto the conductometric transducers, Huang et al. [12] formed polyaniline nanostructures sensing films and investigated its sensitivity towards HCl vapour. Unlike the conventional polyaniline thin film gas sensors which their sensitivity depends on the film thickness [59], the performance towards HCl vapour is found unaffected by the thin film thickness of drop-casted polyaniline. They also showed that dedoped polyaniline nanofibers based conductometric sensors are much less responsive than their doped counterparts [12]. However, Sadek et al. [67] work on dedoped polyaniline based gas sensors recently has proven that previous statement is not completely right for many gas targets. Dynamic responses of the tested sensors revealed that dedoped polyaniline based sensors have faster response towards H_2 gas and good repeatability compared to doped polyaniline based sensors.

In review presented in Table 2.1, most researchers employed drop-casting method for polyaniline deposition on SAW devices. Except for electropolymerization method, others required separate polymerization (chemical polymerization) before being deposited onto the SAW transducers. In this research, the electropolymerization technique is the author's interest in deposition of polyaniline nanofibers onto SAW transducers. Besides its ability to polymerize and deposit the polyaniline at the same time, this technique provides better control of film thickness and morphology. Furthermore, this method produces more homogeneity distributed polymer when compared to chemical polymerization [74]. The details of the electropolymerization method will be given in chapter 5. Kalantar-zadeh et al. [75] have pioneered the deposition of polyaniline nanofibers on SAW device via this technique. They electropolymerized continuous films even in between electrodes and obtained a 6.2 kHz frequency shift when a polyaniline nanofibers based 64° YX $LiNbO_3$ SAW sensor was exposed to 0.125% H_2 gas. They observed that non-agglomerated, continuous and homogenous films could be obtained when the gaps on the working electrodes were smaller than several tens of microns.

For the electropolymerized polyaniline, the author deposited polyaniline nanofibers thin films with different thicknesses onto SAW sensors. Besides, the author also varied the acid concentration of the electrolytes to investigate the effect on gas sensing performance. In addition, the author replaced HCl acid with HNO_3

Table 2.1: SAW based sensor device comparison.

Sensitive Layer	Deposition Method	Analyte Gas	Freq. shift	Ref.
PANI	drop-cast	H_2	3 kHz	[68]
PANI**	airbrush	NH_3	4 ° (phase shift)	[72]
PANI	drop-cast	NH_4OH	20 kHz	[70]
PANI**	airbrush	NH_3	0.03 (sensitivity)	[76]
PANI	electropolymerization	H_2	6.2 kHz	[75]
PANI/In_2O_3	drop-cast	H_2, NO_2, CO	11, 2, 2.5 kHz	[77]
PANI	drop-cast	H_2	3.04 kHz	[68]
PANI#	drop-cast	H_2	28 kHz	[66]
PANI*	drop-cast	H_2	79 kHz	[71]
PANI/WO_3	drop-cast	H_2	7 kHz	[78]
PANI/SnO_2	drop-cast	H_2	7 kHz	[61]

**PANI dissolved in NMP, #PSSA doped PANI, *CSA doped PANI

acid to obtain different morphology of polyaniline. The gas sensing performance of all the developed sensors will be presented in chapter 7.

2.2.2 Polyaniline/Inorganic Materials Nanocomposite Based Gas Sensors

There has been tremendous effort for enhancing polyaniline performance by combining it with inorganic materials to form composites. The composite may be tuned to alter the physical and chemical properties of polyaniline, thus may improve the sensing properties. Such composite can operate at room temperature and the sensitivity can be optimized by the volume ratio of nanosized inorganic materials. The morphology of the nanocomposite materials not only depends on the properties of their constituents, but also on their combined morphology and interfacial characteristics [31]. This may lead to the enhancement of the properties of the pure polyaniline materials for applications in electronics and optics.

A number of researchers have already developed polyaniline/inorganic nanocomposite sensors. Geng et al. [79] reported that their polyaniline/SnO_2 composite based sensors are sensitive to acetone and ethanol vapours when operated at 60-90 °C. Sadek et al. [77] have fabricated a polyaniline/In_2O_3 nanofiber composite sensor for CO, NO_2 and H_2 gas sensing applications. Then another

composite of polyaniline/inorganic material has been developed by Conn et al. [65]. They investigated that the polyaniline/PtO_2 based sensors produces 10 times larger response magnitude for H_2 gas compared to pure polyaniline sensors. Ram et al. [80] have developed polyaniline/SnO_2 and polyaniline/TiO_2 ultrathin films and showed that both are sensitive to CO gas. Furthermore, few attempts also have been carried out involving polyaniline and titanium dioxide to improve the sensitivity [81-82]. Su et al. [81] have carried out in-situ polymerization to synthesize polyaniline/TiO_2 composite. Moreover, Tai et al. [82] have synthesized polyaniline/TiO_2 nanocomposite thin films using a combination of electrostatic self-assembly and in-situ chemical oxidation polymerization technique. They examined the effect of NH_3 and CO on the thin films.

In the following subsection, the author will present the literature review on composites of carbon nanotubes (CNTs) and diamond based gas sensors. These two materials that have been used as a composite materials with polyaniline.

Polyaniline/Carbon Nanotubes Based Gas Sensors

The advent of CNTs has strong influence in the field of materials. As mentioned previously, the author believes that another option in improving the sensitivity of polyaniline based sensors is employing its via composite with other materials. This is due to the new synergetic or complementary behaviours of the composite of organic and inorganic materials can be obtained which may show possible sensing applications.

Ma et al. [83] suggested that addition of CNTs is one of the effective ways to modify the properties of polyaniline. They prepared the nanostructured polyaniline composite film via carbon nanotube seeding approach. The conductivity of the prepared composite film based conductometric sensor was measured on exposure to the trimethylamine and HCl vapour in N_2 gas. Wanna et al. [84-85] investigated the sensing characteristic of polyaniline-CNTs for CO gas. They found that the existence of CNTs in polyaniline thin film sensor has increased the sensor sensitivity [84]. They also observed that the polyaniline-CNTs composite based gas sensor prepared via electrospinning technique possessed two to four times higher sensitivity from those prepared via solvent casting technique

[85]. This may be attributed by the porosity of the electrospun polyaniline-CNTs composite thin film. Furthermore, the use of polyvyinyl alcohol during the solution preparation may contribute to the CO adsorption.

Chang et al. [86] established one pot synthesis of polyaniline/MWNTs nanocomposite with the Au particles dispersed in polyaniline. The Au/ polyaniline/ MWNTs nanocomposite based gas sensors were exposed towards NH_3 gas. Similar to pure polyaniline based gas sensors, the resistance of the nanocomposite increased upon exposure towards NH_3 gas. Although these sensors showed a good repeatability and stability, they displayed a nonlinear response when the NH_3 concentration was above 10ppm.

Since in this research the author will use electropolymerization technique in depositing polyaniline onto the whole area of SAW transducer, it is necessary for the CNTs to homogeniously dispersed in the aniline monomer. At the same time the CNTs should not be aggloromerated upon adding the HCl [87].

Recently, Li's group has reported on their achievements in obtaining well-dispersed carbon nanotube/polyaniline composite films [88-89]. By refluxing the CNTs in aniline monomer, the composite of CNTs/polyaniline were synthesized successfully via electropolymerization. However, no reports were found in extending the successed deposited composite for gas sensing applications. In this research, the author will use almost a similar method to that of [88-89], and investigate the gas sensing performance.

Polyaniline/Diamond Based Gas Sensors

Unlike polyaniline/CNTs composite material, to the best of author's knowledge, there is no report on polyaniline/diamond composite.

Diamond has been successfully used for sensing applications due to its high stability towards many chemical agents [90]. Diamond also has exceptional mechanical, thermal, electrical and chemical properties. In addition, due to its hardness and high wear resistance, diamond AFM probes were fabricated for MEMS applications [91]. Wide bandgap materials such as diamond are also attractive candidates for developing gas sensitive composites. Gurbuz's group

[48,92-93] has developed polycrystalline layered diamond-based gas sensors using Pd/i-diamond/p-diamond diode structures. The sensors were exposed to hydrogen gas. It was found that the H_2 sensitivity is large, repeatable and reproducible. Due to the distinctive diamond's properties, its combination with conductive polymers can result in materials with unique sensing capabilities. This has attracted the author to deposit polyaniline and diamond composite onto the whole area of SAW transducer. It is proposed that polyaniline/diamond composite based sensor is an excellent choices for gas sensing applications.

2.2.3 Polyvinylpyrrolidone Based Gas Sensors

Polyvinylpyrrolidone or PVP (Fig. 2.1) is one of the acetylene chemistry products founded by Prof Walter Reppe [94]. After 60-years, PVP has been extensively used especially in the pharmaceutical, cosmetic and food industries. It has high solubility in water and various organic solvents, film formation, as well as good adhesiveness to various substrates. PVP is also used as organic capping agent to stabilize clusters and prevent agglomeration of particles. This resulted in an even distribution of the colloidal system [95-97]. By using different polymerization and deposition techniques, as well as through co-polymerization, the properties of PVP can be further modified and improved. In recent years, PVP has found many new applications such as in MEMS [98], photonic [99] and dye-sensitized solar cells [100] applications.

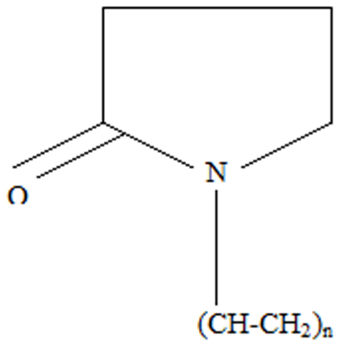

Figure 2.1: Chemical structure of PVP.

In most cases, PVP usually presents as an essential auxiliary, not as an active substance itself. Many reports found that PVP plays a significant role in controlling morphologies of other materials. Tsuji et al. [101] have added PVP in ethylene glycol and $NaNO_3$ solution in the preparation process of Pt nanoparticles. Their finding shows that PVP molecules are important in directing the growth of branched Pt nanoparticles. Besides, by increasing the amount of PVP, the shape of Au nanostructures can be changed from spheres to rods, tubes, and capsules [102]. In other literature, the diameter of polystyrene spheres shown to be controlled by adding and altering the amount of PVP in the polymerization of styrene [103-105].

In literature, PVP has been used in sensing applications. Mirmohseni et al. [44] have casted PVP solution with different PVP concentrations on top of quartz crystal electrodes. The sensors were used for determination of ammonia and aliphatic amines. They also exposed the sensors towards NO_2, CO and CO_2 but the frequency shifts were less than 3 Hz. PVP also has been used to modify the ZnO nanoparticles for gas sensing applications [45]. Tang et al. [45] fabricated conductometric sensors with different molar ratios of Zn^{2+}:PVP. They found that for pure PVP, the sensitivity is smaller than that of equal ratio of Zn^{2+}:PVP. Using the similar materials, Du et al. [106] have prepared ZnO nanoparticle-dispersed PVP composite by sol-gel dip-coating technique for superoxide radical sensor. Then De Queiroz et al. [107] have utilized the sorption and diffusion of water vapour in polymeric membrane [108] by using doped PVP with cobalt (Co) and iodine (I_2) for humidity sensors. By measuring the conductivity, they found that PVP-I_2 sensor gives the best response to the environment humidity. Furthermore, composite of PVP and carbon black also has been used in novel temperature modulation technique for vapour identification [109].

In this research, the author electrospun PVP and it composites onto SAW transducers. The sensing performance of the developed sensors were investigated upon exposure towards H_2 gas. The details of the gas sensing results will be presented in chapter 7.

2.2.4 Graphene Nano-sheets Based Gas Sensors

Graphene is the basic building block of graphitic materials as it comprises of two-dimensional layers of sp^2-bonded carbon [46,50]. This one atom thick, single carbon layer is densely packed; a consequence of its six-fold aromatic (benzene-like) ring structure. The current interest in graphene arises from its possible applications in nano-electronic devices. In contrast to current semiconducting materials and graphite, a single graphene layer has no electronic bandgap. Hence, it has an ability to exhibit a metallic-like conductivity even at room temperature [110]. Ballistic electronic transport [111] and unusual quantum Hall effects [112] have also been reported.

With graphene's large surface area and unique electronic properties, several groups have already begun investigating graphene based chemical sensors [113-115]. As a two-dimensional material, it should be well-suited to the sense of adsorbates. Reversible H_2 gas adsorption isotherms have been reported [113] using different graphene preparations with relatively high loadings, which is an important condition for sensing elements. Schedin et al. [115] have reported that the adsorbed gas molecules are able to increase the graphene charge carrier concentration, augmenting the sensitivity of the material. Their Hall measurements revealed that NO_2 has acted as an acceptor and CO as a donor. This illustrates that upon exposure, the graphene surface has become p-type. Moreover, Joshi et al. [114] have fabricated and tested graphene based field effect transistors for gases such as Cl_2 and O_2. They showed that these gases are also readily desorbed from graphene based sensors.

To investigate the performance of graphene as sensing layers, the author deposited graphene on SAW transducers. The developed sensors then exposed to H_2, NO_2 and CO gases. The gas sensing results will be presented in chapter 7.

2.2.5 Antimony Oxide Nanostructures Based Gas Sensors

Antimony oxide (Sb_2O_3) is an important member of V-VI main group elements which has been widely used in industry. Sb_2O_3 is popularly known as a flame

Table 2.2: Antimony oxide states

Antimony Oxide	Symbol	Melting Point
Antimony (III) Oxide	Sb_2O_3	655 °C
Antimony (III, V) Oxide	Sb_2O_4	-
Antimony (V) Oxide	Sb_2O_5	380 °C

retardant [116-119], usually in combination with halogen compounds [120-122] or used as a synergist in plastic industry [123]. Sb_2O_3 is also broadly used as a catalyst for selective oxidation of substitutes aromatics and oxidation of paraffins [124], fining agents and filler materials [116]. While Sb_2O_3 is an interesting semiconductor material with a unique optoelectronic and optical properties just like other well known metal oxide semiconductors, scant attention has been given to it since it is an indirect-gap semiconductor with low emission efficiency [125]. Sb_2O_3 is the most popular form of antimony oxide, other possible stochiometries are shown in Table 2.2.

Pure antimony oxide has received inadequate attention for its sensing properties. Ozawa et al. [126] found Sb oxide to have high proton conductivity, which makes it a promising humidity sensing material. Gas sensors with a single-phase film of antimony (III) oxide have been tested for their response towards ethanol vapour at variety of operating temperatures and concentrations [127]. This experiment showed the best response (R/R_0) is 1.47 for 100 ppm ethanol at 400 °C operating temperature. Haycock et al. [128] reported that senarmontite Sb_2O_3 based sensor has very high electrical resistance at room temperature and the resistant only drops to a few GΩ at 400 °C. Consequently, they showed that when 663 ppm of methanol gas is given at 400 °C, the response of the senarmontite film depicts a drop of about 450 MΩ, followed by recovery on the removal of the test gas. Myers et al. [129] tested thin films of cadmium doped and nickel doped antimony oxide on three different categories of reducing, oxidising and acid gases. At 300 °C, 50 ppm NO_2 gave the highest sensitivity. This report also showed that there are significant sensitivities for other gases (CO, CH_4, SO_2 and H_2S) but not as high as NO_2. Besides the sensor's performance can be improved by addition of the right catalysts and other compounds.

In this research, the author synthesized Sb_2O_3 nanostructures on conductometric devices for gas sensing applications. Details of the synthesization, char-

acterization and gas sensing results will be explained in chapter 5, 6, and 7 respectively.

2.3 Gas Sensing Mechanism of Nanostructured Material Based Sensor

The theory of gas sensing varies in different materials. Due to the various effects and dependencies in gas sensing mechanism, many models and theories have been proposed [54,130-134]. Several of these gas sensing mechanisms and models will be employed depending on the class materials, in order to gain an overall understanding into the sensing mechanism of polyaniline, PVP, graphene and Sb_2O_3 based sensors.

2.3.1 Gas Sensing Mechanism of Conducting Polymer Based Sensors

Conducting polymers such as polypyrrole, polyacetylene and polyaniline have received enourmous attention for their potential technological applications. This is due to their ability to display simultaneously both mechanical properties of a polymer and electrical properties of a conductor [135]. Besides, these materials offer several other advantages as sensing properties; ease of deposition onto a wide variety of substrates, low fabrication cost, room temperature operation (low power consumption) and rich structural modification chemistry [38,136].

Polyaniline is a special conducting polymer because its doped/dedoped state can be controlled by acid/base reactions. By changing the doping level and morphology, the conductivity of polyaniline can be altered for specific applications such as electrochromic devices [37], rechargeable batteries [36], anticorrosion and antistatic coatings, electromagnetic interference shields [137] and sensors [68-69]. In this PhD research, the author has selected polyaniline from the conducting polymer group and synthesized it in its nanostructured form for gas sensing applications.

Polyaniline gas sensors based on measuring the resistance changes in thin film structures have been previously investigated by a number of researchers. A

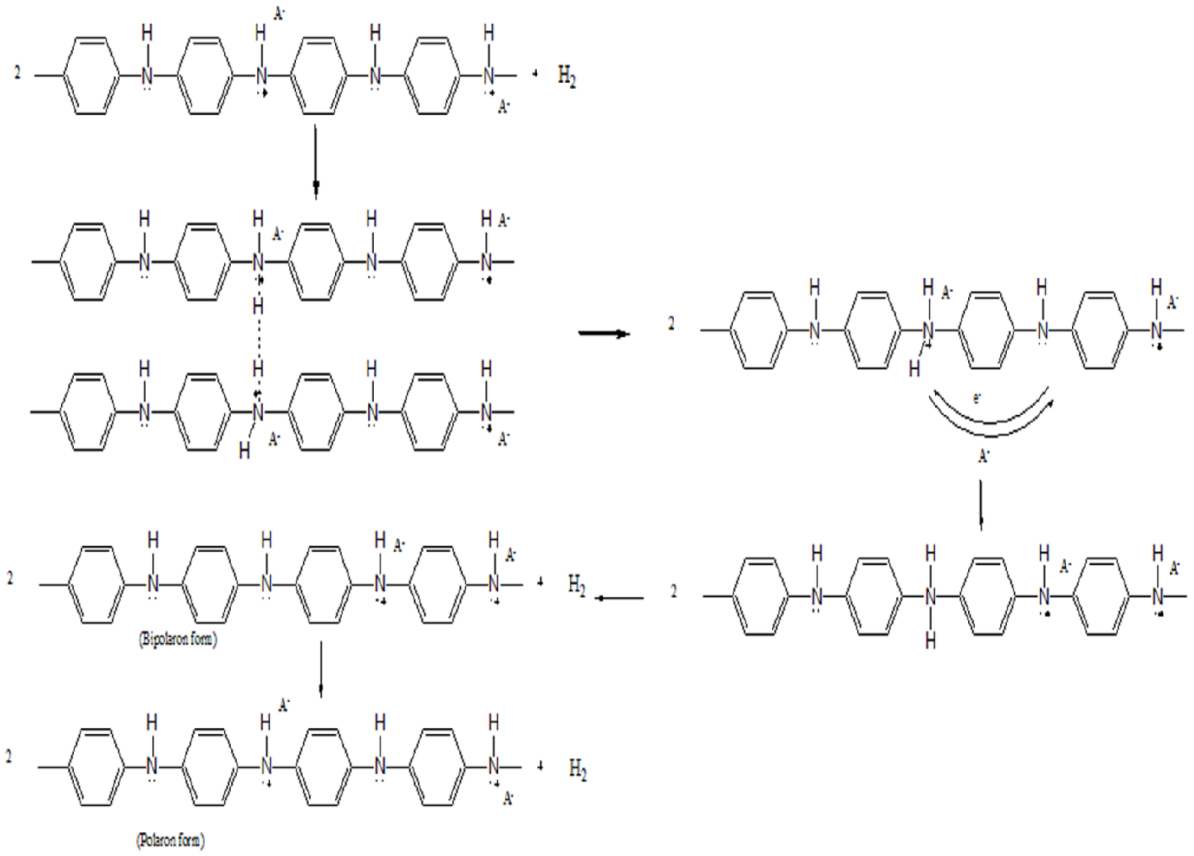

Figure 2.2: Possible mechanism for hydrogen interaction with polyaniline where A^- represents the counteranion [130].

detailed review of polyaniline sensors can be found in several references such as [138-139]. The mechanism for polyaniline and hydrogen interaction is still not completely clear. The author believes that the H_2 may form a bridge between nitrogen atoms on two adjacent chains or there may be partial protonation of some of the imine nitrogen [54]. McDiarmid [54] has proposed a possible mechanism of hydrogen gas sensing with polyaniline. The proposed mechanism is presented in Fig. 2.2 where A^- represents the counteranion [130]. Here, hydrogen interacts with doped polyaniline at the charge amine nitrogen sites. H_2 bond dissociation follows with formation of new $N-H$ bonds to the amine nitrogen of the polyaniline chain. Subsequent charge transfer between adjacent amine nitrogen returns the polyaniline back to its polaronic, doped, emeraldine salt state with a release of H_2, making this reaction fully reversible [31,130].

In this PhD study, the author also assessed the sensing performance of dedoped polyaniline based sensor towards H_2 gas. Although, Virgi et al. [130] found no response towards H_2 gas for dedoped polayniline nanofibers, Sadek et al. [67] verified that there is interaction between hydrogen molecules and polymer chain of dedoped polyaniline. As imine/amine ratio of emeraldine film can be affected by the base concentration [63], it is known that only upon exposure to a very strong base the emeraldine salt can become an insulator [73]. As the weak base is used in these experiments, author believes this attributes to the amount of imine and amine in the polymer chains. Therefore, this probably enables the interaction of hydrogen molecules with dedoped polyaniline. H_2 gas may formed a bridge between nitrogen atoms on two adjacent chains or there may be partial protonation of some of the nitrogens in imine group [54].

The mechanism for the conductivity change in polyaniline nanocomposites with other inorganic materials due the interaction with H_2 is not yet fully understood. Sadek et al. [61,77-78] have proposed two possible mechanisms of polyaniline/metal oxide nanocomposite towards H_2 sensing. The first one is the activation of hydrogen molecules by the metal oxide due to the formation of metal-dihydrogen complexes. Second possible mechanism is due to the closer packing by the inorganic material, thus dissociation of the hydrogen molecules is stimulated by interaction with free spin on adjacent polyaniline chains. Conn et al. [65] have developed polyaniline/PtO_2 based sensors and exposed them to H_2 gas. They found that PtO_2 is partially reduced after H_2 treatment. Therefore, the increment in H_2 sensitivity can be reponsible by PtO or reduced Pt metal.

2.3.2 Gas Sensing Mechanism for non-Conducting Polymer Based Sensors

It is well known that polymer films are one of the alternatives of chemical interfaces to detect organic vapors due to their ability to work at room temperature, high sensitivity, fast vapor diffusion, and reversible response [140]. For polymer film, viscoelastic properties are important for chemical sensors. Polymers with this property have high vapour permeability and low crystallinity [131,141].

Polymer coated acoustic wave devices are well established in the research community and have already entered several stages of commerciallization. The

interaction between polymer and analyte gas is based on sorption-desorption phenomena [141]. The sorption or desorption of analyte gas into the polymer matrix is kinetic in nature. During the exposure of the polymer based gas sensor, the analyte molecule is transported to the surface of a coating and adsorbed to the polymer surface. The adsorbed molecule then diffuses into the bulk of the material, and experience some residential time before returning to the surface and desorbs [141]. Fig. 2.3 illustrates the absorption of vapour molecules from the gas phase into the sorbent thin film of the sensor device [131].

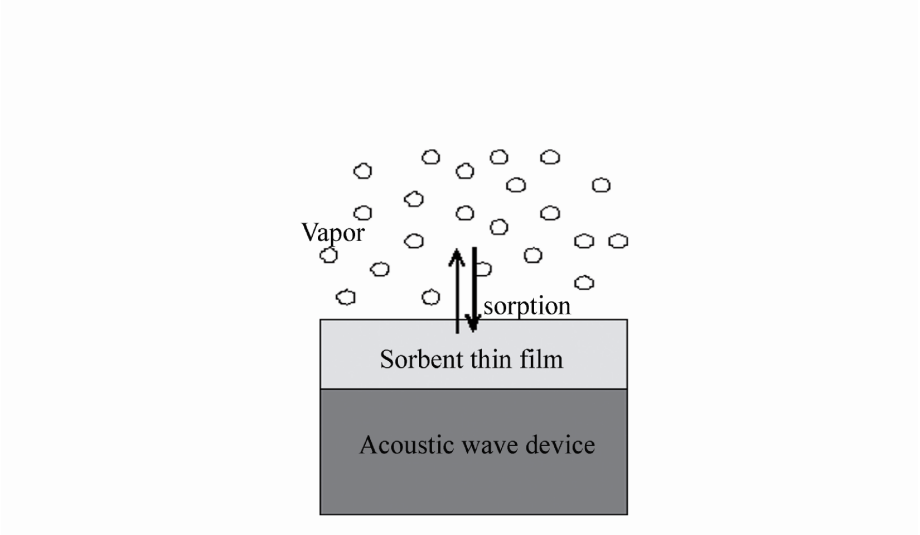

Figure 2.3: Schematic diagram of the sorption of vapour molecules into thin film on a sensor [131].

The mechanism between PVP with analyte molecules is mainly based on hydrogen-bond based interactions [44,142-143]. PVP is considered as a strong hydrogen bond acceptor due to the carbonyls of nitrogen in its chemical structure as shown in Fig. 2.1. This carbonyl group enables a hydrogen atom attach to an adjacent atom [144]. Therefore, upon exposure to H_2 gas, the following reactions may occur:

$$H_2 \rightleftarrows 2H^+ + 2e^- \tag{2.1}$$

$$\begin{array}{ccccccccccccc} & & O & & & & & & O & & & & \\ & & \| & & & & & & \| & & & & \\ - & C & - & N^- & + & H^+ & \rightleftarrows & - & C & - & N & - & H \end{array} \tag{2.2}$$

Besides the hydrogen-bond based interactions, PVP's interaction with analyte molecules can also depend on solubility properties [143]. For example, although dimethyl methylphosphonate (DMMP) does not show any exceptional hydrogen bonding ability, PVP based sensor is still able to show significant response towards this vapour. Therefore there is a possibility that such a response is contributed by the solubility property [143].

2.3.3 Gas Sensing Mechanism for Graphene Based Sensors

Graphene has emerged to become an exciting new material of carbon with many fascinating electronic properties such as the fractional quantum Hall effect at room temperature [112], ballistic electronic transport and zero band gap. These properties make graphene a promising material for future electronics devices.

The good sensing properties of carbon nanotubes are well known, but recently the possibility to use graphene as a gas sensing layer has also been reported. There are three important facts that make graphene an excellent material for gas sensors:

- graphene is highly conductive, exhibiting metallic-like conductivity even in the limit of zero carrier density [115,132];
- graphene is a 2D crystal with only a surface and no volume. This in fact helps in maximizing the effect of surface dopants [115,132];
- graphene has few crystal defects [145]. This will ensure a low level of $(1/f)$ noise caused by their thermal switching [115].

The operational principle of graphene based devices can be described by the increase or decrease in graphene charge carrier concentration which is induced

by the adsorbed gas molecules on graphene surface. The sensor response is measured on changes in resistivity due to molecules adsorbed on the graphene. Therefore, the adsorbed molecules act either as donors or acceptors.

Graphene is a p-type material [114-115], therefore holes are the majority carriers. Upon exposure towards reducing gas such as H_2 and CO, these gases always act as donors [132-133]. The reducing gas releases electrons, induces extra recombination with holes. Therefore, resulting in a decrease in concentration of the majority carriers and increase of resistance [115].

Opposite to the CO and H_2 gases is the charge transfer from the oxidising gas molecule NO_2 to graphene [132]. Upon exposure towards NO_2, more holes are created as a charge carrier on graphene surface, thus decrease the resistance.

Leenaert et al. [132] and Arellano et al. [133] have proposed three possible configurations of graphene's adsorption sites which are (A) upon one carbon atom, (B) upon the center of a carbon-carbon bond, and (C) upon the center of a hexagon of carbon atoms. Both have used density functional theory (DFT) to perform the first principles calculations of gas molecules adsorbed by graphene.

The investigation towards H_2 began by identifying the four unique orientations and positions that might occurs onto the surface of graphene based sensor. It is assumed that hydrogen could either lie perpendicularly or parallel to the plane of graphene sheet. From these configurations, the binding energy are calculated to be less than 0.1 eV and the adsorbate surface distances are between 5.07 Å and 5.50 Å [133]. The details of calculated binding energy and distance for H_2 being adsorbed by graphene surface are shown in Table 2.3. From the table, the most favorable position for H_2 being adsorbed by graphene surface is in the position above the center of a carbon hexagon. Whereas, the parallel position is slightly preferable than the perpendicular one.

Similar to H_2, CO also has been investigated via the DFT method [132]. Three different orientations were used for the CO molecules. One is parallel to the surface and the other two are perpendicular to the surface, either with the O atom above the C atom (O-C) or the other way around (C-O). The details of the adsorbate surface distances and binding energy with respect to their orientations are shown in Table 2.4. From the table, it is calculated that the binding energy

Table 2.3: H_2 on graphene: the binding energy and distance of H_2 above graphene surface [133].

Position	Orientation	Binding Energy (eV)	Distance (Å)
A	perpendicular	0.070	5.50
B	perpendicular	0.072	5.49
C	perpendicular	0.083	5.25
C	parallel	0.086	5.07

Table 2.4: CO on graphene: the binding energy and the distance of CO above graphene surface [132].

Position	Orientation	Binding Energy (eV)	Distance (Å)
B	O-C	0.01	3.75
A	O-C	0.0096	3.75
C	O-C	0.0131	3.73
A	C-O	0.0084	3.72
C	C-O	0.0096	3.70
B	parallel	0.014	3.74
C	parallel	0.0141	3.74

falls between 0.008 to 0.02 eV. Furthermore, the distance between adsorbed CO molecules are in the range of 3.70 - 3.75 Å above the surface of the graphene.

Leenaerts et al. [132] reported the adsorption of NO_2 onto graphene, with three different orientations of NO_2 molecules at 0 K. The three orientations are the N-O bonds pointing up (O-N), down (N-O) and parallel to the graphene surface. It is found that NO_2 adsorbs between 3.61 Å and 3.93 Å above the surface of the graphene sheet, with binding energies ranging between 0.05 and 0.07 eV. The large spacing between the adsorbate and the graphene surface combined with the small binding was energies reported. Table 2.5 presents the details of the calculated parameters mentioned previously.

Referring to the calculated binding energy presented in these three tables, less than 0.1eV of binding energy are obtained. Therefore, it is concluded that the gas molecules are being physisorbed [133] by the graphene surface.

Table 2.5: NO_2 on graphene: the binding energy and the distance of NO_2 above the graphene surface [132].

Position	Orientation	Binding Energy (eV)	Distance (Å)
B	O-N	0.0674	3.61
A	O-N	0.0653	3.61
B	O-N	0.0626	3.64
A	N-O	0.0547	3.83
C	N-O	0.0545	3.93
C	parallel	0.0667	3.83

2.3.4 Gas Sensing Mechanism for Metal Oxide Based Sensors

Semiconducting metal oxides (MOS) such as tin oxide (SnO_2), titanium dioxide (TiO_2), zinc oxide (ZnO) and indium oxide (In_2O_3) have been investigated comprehensively as gas sensing layers since the first report by Seiyama et al. [146]. The metal oxide gas sensing mechanism begins at the surface of the material. It involves adsorption of the gas molecules which can be distinguished to physisorption and chemisorption. Physisorption is defined by weak attraction caused by van der Waals forces and usually occurs betwen the gas molecules on oxide surface at the range of -200 to 0 °C. Whereas for chemisorption, it occurs at operating temperature of 0-500 °C. This type of adsorption can be defined as the high surface energy results in the gas adsorbing and exchanging electrons with the surface. At high temperatures, oxygen vacancies diffuse quickly from the interior of the grain to the surface or vice-versa.

At elevated temperatures, stoichiometry of MOS changes as a function of the ambient oxygen. The well-known relation between the electrical conductivity of the metal oxide, σ and the partial pressure of the gaseous oxygen, $p(O_2)$ is [31,147]:

$$\sigma = \sigma_o \exp(-E_a/k_B T) p(O_2)^{1/n} \tag{2.3}$$

where, k_B and T are Boltzmann's constant and temperature, respectively. E_a is the sum of the activation energies that are required to form the ionic defects, and the subsequent ionization to form charge carriers in the conduction or valence band. The absolute value of n from previous equation depends on the nature of

the point defect arising when oxygen is removed from the lattice. The sign of $1/n$ depends on the conduction type. For n-type conduction, the value of $1/n$ is negative and for p-type conduction it is positive. It is widely known that most MOS gas sensors operate by the adsorption of ambient oxygen, which leads to a high resistance for n-type metal oxide and a low resistance for p-type metal oxide. From Eq. 2.3, it is important to select oxygen sensitive materials with small E_a and large $1/n$ to obtain oxygen sensors with a good sensitivity to changes in the specific oxygen pressure.

The chemistry of metal oxide and gas molecules interactions is similar to both polycrystalline and nanostructured materials based sensors. Therefore at some extent, the theories of conventional gas sensing still apply to the nanostructured MOS based sensors. In addition to that, gas sensing mechanism for nanostructured material based sensors are also influenced by crystallinity and quantum effects.

The sensing mechanism in metal oxides is related to ionosorption of species over the surface. Oxygen and water are the most important ionosorbed species when a sensor operates in ambient air. In the operating temperature range between 100 and 500 °C, oxygen in molecular (O_2^-) and atomic (O^-) forms ionosorb over metal oxide. O^- dominates the ionosorption at higher temperatures while for lower operating temperature up to 200 °C, it dominates by O_2^- since it has a lower activation energy than the other one [134]. These negatively charged oxygen adsorbates play an important role in sensing gases such as H_2, CO and NO_2. When the metal oxide based sensor is exposed to a reducing gas such as H_2, the following reactions may occur:

$$H_{2,gas} \rightleftarrows H_{2,ads} \tag{2.4}$$

$$H_{2,ads} + O^-_{ads} \rightleftarrows H_2O + e^- \tag{2.5}$$

From the Eq. 2.5, it is obvious that the electrons trapped by the oxygen adsorbates return to the oxide surface. The overall effective change in the density of the ionosorbed oxygen is detected as an increment in sensor conductivity. Direct adsorption is also proposed for oxidising gaseous species such as NO_2 result in the decrease of sensor conductivity [134]:

$$NO_{2,gas} \rightleftarrows NO_{2,ads} \tag{2.6}$$

$$e^- + NO_{2,ads} \rightleftarrows NO^-_{2,ads} \tag{2.7}$$

The Eqs. 2.6 and 2.7 show that the occupation of surface states increases the surface potential and reduces the overall sensor conductance.

Korotcenkov's review on the structural and physical-chemical properties of nanoscaled metal oxide film has shown that both film thickness and agglomeration also play an important role in gas response [148]. According to Korotcenkov et al. [149], the gas sensing matrix of agglomerated polycrystalline films can be schematically presented as an equivalent circuit (Fig. 2.4). In Fig. 2.4, $R_{(a-a)}$ represents the resistance of inter-agglomerate contacts, R_c is the resistance of inter-crystallite contacts, R_b is the bulk resistance of crystallites, and R_{agl} is the resistance of agglomerate. This scheme shows that four gas sensitive elements can determine the gas response, which are:

- inter-grain (inter-crystallite) contacts (R_c);
- interagglomerate contacts ($R_{(a-a)}$);
- agglomerates (R_{agl});
- grains (R_b).

In Fig. 2.4, the agglomerate resistance is an integral resistance, representing of three dimension grain network. It is observed that the change in the above-mentioned gas sensing elements will effect the sensor's gas sensing parameters, therefore effect the gas response. Low gas permeability of agglomerates promotes the increase of influence of inter-agglomerates contact on gas response.

With regards to morphology, simple distinction can be made between compact layers and porous layers. For compact layer, the interaction between gases occurs only at the surface. Furthermore, there are at least two types of depletion formed: completely or partly depletion layers, depend on the ratio between layer

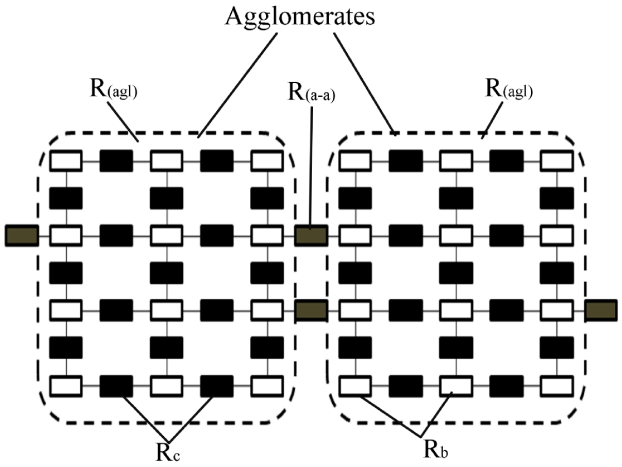

Figure 2.4: Principle electrical circuit of agglomerated polycrystalline film.

thickness and Debye length λ_D. λ_D (the space charge layer thickness) can be defined using the formula of Debye length obtained in the Schottky approximation [150]:

$$\lambda_D = \sqrt{\frac{\varepsilon\varepsilon_0 k_B T}{q^2 n_b}} \tag{2.8}$$

where ε and ε_o are the permittivity of the medium and vacuum, respectively, k_b is the Boltzmann constant, T is the absolute temperature in Kelvins, q is the elementary charge and n_b is the concentration of free charge carriers (electrons).

In contrast with compact layers, the whole volume of porous layer is accessible to the gases. Fig. 2.5 depicts the porous sensing layer with its geometry and energy band λ_D and mean diameter of grain size X_g [150]. X_g of grains and crystallites in metal oxide have great influences on the gas sensing properties. For example, the sensing performance of SnO_2 nanoparticles based sensors towards target gases increases drastically if the particle diameter is placed in the range of several nm [151]. Therefore, it shows that sensor sensitivity increases with decreasing grain size [152-153]. For polycrystalline, the grain size effect can be summarised as follow;

- Grain/crystallites large enough to have bulk region unaffected by surface phenomena ($d \gg \lambda_d$);

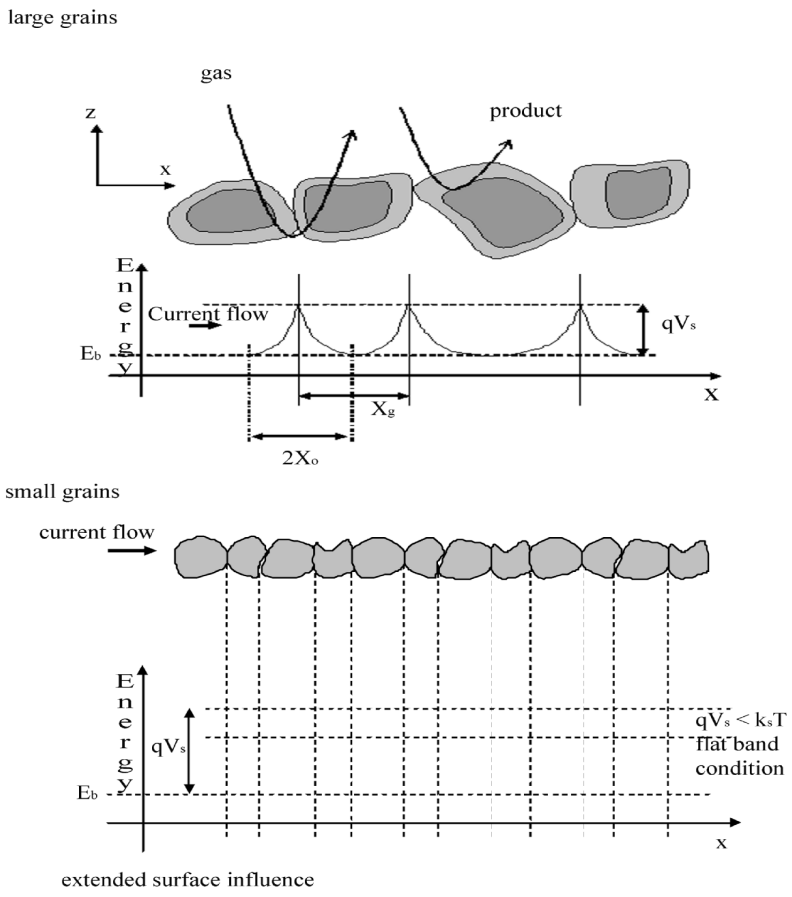

Figure 2.5: Schematic representation of a porous sensing layer with geometry and energy band (λ_D - Debye length, X_g - grain size) [150].

- Grain/crystallites smaller than or comparable to λ_d ($d \leq \lambda_d$)

For the first case ($d \gg \lambda_d$), the electroneutrality and Poisson equations for energy (E) can be written as:

$$\alpha \cdot \theta \cdot [S_t] = n_b \cdot z_0 \cdot A = Q_{ss} \tag{2.9}$$

$$\frac{d^2E(z)}{dz^2} = \frac{q^2 \cdot n_b}{\varepsilon \cdot \varepsilon_0} \tag{2.10}$$

where α is the ionization state of oxygen, θ is the surface coverage, $[S_t]$ is a material constant, z_0 denotes the depth of the depletion region and Q_{ss} is the

charge in surface states. The definition of q, n_b, ε and ε_0 are similar to that of Eq. 2.8.

Given that $V = E/q$, where V is the general dependence of band bending. Therefore V is written as:

$$V(z) = \frac{q \cdot n_b}{2 \cdot \varepsilon \cdot \varepsilon_0} \cdot (z - z_0)^2 \tag{2.11}$$

and for the surface band bending:

$$V_s = \frac{q \cdot n_b}{2 \cdot \varepsilon \cdot \varepsilon_0} \cdot z_0^2 \tag{2.12}$$

By combining Eqs. 2.9 and 2.12, and using the charge carrier concentration, n_s:

$$n_s = n_b \exp\left(-\frac{qV_s}{k_B T}\right) \tag{2.13}$$

Therefore

$$\theta = \sqrt{\frac{2 \cdot \varepsilon \cdot \varepsilon_0 \cdot n_b \cdot k_B \cdot T}{\alpha^2 \cdot [S_t]^2 \cdot q^2} \cdot \ln \frac{n_b}{n_s}} \tag{2.14}$$

From the Eqs. 2.13 and 2.14, the charge carrier and surface coverage can be determined.

The second case ($d \leq \lambda_d$) is also important for the evaluation of band bending between the surface and centre of the grain. For the calculation, it is assumed that a conduction taking place in cylindrical filaments obtained by the sintering of small grains. Based on this assumption, the Poisson equation for energy E using the Schottky approximation is:

$$\left(\frac{1}{r}\frac{d}{dr} + \frac{d^2}{dr^2}\right) E(r) = \frac{q^2 n_b}{\varepsilon \varepsilon_0} \tag{2.15}$$

and

$$\Delta E = \frac{q^2 n_b}{4\varepsilon\varepsilon_0} R^2 \tag{2.16}$$

where R denotes the radius.

If the ΔE is comparable with the thermal energy, this leads to a homogeneous electron concentration in the grain. Therefore a flat band case is considered. The following electroneutrality equation is given in flat band condition:

$$\alpha \cdot \theta \cdot [S_t] \cdot A + n_s \cdot V = n_b \cdot V \tag{2.17}$$

where V is the volume of the cylindrical filaments and n_s is now the homogenous concentration of electrons throughout the whole metal oxide crystallites. By combining Eq. 2.17 and the following two equations:

$$A = 2\pi R(R + L) \tag{2.18}$$

and

$$V = \pi R^2 L \tag{2.19}$$

where L is the cylinder length and A is the surface of the cylinder. Therefore θ for the second case can be written as:

$$\theta = \frac{n_b \cdot R}{2 \cdot \alpha \cdot [S_t]} \left(1 - \frac{n_s}{n_b}\right) \tag{2.20}$$

A schematic representation of nanorods based oxide surface is shown in Fig. 2.6 with potential barriers formed at nanorods contacts [31]. This barrier potential varies with the amount of adsorbed oxygen. By comparing the potential barriers of nanostructured metal oxide with the conventional inter-grain potential barrier, it is noted that the first one has much higher potential barrier than the second one. This is due to the complete depletion of electrons in nanorods. Therefore the scale of conductivity modulation is much greater in nanostructures than the conventional grains after exposure to gases.

Furthermore, during the exposure towards gas species, gas can access all of the volume of the porous sensing layer. The gas sensing reaction can take place at the surface of the individual grains/nanostructures, at grain-grain boundaries and interface between the grain and electrodes [150]. This evidently shows that nanostructured metal oxide has much greater exposed surface area and penetration depth for gas molecules, relative to compact sensing layers. Hence, the use of nanostructured metal oxide as a sensing layer can greatly improve gas molecules diffusion.

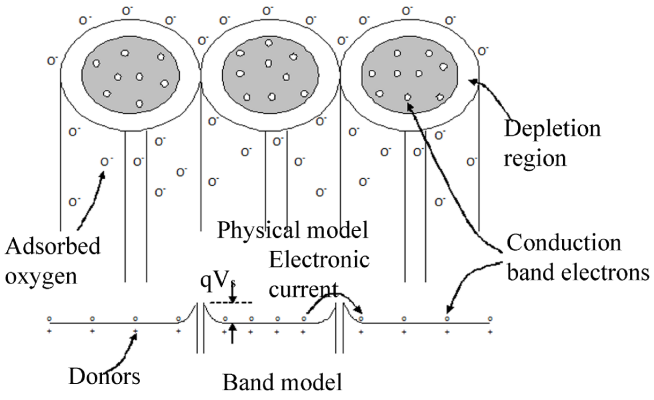

Figure 2.6: Schematic diagram of a sensing layer based on nanorods semiconducting oxide showing inter-rod contact resistance [32].

2.4 Summary

The author's intention in this research program is to develop highly sensitive gas sensors based on nanostructured materials. In this chapter, a critical literature review was conducted for the nanostructured materials used in this PhD research, including the justification of the author's rationale for proposing these materials for gas sensing applications. It was then followed by the explanation of gas sensing mechanism of conducting polymer, non-conducting polymer, graphene and metal oxide based sensors. The material structural morphology, film porosity, crytallinity, orientation and operating temperature must be optimised for nanostructured materials, therefore the best possible gas sensing performance can be obtained. To achieve this, the nanostructured materials will be synthesized via different methods, which the rationale of choosing the method will be presented in chapter 5.

Chapter 3

Theoretical Background of Surface Acoustic Waves Based and Conductometric Transducers

3.1 Introduction

In previous chapter, the critical literature review of the nanostructured materials used in this PhD work was given. Following this review, the author presented the gas sensing mechanism for each nanostructured material based sensors.

In this chapter, the properties of Surface Acoustic Wave (SAW) transducers as well as their sensing principal of operation will be explored. Prior to that, the author will provide general overview on transducers that commonly used for gas sensing. The author also will present the SAW and conductometric gas sensors structure that used in this reseach. The rationale of the gas sensors structure will also be described. In addition to that, the fundamental properties of conductometric transducers will be given at the end of this chapter. Finally the author will provide the summary of the chapter.

3.2 Transducers for Gas Sensing

A gas sensor interacts with a gas to initiate the measurement of its concentration. The gas sensor then provides output signal as a function of gas concentration. A gas sensor can be described as a device, which upon exposure to a gas, alters

one or more of its properties (e.g: capacitance, mass, or electrical conductivity) in a way that can be measured and quantified directly or indirectly [154]. In general, a gas sensor posseses two basic functions; a function to recognize a particular gas analyte and the other one is to transduce a gas recognitions into a sensing signal [15]. The gas information is converted into a form of energy which may be measured by the transducer. The transducer device then transforms the energy carrying the information about the gas concentration into a useful electrical signal [155].

Nylander's review [156], Hulanicki et al. [155] and Jimenez-Cadena et al. [157] have given important overviews in the classification of gas sensors and their configuration. They classified these sensors according to the operating principle of the transducers [155-156]. Gas sensors also can be grouped depending on the gas sensitive materials [157]. Although there are many other ways in classifying the sensors, these groups can be overlapped. For example, conductive polymer and metal oxide based sensors can employ any transducing platforms (such as conductometric and SAW based) and then are classified as conductometric and SAW based sensors. In addition to SAW and conductometric transducers, there are many other different transduction platforms that have been integrated with nanostructured materials for sensing applications. For example, Mach-Zehnder interferometer, surface plasmon resonance (SPR) and optical fibre based transducers are among the common structures for optical based gas sensors. Whereas, bipolar junction, Schottky diode, field effect transistor and metal oxide semiconductor capacitor based transducers, which are generally categorized as solid-state transducers, have also been used as platforms to deposit nanostructured materials for gas sensing purposes.

In the following section, the author will explore some of the most common approaches for gas sensing based on their transduction types. The author will focus on SAW and conductometric transducers in addition to the other common approaches for acoustic wave based gas sensors.

Conductometric Transducer

Conductometric also known as chemiresistor, is the most common type of transducers. It can be fabricated through a convenient and cheap process [38].

The technology of this type of transducers have been maturely developed. Typically, a conductometric transducer is formed by patterning metal interdigitated transducers (IDTs) on an insulating substrates as shown in Fig. 3.1. Then a sensing layer is deposited in contacts with the electrodes, forming the sensor. The sensing layer can be a metal oxide, conductive polymer or carbon nanotube. The electrical resistance change of the sensing materials is measured as the output. Conductometric sensors are low cost, have very good linearity and can measure up to ppb ranges of gas concentrations.

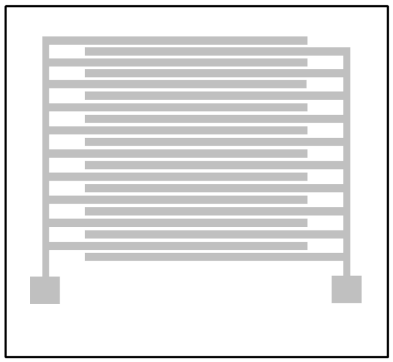

Figure 3.1: Design of a conductometric transducer. The gray pattern is the conducting electrode to be deposited on an insulating substrate.

Quartz Crystal Microbalance (QCM)

QCM or also known as the Thickness Shear Mode resonator is the oldest and simplest acoustic wave device. It is categorized as a bulk acoustic wave sensor, where a wave propagates through the substrate. Typically a QCM consists of a thin disk of quartz substrate with parallel circular electrodes patterned on both sides. The electrodes then are coated with gas sensitive films. Fig. 3.2 shows the configuration of a QCM sensor coated with conducting polymers.

Originally QCMs are used in oscillator circuits to measure metal deposition rates in vacuum systems [158]. The oscillation frequency tracks the crystal resonance and shows the mass accumulation on the device surface. QCM has been shown to operate as a vapour sensor in late 1950s [159].

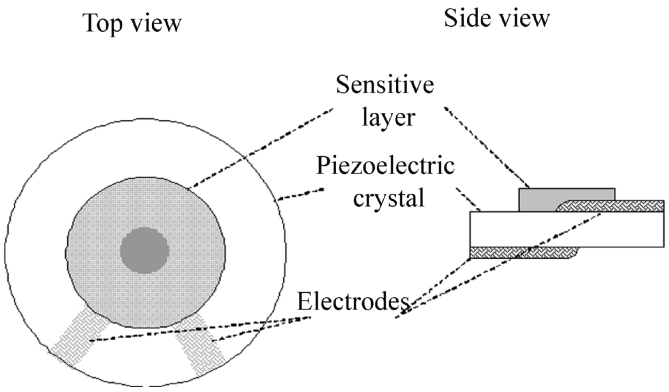

Figure 3.2: Schematic configuration of a QCM sensor device.

For operating in gas media, it is shown that the fractional frequency change due to mass loading increases linearly with operating frequency [159]. The operating frequency of this device is given by the material, plate thickness and crystal orientation. Typical QCM operating frequencies are between 5 to 30 MHz [160]. Making a very thin device that operate at higher frequencies can increase sensitivity, however it will make it more fragile and difficult to manufacture.

SAW Transducer

Surface wave based devices were reported by White and Voltmer [161]. In their design, metal thin film interdigitated transducers (IDTs) were fabricated on a piezoelectric substrate and then acted as electrical input and output ports. An appropriate AC voltage were applied to the input transducer, launched and propagated a SAW. The output or receiving transducer then detect the incident SAW and convert back to suitable electrical signal.

Telecommunication industry is the largest user of SAW devices. The devices are widely used as resonators, delay lines, and electronic filters. In addition to that, SAW devices also show interesting features in medical (biosensor), automotive (torque and tyre pressure sensor), industrial, and environmental (mass, humidity, temperature and gas sensor) applications. In 1979, Wohltjen et al. [162] has reported the first SAW sensor. For gas sensing applications, the delay lines of the SAW devices are coated with sensing layers (eg: metal oxide or conducting polymer), which then react with entity under analysis. A SAW

sensor can respond to three mechanisms; mass loading effect, viscoelastic effect and acoustoelectric interaction [72], which can contribute to the change in propagation of the surface waves. These interactions produce a shift in the resonant frequency of the SAW device. By measuring the shift, a detailed analysis of the target analytes can be completed. The details of the SAW transducers for sensing applications will be given in later in this chapter.

Thin-film Bulk Acoustic Wave Resonator (TFBAR)

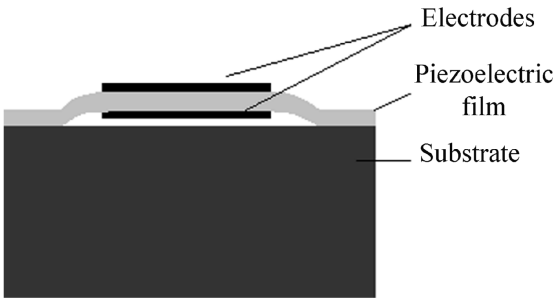

Figure 3.3: Schematic diagram of a TFBAR (Side view).

Similar to QCM, the operating principle of TFBAR is based on bulk waves. A configuration of TFBAR in Fig. 3.3 shows a thin film of piezoelectric material sandwiched between two metal electrodes [163]. When an electric field is created between the electrodes, the structure is mechanically deformed by the inverse piezoelectric effect. After that, an acoustic wave is launched into the structure propagated parallel to the electric field and reflected at the electrode/air interfaces [163].

Theoretically, this type of resonator is more sensitive than the other acoustic wave devices. It has a potential to sense the analyte concentrations at ppb level. This high sensitivity is due to the operating frequency of TFBAR, which is calculated similar to QCM with an extention that the operational frequency up to several GHz. Therefore, TFBAR transducer can greatly improve the performance of mass sensitive gas sensors [164].

3.3 Fundamentals of SAW Transducers

3.3.1 Overview of SAW Devices

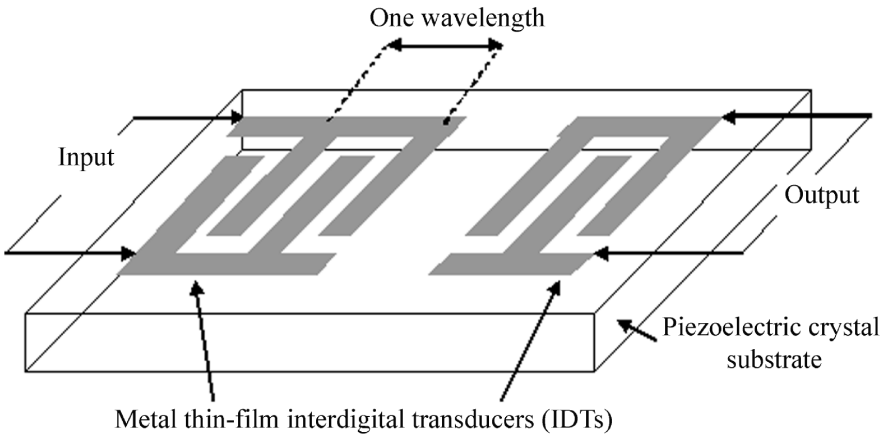

Figure 3.4: Schematic configuration of a basic SAW device.

Rayleigh wave is named after Lord Rayleigh, who discovered this type of propagation in which acoustic energy is confined very near to the surface of an inisotropic piezoelectric substrate [158,165]. This feature was then utilised in sensor applications, where due to the surface confinement of energy, allowing them to be excited by surface electrodes [166] in piezoelectric materials and making the wave extremely sensitive to surface perturbations [158].

The piezoelectricity phenomenon was discovered by Pierre and Jacques Curie in 1880 [167]. This phenomenon occurs in crystals which do not have a centre of symmetry. When stress is applied to a crystal, its lattice is deformed and an electrical field is developed. This phenomenon is also observed in the reverse direction where an electrical field is transformed to a mechanical stress when it is applied to the piezoelectric crystal.

SAW devices were first invented by White and Voltmer in 1965 [161]. They fabricated metal thin film interdigitated transducers (IDTs) on the surface of piezoelectric crystal. The crystal was cut in such a manner that allowed propagations of SAW. Application of an appropriate AC voltage stimulus to the input

transducer launched the SAW. Then the receiving transducer detected the incident surface acoustic wave and converted it back to an electric signal. Fig. 3.4 shows the schematic configuration of basic SAW transducer.

It is essential in SAW device to use a piezoelectric crystal substrate for converting the electrical field to mechanical disturbance. Piezoelectric substrates, 36 ° YX $LiTaO_3$ and 64 ° YX $LiNbO_3$ are of interest for the base devices as both substrates show high K^2. In this study, it is important to choose piezoelectric substrate with high K^2 as it will contribute to the enhancement of high gas sensing performance. For this study, low operating temperature is used in the investigated SAW sensor, therefore these substrates are suitable choices.

3.3.2 Theoretical Analysis of SAW

SAW can be generated on the free surface of an elastic solid. The generation of a SAW in transducer is achieved by the application of voltage to the metal film IDT deposited on the surface of the piezoelectric substrate. Although the details of theoretical interpretations of acoustic wave propagation and piezoelectric effect can be found in numerious texts [158,168], a simple and systematic derivation of the equations is included in this chapter for clarity.

Stress and Strain in Non-piezoelectric Elastic Solids

Acoustics concern the study of the time varying deformations or vibrations within a given material media. In a solid, an acoustic wave is the result of a deformation of the material. The deformation occurs when atoms within the material move from their equilibrium positions, resulting in internal restoring forces that return the material back to equilibrium [169]. The deformation or strain of the material applies only where particles of a medium are displaced relative to each other [170], while stresses or elastic restoring forces are developed between neighbouring particles when a body vibrates acoustically.

By assuming a displacement component of a point in a solid elastic medium u_i for the corresponding position vector component x_i in Cartesian co-ordinate, the tensor equation for stress (T) and strain (S) component can be written as:

$$\frac{\delta T_{ij}}{\delta x_j} = \rho \frac{\delta^2 u_i}{\delta t^2} \tag{3.1}$$

And:

$$S_{ij} = \frac{1}{2}\left[\frac{\partial u_i}{\partial x_j} + \frac{\partial u_j}{\partial x_i}\right] \tag{3.2}$$

where $i, j = 1, 2, 3$, ρ is the mass density, and u_i is the component of particle displacements along i direction.

Stresses and strains exerted within an elastic solid can exist in compressional or shear forms. In either case, they can be related proportionally by Hooke's Law (for elastic deformation), which can be written as [168];

$$T_{ij} = c_{ijkl} \cdot S_{kl} \tag{3.3}$$

where c_{ijkl} denotes the elastic stiffness constant. This constant is also known as Young's modulus with unit N/m^2. Here, c is a fourth-rank tensor, as its components have four suffixes c_{ijkl}. Similarly, stress and strain are classified as a second-rank tensor. Tensors are usually used to identify the crystal classifications of various SAW piezoelectrics. They are also used to relate parameters that are dependent on more than one coordinate axis sets (T_{ij}) to those measured in another (S_{ij}). Therefore, Hooke's Law tensor equation (Eq. 3.3) can be reduced to matrix equation:

$$[T] = [c]\,[S] \tag{3.4}$$

From Hooke's Law matrix equation, the elastic stiffness constant is reduced to a 6 x 6 matrix, with 36 possible independent values relating to the six components of stress to the six components of strain. By considering the crystal symmetry of a material, the 36 constants can be further reduced to the maximum number of independent elastic constant for any crystals, which is 21.

Piezoelectric Interactions

The stress-strain relations given in previous subsection are only sufficient to be applied to such a solid. Application of electric field to the nonpiezoelectric dielectric solid would have no effect on its mechanical stress-strain characteristics. For

a piezoelectric material, the relations between mechanical and electrical variables for a crystal are shown in the following equations, where the coupling between electrical and mechanical parameters are included.

Mechanical stress, T_{ij} equation is given by;

$$Tij = c'_{ijkl} S_{kl} - e_{mij} E_m \tag{3.5}$$

where c'_{ijkl} is the elastic stiffness constant, e_{mij} is the piezoelectric constant, and E_m is mth component of the electric field, E.

The equation for electric displacement density, D_n is written as:

$$D_n = e_{nkl} S_{kl} + \varepsilon'_{nm} E_m \tag{3.6}$$

where ε'_{nm} is the dielectric constant measured under constant or zero strain, and e_{nkl} is the piezoelectric constant. The value of e_{nkl} and e_{mij} depend on the crystal symmetry of the piezoelectric material and can have a maximum of 27 independent constants.

For a simplification of the numerical analysis of acoustic wave propagation, the quasistatic approximation is employed. The approximation relies on the fact that at the same frequency, the wavelength of elastic waves is much smaller than that of electromagnetic waves [171] and that the subsequent magnetic field generated by the electric field can be neglected. From this approximation, the electrical pontential component E_k can be written as [170]:

$$E_k = -\frac{\partial \phi}{\partial x_k} \tag{3.7}$$

where ϕ is the electrical potential associated with the acoustic wave. By substituting Eqs. 3.1 and 3.7 in the constitutive Eqs. 3.5 and 3.6, the equations are further simplified using $A_i = \delta_{il} A_l$ and $\Gamma'_{il} = c'_{ijkl} n_j n_k$. Finally, the equation is re-expressed in the form of Christoffel's equation:

$$\left(\bar{\Gamma}_{il} - \rho v^2 \delta_{il}\right) A_i = 0 \tag{3.8}$$

where

$$\bar{\Gamma}_{il} = \Gamma'_{il} + \frac{e_{kij} n_j n_k \gamma_l}{\varepsilon'_{kl} n_j n_k} = \Gamma'_{il} \left(1 + K^2_{il}\right) \tag{3.9}$$

with

$$K_{il}^2 = \frac{e_{kij} n_j n_k \gamma_l}{\Gamma'_{il} \varepsilon'_{jk} n_j n_k} \tag{3.10}$$

Eqs. 3.9 and 3.10 show that the effect of piezoelectricity on the propagation velocity of the plane wave can be expressed as a change in the effective elastic constants. Electromechanical coupling constant tensor, K_{il}^2 is a measure of the efficiency of the coupling of the electrical and mechanical energies for a given piezoelectric material [171].

Campbell et al. [172] have shown that the electromechanical coupling coefficient can be calculated by determining the perturbed wave velocity caused by a change in the electrical boundary conditions. It can be obtained theoretically or experimentally by:

$$\frac{K^2}{2} = \frac{v_f - v_m}{v_f} \tag{3.11}$$

where v_f and v_m are the free surface and metallised surface phase velocities, respectively.

The author has mentioned that K^2 is a measure of the efficiency of a given piezoelectric in converting an applied electrical signal into mechanical energy associated with a surface acoustic wave. In the case of conductivity based sensing applications, piezoelectric materials with high K^2 are of prime interest. In this PhD work, two substrate materials, $LiNbO_3$ and $LiTaO_3$ are chosen as they have a high K^2 [168-173].

3.3.3 Principal SAW Sensors Operation

Fig. 3.5 shows a typical SAW based sensor which consists of a 2-port SAW delay line with a thin film of gas sensitive material deposited onto the active surface of the device. For gas sensing applications, thin film of material should be sensitive to a specific gas analyte. Generally, the sensitive layer is deposited between the input and output IDT electrodes. The sensing mechanism involves the physicochemical interaction between the sensitive layer and the analyte gas. The sensor response is obtained from the measureable shift in the SAW mode's phase velocity caused by the perturbations which will be described in Eq. 3.13.

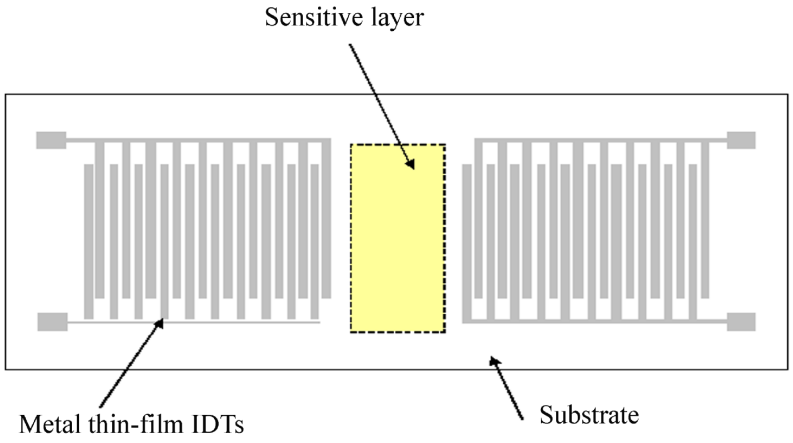

Figure 3.5: Schematic diagram of a conventional SAW gas sensor structure (top view).

As mentioned previously, the change in the surface boundary conditions of the device is due to the chemical reactions between the analyte gas and the sensitive layer. This results in a change in the acoustic phase velocity of the propagating SAW. The change in SAW velocity can be measured by the most common methods: phase and frequency measurement techniques [174].

The frequency measurement technique is the convenient method in interpreting the sensing interaction. This is due to the resonance frequency of the device can be related to the change in acoustic phase velocity (assuming negligible dispersion):

$$\frac{\Delta f}{f_o} \cong k\frac{\Delta v}{v_o} \tag{3.12}$$

where k is the function of the centre-to-centre distance between input and output IDT affected by the perturbations, Δv is the change of SAW velocity when a free surface of piezoelectric is electrically shorted by a highly conducting metal film, v_o is the unperturbed SAW velocity and f_o is the fundamental frequency of the SAW sensor [175]. Similarly, the velocity of the SAW device can be measured by different attenuation and phase measurement techniques [176]-[178]. The measured quantities should be ideally correlated to the relative concentration of the gas analyte.

The first application of a SAW device as a gas sensor was reported in 1979

by Wohltjen and Dessy [179]. They investigated and reported the operation of $LiNbO_3$ based SAW devices (coated and uncoated with sensing layers) as gas sensors. Consequently, a variety of studies for different types of gas have been reported. D'Amico et al. have developed H_2 sensor using a paladium sensitive layer on the active area of SAW device [180-181]. Meanwhile, Rapp et al. [182] conducted NO_2 gas measurement in the ppb-range with high frequency SAW transducers. WO_3 thin film based SAW sensors has also been utilized to measure NO and NO_2 in the concentration range of 0-4400ppm and 0-100ppm respectively. Furthermore, SAW gas sensors have been utilized towards H_2S [183], CO [184], toxic gas, sarin [185] as well as many others. The comprehensive studies on the development of SAW sensors have been investigated and reported by D'Amico et al. [186] in 1989, Ballantine and Wohlten [187] in 1989 and Grate et al. [188-189] in 1993, and [131] in 2000. Following these reports, several other reviews on acoustic wave gas sensor technology have been completed by Martin et al. [190], Cheeke et al. [191], Vellekoop [192], Drafts [193] and Anisimkin et al. [194].

In a SAW device the parameters involved with sensor applications concerns either electrical or mechanical pertubations. Any change in these physical properties of the device affect either one or both of the wave propagation parameters; velocity (v) and attenuation (α). The most common technique for SAW device is measuring the deviation in propagation velocity of the surface wave as a change in resonant frequency of the device [195].

Eq. 3.13 illustrates the factors that can effect the generic acoustic wave propagation in a SAW device:

$$\Delta\gamma = \frac{\partial\gamma}{\partial m}\Delta m + \frac{\partial\gamma}{\partial\sigma}\Delta\sigma + \frac{\partial\gamma}{\partial\mu}\Delta\mu + \frac{\partial\gamma}{\partial\eta}\Delta\eta + \frac{\partial\gamma}{\partial\varepsilon}\Delta\varepsilon + \frac{\partial\gamma}{\partial p}\Delta p + \frac{\partial\gamma}{\partial T}\Delta T... \quad (3.13)$$

where γ is the complex SAW propagation factor:

$$\Delta\gamma = \frac{\Delta\alpha}{k} - j\left(\frac{\Delta v}{v_o}\right) \quad (3.14)$$

and k is the wave number.

Eq. 3.13 shows that the perturbations affecting acoustic wave velocity can be attributed to many factors, each of which represents a potential sensor response [175]:

- m - Mass
- σ - Conductivity (electrical)
- μ - Shear elastic modulus
- η - Viscosity
- ε - Permittivity
- p - Pressure
- T - Temperature

These interactions change the boundary conditions, thus producing a measurable shift in the propagating SAW mode's phase velocity.

For a SAW device surface three perturbations mechanisms (mass, elasticity and conductivity) are considered. Using these mechanisms, the SAW velocity shift and normalised attenuation are calculated as [175]:

$$\frac{\Delta v}{v_o} = -c_m f_o \Delta\rho_s + c_e f_o h \Delta \left[\frac{4\mu}{v_o^2}\left(\frac{\lambda+\mu}{\mu+2\mu}\right)\right] - \frac{K^2}{2}\Delta\left[\frac{\sigma_s^2}{\sigma_o^2 + v_o^2 C_o^2}\right] \tag{3.15}$$

and

$$\frac{\Delta\alpha}{k} = \frac{K^2}{2}\Delta\left[\frac{v_o C_o \sigma_s}{\sigma_s^2 + v_o^2 C_o^2}\right] \tag{3.16}$$

where c_m and c_e are the coefficients of mass sensitivity, f_o is the fundamental frequency of the SAW sensor, ρ_s is the mass surface density (mass per unit area) of the coating and h represents the film thickness. K^2 is the electromechanical coupling coefficient which gives a measure of the piezoelectric strength of the medium, σ_s is the sheet conductivity of the film. This sheet conductivity can be calculated using $\sigma_s = \sigma h$, where σ is the film bulk conductivity. C_o is the capacitance per length of the SAW substrate material, k is the wave number ($k = 2\pi/\lambda$), where λ is an elastic module.

Mass Sensitivity

One of the most interesting sensing mechanisms of acoustic sensor response is mass sensitivity. It is defined as the frequency shift caused by the addition of a mass such as thin film materials and chemical species onto the surface of a SAW device. This type of sensitivity is related to the device structure geometry, properties of the substrate, as well as operating frequency and nature of the acoustic waves. The sensitivity is also strongly related to the surface confinement; the guiding of the acoustic energy near the surface. Applications of this mechanism are found in areas such as film thickness monitoring, gas and liquid media, as well as bio-sensing [196]. In term of velocity change that was presented in Eq. 3.15, mass sensitivity can be defined as:

$$\left(\frac{\Delta v}{v_o}\right)_{mass} = -c_m f_o \Delta \rho_s \tag{3.17}$$

Earlier, the author has mentioned that mass sensitivity can be affected by the device's properties, the viscosity, stiffness and geometry of the material also affect the response. The most widely used definition of a SAW sensitivity is [197]:

$$S_m^v = \lim_{\Delta m \to 0} \left(\frac{\Delta v / v_o}{\Delta m / a}\right) \tag{3.18}$$

where Δv represents the velocity change due to mass change per unit area $(\Delta m/a)$ and v_o is the unperturbed SAW phase velocity.

Change in frequency is the common parameter to measure. Therefore, the corresponding sensitivity as a function of output frequency is defined as [198]:

$$\left(\frac{\Delta f}{f_o}\right)_{mass} = \left(\frac{\Delta v}{v_o}\right)_{mass} = -c_m f_o \Delta \left(\frac{m}{a}\right) \tag{3.19}$$

$$S_m^f = \lim_{\Delta m \to 0} \left(\frac{\Delta f / f_o}{\Delta m / a}\right) = \left(\frac{v_g}{v_o}\right) S_m^v \tag{3.20}$$

where, v_g denotes the group velocity of the SAW mode which can be calculated from the phase velocity.

Conductometric Sensitivity

Piezoelectric phenomenon is related to the electromechanical coupling cofficient (K^2) of the piezoelectric materials employed in the SAW device structure. In conductometric gas sensing applications, the interaction of the analytes gas molecules with the sensitive layer perturbs the electrical boundary condition at the surface of the SAW device. This results in the perturbation of the velocity and attenuation of the electro-mechanical waves. The basic theory of a SAW response to a conductivity change has been developed by Ricco et al. [199]. They proposed that the change in velocity and attenuation due to the sensing layer conductivity modulation can be approximated from the Eqs. 3.15 and 3.16 resulting in the following equations:

$$\frac{\Delta v}{v_o} = -\frac{K^2}{2}\frac{1}{1+\left(\frac{\sigma_s}{\sigma_{or}}\right)^2} \tag{3.21}$$

$$\frac{\Delta \alpha}{k} = -\frac{K^2}{2}\frac{\frac{\sigma_s}{\sigma_{or}}}{1+\left(\frac{\sigma_s}{\sigma_{or}}\right)^2} \tag{3.22}$$

where σ_s is a sheet conductivity of the sensing film and σ_{or} is the sheet conductivity of substrate.

To optimise the electroacoustic interaction for sensing applications, the sensing layer conductivity must fall within the range where the curve has a significantly large gradient. Fig. 3.6 demonstrates the electroacoustic effect on SAW propagation, the theoretical dependence of the relative changes of the SAW velocity and attenuation as a function of σ_s normalised to σ_{or}.

To obtain high sensitivity, the sheet conductivity of the layer must be matched to the velocity-permittivity product of the SAW device. Referring to Fig. 3.6, the diagrammatic explanation of the change in velocity to the sheet conductivity have been divided into five regions. Region C in Fig. 3.6 shows the optimum operating region. At this point, the velocity shifts for both oxidising and reducing gases are of equal magnitude. The magnitude shift at region B and D are not proportional equally for the same oxidising and reducing conditions. Furthermore, in the layer conductivity ranges of region A and E, little or no velocity shift are observed. Eq. 3.12 has shown the relation between frequency shift

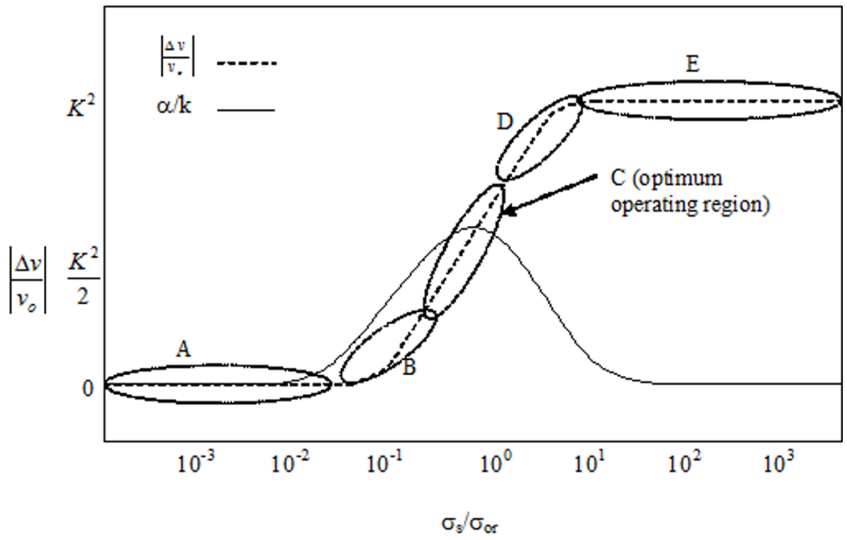

Figure 3.6: Surface wave velocity and attenuation as a function of layer conductivity [31,173].

to the velocity shift. Therefore, to obtain the maximum frequency shift, layer conductivity must fall in region C.

Viscoelastic Effects

The mechanical interaction between the acoustic wave and the film occurs when the film is either acoustically thick and/or the film is in the viscoelastic regime. Therefore, the interaction must include the viscoelastic effect. In term of velocity change that presented in Eq. 3.15, the influence of viscoelastic effect can be calculated from equation:

$$\frac{\Delta v}{v_o} = c_e f_o h \Delta \left[\frac{4\mu}{v_o^2} \left(\frac{\lambda + \mu}{\mu + 2\mu} \right) \right] \tag{3.23}$$

If polymer layers are used for SAW sensors, high energy loss in polymer materials causes viscoelastic behaviour by relaxation of the polymer chains. Besides, the viscoelasticity also can be caused by the considerable swelling of the polymers which is due to the adsorption of vapour/gas analyte [200]. The phenomenon of sorption of gases into polymers can be described by the following equations [201]:

$$C = C_D + C_H = k_D p + \frac{C'_H b}{1 + bp} p \tag{3.24}$$

where C_D is the Henry's law solubility term and C_H is a Langmuir sorption term that accounts for the characterization of a polymer matrix [202]. The hole capacity of the polymer is quantified by C'_H, b is for the sorption affinity that the polymer holds for the gas, k_D represents the solubility parameters in the Henry's law limit and p is the partial pressure of the gas or vapour.

3.3.4 SAW Gas Sensor Structure Used in This Project

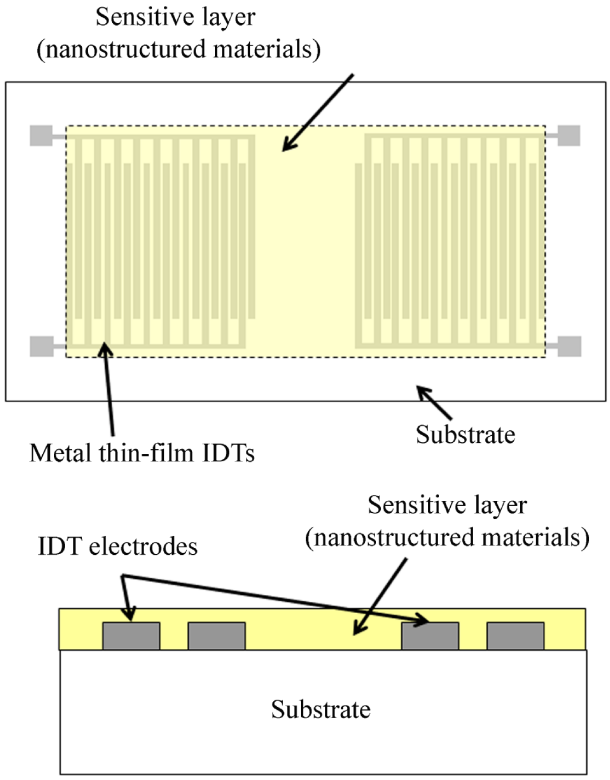

Figure 3.7: Schematic diagrams of nanostructured material/SAW sensor. Above: Top view. Below: Cross sectional view.

For this work, the author deposits the selected nanostructured materials directly over the whole area of SAW transducers. It is known that the thin film of the sensing layer can be deposited either in between the input and output IDTs

(refer Fig. 3.5) or by expanding the deposition area to include the input and output IDTs, depending on the conductivity of the deposited materials.

For delay line type devices, there should be negligible reflections at points between the input and output IDTs. Hence the delay is the accumulated phase change accross the device surface due to the surface propagation. This shows that the response should be independent of the location of the sensing layer, considering the sensing material was deposited between the input and output IDTs [203]. However, in the very same paper, it was also shown that the sensitivity (in this case is mass sensitivity) in the electrode regions can differ from that in the region between electrodes. Recently, Powell [198] had investigated the sensitivity distribution across the SAW device surface. He showed that the best region for depositing a sensing materials in order to obtain the optimum sensitivity, is by expanding the deposition of thin film area and including the input and output IDTs. Considering this, the author employed the same region for the SAW sensor structure used in this research. As the thin film based on nanostructured materials are porous and have high surface to volume ratio, it is anticipated that the conductivity of the sensitive layer is highly modulated by gas species. The author believes that by employing the novel nanostructured materials on the SAW transducers, the performance of conventional non-layered SAW sensors can be greatly enhanced. By maximizing the sensing layer deposited on the whole area of SAW transducer, the interaction area for the gas molecules to the nanostructured materials is increased.

Although layered SAW sensors have shown a number of advantages compared to non-layered structures [31,173], they are not feasible for certain methods of synthesized nanostructured. In a layered SAW sensor, generally a layer of inert material such as ZnO or SiO_2 is used as an intermediate layer. In this PhD study, the nanostructures were synthesized directly onto the SAW transducer. The use of acid during electropolymerization would dissolve the intermediate layer. Furthermore, the use of hydrazine to reduce graphite oxide to graphene might also remove the oxygen from ZnO. The details of the synthesization of nanostructured materials will be presented in chapter 5.

3.4 Fundamentals of Conductometric Transducers

Conductometric transducers are among the most common devices used in sensing applications [65,67,204]. This is due to their inexpensive and simple fabrication and set-up. In conductometric sensors, sensing material is deposited in between conducting electrodes. For conductometric measurements, a voltage can be applied accross the electrodes, which generates an electric field. The electrical conductivity of the deposited material can be determined from the measured current. The relation between current density J, electrical conductivity σ, and electric field E can be written using *Ohm's law*:

$$J = \sigma E \tag{3.25}$$

Ohm's law also can be written in its common form:

$$V = IR \tag{3.26}$$

where V is the voltage, I is the current, and R is the electrical resistance.

Conductometric measurements can be conducted in either AC or DC conditions. The applied voltage and current are generally selected such that the conductivity remains in a relatively linear region. Upon exposure towards analyte gas, the change in electrical resistance of a sensing material is recorded.

In this PhD study, thin film of nanostructured materials are deposited onto the electrodes and the area between them. The fabrication method of transducers will be explained in the next chapter. The details of the material characterization and gas sensing performance will be given in chapter 6 and 7, respectively.

3.5 Summary

In this chapter, the author has presented the literature review and theoretical aspects of SAW transducers. The non-layered SAW transducer was presented. The author also described the principle operation of SAW based gas sensors. Three important SAW sensing mechanisms; mass loading, viscoelastic effect and

conductometric change, were also explained here. The author also presented the fundamental theory of conductometric transducers.

The synthesis and deposition of nanostructured materials will be explained in chapter 5. The author will deposit nanostructured materials as sensing layers on SAW and conductometric transducers as proposed in this chapter. This incorporation of SAW and conductometric technology into nanotechnology are believed to pave the way for highly sensitive commercial gas sensors.

In the next chapter, the author will describe in detail the fabrication of SAW and conductometric transducers. This step-by-step fabrication process for these transducers will be presented before they are ready for nanostructured materials depositions.

Chapter 4

Fabrication of SAW and Conductometric Transducers

4.1 Introduction

Prior to this chapter, the author has introduced SAW and conductometric transducers in the following aspects; the basic operating principle and transducing mechanism.

In this chapter, the fabrication process of SAW and conductometric devices is described. There are many steps involved in the fabrication of such devices, which include metallization layer deposition and photolithography. This stage is highly crucial as defect in any fabrication stage can lead to an irreversible error that requires restarting the entire process. The author will first outline the fabrication of SAW device in section 4.2. Section 4.3 provides the parameters of the fabricated SAW transducers. For conductometric transducer, the author will combine the explanation of the fabrication technique and device parameters in section 4.4. This is due to the similar fabrication process which is employed for conductometric transducers. Section 4.5 provides the summary of the chapter.

4.2 SAW Transducer Fabrication Process

In this section, the process that is used for the fabrication of the SAW transducers is described. All fabrication steps were performed by the author and were undertaken within the Microelectronics and Materials Technology Centre (MMTC)

clean room and vacuum laboratory facilities at RMIT University. The transducers fabrication process was accomplished using standard fabrication techniques such as electron beam evaporation, photolithography and chemical etching.

4.2.1 Sample Cleaning

Cleaning process during sample preparation is one of the most important parts of the fabrication procedure. Using class-1000 cleanroom facilities, the surface of the 75 mm (3 in) 36 ° YX $LiTaO_3$, 64 ° YX $LiNbO_3$ and langasite (LGS) substrates was cleaned prior to metal layer deposition. This is to ensure no particles or dust left in between metal layers and wafer. Therefore this step is significant to a final success of the IDTs patterning. In order to obtain good edge definition of the metallic thin films used to form the IDTs patterns, a uniform metallic film with high adhesion is required.

Initially, the wafer was cleaned in acetone bath for five minutes to de-grease the wafer and enhance the adhesion of metallic film. The wafer was then rinsed in isopropyl alcohol (IPA) for approximately two minutes. After that, it was rinsed in deionised (DI) water to remove the acetone and IPA. Finally, the wafer was blown to dry in compressed nitrogen.

If necessary, after inspection, further cleaning of the samples was attempted in AZ-100 stripper or acetone bath heated between 70 °C to 85 °C and rinsed for 20 min. To confirm that the wafer was cleaned and ready for metal layer deposition, a thorough visual inspection was conducted under microscope. The cleaning process was repeated to see if any dust of particles were found on the wafer. Cotton swab with methanol was used to clean and remove any further particles contaminations.

4.2.2 Metallization of Wafers

Gold (Au) and titanium (Ti) metallization layers were deposited on the samples using a *Balzers*^{TM} electron beam evaporator. Au with a thickness of 80 nm was chosen for IDTs patterns as it is highly inert to most analytes and provides high conductivity. A 20 nm thick of Ti was deposited in between the Au and the substrate to promote the adhesion of the Au to the surface.

4.2.3 Wafer Dicing

After the Au and Ti metallization, the wafer was cut into smaller pieces that fitted the designed transducers using a *Tempress (Model 602)* dicing saw. Before the dicing process, thick photoresist (AZ4620) was spin-coated on the surface of the metallized layer. This spin-coating was necessary to avoid any damage to the thin films.

4.2.4 Photolithographic Mask

Photolithographic masks were designed and fabricated to pattern the substrates samples with the IDT designs. For this research, the existing mask designed by other researchers from RMIT's Sensor technology laboratory was used. The design of IDTs structures were written in computer scripts for *Agilent ADS* software package in layout mode and the designed parameters used in this research are presented in Table 4.1 and 4.2. The designed masks were fabricated on quartz substrates for the photolithography process.

4.2.5 Photolithography

Photolithography is a process of transferring the mask pattern onto the metal layer. At first, the metallization layer surface was cleaned thoroughly. This cleaning process was similar to that of subsection 4.2.1. After that, a thin film of photoresist was spin-coated on top of the metallized surface of the substrate. A positive photoresist AZ1512 was utilized due to its ability to become soluble in developer upon exposure to UV light. The metallized surface of the sample was deluged with photoresist AZ1512, and then spun at 3000rpm for 30 s to obtain a uniform layer photoresist of approximately 0.5 μm. After that, the soft baking process was performed at 90 °C for 20 min. This is necessary to harden the photoresist by forming a cured film. After soft baking, the sample was cooled at room temperature for approximately 10 min.

A *Carl Suss MRK-3* mask aligner was used for transferring the mask pattern onto the metallized samples. The cured photoresist film was exposed to the UV light source for approximately 10 s. However the exposure time could be varied between 8 to 15 s, depending on the UV power intensity. The placement of the

wafer was such that the IDTs structures were parallel to the wafer refence cut. Therefore, the resulting devices will have the acoustic propagation parallel to the crytallographic x-direction.

Afterwards, the UV exposed sample was developed using 1:4 AZ400:H_2O developer. The deleveloping time ranged between 12 to 18 s, depending on the concentration of the developer and the exposure time under UV light. The samples were then washed with DI water to remove any excess developer solution. Subsequently, the samples were visually inspected under microscope to confirm that the exposure and development process were successful. All the aforemention photolithography processes were repeated if defects were observed.

A post baking process at 110 °C for 20 min followed the developing process. This was required to harden the patterned photoresist layer before the etching process. The post baking process was found to be more durable during the chemical etching process.

4.2.6 Chemical Etching

Etching processes fall into two categories; wet etching and dry etching [33]. Wet etching is an etching process that utilizes liquid chemicals or etchants to remove materials from the sample. In contrast to wet etching, dry etching refers to the removal of the material from a substrate through bombardment with energetic ions that etch the surface.

In this research, wet chemical etching was used to remove the unwanted area of Au/Ti metallisation on the samples. This process was highly important as the incorrect etching time could lead to either over or under etching of the metallized IDTs. Subsequently, this would cause distortion of the electrical characteristic of the device.

The etching process started by etching the top metallization layer, Au. 94:6 H_2O: "*Technistrip Au*" (17% Potassium Cyanide) solution was used to etch the Au layer of the sample. The ecthing time was approximately 40-60 s, depending on the strength of the etchant. Then the sample was immediately rinsed under DI water to remove the etchant solution from the sample. The same process was

repeated to remove the unwanted Ti layer. To etch the Ti layer, a solution of 1.5:98.5 HF:H_2O is used. The sample was immersed in the Ti etchant for 20 s or until the unwanted Ti layer was etched. After Ti layer was successfully removed, the sample was rinsed under flowing DI water for few minutes to remove the excess Ti etchant from the sample. Finally the sample was dried under flowing compressed nitrogen. A thorough visual inspection was performed by the author using microscope to make sure that the IDT was successfully developed. The photoresist layer was removed by the process described in section 4.2.1.

The electrical performance of the fabricated transducers was measured using network analyzer. The details of this measurement will be presented in chapter 7.

4.3 SAW Transducer Parameters.

Throughout this research program, SAW transducers were patterned on 36 ° YX $LiTaO_3$ and 64 ° YX $LiNbO_3$ substrates. As mentioned in previous section, most of the devices were fabricated using the standard fabrication method. SAW transducers without sensitive layer were also fabricated in large amount by an external contractor. Since the repeatability between devices were found to be better, these devices were used in this research. Two different pattern parameters were used and summarised in Table 4.1 and 4.2. These two types of SAW devices were chosen to yield a center frequency of approximately of 102 MHz and 200 MHz, found to provide good compromise between insertion loss and loaded Q-factor. A schematic representation of the SAW transducers of 200 MHz is shown in Fig. 4.1.

Table 4.1: Parameters of SAW transducers fabricated using; 36^o YX $LiTaO_3$ and 64^o YX $LiNbO_3$ substrates.

IDT Metallization Layer	Ti/Au : 20/80 nm
Electrode pairs	38
Grating electrodes	160
Aperture width	700 μm
Periodicity	40 μm
Centre-to-centre distance	1920 μm

Table 4.2: Parameters of SAW transducer fabricated on 36^o YX $LiTaO_3$.

IDT Metallization Layer	Ti/Au : 20/80 nm
Electrode pairs	16
Grating and reflector electrodes	20 and 120
Aperture width	350 μm
Periodicity	80 μm
Centre-to-centre distance	200 μm

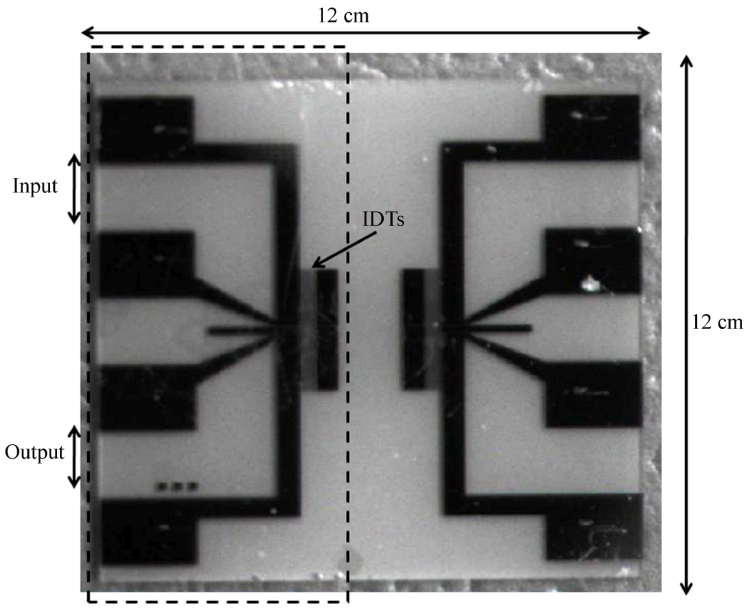

Figure 4.1: A fabricated 36 ° YX $LiTaO_3$, showing two identical resonators.

4.4 Conductometric Transducer Fabrication

LGS conductometric transducers were fabricated by the author at RMIT University using the MMTC facilities. Before the substrate was chosen, the author has performed thermal evaporation testing on several bare substrates namely; silicon, $LiTaO_3$, $LiNbO_3$ and LGS to grow Sb_2O_3 nanostructures. Surface morphology scanning using SEM was conducted on the surface of each sample after the thermal evaporation. The details of the thermal evaporation method, SEM and gas testing results will be presented in chapter 5, 6, and 7 respectively.

For LGS conductometric transducer fabrication, the similar process to SAW transducer fabrication process was used. Therefore in this chapter, the details of

the conductometric fabrication is not provided. The conductometric transducer consists of IDTs with Ti, nickel (Ni) and Au (in order of deposition) metallization layer film thicknesses of 20, 30, and 50 nm, respectively. The etching process of the Ti and Au layers were presented before. Ni layer acts as a lattice relaxation layer in between the Au and Ti layers. A solution of 15 g of ammonium persulfate, 25 ml nitric acid (70% concentration) and 100 ml of DI water was used as Ni etchant. The sample was immersed for approximately 30 s and then rinsed under DI water to remove the excess etchant. On this substrate, 113 electrode pairs with 8.5 μm of an electrode width were patterned with 5600 μm aperture width. Fig. 4.2 shows the fabricated LGS transducer.

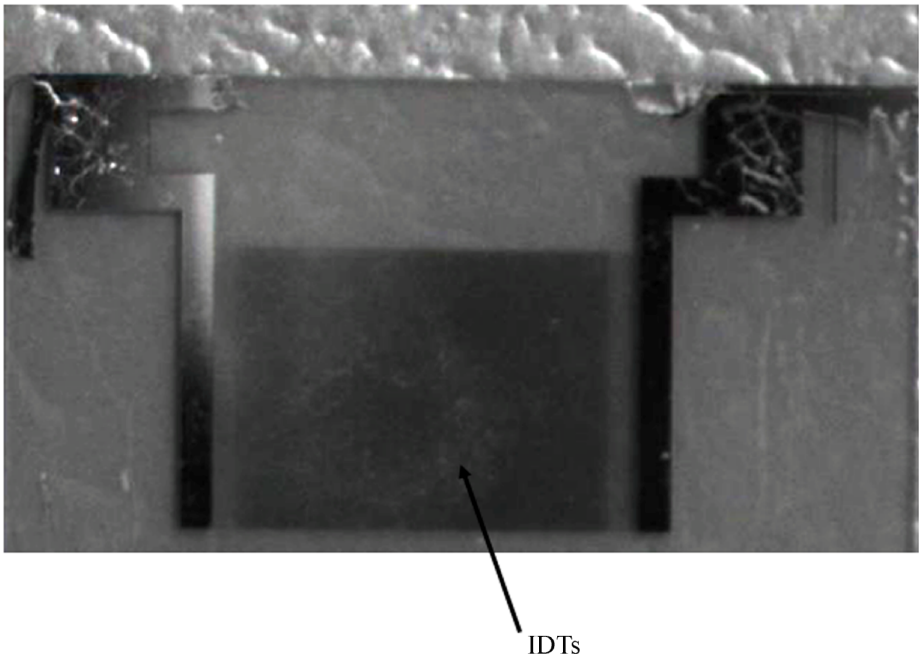

Figure 4.2: A fabricated LGS conductometric transducer.

4.5 Summary

In this chapter, the fabrication steps of the SAW and conductometric devices were outlined. The steps involved; cleaning the substrates, metallization layer deposition, wafer dicing and photolithography, as well as chemical etching. Each

device was systematically inspected throughout the fabrication process to avoid any defect that could affect the performance of the device. Any devices with unsatisfactory visual or/and electrical characteristic were rejected.

In the next chapter, the author will describe the syntheses and depositions of nanostructured materials on transducers. In this PhD study, four materials were used as sensitive layers. Each material was employed via different deposition techniques, which will be explained in details in chapter 5.

Chapter 5

Nanostructured Material Synthesis and Deposition

5.1 Introduction

Prior to this chapter, the author presented the motivation of conducting research into nanostructured materials for gas sensing applications. Based on this motivation, the author chose to investigate four different materials, which were polyaniline, PVP, graphene and Sb_2O_3. The literature review on these materials were given in chapter 2. After that, the author described the theory and fabrication of the SAW and conductometric transducers in chapter 3 and 4, respectively.

In this chapter, the author will describe the synthesis methods that were used in this research. Apart from the introduction, this chapter is divided into six sections. Section 5.2 presents the general overview in synthesis nanostructured materials. Then section 5.3 presents the details of synthesizing polyaniline nanofibers. This is followed by the development of PVP, graphene and Sb_2O_3 which will be explained in sections 5.4, 5.5 and 5.6, respectively. Finally, section 5.7 gives the summary of this chapter.

5.2 Synthesis of Nanostructured Materials

Nanostructured materials are those with at least one dimension falling in nanometer scale including; nanorods, nanowires, nanofibers, nanoparticles and thin films that are made of nanoscale blocks, or consisting of nanoscale structures.

Synthesis and processing of nanoscale materials are the integral aspects in nanotechnology. Good understanding of these aspects help in exploring the novel chemical and physical properties and phenomena, as well as in realizing the potential applications of nanostructured materials.

Many technologies have been explored for the fabrication of nanostructures and nanomaterials. These technical approaches can be grouped into several ways. One of the methods of grouping is via the classification based on 'top-down' and 'bottom-up' approaches. Top-down approach is considered when the existing coarse-grained materials are processed to produce substantial grain refinement and nanostructures. This technique is most likely to introduce internal stress, in addition to surface defects and contaminations [205]. The disadvantage of top-down approach is the imperfection of the surface structure [205]. Since surface-to-volume ratio in nanostructured material is high, such imperfection will have a significant impact on surface chemistry and physical properties. However, regardless to the surface imperfections and other defects that top-down approach may introduce, this approach will continue to play an important role in syntheses and fabrications of nanostructures. Among the successful top-down approaches are severe plastic deformation [206] and milling techniques.

Meanwhile, a bottom-up approach refers to the build-up of a material from the bottom: atom-by-atom, molecule-by-molecule, or cluster-by-cluster to form a nanostructured material. The bottom up approach utilizes methods of self-organization at molecular and nanocrystalline levels. Crystal growth is a bottom-up approach, where growth species such as atoms, ions or molecules, after impinging onto the growth surface, and assemble onto crystal structure one after another. This method also shows good capability to obtain nanostructures with more homogeneous chemical composition as well as less defects [205].

Methods such as lithography are considered as hybrid approaches. In lithography the growth of thin film is bottom-up whereas etching is top-down. While nanolithography is commonly classified as a bottom-up approach.

In this research, the synthesis of polyaniline involves in polymerizing the aniline monomer to polyaniline nanofibers. The aniline monomer was used as electrolyte in acidic solution for electropolymerization. Polyaniline nanofibers were then polymerized on a working electrode upon application of a voltage.

Meanwhile for PVP, the PVP powder was dissolved in DI water and then electrospun to form fibres. For graphene, the material was synthesized via exfoliating graphite oxide (GO) in water before reducing GO to graphene. Whereas Sb_2O_3 was thermally evaporated at high temperature, forming nanostructured Sb_2O_3. The details of the synthesis and deposition of these materials are described in sections 5.3 to 5.6.

5.3 Synthesis of Polyaniline Nanofibers and Its Composite

To date, several synthetic methods have been employed for the synthesis of polyaniline nanostructures. Most popular polyaniline synthesis techniques are via chemical polymerization, where an oxidant is required to be added to an acid aqueous mixture of aniline monomer to initiate the polymerization [63-66]. The synthesized polyaniline is then spin-coated [65] or drop-casted [67-69] onto respective transducer to be used as sensors. Other synthesis methods reported are in-situ polymerization [207], vacuum-depositing polyaniline films [208], and photolithographic synthesis [209].

The synthesis of polyaniline via electropolymerization technique [37,210-212] is quite common. This method allows controlling the thickness of the deposited polymer [211-212]. However, the use of inter-digitated transducers (IDTs) as working electrodes when forming an electropolymerized polyaniline film can be a tricky task as the gaps between electrodes need to be short-circuited to establish a continuous film. Recently, Kalantar-zadeh et al. [75] have successfully deposited polyaniline nanofibers onto SAW transducer with this method. The observed result was a 6.2 kHz frequency shift when polyaniline nanofibers based 64° YX $LiNbO_3$ SAW sensor was exposed to 0.125% H_2 gas. In this research, the author employed the IDTs of a SAW transducer as the working electrode for electropolymerization, so that the polyaniline nanostructures would be deposited directly onto the transducer. The SAW sensors were then exposed to different concentrations of H_2 gas at room temperature. The results of the gas sensing performance will be presented in chapter 7.

5.3.1 Sample Preparation

The IDTs of the SAW devices need to be short-circuited before the polyaniline are electropolymerized on the IDTs. Fig. 5.1 shows the prepared SAW transducer as a working electrode in electropolymerization experiment.

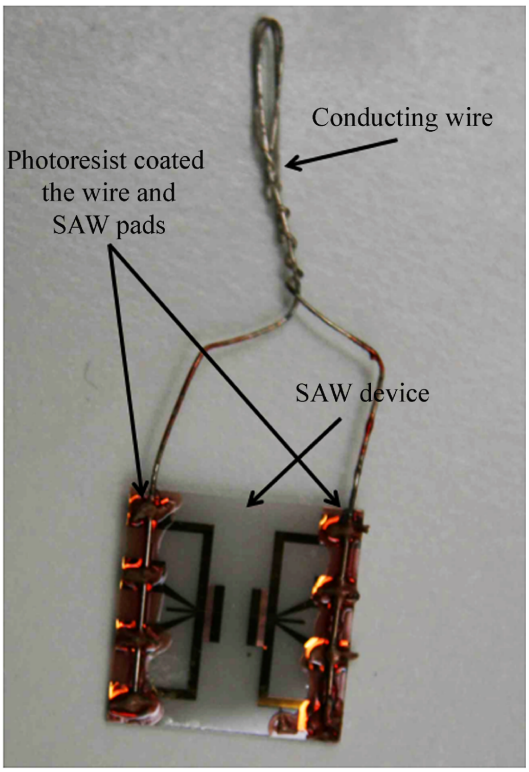

Figure 5.1: A sample of the prepared SAW transducer as a working electrode for electropolymerization of polyaniline.

Firstly, a 0.5 mm^3 tin-copper wire was attached to the SAW transducer pads using conducting silver paste (mixture of EPOTEK Part A and EPOTEK Part B with a ratio of 1:1). The tin-copper wire was used as a connector from the power supply to the metalization part of the transducer as well as the transducer's holder. To harden the silver paste, the prepared sample was baked in the oven for one hour at 100 °C. After that, the sample was left to cool before the surface of the SAW transducer was cleaned. The detail of the cleaning process was presented in chapter 4, section 4.2.1. Afterwards, the transducer pads, hardened silver paste and tin-copper wires were coated with photoresist AZ1512 and baked

for 30 min at 90 °C. This process was important to avoid the deposition of polyaniline during the electropolymerization process on the unwanted area. To confirm that the unwanted area of the sample was covered, a thorough visual inspection of the sample was conducted under microscope. The coating process was repeated until there was no exposed area found on the transducer pads, hardened silver paste and tin copper wires.

5.3.2 Electropolymerization of Polyaniline Nanofibers

Polyaniline nanofibers can generally be prepared via two types of polymerization: chemical polymerization and electrical polymerization. In this research, polyaniline nanofibers and its composite were synthesized via electropolymerization except for polyaniline/diamond nanostructured composite which was synthesized using chemical polymerization. The electropolymerization technique was preferred due to its ability to enable a better control of film thickness and morphology compared to chemical oxidation. The synthesis of polyaniline via this method is generally conducted in a highly acidic solution of aniline monomer as the aniline monomer is soluble in water under such a condition. A thin film of polyaniline nanofibers was deposited onto an electrode surface of the SAW transducer by the anodic oxidation of aniline monomer in the presence of an electrolyte solution [74]. Different electrochemical routes can be used to obtain the polyaniline nanofibers including potentiodynamics, galvanostatic [211] and potentiostatic [37]. The kinetics of the electropolymerization of aniline monomer in sulfuric acid have been investigated by Mohilner et al. [213]. They deduced that the initial oxidation requires the formation of aniline radicals. Recently, Liu et al. [211] and Yu et al. [37] have investigated the growth mechanism of electropolymerized polyaniline with controlled nucleation and step-wise deposition. Both pointed out that initially a high current density [211-212] or high voltage [37] is necessary to form homogeneous distribution of nucleation sites. After the nucleation sites are formed, lower current density or voltage was applied to the system to allow polyaniline nanofibers grow perpendicularly on the basis of these sites.

The processes of electropolymerization can be carried out in a simple two-electrode electrochemical cell. Fig 5.2 shows the experimental set-up used by the author for synthesizing the polyaniline nanofibers. The deposition was con-

ducted in HCl electrolyte containing aniline monomer at room temperature. A piece of platinum sheet was employed as the counter electrode and the IDTs of SAW transducer were used as the working electrode. The distance between these two electrodes was set at 3 cm. Upon application of positive potential between the working and counter electrodes, the oxidation reaction took place and subsequently the insoluble polyaniline nanofibers was deposited onto the working electrode.

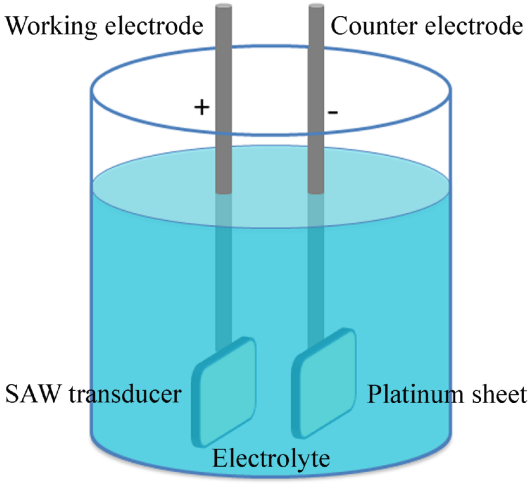

Figure 5.2: Schematic illustration of experimental apparatus for the electropolymerization polyaniline nanofibers.

The electropolymerized polyaniline nanofibers were grown using a two-step polymerization. To synthesize the polymer, the author applied two different voltages consequently. The high voltage of 0.75 V was used for controlled nucleation which then acted as the base scaffold of the next step of polymerization. At this stage, to allow the polyaniline grow from the nucleation sites, the potential was reduced to 0.65 V.

Previously, the better control of film thickness and morphology were mentioned as the advantages of electropolymerization in comparison to chemical polymerization. Different thickness of polyaniline nanofiber film can be achieved by varying the deposition time. One of the objectives of this research program is to investigate the effect of the thickness of polyaniline nanofiber thin films on gas sensing. To accomplish this, the electrolyte containing 1M HCl and 0.3M

aniline monomer was used. After that, the varied thickness of polyaniline thin films on SAW devices were dedoped in NaOH solution (pH 12.2) for 10 s. The novel dedoped polyaniline nanofibers based 36° YX $LiTaO_3$ SAW sensors then were investigated towards H_2 gas.

For the optical characterization, the author electropolymerized polyaniline nanofibers on indium tin oxide (ITO) glass. By varying several deposition parameters, UV-Vis adsorption spectra measurement was conducted. The author investigated the optical characterization of the polyaniline deposited at different acid concentrations, different temperatures (refer to Table 5.1), and voltages (refer to Table 5.2).

In electropolymerization, the use of correct electrolyte is critical as the deposited polyaniline nanofibers will be used as the sensitive layer of gas sensors. The author varied the concentration of HCl used in electrolyte to investigate the optimum acid concentration for the deposition of polyaniline. Polyaniline was electropolymerized at 0.1, 0.3, 0.5, 1.0 and 1.5M HCl concentrations. The dedoped polyaniline based 36° YX $LiTaO_3$ SAW sensors were then exposed to H_2 gas, and the effect of different acid concentrations on gas sensing were investigated.

To see the effect of temperature on electropolymerization, the author used two different temperatures; ∼0 °C and 25 °C. To maintain the temperature of the electrolyte at ∼0 °C, the solution was kept in ice bath during the whole process. The experiment was conducted as described previously. For the 25 °C, the ice bath was removed and newly prepared solution with similar parameters was used. At each temperature a set of voltages were applied as presented in Table 5.1.

As for the polyaniline prepared at different voltages (Table 5.2), the temperature was kept at 25 °C. Five different voltages were applied on ITO glasses. The polyaniline nanofibers were electropolymerized for 7 mins and then left to dry at room temperature.

The optical property of both types of deposited polyaniline were investigated and will be presented in the next chapter.

Table 5.1: The prepared polyaniline samples under given sets of voltages, time and temperatures.

Sample prepared	$\mathbf{V_1}$ (time, min)	$\mathbf{V_2}$ (time, min)	**Temperature** (°C)
1	0.75V (5)	0.65V (25)	25
2	0.65V (5)	0.55V (95)	25
3	0.75V (5)	0.65V (25)	∼0
4	0.65V (5)	0.55V (95)	∼0

Table 5.2: The prepared electropolymerized polyaniline nanofibers on ITO glasses at different voltages

Sample prepared	**Voltage** (V)
1	3.0
2	3.5
3	4.0
4	4.5
5	5

Several reports on polyaniline reveal that different morphology of polyaniline can be obtained when different types of acids are used. To investigate this, the author conducted an experiment using HNO_3 as electrolyte. Similar setup was used in depositing polyaniline nanofibers directly onto SAW transducers except 1M of HCl that was replaced by 1M HNO_3.

The nanostructural characterizations of the deposited films will be presented in chapter 6 and the gas sensing performances in chapter 7.

5.3.3 Electropolymerization of Polyaniline/Multiwall Carbon Nanotube

The dispersion of carbon nanotubes (CNTs) into a polyaniline matrix for the fabrication polyaniline/CNTs composite has stimulated significant interest among researchers. Recently, Zengin et al. [214] have reported that aniline could be utilized to functionalize and solubilize CNTs via the formation of donor-acceptor complexes. The method of dissolving multiwall carbon nanotubes (MWNTs) in aniline has been studied by Guo et al. [88] and their results suggested that no damage had occured to MWNTs during the preparation process. However, no report was found to show the application of this method for the fabrication of

polyaniline/CNTs composite as a gas sensitive layer. Therefore, the author used a similar method to Guo et al., and deposited the composite directly onto the SAW transducers.

MWNTs with an outer diameter of 20 - 50 nm and length of 0.5 - 2 μm were purchased from Aldrich and used as received without further purification. In the early attempt of synthesizing polyaniline/MWNTs composite, firstly 4% wt of MWNTs were added in a vial containing DI water. The mixture was ultrasonicated for 90 mins in order to obtain good dispersion of MWNTs. Later, the mixture was added into aniline monomer solution before it was filtered. A very homogeneous dispersion of MWNTs in aniline was observed at this stage. However after adding 1M of HCl in 0.3M of filtered aniline/MWNTs, the agglomeration of MWNTs occured within few seconds. The observation was similar to the observation of Sainz et al. [87], who suggested that the HCl had led to the fall-out of small agglomerates, until all of the MWNTs settled down at the bottom of the solution.

To improve the previous experiment, the author modified the method used by Guo et al. [88] and Huang et al. [89]. In this attempt, 2% of MWNTs was added into 2 ml of aniline in a closed vial. The weight percentage of MWNTs was measured with respect to aniline monomer solution. The mixture was heated in a water bath for 11 hrs. The temperature of the water bath was approximately 80 °C. At the initial stage, the colour of the mixture was light brown, then it changed to dark brown after a few hours of heating. The colour of the mixture finally changed to dark red after 11 hrs of heating. Guo et al. [88] and Huang et al. [89] suggested that the dark red colour indicates that the MWNTs have been dissolved in the aniline. It was also observed that the undissolved MWNTs settled down at the bottom of the solution.

For electropolymerization, 0.3M of aniline containing MWNTs was mixed in 1M HCl and used as the electrolyte. The mixture of aniline and MWNTs was taken from top of the solution. The IDTs of SAW device were used as the working electrode, while a platinum sheet was used as the counter electrode. A 15 min deposition was conducted at 0.75 V. The sensing performance of polyaniline/MWNTs composite based SAW sensors was investigated. The nanostructural characterizations will be presented in chapter 6 and the gas sensing performance in chapter 7.

5.3.4 Chemical Polymerization of Polyaniline/Diamond Nanoparticles

Chemical polymerization of polyaniline is generally conducted using aniline monomer, strong acid dopant and an oxidant. Using this method, polyaniline nanofibers/metal oxide composites [61,77-78] were synthesized and used as the sensitive layers in gas sensing application. This combination has shown promising results towards H_2, NO_2 and CO. For this study, novel polyaniline nanofibers/diamond nanoparticles composite were synthesized using similar method. Ammonium persulfate (APS), aniline, camphor sulfonic acid (CSA) and diamond nanoparticles of average part size 3.2 nm were purchased from Aldrich. All were used as received without further purification, except for aniline which was distilled prior its application. A dispersion of diamond nanoparticles was obtained by adding a desired amount of diamond nanoparticles in 20 ml of 1.0M CSA solution while sonicating the mixture. The 3 mmol of aniline was then added into the dispersion of diamond nanoparticles under constant sonication. APS (0.75 mmol) was rapidly mixed to the above solution at room temperature and the resulting solution was stirred continuously for an hour. The product was washed 4 times with DI water.

The whole area of the SAW transducer was coated with CSA doped polyaniline/diamond nanofibers by drop-casting and then left to dry at room temperature.

The author characterized the aforementioned composite using methods such as SEM and XRD. The characterization results will be presented in chapter 6. The developed polyaniline/diamond nanoparticles based SAW sensors then were exposed to H_2 gas. The gas sensing performance will be presented in chapter 7.

5.4 Synthesis of Polyvinylpyrrolidone Fibres and Its Composites

5.4.1 Electrospinning of Polyvinylpyrrolidone (PVP) Fibres

Over the past decade, electrospinning has grown from a small niche process to a widely used fibre formation technique. It only required a relatively simple set-up as shown in Fig. 5.3. The set-up for electrospinning consists of three major parts: a spinneret (a metallic needle), a collector (eg: whole area of the SAW transducer) and a high voltage power supply.

The author prepared the PVP solution by dissolving the PVP powder in DI water. The mixture was kept in a closed vial and stirred continuously for few hours until the PVP powder totally dissolved in DI water. The mixture was then left unstirred to let bubbles produced during the stirring process dissapeared as the existence of bubbles might cause the discontinuity in the produced fibres during the electrospinning process. The prepared PVP solution was poured in a glass syringe with a metallic needle attached at one end. The applied voltage was kept constant at 12 kV and the distance was varied between 5.5 to 11.5 cm. During the electrospinning, the PVP solution produces jets that travel further before the first bending instability, which is caused by the electrical forces, appears. The droplet of the PVP solution was supported at the tip of the metallic needle. Then liquid jets were formed on the surface of the droplet. The high electrical potential difference between the metallic needle and the collector causes the electrical field to charge the surface of the liquid. Therefore, the migration of ions were induced through the liquid. When the potential difference is high enough, the electrical forces overcome the forces associated with the surface tension, causing the instability of the droplet. The charged liquid then transfers the charge to the collector, and thereby completes the electrical circuit.

For this experiment, the author used a SAW transducer as a collector. The SAW transducer was located on the grounded base. The transducer pads were covered using teflon tape to ensure that the electrospun fibres were only deposited onto the area that shown in Fig. 3.7.

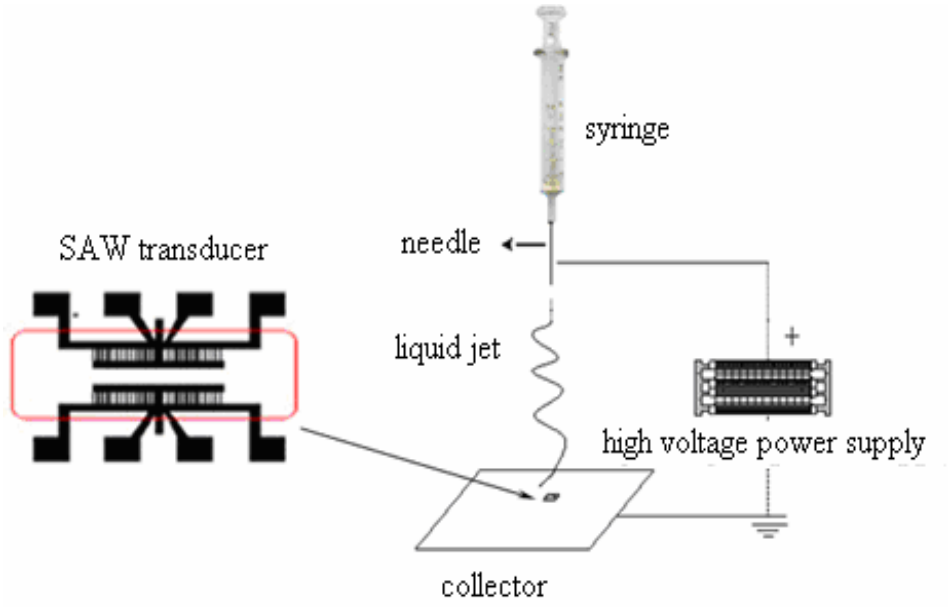

Figure 5.3: The schematic illustration of the set-up for electrospinning.

The characterization results of the PVP formation on the collector will be provided in the next chapter.

For electrospinning, viscosity of the solution is crucial in obtaining the desired fibers. In this research, the author investigated the effect of the different weight percentage of PVP (M_w: 30000) on surface morphology and gas sensing performance. Table 5.3 presents the details of the prepared PVP. For the characterization purposes, silicon substrate was used as a collector. Whereas for gas sensing purposes, the whole area of SAW transducer was used as a collector with a distance of 8.5 cm. Referring to the characterization results in chapter 6, this distance showed better deposition rate and morphology than any other distance for either PVP particles or PVP fibres. All substrates were cleaned prior to the deposition of the electrospun PVP. The details of the cleaning process are similar to those presented in chapter 4. The results of the gas sensing experiments will be presented in chapter 7.

Table 5.3: The prepared PVP solution at different concentrations for electrospinning process.

PVP (g)	DI Water (ml)	wt %
1.4443	2.0	42
1.8462	2.0	48
2.0000	2.0	50
2.1667	2.0	52
2.3478	2.0	54
2.5455	2.0	56
2.7620	2.0	58

5.4.2 Electrospinning of PVP/Polyaniline Composite

Polyaniline emeraldine salt (ES) and emeraldine base (EB) were purchased from Aldrich and used without further purification. Due to hydrophobic nature of polyaniline, either chloroform ($ChCl_3$) or N-Methyl-2-pyrrolidone (NMP) were mostly used for dissolving the polyaniline particles. Prior to the experiment, the author had drop-casted solution of ES/$ChCl_3$ and ES/NMP onto conductometric transducers and investigated their effects towards gas sensing. The results showed that NMP reduced the conductivity of the polyaniline emeraldine salt, and possibly transformed it to the emeraldine base form. Therefore, $ChCl_3$ was used for dissolving polyaniline to maintain the conductivity.

The composite of ES (M_w = 15000) with PVP was prepared by the author prior to the experiments. Firstly, the ES was mixed with $ChCl_3$ and kept in a closed vial. The mixture of ES/$ChCl_3$ was stirred for 20 hrs until the ES powder dissolved in $ChCl_3$. Then the solution was filtered using a 0.2 μm filter, hence the undissolved ES could be removed. 0.9 g of the PVP powder was then mixed into the 2 ml of filtered solution and stirred continuously to dissolve the PVP. Similar to the preparation of pure PVP, the mixture was then left unstirred until all bubbles disappeared.

The author also prepared the composite of EB (M_w = 10000) with PVP. By repeating the similar preparation processes as mentioned before, the mixture of EB/$ChCl_3$ was prepared. However, due to the lower M_w of EB compared to ES, 1.0 g of PVP was added in the prepared solution and then kept stirred continuously. Again, the mixture was left unstirred for few hours before the

electrospinning experiments were conducted. The electrospinning experiments were then conducted as described previously.

5.4.3 Electrospinning of PVP/ Multiwall Carbon Nanotubes Composite

The composite of PVP/MWNTs was prepared by adding PVP powder into the dispersion of MWNTs. MWNTs with an outer diameter of 20 - 50 nm and length of 0.5 - 2 μm were purchased from Aldrich and used as received without further purification. At first, 5% wt of MWNTs was added in a vial containing 1.5 ml DI water. 0.5 ml of ethanol was then added into the solution to obtain a good dispersion of MWNTs. After that, 1.525 g of PVP was added into the mixture and stirred continuously, resulting in the PVP and MWNTs being very well dispersed. Then again the solution was left unstirred to ensure no bubbles in the mixture that might effect the electrospinning experiment. The electrospinning experiments were then conducted as described previously.

The surface morphology and gas sensing performance of the PVP composites will be presented in chapter 6 and 7, respectively.

5.5 Synthesis of Graphene-like Nano-sheets

A great deal of attention has been drawn recently to graphene due to its unique electrical and mechanical properties. As a monoatomically thick two-dimensional layer of sp^2-bonded carbon, graphene can be considered as the basic building block of many graphitic materials, arranging itself into large planar sheets with repetitious benzene ring motif [46,50]. Graphene sheets are usually obtained by mechanical exfoliation of highly oriented pyrolytic graphite e.g. using 'Scotch-tape' technique [50]. While simple to perform, this method is evidently difficult to employ for large-scale applications. Graphene can also be produced by the reduction of SiC [215] and conversion from nanodiamond [113]. Unfortunately, these methods have high associated production costs, making them unsuitable for large-scale applications. Alternative methods for isolating single layers of graphene include; exfoliation from graphite crystals [114], pyrolysis of camphor

under reducing conditions [113], and thermal exfoliation of reduced GO into single functionalized graphene sheets [216].

In this PhD research, the graphene-like nano-sheets were chemically synthesized via the reduction of spray-coated graphite oxide (GO) with hydrazine [217]. Prof Richard Kaner's group from UCLA, who is the collaborator of this work, has synthesized GO using Hummer's method. The GO was then dispersed in water. The presence of oxygen-containing groups including carboxylic acid and hydroxyl moieties in GO makes it readily exfoliatable upon sonication in water. The device was preheated prior to spray coating with with GO. This step helped to achieve a highly uniform deposition of GO on the device. The GO platelets were freezed upon contacted with the device as the solvent flash evaporated. Then the as-deposited GO device was placed in a flow cell and heated at 80 °C under flowing helium gas. Hydrazine vapor was supplied via a bubbler to the system to reduce GO to graphene.

It is believed that GO contains a number of carbonyl-containing oxygen functionalities such as quinones. Since hydrazine can react with this moiety to form hydrazone, the GO can be reduced by removing the oxygen [218]. Additionally, further reduction of hydrazone can cause a deoxygenated sp^2-carbon if it is situated adjacent to an epoxide [219]. Stankovich et al. [220] suggested another possible mechanism for reducing GO by hydrazine. They believed that the initial derivative produced by the epoxide opening with hydrazine reacts further via the formation of an aminoaziridine moiety. The moiety then would undergo thermal elimination of diimide to form double bonds. Therefore, the reaction might be further driven in GO by re-establishment of the conjugated graphene network.

In this study, 36 ° YX $LiTaO_3$ SAW transducers were used as the device for spray coating the GO. The graphene-like nano-sheets/36 ° YX $LiTaO_3$ SAW sensors were characterized and the results will be presented in chapter 6. Subsequently the sensing performance of the graphene-like nano-sheets/36 ° YX $LiTaO_3$ SAW sensors were investigated and the results will be presented in chapter 7.

5.6 Deposition of Antimony Oxide Nanostructures

To date, several synthesis methods have been used in synthesizing of 1D Sb_2O_3 nanostructures. Previous literature reported that 1D Sb_2O_3 nanoparticles have been prepared using vapour condensation method [116], hydrolysis-precipitation process [221], thermal oxidation method [222] and microemulsion method [120-121]. It is shown that in thermal oxidation method, similar nanoparticles features are obtained on different substrates [222]. Meanwhile, microemulsion methods are able to synthesize both Sb_2O_3 nanorods [120] and nanoparticles [121]. Sb_2O_3 nanorods have also been produced by hydrothermal method [223], templating carbon nanotubes [224] and vapour-solid synthetic route [117]. More than one type of Sb_2O_3 nanomaterials, such as nanowires and nanobelts are formed using surfactant-assisted solvothermal method [118-123]. Recently, Deng et al. [125] have reported that Sb_2O_3 nanowires with rectangular cross sections can be obtained by direct oxidation of bulk metal antimony in a mixed solution of ethylenediamine (EDA) and DI water. The synthesized nanowires are in the range of 80-100 nm in width and 60 - 80 nm in thickness. Although many reports are found on depositing Sb_2O_3 nanostructures, only few literature extended their applications as sensing layers. In this research, the author had employed a simple thermal evaporation method to obtain Sb_2O_3 nanostructures. The deposition of nanostructured Sb_2O_3 via this method is similar to the vapour-liquid-solid (VLS) growth technique. Fig. 5.4 shows the principal steps of VLS technique.

VLS is one of the most popular methods which is used in growing nanostructured materials since its introduction by Wagner et al. [225] in 1964. Typically, VLS process starts with the dissolution of gaseous reactants into nanosized liquid droplets of a metal catalyst. This process is followed by the nucleation and growth of single crystalline rods, and then the continual feeding of the vapour elongates the nanorods.

In subsection 4.4, the author has mentioned langasite (LGS) as the substrate for conductometric transducer. However, several experiments were conducted on other bare substrates prior to the chosen of LGS. In these experiments, Sb_2O_3 nanostructures were synthesized on different substrates; LGS, silicon (Si), $LiTaO_3$ and $LiNbO_3$. To grow the Sb_2O_3 nanostructures, thermal evaporation

method was used. Fig 5.5 shows the schematic diagram of the experimental setup for growth of antimony oxide.

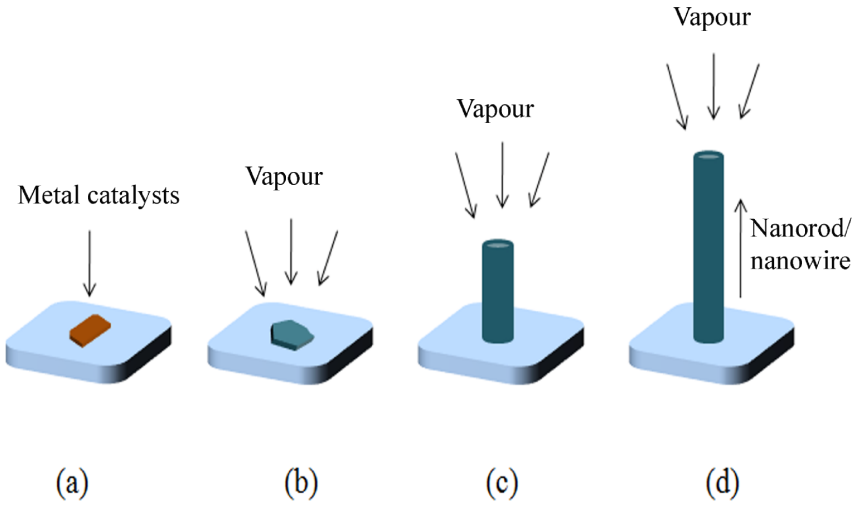

Figure 5.4: The schematic illustration of principle steps for the VLS growth technique: from initial nucleation to continual growth.

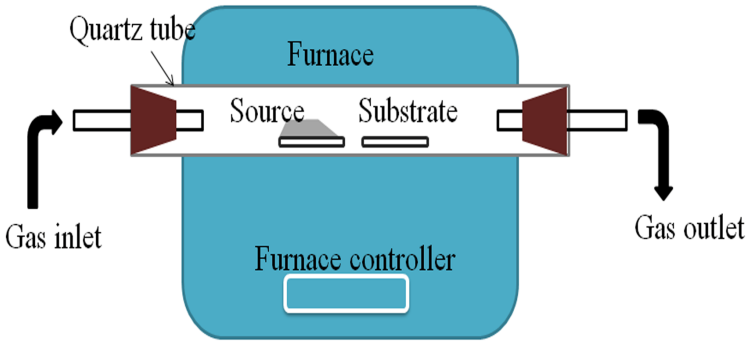

Figure 5.5: Schematic diagram of experimental apparatus for growth of Sb_2O_3 nanostructures by thermal exaporation method.

Prior to the deposition, the substrates were cleaned using the same method of subsection 4.2.1. This was important to minimize the existence of unknown particles on the substrates that might affect the deposition. After that the substrates were coated with Au (thickness of 60 nm). Au had earned its reputation as an outstanding catalyst in nanotechnology and in gas sensing performances

[226-227]. Sb_2O_3 powder was used as the source and loaded on an alumina boat and then placed in an 18.5 mm diameter quartz tube in a horizontal furnace. The substrates were then located 2 cm, 4 cm and 6 cm from the powder downstream in the quartz tube. To investigate at which temperature the Sb_2O_3 nanostructured could grow, the experiments were conducted at different temperatures. The furnace was then rapidly heated to the required operating temperature and held at this temperature for 2 hrs. A mixture of 90% argon and 10% oxygen was flown into this containment area and used as carrier medium at a constant flow rate during the heating process.

Afterwards, the experiment was repeated on LGS based conductometric tranducers for gas sensing measurement using the successive parameters. The characterization and gas sensing performance results will be presented in chapter 6 and 7, respectively.

5.7 Summary

In this chapter, the syntheses steps of the nanostructured materials (polyaniline, PVP, graphene and Sb_2O_3) deposited on SAW and conductometric transducers have been outlined. The author also provided the details of the bottom-up and top-down approaches.

In this PhD research, the author had successfully depositing the nanostructured polyaniline and its composites, PVP and its composites, graphene and Sb_2O_3 onto the fabricated transducers to develop novel sensors. The electropolymerization technique was conducted to obtain polyaniline nanofibers which were deposited directly onto the proposed area of $LiTaO_3$ SAW transducers. The author also synthesized polyaniline nanofibers thin films with different thicknesses, electropolymerized polyaniline nanofibers using different HCl concentrations and different acids. Via electrospinning method, the author deposited PVP fibres with different concentrations, PVP/polyaniline, and PVP/MWNTs composites onto SAW transducers. Whereas for deposition of graphene, the chemical reduction of GO method was used. For Sb_2O_3 deposition, the author employed thermal evaporation technique to obtain nanostructures of Sb_2O_3.

In the following chapter, the characterization of synthesized nanostructured materials will be presented. Understanding the characterization of the fabricated materials is highly important as it will help in realizing the gas sensing performance, which will be presented in chapter 7.

Chapter 6

Micro-nano Characterization Methods and Results

6.1 Introduction

In chapter 4, the author presented the fabrication of the SAW and conductometric transducers that were utilized to deposit the gas sensitive nanotructured materials. It was then followed by the synthesis and deposition of nanostructured materials, which was presented in chapter 5.

The synthesized nanostructured materials were then characterized to obtain more understanding on the materials' physical and chemical properties. Furthermore, through these characterizations, the gas sensing performance behaviour could be anticipated or envisaged.

Apart from the introduction section, this chapter is divided into three sections. In section 6.2, the author introduces several techniques that are commonly used for material characterizations. These techniques include Scanning Electron Microscopy (SEM), X-Ray Diffraction (XRD), Atomic Force Microscopy (AFM), X-Ray Photoelectron Spectroscopy (XPS), Energy Dispersion X-Ray (EDX), and Raman Spectroscopy analyses. Section 6.3 details the characterizations of the synthesized materials. This section is divided into four main subsections, which are characterizations of polyaniline, PVP, graphene, and Sb_2O_3. Finally in section 6.4, the summary of the findings are presented.

6.2 Micro-nano Characterisation Techniques

6.2.1 Scanning Electron Microscopy (SEM)

The SEM is the most routinely used instrument for the characterization of deposited nanomaterials. As it is designed for direct studying of the surfaces of solid objects, SEM provides morphology and structural information of the materials in nanoscale resolution by scanning an electron beam across a sample, and collecting signals from the beam-surface interaction. In this PhD study, the author investigated the surface morphology of the deposited nanostructured materials using *FEI NovaNano SEM* provided by the Physics Department, RMIT. These SEM images helped the author to understand the interaction between the sensing layer and the analyte gas. This is due to the fact that the sensitivity is strongly dependant on the surface morphology. Therefore information obtained via SEM was related to the response of the sensors.

Fig 6.1 shows the schematic diagram of an SEM set-up. A stream of electron is emitted from a heated filament (commonly a tungsten), either by applying a voltage or via field emission [33]. The stream is then condensed by the condenser lens forming the beam and limiting the current of the beam. In conjunction with condenser aperture, condenser lens then eliminate some high-angle electrons. The second condenser focuses the beam of electrons. Subsequently, the objective aperture further eliminates high angle electrons from the beam, and scans over the sample by scanning coils. The final lens then focuses the scanning beam onto the desired area of the sample.

The samples placed in the SEM chamber must be either conducting or coated with a thin metal layer to avoid electric charging. For this purpose, the author normally sputtered the samples with a thin film of gold. Moreover, the scanning was conducted in a low pressure to ensure the electrons were not scattered by gas molecules in SEM chamber. The details of the SEM investigation results will be presented in later part of this chapter.

6.2.2 X-Ray Diffraction (XRD)

The XRD is employed for the identification and quantification of various crystalline phases present in solid materials and powders [33]. In this research,

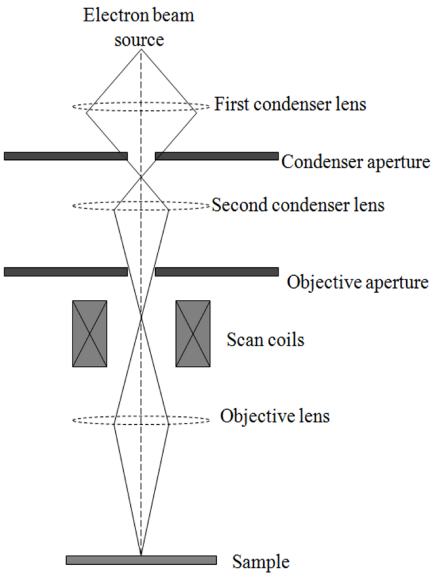

Figure 6.1: Schematic diagram of an SEM set-up.

the author used XRD for the determination of the structural properties of the nanostructured sensing materials. The crystal structure, and size of grains and nanoparticles can also be determined using this method. When a beam of X-rays incident on a crystal, a proportion of the X-rays is diffracted to produce a pattern. The diffracted pattern of the crystal phases can be identified by comparing to the reference patterns.

A set of parallel crystal planes is represented by the horizontal lines in Fig. 6.2. An incident beam of monochromatic X-rays of wavelength λ strikes this set of planes at a certain angle, the diffracted wave beam are produced leaving the various plane. The diffracted wave pattern can be either in phase or not, therefore either destructive or constructive interference can occur. Each diffracted X-ray signal corresponds to a coherent reflection which is known as Bragg reflection. The relation between the interplanar spacing and the incident rays can be described as:

$$n\lambda = 2d\sin\theta \tag{6.1}$$

where $n = 1, 2, 3, ...$ is the order of diffraction, λ is the X-rays wavelength, d is the interplanar spacing of the the crystal planes and θ is the incident angle.

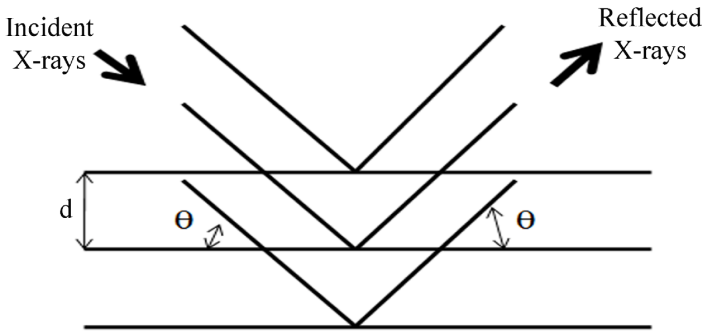

Figure 6.2: The reflection of an X-ray beam by lattice planes in a crystal [31].

In most cases, the first order of diffraction where $n = 1$ is used, therefore the Bragg's law is written as:

$$\lambda = 2d \sin \theta \tag{6.2}$$

In this PhD research, the crystalline phases of the synthesized nanostructured materials were examined by a wide angle *XRD (PW1820, Philips)* with a Cu-Kα source. The intensity of the diffracted X-rays was measured and recorded as a function of the diffracted angle 2θ and the specimen's orientation. Detail results of XRD investigation of the nanomaterials will be given in later parts of this chapter.

6.2.3 Atomic Force Microscopy (AFM)

The AFM has become the most widely used form of scanning probe microscopy since its invention by Binnig, Quate and Gerber in 1986 [228]. It is one of the most applied tools for imaging, measuring and manipulating matters at nanoscale. It gathers 3D information about the scanned sample by probing the surface structure with a sharp and vibrating tip. As the tip scans across, the vertical movements of the tip are recorded. Unlike SEM, AFM does not require special treatment (such as metal coating) for viewing purposes that can likely change or damage the samples. The tip is usually found at one end of AFM microscale cantilever. Forces between the tip and the surface sample cause the

cantilever to bend and deflect. By measuring the cantilever's deflection, forces are calculated using Hooke's law which can be written as:

$$F = -kz \tag{6.3}$$

where F is the force, k is the stiffness of the cantilever and z is the distance when the lever is bent.

In this research, the AFM characterization was conducted in collaboration with Prof Kaner's group at UCLA to investigate the deposited graphene layers. The details of the AFM results will be presented later parts of this chapter.

6.2.4 Energy Dispersion X-Ray (EDX)

The EDX is an analytical technique used for identifying the elemental composition of specimen. The EDX system cannot operate on its own and it works as an integrated feature of SEM equipments.

During the EDX analysis, the specimen is bombarded with an electron beam inside the SEM. The bombarding electrons collide with the electrons of the specimen atom, 'knocking' them out of their orbits. The vacated positions are then replaced by electrons from outer shells. However, this event only occurs if the outer electrons release some of their energies by emitting X-rays.

From the emitted X-rays, the identity of the atoms can be established. This can be carried out by measuring the amount of energy presents in the X-rays being released by specimen during the electron beam bombardment. Furthermore, the amount of energy released by the transferred electrons depends on which shell it is transferred from, as well as which shell it is transferred to. The atoms of every element release X-rays of unique amount during the transferring process.

The EDX spectrum is a plot on how frequently X-rays of special wavelengths are received for each energy levels. It displays peaks corresponding to these energy levels. These peaks are unique to individual atoms, hence corresponds to single elements.

6.2.5 Raman Spectroscopy

Raman spectroscopy is a popular characterization technique for monitoring the intensity and wavelength of light that is scattered inelastically from molecules or crystals. The Raman effect occurs when light strikes molecules and interacts with the electrons of the bonds of those molecules. Subsequently, the inelastic or Raman scattering occurs and the wavelength of the scattered light is shifted with respect to the wavelength of incident light. The change in its wavelength is determined by analyzing the spectrum of the scattered light.

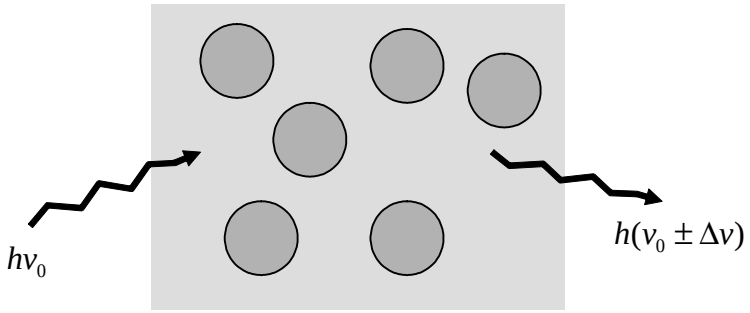

Figure 6.3: Representation of Raman scattering from particles [31].

For a Raman spectrum, the wavelength numbers of Raman shifts are plotted versus their respective intensities, which are generated from the interaction between photons and molecular vibrations (phonons in a crystal) [229]. These phonon modes are related to the chemical bondings, therefore Raman spectrum may provide information of which molecules or defects can be identified.

The Raman characterizations for this PhD study were conducted in Microanalytical Research Centre, University of Melbourne. Raman spectrum results for the deposited nanostructured materials will be presented later in this chapter.

6.2.6 X-Ray Photoelectron Spectroscopy (XPS)

For this PhD research, the chemical bonding arises from the deposited sensitive layers were investigated using XPS with the help of Prof. Johan du Plesis at RMIT University.

The XPS is usually utilized to measure the chemical and electronic states, elemental compositions, and assess the empirical formula of the elements that exist within a material. The samples or materials are irridiated with a beam of aluminium or magnesium X-rays, and the kinetic and the escape numbers of electrons of the analyzed materials are measured. As the XPS is based on the photoelectric effect, the source of the X-rays causes the photoelectron to be ejected from a surface. Generally, the X-rays are the K_α emission either from aluminium ($K_\alpha = 11486.58$ eV) or magnesium ($K_\alpha = 1253.56$ eV). The X-rays hit the surface of the sample and interact with the atomic electrons in the sample, mainly via photon absorption, therefore causing the ejection of photoelectron. The kinetic energies and the number of the ejected photoelectrons are plotted as a spectrum of their binding energies.

6.3 Micro-nano Characterizations Results

6.3.1 Analysis of Electropolymerized Polyaniline Nanofibers

The FE-SEM images in Fig. 6.5 to 6.6 reveal that the electropolymerized polyaniline nanofibers are grown densely and uniformly on the SAW transducers. It is also seen that the nanofibers formed 3-dimensional porous structures which are connected together in a network. The diameters of the nanofibers are in a range of 40-50 nm. It is found that no morphology change occurs on polyaniline nanofibers before and after dedoping with NaOH, which is similar to the observations reported by Huang et al. [73].

A current-time curve for the electropolymerization of polyaniline nanofibers is given in Fig. 6.4. Stage 1 occurs when a voltage of 0.75 V was applied to the system. Once the voltage was given, the current decreases as shown in stage 2. This was attributed to the formation of the uniform polyaniline nucleation through the radical-coupling polymerization. In the radical-coupling polymerization, the current was controlled by the diffusion of aniline, therefore the drop in current was observed [230]. After the initial decrease, the anodic current rises with the time. It is proposed that the elongation of nucleation occurs during this

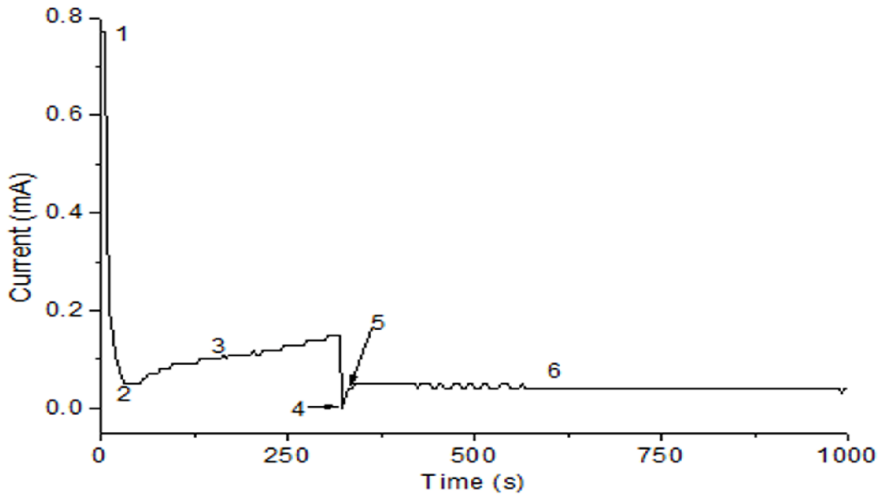

Figure 6.4: A current-time curve for the electropolymerization of polyaniline nanofibers.

time, therefore the surface becomes more conducting causing decrease in resistance. At this stage, the anodic current continuously increases. Afterwards, the voltage was reduced to 0.65 V. The current falls as in stage 4. During this time the voltage was reduced to guarantee that the growth of the nanofibers from the nucleation sites proceeds steadily [37]. Then, again the current increases which is similar to stage 3. In stage 6, it was observed that the current started to stabilize. Highly ordered pore structures can be obtained under the equilibrium conditions [231]. Therefore at this stage, highly ordered fibre-like structure of polyaniline is clearly formed.

Fig. 6.5 shows the surface morphology obtained after the second electropolymerization step. Similar to the investigation by Liu et al. [211] and Yu et al. [37], higher voltage formed homogeneous distribution of nucleation particles which acted as a scaffold for the secondary growth. [37] suggested that by applying high voltage for a short time, the overgrowing of the nucleation particles is prevented. The lower voltage of 0.65 V was then applied to ensure that the growth proceeded steadily. At this point, polyaniline nanofibers started to grow perpendicularly from the basis of the nucleation sites and the morphology which is observed in Fig. 6.6 was obtained.

In Fig 6.6, it is observed the insulated gap (on the right side) was bridged,

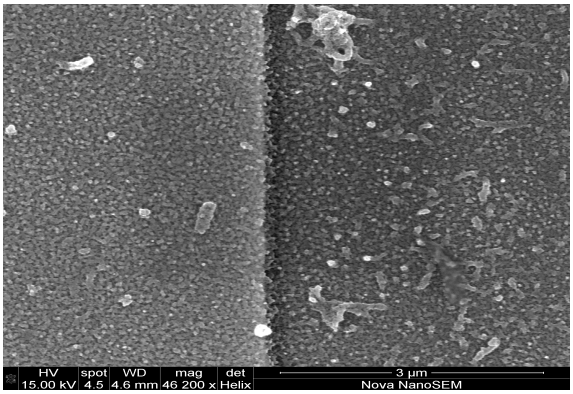

Figure 6.5: Electropolymerized polyaniline deposited for 6 min.

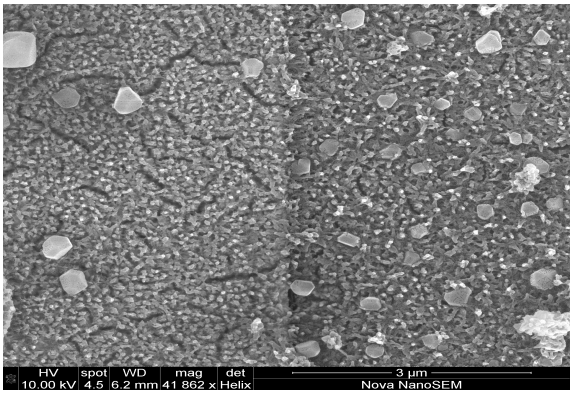

Figure 6.6: Electropolymerized polyaniline deposited for 35 min.

showing gradual polyaniline nanofibers growth between the electrodes [137,232]. The resistance of either input or output IDTs was measured before the electropolymerization and showed open circuit. This indicates that the electrodes were perfectly separated by gaps. The resistance was dramatically decreased to 34 Ω after electropolymerization, confirming that the neighbouring electrodes were bridged by polyaniline nanofibers. In this study, the author deposited various thicknesses of polyaniline nanofibers thin films. By using profilometer, the thickness of polyaniline nanofibers thin films was measured and presented in Table 6.1, as a function of the deposition time. In the following chapter, the author will present the effects of the film thickness on gas sensing performance.

Table 6.1: The film thickness of electropolymerized polyaniline nanofibers as a function of the different deposition time.

SAW	Deposition Time (min)		Thickness (μm)
	0.75 V	0.65 V	(less than 15% error)
SAW A	5	40	7.0
SAW B	5	25	3.5
SAW C	5	15	1.0
SAW D	5	2	0.3
SAW E	5	0	0.2

Electropolymerization at Different Temperatures

For the optical characterization purposes, polyaniline nanofibers were deposited onto ITO glass. Three deposition parameters were investigated while the other parameters were remained the same. First, the author performed UV-Vis absorption spectra measurements using *Ocean Optic HR4000CG-UV-NIR High Resolution Spectrometer* and investigated the deposition temperature effect. Fig. 6.7 compares the curves obtained for polyaniline deposited on ITO glass substrates under the sets of conditions that was given in Table 5.1.

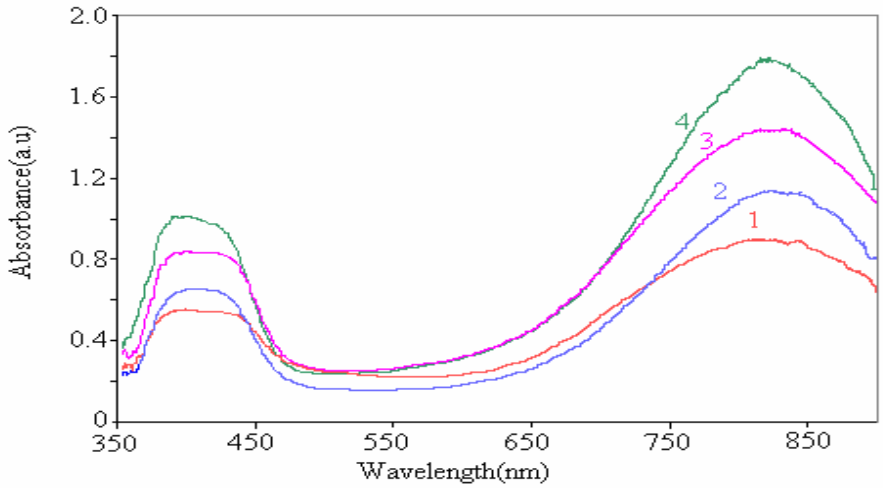

Figure 6.7: UV-visible absorption spectra of polyaniline nanofibers deposited on ITO glass at different temperatures.

In. Fig. 6.7, the two absorbance bands at around 400 and 825 nm are probably characteristics of polaronic charge carriers for polyaniline. The increased

absorbance is indicative of the control growth process. Changing the temperature from room temperature to the one close to ice bath while keeping the polymerizing potential constant. The change in temperature is found to increase the absorbance, justifying the fact that the temperature does influence the formation of nanofibers. This result was published in Proc. Device and Process Technologies for Microelectronics, MEMS, Photonics, and Nanotechnology, SPIE, vol. 6800, 2007.

Electropolymerization at Different Voltages

For the electropolymerization of polyaniline of different voltages (Fig. 6.8), the UV-Vis absorption spectra measurements show that two adsorption peaks centred at ∼410 and ∼720 nm are found for all voltages (except for 0.65 V where the peak is small). This revealed that the deposition of electropolymerized polyaniline nanofibers with high voltage increases the thickness of the films, therefore, the intensity of absorption peak increases as the voltage increases.

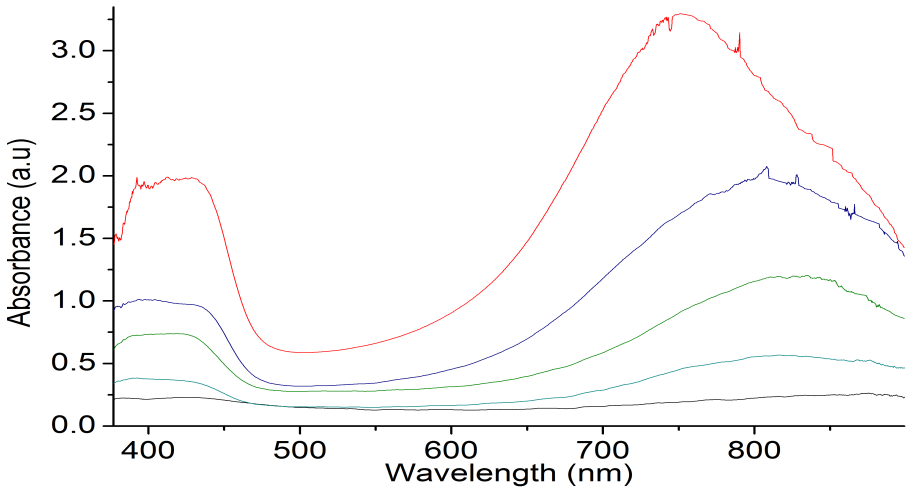

Figure 6.8: UV-visible absorption spectra of polyaniline nanofibers deposited on ITO glass electropolymerized at different voltages.

Electropolymerization with Different Acid Concentrations

SEM images in Fig. 6.9 show the electropolymerized polyaniline at different acid concentrations. Image of the polyaniline nanofibers in Fig. 6.9(a) is similar to

the previous figure (Fig. 6.6).

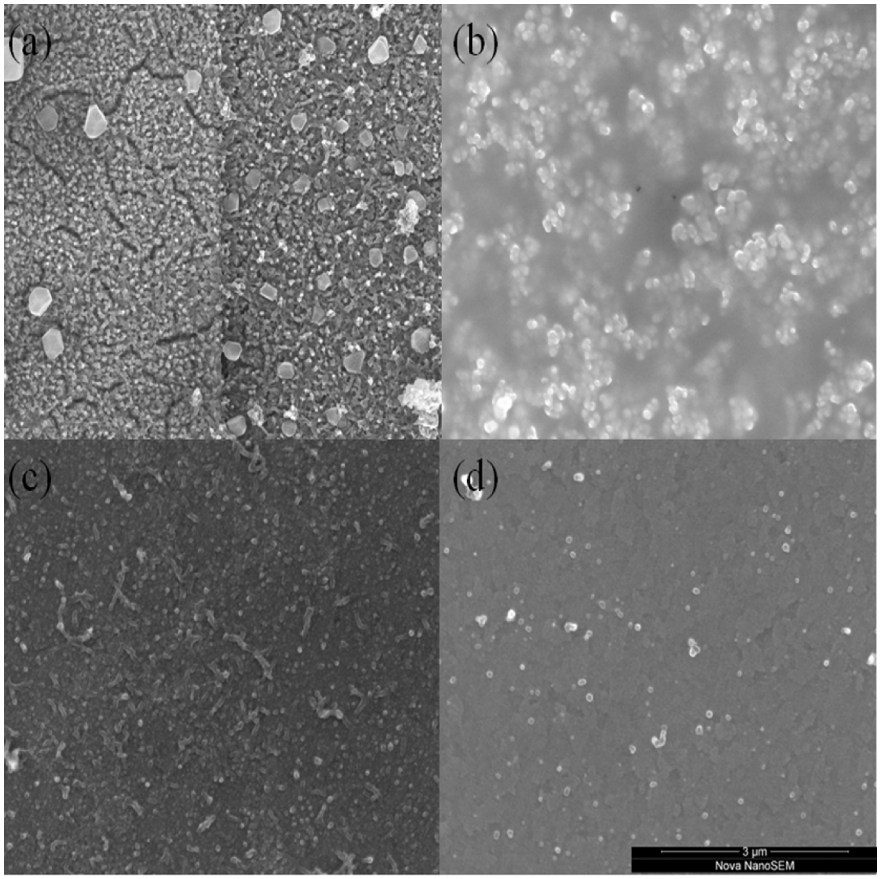

Figure 6.9: SEM images of electropolymerized polyaniline at different acid concentrations; (a) 1.0M HCl, (b) 0.5M HCl, (c) 0.3M HCl, and (d) 0.1M HCl.

In Fig. 6.9(b), short nanofibers are observed grown on the top of each other. The width of the nanofibers are in the range of 50 to 150 nm which were larger than the nanofibers obtained when using 1.0M HCl in the electrolyte. For the polyaniline obtained during electropolymerization in 0.3M HCl, the surface morphology of the polyaniline is shown in Fig. 6.9(c). From this image, less nanofibers are observed as compared to that of 1.0M HCl. The diameter of the nanofibers are in the range of 40 to 70 nm with lengths from 100 to 650 nm. Apart from the nanofibers, polyaniline nanoparticles are also found distributed evenly on the surface with average diameter of 50 nm. The author also conducted electropolymerization experiment using 0.1M HCl electrolyte (Fig. 6.9(d)). The image only contains nanoparticles with diameters in the range of 20 to 150 nm.

As seen from the SEM images, the rate of polyaniline growth increases with increasing HCl concentrations. This observation is similar to the results obtained by Pournaghi-Azar and Habibi [233] who conducted experiments on polyaniline using various concentrations of H_2SO_4.

Polyaniline requires 50% of the nitrogen to be protonated to form emeraldine salt. Low concentration of HCl means less H^+ available for protonating the nitrogen. Based on visual observations, different colours of polyaniline were observed because the different oxidation states of polyaniline were formed. The UV-Vis absorption spectra measurement (Fig. 6.10) compares the absorption of polyaniline nanofibers electropolymerized at different HCl concentrations. At the absorption range of 650 to 910 nm, the low concentration of HCl causes the peak wavelength gradually shifts to the longer wavelengths. On the other hand, in the very low concentration of HCl, the observed spectrum is different with peak appearing at 410 nm. While for other spectra, two peaks centred upon ~390 and ~800 nm were observed, only one peak was found for 0.1M spectrum.

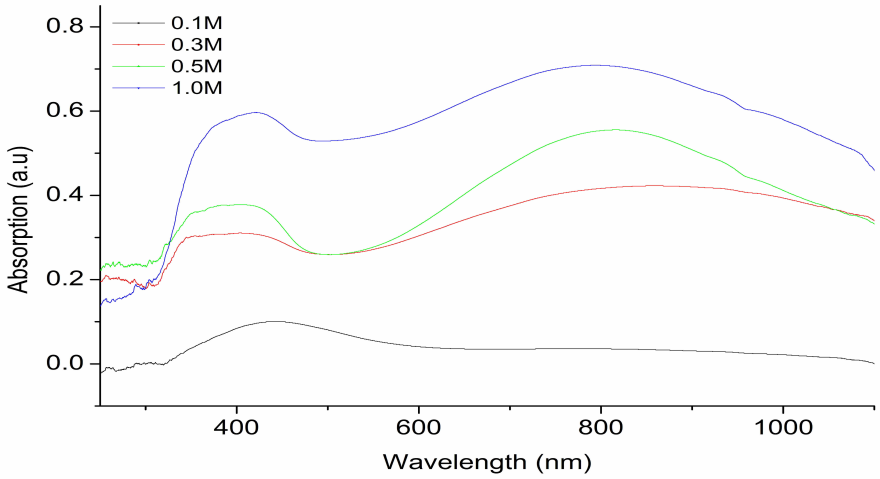

Figure 6.10: UV-visible absorption spectra of polyaniline nanofibers deposited on ITO, electropolymerized with different acid concentrations.

In the following chapter, the author will present the gas sensing properties for the electropolymerized polyaniline nanofibers synthesized with different acid concentrations. The gas sensing performance of films deposited with different acid concentrations were investigated and will be discussed in chapter 7.

Electropolymerization with Different Type of Acids - Nitric Acid

Fig. 6.11 shows the electropolymerized HNO_3 doped polyaniline nanofibers. From the SEM image, the average diameter of polyaniline nanofibers is about 30 - 50 nm, whereas it was about 40 - 50 nm when HCl was used as the electrolyte during electropolymerization (refer to Fig. 6.6). The nanofibers which were grown in HNO_3 medium had random directions, and were not as ordered as HCl polyaniline. The EDX spectra (Fig. 6.12) revealed the existance of Cl when HCl dopant acid was used. However the Cl peak does not appear when the HNO_3 doped polyaniline nanofibers were characterized using EDX. Instead, N peak is more obvious than that of HCl doped polyaniline nanofibers.

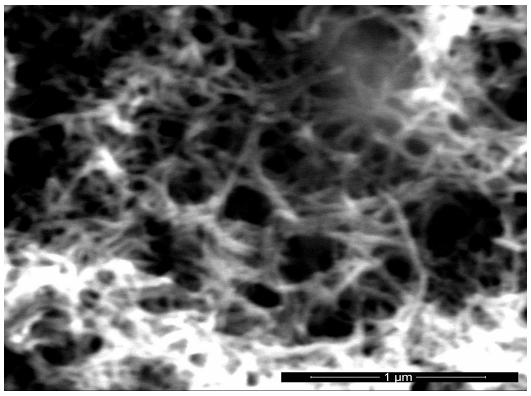

Figure 6.11: Electropolymerized polyaniline nanofibers using electrolyte containing HNO_3 and aniline monomer.

It is observed that the use of different anions in electrolyte affected the morphology of the polyaniline. Taking into account the configuration of the investigated anions, it is obvious that two different species are involved. HCl contains Cl^- anion whereas the HNO_3 contains oxygen atoms in a trigonal valence state [234]. Therefore it is expected that the anions structure might influence the morphology of the electropolymerized polyaniline. It is suggested that anions like Cl^- can be easily accommodated as a counter-ion along the polymer chain. While for HNO_3, more room is required to accomodate NO_3^- as a counter-ion, thus might cause a higher degree of polymer chain branching. This is probably attributed to the better ordered morphology for the nanofibers formed in HCl medium compared to the HNO_3 medium polyaniline nanofibers.

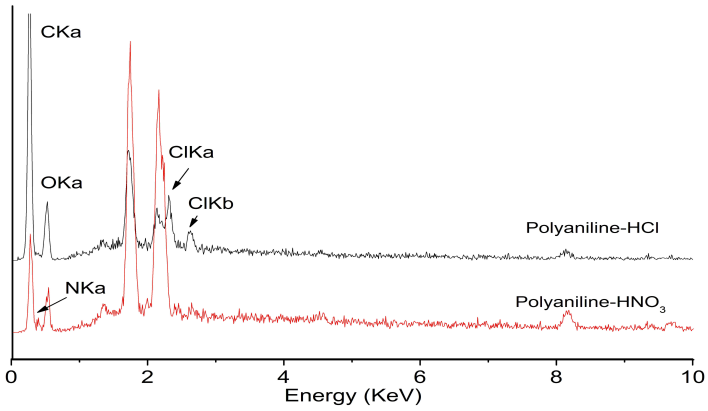

Figure 6.12: EDX spectra for HCl and HNO_3 media electropolymerized polyaniline.

6.3.2 Analysis of Electropolymerized Polyaniline Nanofibers/ MWNTs Composite

In previous chapter, the author described the synthesis of electropolymerized polyaniline/MWNTs composite on SAW transducers. SEM was utilized to examine the surface morphology of the deposited composite. Fig. 6.13 shows the image obtained from the composite materials. The polyaniline/MWNTs composite shows compact fibres structure compared to the electropolymerized polyaniline itself (inset Fig. 6.13). The average fibres' diameter of polyaniline/MWNTs composite was 50 nm.

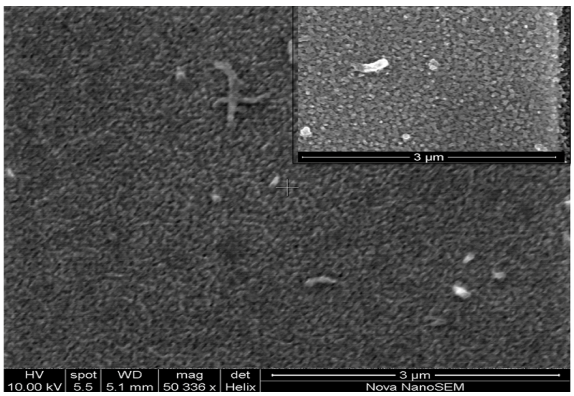

Figure 6.13: SEM image of electropolymerized polyaniline/MWNT composite. Inset figure is the SEM image of electropolymerized polyaniline.

It is anticipated that the existence of MWNT in polyaniline chain increases the electrical conductivity [88,235]. Resistance of either input or output IDTs after the electropolymerization of pure polyaniline is 5.5x10^3 Ω, whereas the resistance of electropolymerized PANI/MWNTs is 40 Ω. The enhanced conductivity is probably due to the dopant effect or charge transfer from the quinoid unit of polyaniline to the carbon nanotubes [214]. Polyaniline can be considered as a good electron donor while CNT is a good electron acceptor. Besides, the large aspect ratio and surface area of MWNTs may served as conducting bridges, connecting polyaniline conducting domains and increasing the effective percolation [214,236]. In addition, the enhancement in conductivity probably attributed to the effectiveness of electron delocalization that is increased by the interaction between MWNTs and polyaniline [83]. The gas sensing measurements of the developed polyaniline/MWNTs SAW sensors were conducted to H_2 gas. The obtained results will be presented in the next chapter.

6.3.3 Analysis of Chemically Polymerized Polyaniline Nanofibers/ Diamond Nanoparticles Composite

The morphology of nanocomposite structure was studied using SEM as shown in Fig. 6.14. It is observed that polyaniline and diamond form nanofibers and clusters of coral-like structures, respectively, and are connected together in a network. The average diameter of nanofibers is ∼50 nm.

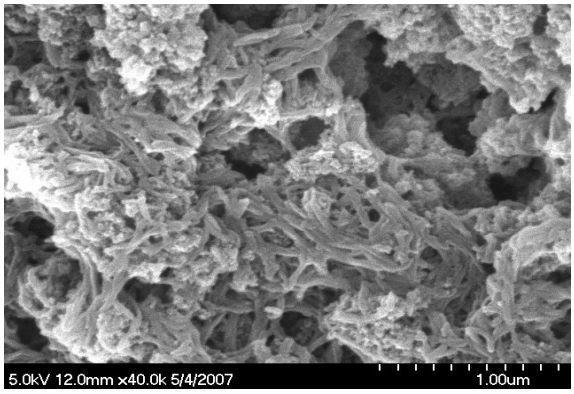

Figure 6.14: SEM image of the polyaniline/diamond nanofibers.

The X-ray diffraction pattern of the dropcasted layer is shown in Fig. 6.15

where broad peaks are observed at ∼16 ° and 44 °. The second diffraction peak from the nanocomposite sample is matched to the peak from the pure standard diamond, signifying the presence of diamond particles in the CSA doped polyaniline/diamond film.

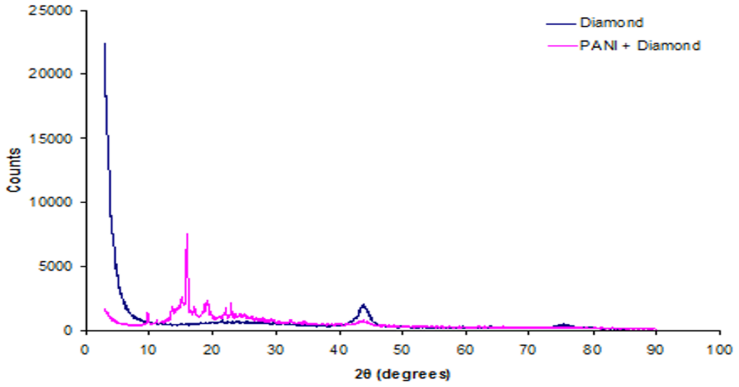

Figure 6.15: XRD pattern of the polyaniline/diamond nanofibers.

6.3.4 Analysis of Electrospin Coated PVP Fibres

As mentioned previously in chapter 5, viscosity of the solution is one of the most important factors influencing electrospinning. Generally, the morphologies and the diameters of the electrospin coated fibres change correspondingly as the concentration varies. Different concentrations of PVP (M_w = 30000) were electrospun (refer Table 5.3) on silicon substrates. The substrates were cleaned prior to the deposition of the electrospun PVP. The details of the cleaning process were presented in chapter 4. The preparation of the different concentrations of PVP solution was explained in details in previous chapter. Fig. 6.16 shows the selected SEM images which depict the effect of the PVP viscosity on the morphological appearance of films. Whereas Fig. 6.17 shows the diameters of the particles, beads and fibres for every PVP concentrations.

For the lowest concentration of PVP (42%) which is shown in Fig. 6.16(a), only particles with diameter of 0.2 to 1.5 μm are observed. There are no fibres which are formed at this concentration. Then at the PVP concentration of 48% (Fig. 6.16(b)), the fibres with large orbicular beads appear. The thickness of the

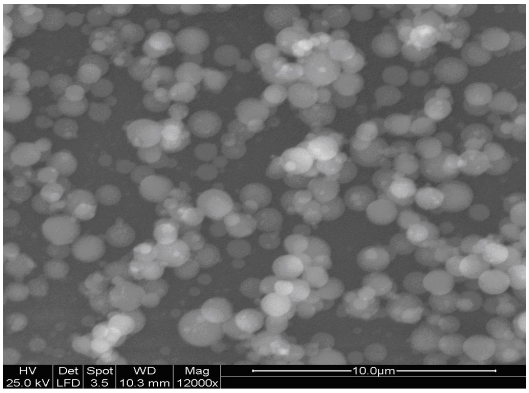

(a) 42%

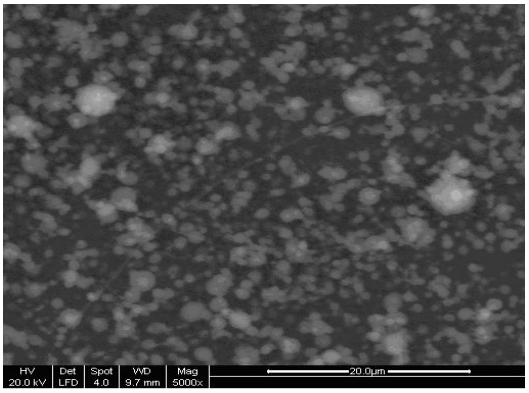

(b) 48%

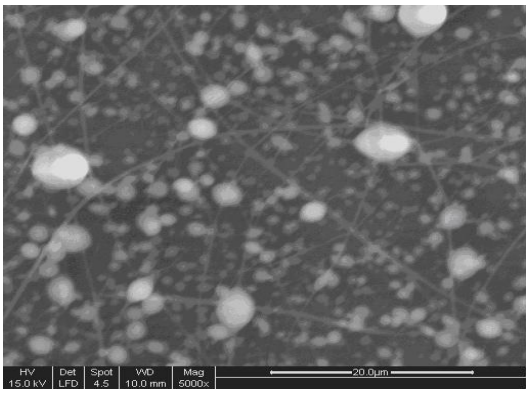

(c) 50%

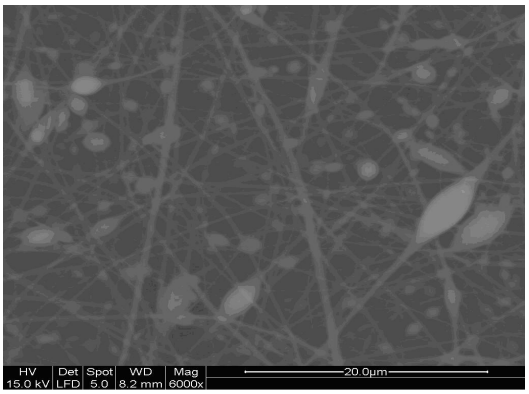

(e) 52%

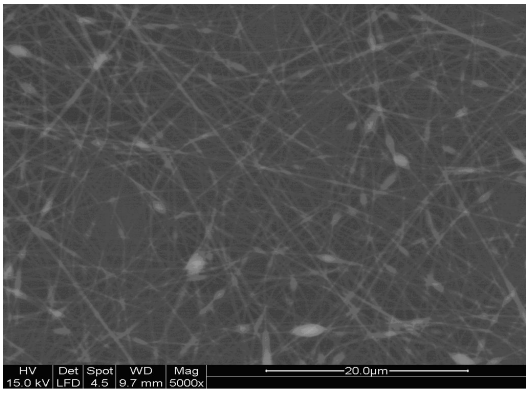

(d) 56%

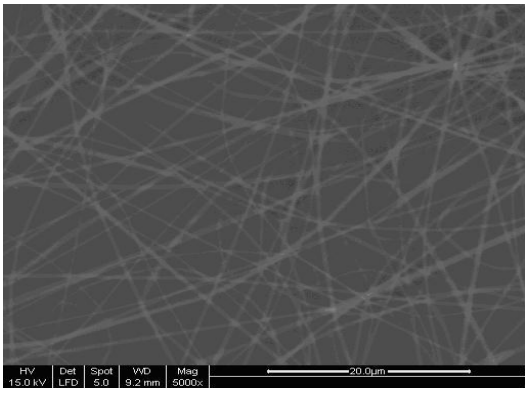

(f) 58%

Figure 6.16: SEM images of electrospin coated PVP on silicon substrates, prepared at different PVP concentrations.

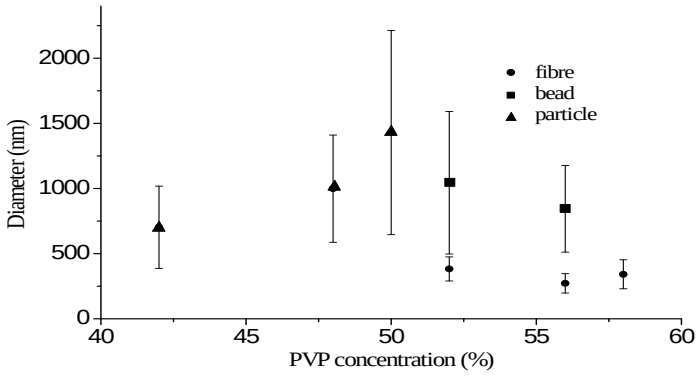

Figure 6.17: Diameter distribution of PVP at different concentrations.

fibres are varied from 90 to 400 nm. Here, the similar particles as in the 42% electrospun films are observed. With the increase of PVP concentrations, the number of the particles are reduced and most of the fibres have spindly beads. The diameter of the beads decrease with the increase of the PVP concentrations. The formation of the beads can be related to the formation of droplets in electrospray. The presence of the combination of beads and fibres has been reported by Fong et al. [237]. They suggested that the surface tension and the viscoelastic properties of the polymer solution are among the key factors in electrospinning process. Further increase in the solution concentrations cause the beads to totally disappear. At 58% concentration of PVP, the electrospun PVP fibres are formed. The width of the fibres are in the range of 100 to 600 nm. The increased viscosity enabled the charged jet to totally withstand the coulombic streching force, therefore resulting in the observed fibres.

As mentioned previously, there were three differents morphologies observed: particles, beads, and fibres. The dimensions of these morphologies were measured using Image J software. For each spinning condition, at least 100 measurements for each figure was obtained. In Fig. 6.17, although fibres were found at 45% and 50% concentrations of PVP, the author has removed their effects from the graph as the number was insignificant. For the particles observed at PVP concentration of 42%, 48% and 50%, the diameter range was increased as the concentration increased. In addition to that, the 56% viscosity polymer was observed to have smaller range of length and thickness for beads and fibers. However at this point,

less fibres were observed. The content of solution was finally tranformed totally to fibre through electrospinning at 58% concentration.

The effect of the distance between the tip of the needle and ground collector during electrospinning process was investigated. To examine the effect, the experiments were conducted with two different concentrations; 42% and 58% PVP solutions under 12 kV. Three different collection distances of; 5.5, 8.5 and 11.5 cm were chosen. The morphology of the fibres and particles were investigated via SEM and Image J software. Obviously, the morphology of the as-spun fibres which are shown in Fig. 6.20(a), (b) and (c) are similar. However, it has impacted on the thickness of the fibres and also the deposition rate during electrospinning. Fig 6.18 reveals the number of fibres formed at each distances. The shortest distance has the highest number of fibers showing the highest deposition rate. The number of the fibres decreases as the distance increases. Histrograms in Fig 6.20 reveal that the fibres formed at 5.5 cm collector distance tend to be thicker than the other distances. Apparently, at the distance of 8.5 and 11.5 cm, majority of the fibres have a thickness of about 300 to 400 nm. However, far collection distances result in less quantity of fibres.

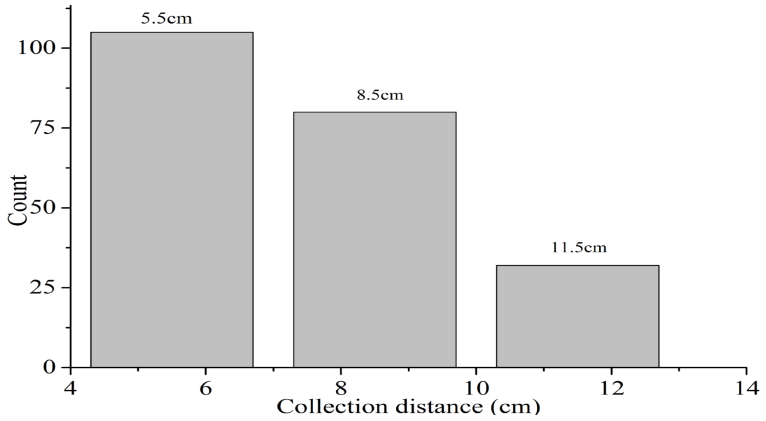

Figure 6.18: Distributions of PVP (concentration of 58%) fibers at different collection distances.

This impact occurs equally on the other PVP solution (42%). The distribution of the electrospun particles were much closer as the distance decreases. Too close collection distance causes the solvent not to evaporate thoroughly before reaching the target, therefore the solvent remains and the collected particles

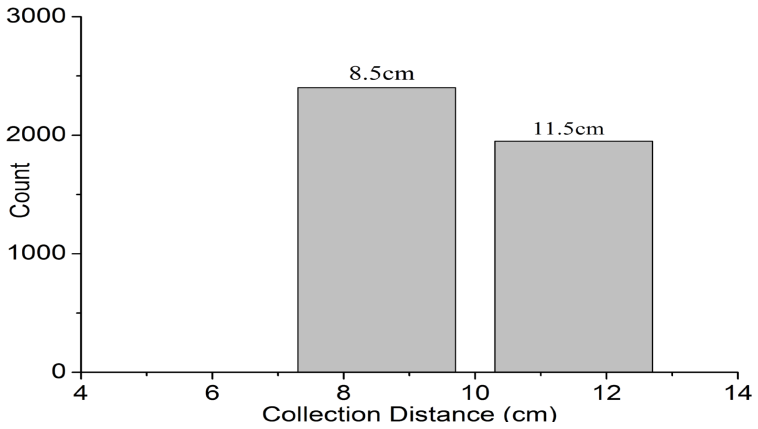

Figure 6.19: Distributions of PVP (concentration of 42%) fibers at different collection distances.

re-dissolve and conglutinate. Fig 6.19 reveals the number of fibres formed at each distances for the 42% of PVP. Fig. 6.21(a), (b) and (c) show the images of electrospun PVP at different collection distances whereas the histograms in Fig. 6.21 show the subsequent results of different collection distances for 42% PVP concentration.

The author investigated the effect of the PVP morphologies and utilized the electrospun PVP as sensitive layers for gas sensing. The details of the gas sensing performance for PVP/$LiTaO_3$ SAW sensors will be presented in the following chapter.

6.3.5 Analysis of PVP/Polyaniline Fibres

In chapter 5, the author described the electrospinning of PVP/ES and PVP/EB composites on the whole area of $LiTaO_3$ SAW transducers. For the characterization purposes, the author also electrospun both composites on silicon substrates. The SEM was used for investigating the surface morphology of the electrospun composites, and the obtained images are shown in Fig. 6.22 and 6.23 for PVP/ES and PVP/EB composites, respectively.

It is observed that both composites show similar surface morphologies which are fibres and beads. By using Image J software, the width of the fibres are measured to be in the range of 50 to 650 nm. It is observed that the electrospun

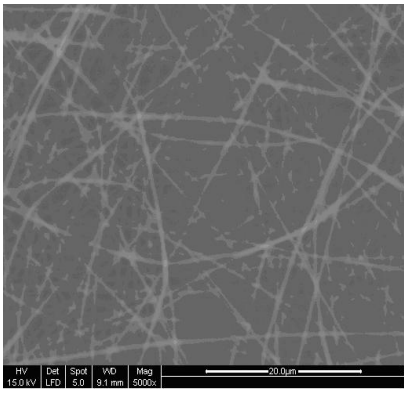

(a) 5.5 cm

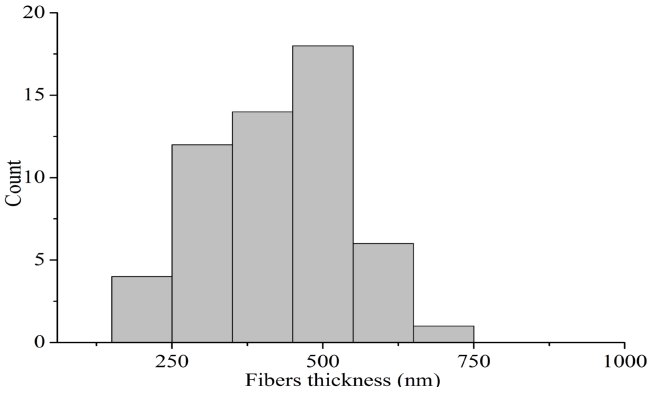

Fibers thickness at 5.5 cm

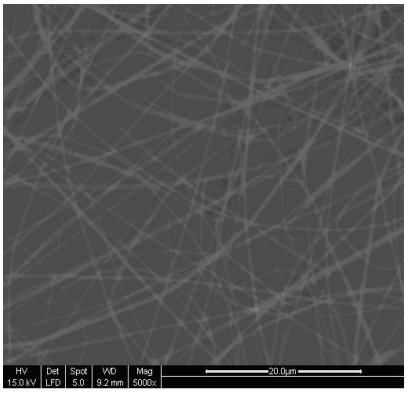

(b) 8.5 cm

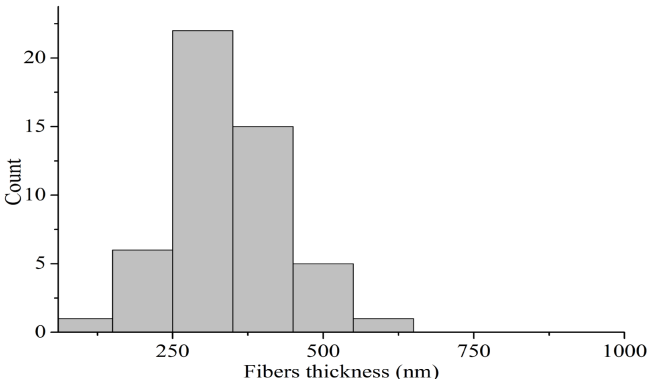

Fibers thickness at 8.5 cm

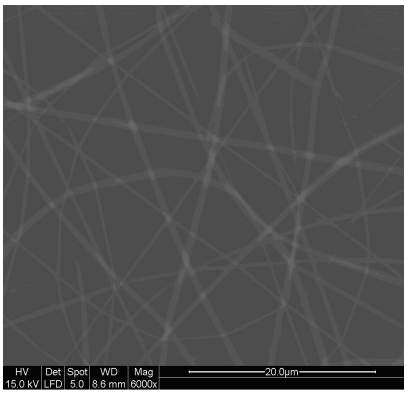

(c) 11.5 cm

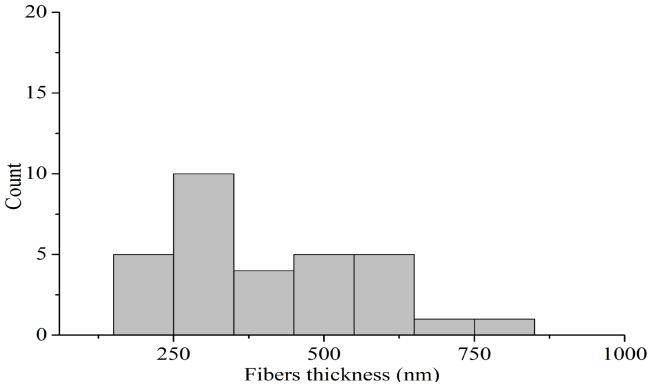

Fibers thickness at 11.5 cm

Figure 6.20: SEM images of electrospun 58% collection distances. On the right, the subsequent fibres thickness histograms are presented.

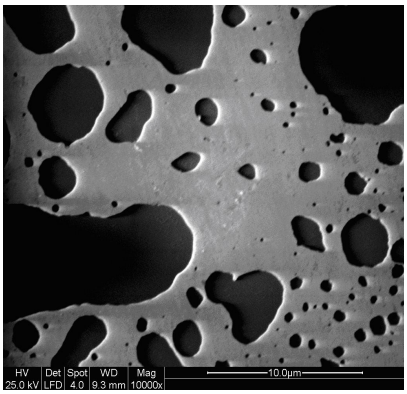

(a) 5.5 cm

No particles formed

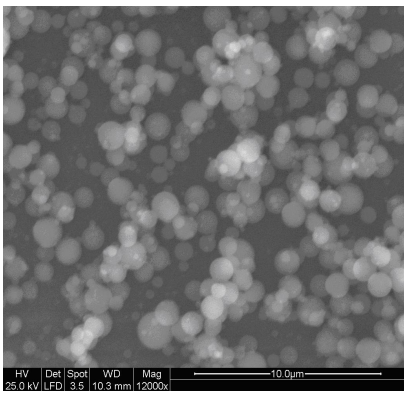

(b) 8.5 cm

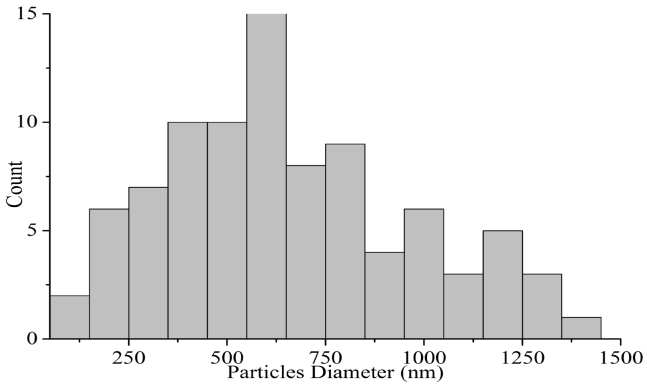

Particles diameters at 8.5 cm

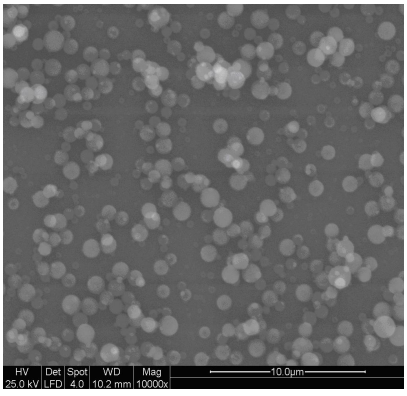

(c) 11.5 cm

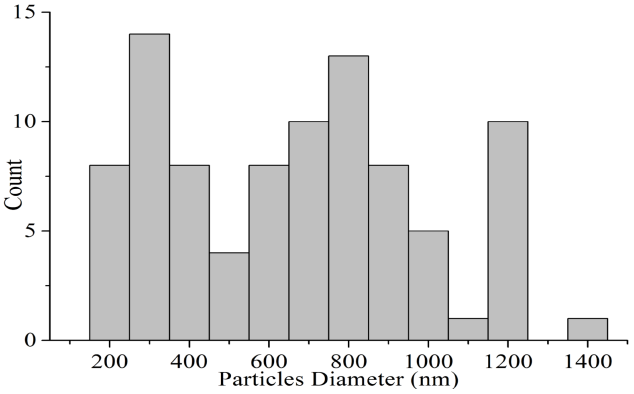

Particles diameter at 11.5 cm

Figure 6.21: SEM images of electrospun 42% PVP concentrations at different collection distances. On the right, the subsequent particles diameter histograms are presented.

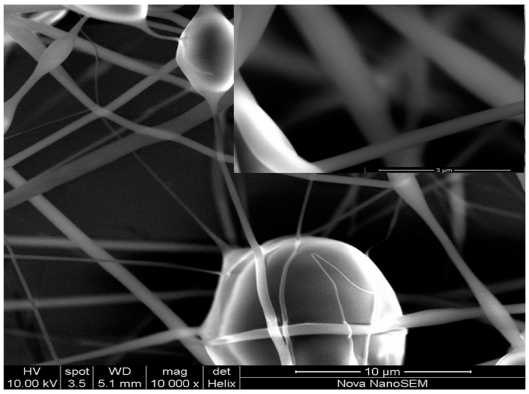

Figure 6.22: SEM images of PVP/ES composite, inset figure shows the higher magnification image.

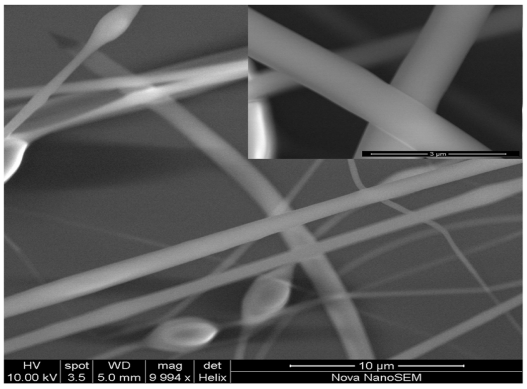

Figure 6.23: SEM images of PVP/EB composite, inset figure shows the higher magnification image.

fibres are in random directions in planes parallel to the substrate. At this stage, the author also found beads with diameters of up to 11.6 μm. The beads appear due to the viscosity of the PVP/ES composite which is not high enough to produce perfect fibres during electrospinning. The effect of the viscosity on the electrospun morphology were discussed in the formation of pure PVP with different concentrations.

Similar to PVP/ES composite, PVP/EB also produced fibres and beads. However, the width of the fibres were in between 322 to 1000 nm, which was larger that PVP/ES fibres. Whereas, the beads were found to be smaller than the other composite.

PVP is categorized as non-conducting polymer, while polyaniline is a conducting polymer. In this PhD study, PVP/ES and PVP/EB composites were electrospun on SAW transducers. It was expected that various SAW sensing mechanisms, which were introduced in chapter 3, are involved during the exposure of the PVP/ES and PVP/EB based sensors to H_2 gas. The gas sensing performance will be discussed in the next chapter.

6.3.6 Analysis of Electrospin Coated PVP/MWNTs Fibres

The surface morphology of the electrospun PVP/MWNTs composite was investigated via SEM and are shown in Fig. 6.24 and 6.25. In Fig. 6.24, both fibres and beads are observed in random directions, in planes parallel to the substrate. The average diameter of the fibres are 250 nm, while for the beads, the diameters are between 500 to 1500 nm. PVP is well known to prevent agglomeration of the particles, resulting in stable size distribution. In Fig. 6.25, it is observed that MWNTs are everywhere in the particles. Particles in Fig. 6.25 were obtained by synthesizing the PVP/MWNTs via the same method with reduced PVP concentration in the solution. Although no fibres were observed, MWNTs are clearly seen inside the PVP particles and distributed evenly in the particles.

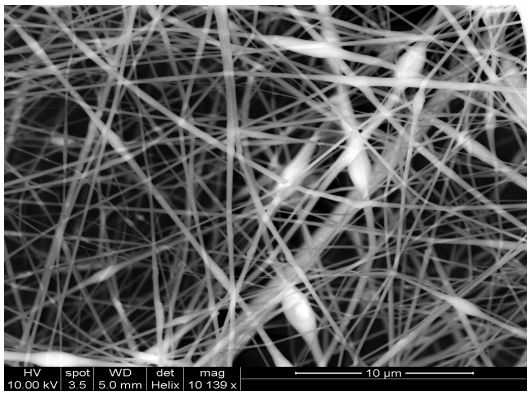

Figure 6.24: SEM image of electrospun PVP/MWNTs composite (with 1.525g PVP).

For the gas sensing applications, the author electrospun the PVP/MWNTs

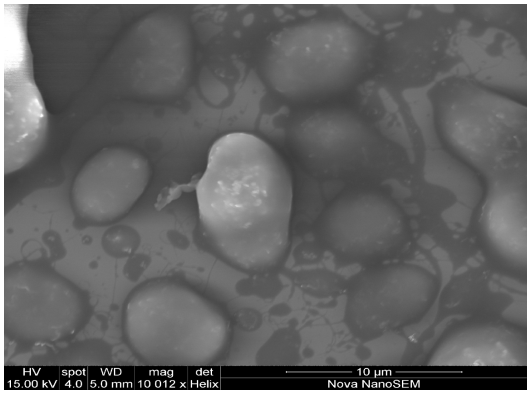

Figure 6.25: SEM image of electrospun PVP/MWNTs composite (with 1.025g PVP).

composite onto the whole area of the SAW transducers. The gas sensing performance will be presented in chapter 7.

6.3.7 Analysis of Graphene-like Nano-sheets

The chemically reduced graphite oxide forming graphene sheets were investigated using several nano-characterization methods. SEM and AFM were used to examine the surface morphology of the deposited graphene. In addition to that, XPS and Raman spectroscopy were conducted in order to investigate the chemical properties of the deposited sensitive layer.

It can be seen in Fig. 6.26 that the graphene-like sheets which are visible as pale grey regions cover both metallized electrodes and substrate of the SAW devices. However, it is observed that there are multiple layers of deposited graphene. The AFM image which is shown in Fig. 6.27 depicts numbers of graphene layers. It is estimated that the graphene-like sheets are monoatomically thick.

Visible Raman spectroscopy is well established as a powerful tool for characterizing graphene [238]. Fig. 6.28 shows that the spectrum is dominated by the so called G band (graphitic, sp^2) at $\sim$1580 cm^{-1}, a D band at $\sim$1350 cm^{-1} and a D' band at 1620 cm^{-1}. Also evident are the 2D (i.e. G') band at $\sim$2700 cm^{-1} (an overtone of the D band) and the D+G combination mode at $\sim$2950 cm^{-1}.

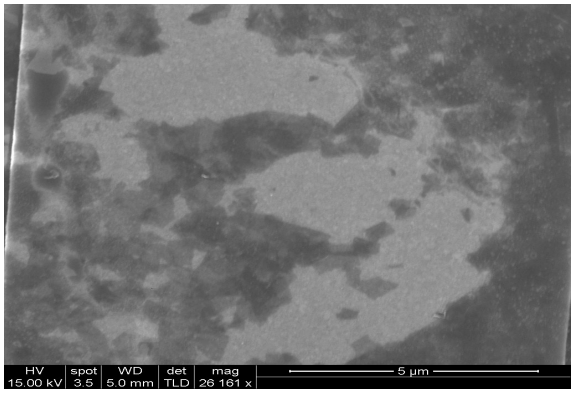

Figure 6.26: SEM image of graphene-like nano-sheets on a SAW transducer.

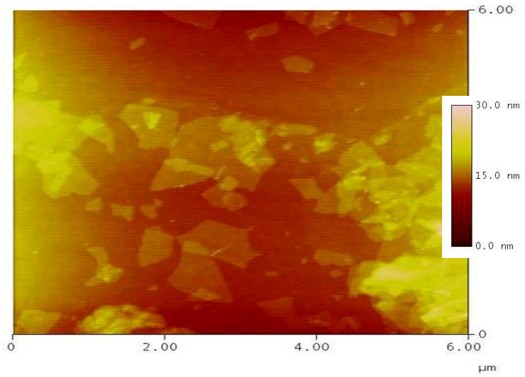

Figure 6.27: AFM image of chemically reduced graphite oxide nano-sheets.

The D, D' and D+G bands are all induced by local defects and disorders, and have been previously observed along graphene and graphite edges [239]. The D band is quite intense compared to the G band in this spectrum and their ratio is related to the in-plane correlation length, La [238,240]. It is calculated that the length for the sample using the expression $La = 4.4(I_G/I_D)$ [238,241] which yields a value of La ∼2.7 nm. This indicates that the nano-sheets contain nano-crystalline graphitic phases with small sp^2 domains following the reduction of GO with hydrazine [220]. The 2D band of the Raman spectrum is also known to evolve with the number of graphene layers for single-, bi- and few-layers allowing unambiguous identification of the number of layers from 1 to 5 [238]. The structure of the 2D band suggests that there are >5 graphene layers associated with the nano-sheets which is consistent with the AFM measurements shown in

Fig. 6.27.

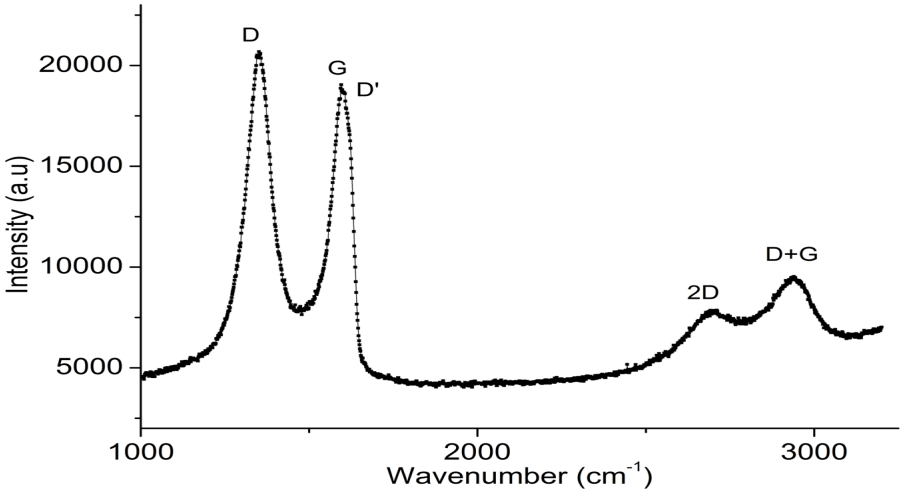

Figure 6.28: Raman spectrum for the deposited graphene-like nanosheets on the $LiTaO_3$ SAW device obtained using 514.5 nm laser excitation.

Fig. 6.29 shows the XPS spectrum conducted on the $LiTaO_3$ SAW device. The XPS analysis indicated that the $C1s$ spectrum signifies $C-C$, $C-O$ and $C(O)O$ bonds at 284.5, 286.3 and 289.4 eV, respectively. Since graphene has a benzene ring-like structure, $C=C$ bond should have been observed in these spectra. The absence of a $C=C$ signature in the XPS spectrum suggests that the graphene structure is imperfect and may be highly saturated which is a consequence of incomplete reduction with hydrazine. In contrast, Raman is particularly sensitive to sp^2 bonded carbon when using visible excitation, hence the presence of the G band indicates that $C=C$ bonding is present but that crystallite size appears to be small. Hence, both the XPS and Raman analyses indicate incomplete reduction of GO by hydrazine.

TGA analysis of GO was performed at temperatures ranging from 25 °C to 900 °C in argon atmosphere. The GO material began to lose weight as soon as the temperature increased. At 100 °C, the graphene-like mass loss was almost 20%. The major weight loss occurred following heating at ∼200 °C and higher. Above 500 °C, no major loss was detected as the mass reduction was already >90%. This indicates that reduced GO is highly unstable upon heating even at modest temperatures (<100 °C) [220].

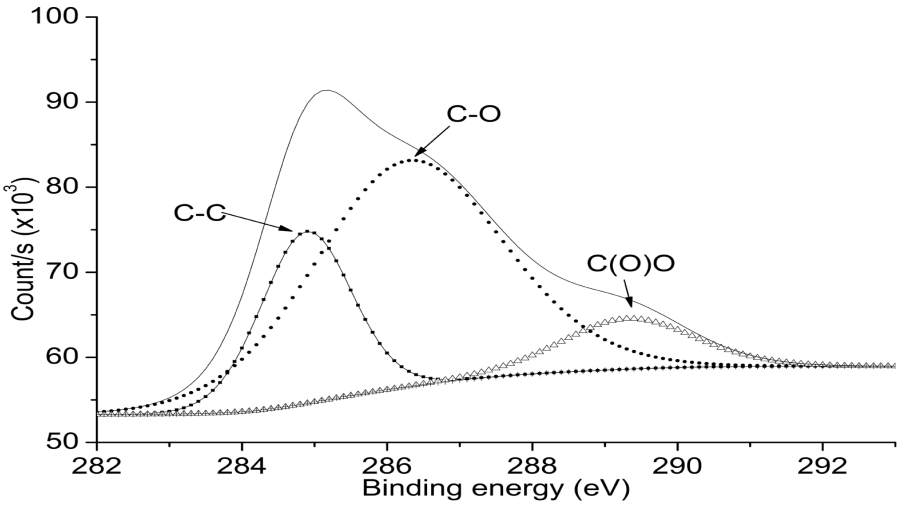

Figure 6.29: C1s XPS spectra for reduced GO.

From the gas sensing point of view, the large surface area of the deposited graphene-like layers should increase the interaction area available for the gas molecules, thus enhancing sensitivity. The author had investigated the gas sensing performance of the deposited graphene-like nano-sheets. The gas sensing results will be discussed in the next chapter.

6.3.8 Analysis of Thermally Evaporated Antimony Oxide Nanostructures

Thermally grown Sb_2O_3 nanostructures were characterised via SEM, XRD and EDX methods. In previous chapter, the author informed that different substrates coated with thin layer of Au were used for the investigation of Sb_2O_3 nanostructures. The author conducted the experiments at different operating temperatures, and the morphology of nanostructures on each substrates were investigated using SEM.

Fig. 6.30(a) to 6.30(b) reveal that various shapes of nanoparticles are found uniformly distributed on the LGS substrates. Although the temperature increased to 600 °C, the dimensions and morphologies of the nanostructures from each substrate did not change. However, sparse nanowires are found in between nanoparticles on LGS substrate after Sb_xO_y films were deposited at 800 °C for 2 h. The thickness of the 1-D nanowires were in the range of 10 nm to 30 nm and

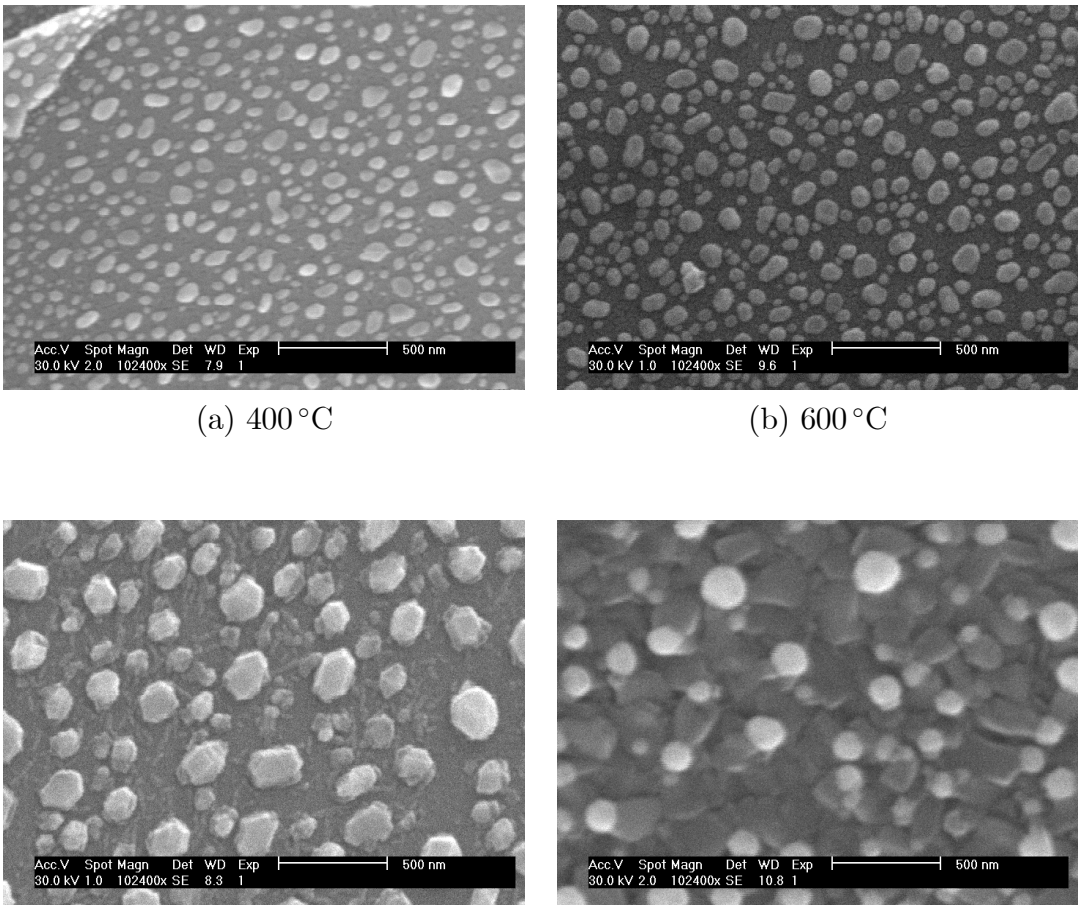

(a) 400 °C (b) 600 °C

(c) 800 °C (d) 1000 °C

Figure 6.30: Thermally evaporated of Sb_2O_3 at different temperatures on LGS substrate.

the length were up to 170 nm. In Fig. 6.30(c), the nanowires and nanoparticles can be seen on the bare LGS substrate. Another deposition was conducted at a higher temperature; 1000 °C of the duration of 2 h. At this point, nanowires were not found. Instead another forms of nanostructures were observed: the spherical particles which were surrounded by denser and non-uniform nanostructures. Fig. 6.30(d) reveals that some of the 1-D samples appear to have trapezoidal and rectangular shapes. Lobe-like and parallelogram shapes were also occasionally observed here. These non-homogeneous structures were between 150 - 200 nm in width, 50 -140 nm in height and up to 300 nm in length.

After successfully growing nanostructures on the bare LGS substrates, an-

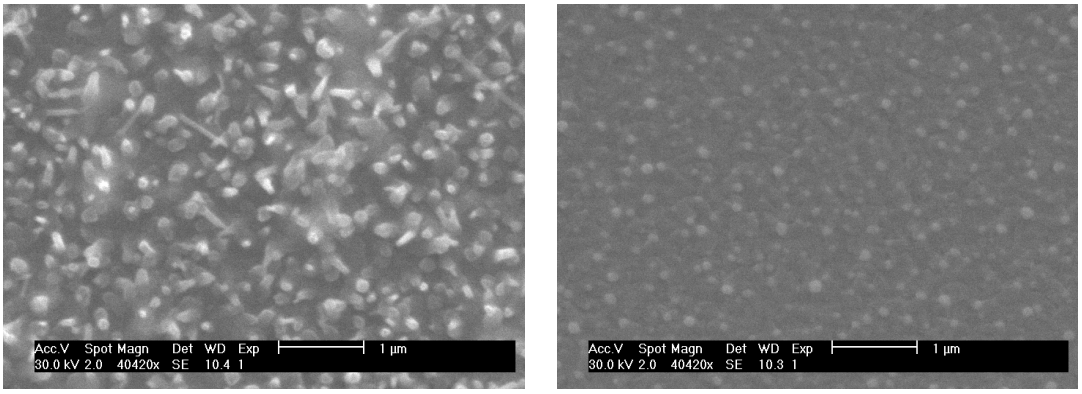

(a) (b)

Figure 6.31: LGS conductometric devices after Sb_xO_y film deposition at 1000°C (a) Nanorods grown on metallized layer electrodes, (b) Nanostructures grown in between the electrodes.

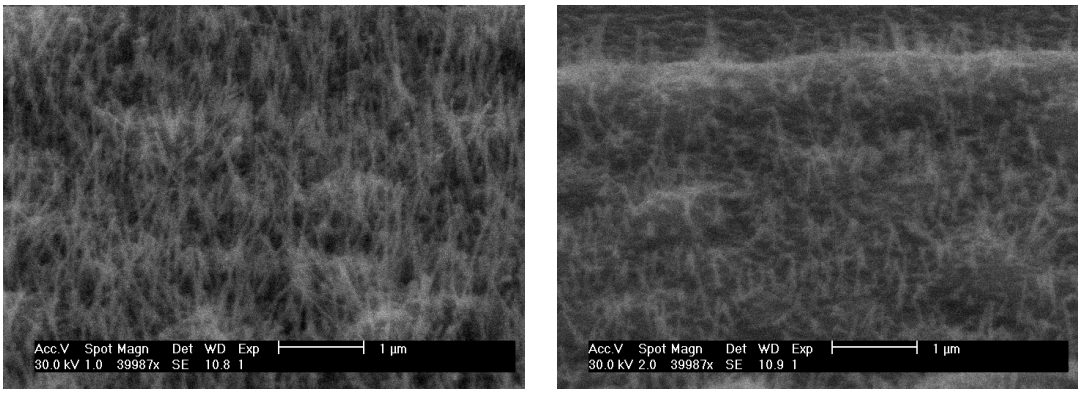

(a) (b)

Figure 6.32: SEM images of nanorods (a) located closer to the source (high temperature), (b) located further from the source (low temperature).

other set of deposition was carried out on LGS conductometric transducers at the similar temperatures and durations. The details of the transducers fabrication and parameters were given in chapter 4. Fig. 6.31(a) and 6.31(b) reveal the results of these experiments. In Fig. 6.31(b), non-homogeneous 1-D structures, which are similar to Fig. 6.30(d), are observed between the electrodes. Fig. 6.31(a) shows rod-like structures, pointing at random orientations which are found on the electrodes. The diameters of the nanorods range from 30 to 50 nm and their lengths are from 150 to 750 nm.

The author believes that the growth reaction of Sb_xO_y's nanorods and other non-uniform nanostructures obtained in this experiment are similar to VLS growth. At elevated temperatures, nanoparticles are found on all substrates. At these temperatures, it is known that the coated Au thin film split into small liquid droplets. When the furnace is heated up to 1000 °C, Au film formed into small half-spherical shapes which are shown in Fig. 6.30(d). At the same time, Sb_2O_3 powder may be transformed to Sb_xO_y vapour. The flowing carrier gas carry the vapour to combine it with Au droplets. From this continual feeding of Sb_xO_y vapour, the alloy droplets lead to the nucleation. The growth of Sb_xO_y 1-D structures occurs when they become saturated with Sb_xO_y. Therefore, synthesizing the non-homogenous 1 and 2-D nanostructures and nanorods on bare LGS and electrodes surface occurs.

These experiments were executed at different operating temperatures and the substrates were placed at different locations from the source. Fig. 6.32(a) – 6.32(b) depict SEM images taken from Sb_xO_y nanorods on LGS at different locations corresponding to the different deposition temperatures. Fig. 6.32(a) was taken from the location near to the source, the Sb_2O_3 powder, than the location of Fig. 6.32(b). Nanorods at closer positions are denser and closely compact. The lengths of these nanorods are longer than nanorods at further distances. This is probably due to the reason that at higher deposition temperatures higher concentration of alloy droplets led to more efficient nucleation and made Sb_xO_y saturated much faster, consequently, nanorods were more compact and elongated.

To determine the crystallinity of the nanostructures product, XRD analysis was carried out. Fig. 6.33 depicts the XRD pattern of the thermally evaporated Sb_2O_3. Some of the peaks can be indexed to various antimony oxides with

different Sb/O ratios; face-centered cubic senarmontite Sb_2O_3, base-centered monoclinic phase of Sb_2O_5, base-centered orthorhombic SbO_2, monoclinic Sb_2O_4, and orthorhombic valentinite Sb_2O_3, which are labelled as A, B, C, D, and E respectively. Furthermore, as can be seen from the XRD pattern of the as-synthesized products, the senarmontite Sb_2O_3 and Sb_2O_5 dominate most of the indexed peaks. Figure 6.33 confirms (400), (421), (620), (422) and (204) are the significant diffraction peaks for Sb_2O_5. Moreover, (222), (622), (731), (644), (662) and (844) are the peaks that show the existence of Sb_2O_3 with lattice parameters $a = b = c = 11.15200$. Meanwhile, the rest of the peaks are detected are from films on Au and LGS substrate.

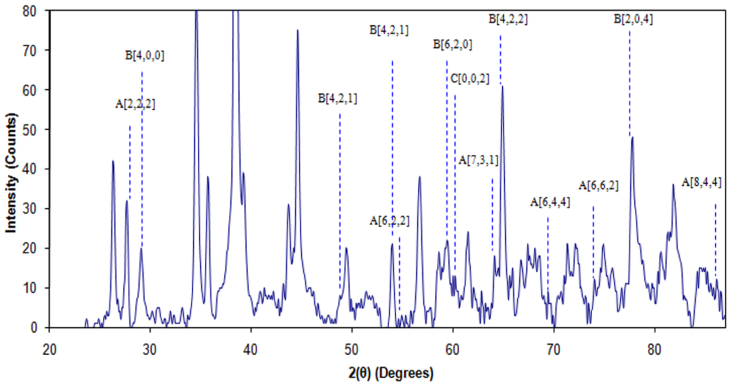

Figure 6.33: XRD pattern of LGS after Sb_xO_y film deposition at 1000 °C.

XRD analysis (figure is not shown in this thesis) was conducted on films deposited on Si substrates, and the result only showed the presence of Au peak. However, no Sb/O peak was observed. This confirms that Sb_xO_y does not grow on Si up to 1000 °C (as well as on $LiTaO_3$ and $LiNbO_3$ at less than 800 °C). Unlike LGS, testing on $LiTaO_3$ and $LiNbO_3$ could not be continued since both substrates cracked after being annealed at high temperature of 1000 °C. This behaviour explains the stability of LGS which does not show any phase transition up to its melting point.

For further investigation on identifying the elements, EDX analysis was also performed for the Sb_xO_y films deposition on LGS substrates. Fig. 6.34 exhibits the EDX pattern of nanostructures in Fig. 6.30(d). The analysis indicates the

existence of Au, Sb and O on the LGS substrate. Whereas the other peaks signify the substrate's elemental content.

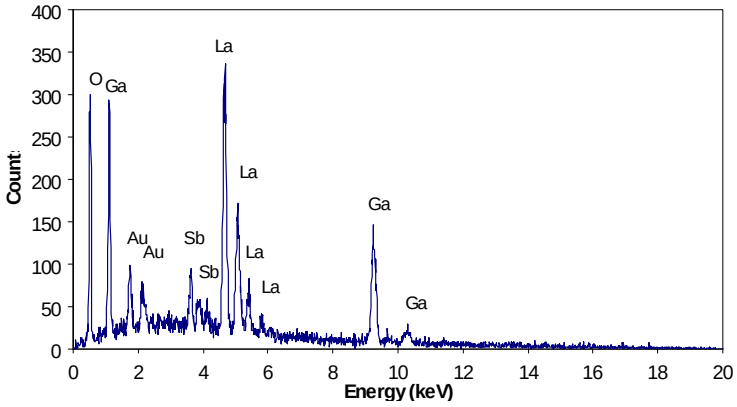

Figure 6.34: The EDX pattern of the Sb_xO_y nanostructured deposited on LGS.

The SEM images confirmed that Sb_xO_y nanostructured films are highly porous. Therefore, it is anticipated that the nanostructures can provide large exposed surface area to gas media. The gas sensing results of the Sb_xO_y nanostructured based LGS conductometric sensors will be presented in the following chapter.

6.4 Summary

In this chapter, the materials characterization results of polyaniline, PVP, graphene, and Sb_2O_3 were presented. SEM, XRD, AFM, Raman spectra analysis and several other characterization techniques were employed to investigate the characteristics of each synthesized material.

Key outcomes from the characterization of the polyaniline, PVP, graphene, and Sb_2O_3 nanostructured thin films can be summarized as follow:

1. Polyaniline sensitive layer

- Characterization of electropolymerized polyaniline by SEM showed highly ordered nanofibers grown on the metallized and non-metallized regions of the $LiTaO_3$ SAW transducers. The growth of polyaniline nanofibers on

non-metallized substrates was confirmed via SEM inspection and resistance measurements before and after electropolymerization.

- Different deposition time for electropolymerization resulted in different thicknesses of polyaniline nanofibers thin films.

- Using SEM, the surface morphology of electropolymerized polyaniline in different acid concentrations were found to be different. Decrease in the polymerization degree of polyaniline was observed from the SEM images as the concentration of acid in the electrolyte was reduced.

- The average diameter of HNO_3 medium deposited polyaniline nanofibers was approximately 30 - 50 nm, growing at random directions on the surface of the working electrodes. On the other hand, more ordered nanofibers with average diameters of 40 - 50 nm were observed for HCl medium deposited polyaniline nanofibers.

- Morphology of electropolymerized polyaniline/MWNTs was more compact than pure electropolymerized polyaniline with average diameter of 50 nm. The existance of MWNTs in polyaniline chain reduced the electrical resistance from $5.5x10^3\,\Omega$ for pure electropolymerized polyaniline to $40\,\Omega$ of electropolymerized PANI/MWNTs (for the same IDT pattern transducers).

- Polyaniline/diamond composite was successfully synthesized via chemical polymerization. It was observed that polyaniline and diamond formed nanofibers and clusters of coral-like structures respectively and were connected together in a network. The X-ray diffraction pattern of the drop-casted nanocomposite layer was shown to match the peak from the pure standard diamond, signifying the presence of diamond particles in the CSA doped polyaniline/diamond sensors.

2. PVP sensitive layer

- The electrospin coated PVP fibres were deposited at diferent concentrations, resulting in three different structures which were fibers, beads, and particles. Only fibres in the range of 100 - 600 nm were appeared at 58%

of PVP concentration. Furthermore, by varying the collection distances, the effect on deposition rate was investigated. The closer the distance, the higher the deposition rate and the denser the film.

- Electrospin coated PVP/ES and PVP/EB composites were successfully synthesized. The width of PVP/ES fibres were smaller than those of from the PVP/EB fibres, which were 50 - 650 nm and 322 - 1000 nm, respectively.
- The morphologies of electrospin coated PVP/MWNTs composites were investigated via SEM which show that MWNTs were dispersed evenly in PVP. The average width of the electrospin coated fibres was 250 nm, while for beads, the diameter was between 500 to 1500 nm.

3. Graphene sensitive layer

- Graphene nano-sheets surface morphology were studied via SEM and AFM. Both showed that the monoatomically thick deposited graphene appeared in pale grey region on the $LiTaO_3$ SAW transducers. However, the absence of $C = C$ bond in the XPS spectra and the existance of more than 5 graphene layers from 2D band of the Raman spectrum concluded that the chemically reduced GO to graphene was not an ideal graphene.

4. Sb_xO_y sensitive layer

- Sb_xO_y nanostructures were succesfully deposited on LGS conductometric transducers via thermal evaporation technique. The surface morphology of the nanostructures grown at different temperatures were investigated using SEM. It was observed that the nanorods growth was dense and closely compacted together when the samples were near to the powder source. Besides, nanorods were longer when compared to that of the nanostructures deposited at further distances. The EDX identified the existance of Au, Sb and O on the LGS substrates. Furthermore, the XRD determined that different Sb/O ratios of nanostructures were successfully grown via this method.

The synthesized and characterized nanostructured materials are used as the sensing layers for SAW based and conductometric transducers. Gas sensing performance of these sensors will be further discussed in chapter 7.

Chapter 7

Gas Sensor Testing Set-up and Results

7.1 Introduction

In chapter 1, the author described the motivation of conducting research regarding selected nanostructured materials for gas sensing applications. Then the literature review of these nanostructured materials were presented in chapter 2. In chapter 3 and 4, the theory and fabrication of SAW and conductometric transducers were presented, respectively. The syntheses and deposition of the nanostructured materials were described in the following chapter. Subsequently, the characterizations of nanostructured materials were given in chapter 6.

In this chapter, the electrical measurement set-ups for SAW and conductometric gas sensors are given in section 7.2. The testing prosedures also are included in this section. Section 7.3 presents the gas sensing performance for all gas sensors. This section is divided into four subsections in which the gas sensing results of polyaniline nanofibers, PVP fibres, graphene nano-sheets, and Sb_2O_3 nanostructures based gas sensors are discussed. Finally, section 7.4 provides the summary of this chapter.

7.2 Electrical Measurement Set-ups

7.2.1 SAW Sensor Measurement Set-up

Changes in SAW velocity can be measured by frequency and phase techniques. The phase technique involves measuring the transfer function of the SAW device with a two-port network analyzer. With the network analyzer, one of the ports acts as an RF signal source for IDTs input while the other one (or the same port) as a vector voltmeter for measuring the amplitude and phase of the IDTs. By measuring the scattering parameters (S-parameters: $S_{11}, S_{12}, S_{21}, S_{22}$), both phase velocity and attenuation of the SAW device over a given frequency range can be determined. In this study, the author employed a Rohde and Schwarz ZVRE network analyzer to measure the S-parameters. The obtained data allow to approximate the oscillation frequency of the SAW device in an oscillator configuration set-up. Although this technique provides a stable platform for analysis, it is a specialized and expensive set-up.

The second method to measure changes in SAW velocity is via the frequency technique. In this method, the SAW sensor is used as the frequency control element in a closed loop oscillator circuit. The SAW sensor functions as a delay line producing a positive feedback which is fed into an RF amplifer as shown in Fig. 7.1. In this configuration, RF amplifier gain compensates the losses incurred by the SAW delay line while maximising the signal to noise ratio of the oscillator circuit. The advantage of using the frequency technique in measuring the changes in SAW velocity is that it requires cheaper equipment when compared to a phase measurement set-up. Furthermore, the system can be established by employing a simple microprocessor to measure the oscillation frequency, which is relatively cheaper than most of the accurate the laboratory equipment (e.g. network analyzer).

The basic principle of the measuring system of a SAW device in a closed loop configuration is well known [242],[243]. In steady state condition the oscillator circuit must satisfy the following conditions [244]:

$$\varphi_{Amp} + \varphi_{SAW} = -2n\pi \tag{7.1}$$

$$|G(\omega)| \cdot |L(\omega)| = 1 \tag{7.2}$$

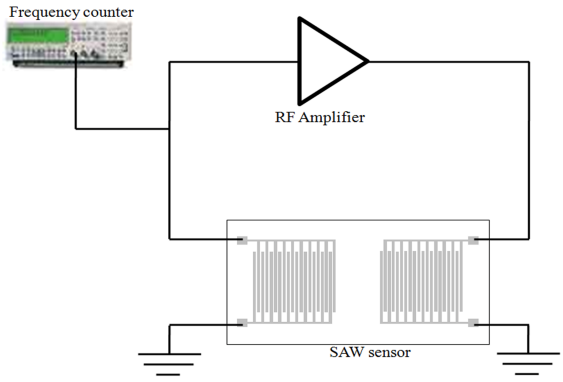

Figure 7.1: Schematic diagram of the feedback loop oscillator.

where φ_{Amp} and φ_{SAW} are phase response of RF amplifier and SAW device, respectively; n is an integer denotes the number of frequency mode; ω is an angular oscillation frequency; $|G(\omega)|$ is the magnitude of amplifier gain, and $|L(\omega)|$ is the magnitude of insertion loss of the SAW delay line.

The φ_{SAW} then is defined as:

$$\varphi_{SAW} = -\frac{2\pi f l}{v} \tag{7.3}$$

where f is the oscillation frequency, l is centre-to-centre spacing between the IDTs and v is the phase velocity of the acoustic waves.

Therefore, using Eqs. 7.1 and 7.3, the oscillation frequency f can be written as:

$$f = \frac{\left(2n\pi + \varphi_{Amp}\right)}{2\pi l} v \tag{7.4}$$

From this equation, it is evident that the RF amplifier must be designed carefully to provide enough forward gain to overcome losses associated with the SAW delay line. Therefore, the conditions of the stable oscillation are fulfilled.

φ_{Amp} can be considered constant if the amplifier is working in a stable condition, then changes in acoustic wave phase velocity (Δv) are proportional to the changes in oscillator centre frequency (Δf) which can be written as:

$$\frac{\Delta f}{f_o} \cong \frac{\Delta v}{v_o} \tag{7.5}$$

where f_o and v_o are the unperturbed oscilation frequency and SAW velocity, respectively.

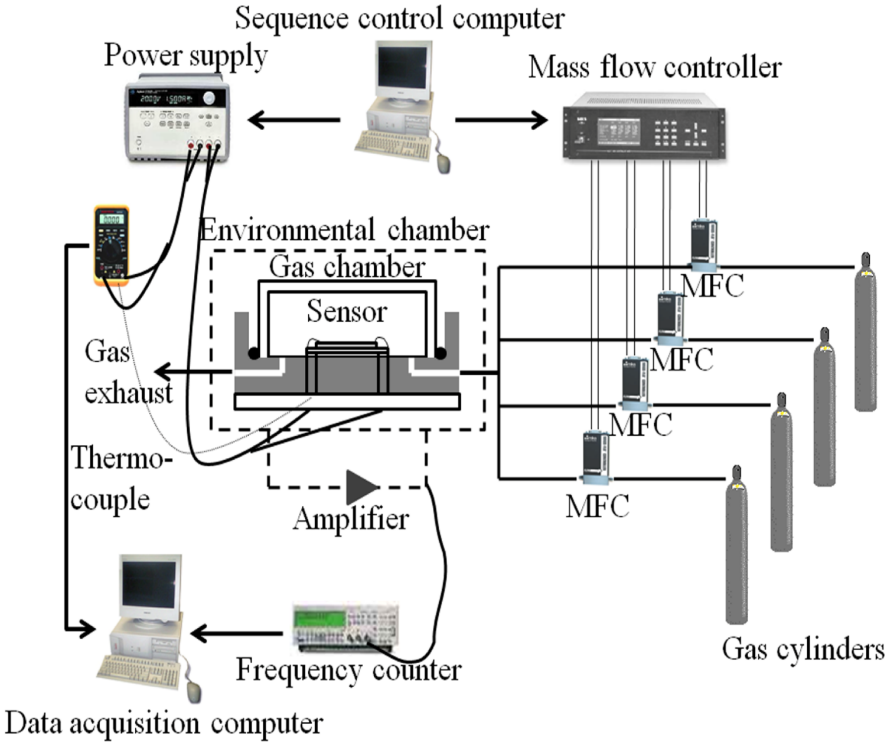

Figure 7.2: Experimental set-up for nanostructured material based SAW gas sensors.

Fig. 7.2 shows a complete experimental set-up for nanomaterial based SAW gas sensors. The custom built SAW system employs a mass flow controller (MFC) processing unit, four MFCs, two computers, a frequency counter, a thermocouple and a 2-channel DC power supply. In this system, the multi-channel gas calibration set-up was based on the volumetric mixing of gases with four MFCs. Certified gas bottles of high purity dry synthetic air (zero air) and low concentration of analytes gas (balanced in synthetic air) were purchased from Coregas. Each gas bottle was connected to a computer controlled MFC. The computer was utilized to produce a total constant flow air of 200sccm. The analyte gas could be further diluted in synthetic air by simply adjusting the flow rates of each MFC.

7.2.2 Conductometric Sensor Measurement Set-up

The author developed nanostructured Sb_2O_3 based conductometric gas sensors. The resistance change of these sensors was recorded using a high precision Keithley 2001 multimeter. A complete experimental set-up of test system connections for conductometric gas sensor is shown in Fig. 7.3.

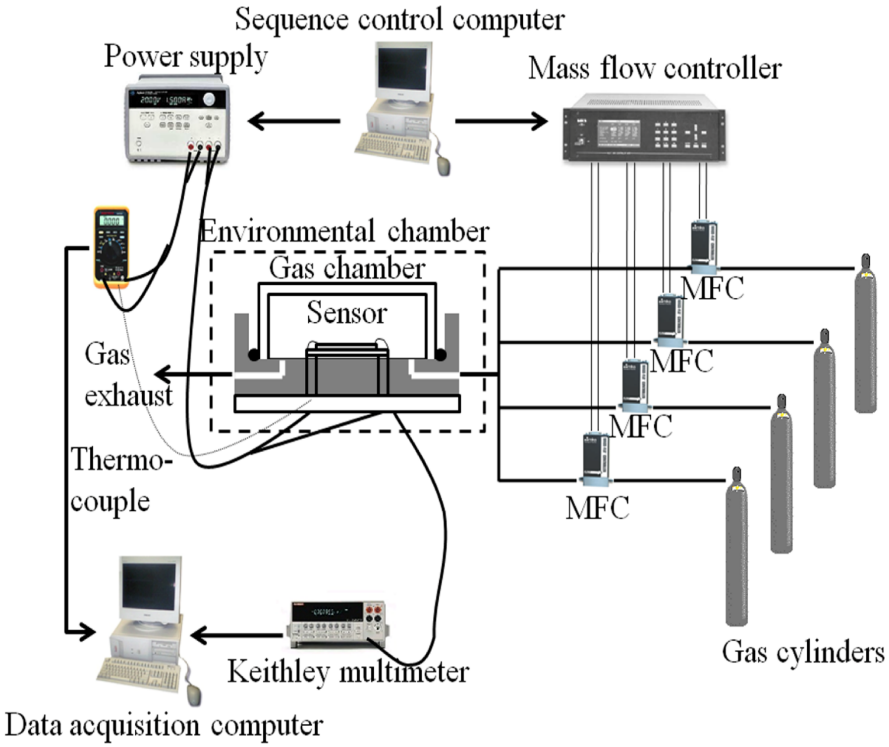

Figure 7.3: Experimental set-up for nanostructured material based conductometric gas sensors

The response, denoted as S is the ratio of resistance for synthetic air (R_{air}) to the resistance of the test gas (R_{gas}):

$$S_{reducing} = R_{air}/R_{gas} \tag{7.6}$$

Eq. 7.6 is true for n-type material gas sensors responding to reducing gases such as H_2 and CO. For the same type of material responding to oxidising gases such as NO_2, the response is defined as:

$$S_{oxidising} = R_{gas}/R_{air} \tag{7.7}$$

7.2.3 Gas Chamber Set-up

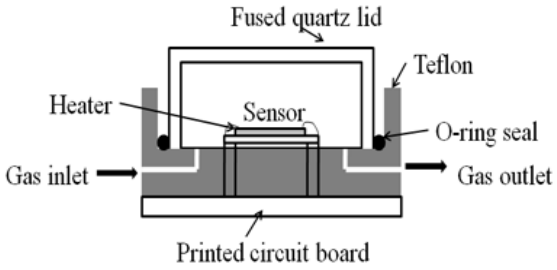

Figure 7.4: Schematic diagram of gas chamber set-up.

Fig. 7.4 shows the schematic diagram of the gas chamber set-up. The chamber was formed from the 20 mm thick machined teflon block and fused quartz lid. The tested sensor was mounted on a planar alumina micro-heater. The external regulated power supply controlled the operating temperatures of up to 300 °C. This gas chamber was then enclosed by an environmental chamber to control the ambient temperature at 22 °C.

7.2.4 Testing Procedure

In this research, the author used both reducing (H_2 and CO) and oxidising (NO_2) gas species to investigate the performance of the developed sensors. Each of the sensors was tested at several operating temperatures, depending on the type of the sensor. A sequence control computer was utilized to computerize the pulse sequence of the analyte gas concentrations and also the operating temperatures.

Initially, the synthetic air was maintained for 60 min. Then the first pulse of the analyte gas was given for 10 min, followed by another 60 min of synthetic air. Exposing sensor to subsequent pulses of analyte gas was utilized to stabilize the baseline. Only after the baseline gas was stable, the actual measurements were started by purging the sequences of the analyte gas.

7.3 Gas Sensing Results

7.3.1 Polyaniline Nanofibers Based SAW Sensors

Frequency and Phase Responses

Fig. 7.5 shows the measured S_{21} transmission parameters (log magnitude and phase) of the doped and dedoped polyaniline nanofibers based 36 ° YX $LiTaO_3$ SAW gas sensors before and after the deposition of polyaniline nanofibers.

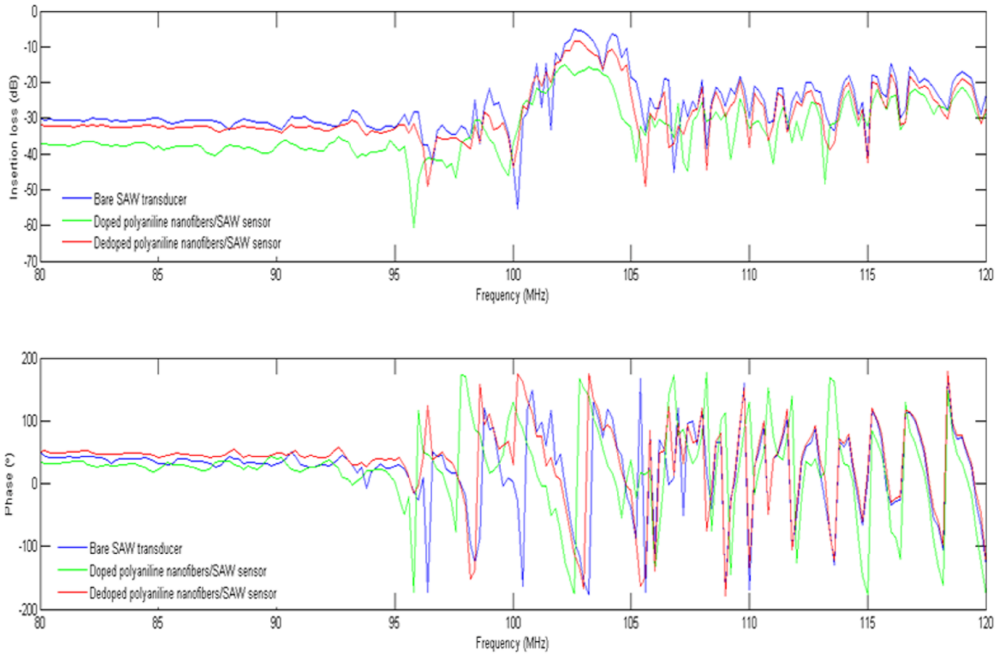

Figure 7.5: Frequency and phase response of bare $LiTaO_3$ SAW device, doped polyaniline nanofibers, and dedoped polyaniline nanofibers on $LiTaO_3$ SAW device in ambient condition.

The $LiTaO_3$ SAW transducer with no sensitive layer showed resonant centre frequency peak at approximately 102.6 MHz, with an insertion loss of -5 dB. Deposition of doped and dedoped polyaniline nanofibers based SAW sensors showed the resonant centre frequency peaks of 102.2 and 102.6 MHz, respectively. Whereas, the insertion losses shifted to -15 and -8 dB for doped and dedoped polyaniline, respectively. It is suggested that the increases in insertion loss is caused by the mechanical wave dampening effect of the nanostructures on the $LiTaO_3$ SAW devices [245]. These results can also be attributed to the scatter-

ing of surface waves. Stability of the phase responses was also good after the deposition of the layers.

Gas Sensing Results

Gas measurements for the polyaniline nanofibers based $LiTaO_3$ SAW gas sensors were carried out in a chamber by exposing the sensors to different concentrations of H_2 gas in synthetic air at room temperature. The response of the H_2 gas was monitored using a frequency counter (Fluke PM6680B). The doped polyaniline nanofibers based $LiTaO_3$ SAW sensor was exposed to H_2 gas pulse sequence of 0.06%, 0.12%, 0.25%, 0.50%, 1.00% and 0.12% in synthetic air. While for the dedoped polyaniline nanofibers based $LiTaO_3$ SAW sensor, it was exposed to H_2 gas pulse sequence of 0.06%, 0.12%, 0.25%, 0.50%, 0.50% and 1.00%. The experimental set-up and testing procedures were outlined in details in section 7.2.1. Dynamic response to H_2 gas for doped polyaniline nanofibers/SAW sensor is shown in Fig. 7.6, whereas the dynamic response for dedoped polyaniline nanofibers/$LiTaO_3$ SAW sensor is shown in Fig. 7.7.

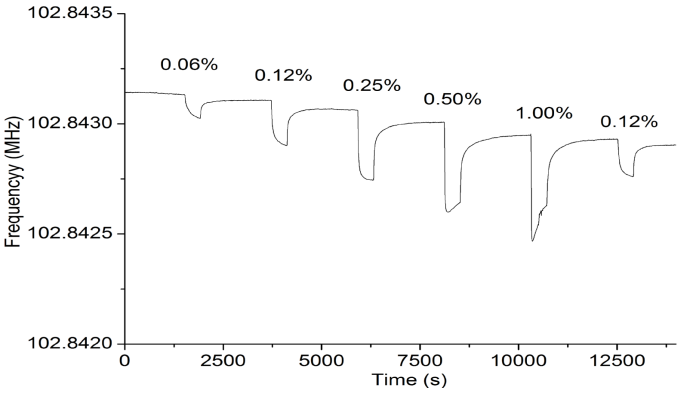

Figure 7.6: Dynamic response of doped polyaniline nanofibers based SAW gas sensor.

Measured response for the doped polyaniline nanofibers based $LiTaO_3$ SAW gas sensor was approximately 480 Hz to 1% H_2. Fast response of 28 s at room temperature was observed at this H_2 concentration. For the dedoped polyaniline nanofibers based $LiTaO_3$ SAW gas sensor, the measured response was approximately 9.46 kHz towards 1% H_2. The response time of this sensor was 12 s for

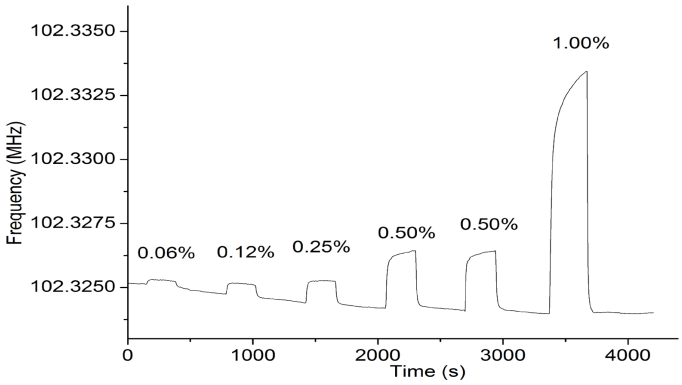

Figure 7.7: Dynamic response of dedoped polyaniline nanofibers based SAW gas sensor.

0.06% H_2 gas concentration. It is observed in Fig. 7.6 that the resonant frequency of the sensor was reduced upon the introduction of the H_2 gas to the gas chamber. With H_2 exposure, the conductivity of the polyaniline nanofibers are increased. This result in a decrease in the acoustic wave velocity, thus decreasing the resonant frequency. However, it was the opposite for the dedoped polyaniline nanofibers based $LiTaO_3$ SAW sensor. The introduction of the H_2 gas to the surface of the dedoped polyaniline/$LiTaO_3$ SAW sensor increases of the device's resonant frequency which is caused by the different oxidation states of polyaniline.

Good reproducibility was observed when second pulses of 0.12% and 0.50% of H_2 were introduced into the chamber for both doped and dedoped polyaniline nanofibers sensors. This room temperature operation is favorable in many applications, especially those involving low power consumptions and operating in inflammable environments.

It is observed in Fig. 7.6 that overshoot occured at 1% H_2 for doped polyaniline sensor. This phenomenon does not happen during the exposure of the dedoped polyaniline sensor to 1% H_2. In electropolymerization, different thicknesses were required to enable doped and dedoped polyaniline nanofibers to respond as SAW sensors. Doped polyaniline nanofibers based $LiTaO_3$ SAW sensor requires a very thin layer. This is due to the high conductivity of the doped polyaniline. If thick layer is deposited, the device will be short-circuited. Whereas for dedoped polyaniline, a thick layer is required. The dedoped polyani-

line nanofibers based $LiTaO_3$ SAW sensor did not respond to H_2 gas if very thin films were deposited. This is due to the assumption that the thin layers of dedoped polyaniline nanofibers do not have the sufficient ability to transport charge carriers along the polymer backbone and for the carriers to hop between the polymer chains. The same phenomenon can also be used for describing as why the thick layers of dedoped polyaniline nanofibers on the SAW transducers prevent the occurance of the overshoot [246-247].

For doped polyaniline, H_2 interacts at the charge amine nitrogen sites. By referring to the polyaniline scheme in Fig. 2.2, H_2 bond dissociation follows with the formation of new $N-H$ bonds to the amine nitrogen of the polyaniline chain. After that, the charge transfer between adjacent amines nitrogen returns the polyaniline chain establishing polaronic state (emeraldine state) with the release of H_2. Therefore, this makes the reaction fully reversible.

Although Virgi et al. [130] found no response towards H_2 gas for dedoped polyaniline nanofibers, Sadek et al. [67] verified that there is interaction between hydrogen molecules and polymer chain of dedoped polyaniline. As imine/amine ratio of emeraldine film can be affected by the base concentration [63], it is known that only upon exposure to a very strong base the emeraldine can become an insulator [12]. As only a weak base was used in these experiments, the author believes this attributes to the amount of imine and amine in the polymer chains. Therefore, this probably enables the interaction of hydrogen molecules with the dedoped polyaniline. H_2 gas may form a bridge between nitrogen atoms on two adjacent chains or there may be partial protonation of some of the nitrogens in imine group [130].

Effect of Polyaniline Nanofibers Thin Film Thickness

Fig. 7.8 shows the frequency shifts of the dedoped polyaniline based $LiTaO_3$ SAW sensors (presented in Table. 6.1) versus different H_2 gas concentrations. Whereas, response time versus H_2 concentrations of electropolymerized polyaniline nanofibers/$LiTaO_3$ SAW sensors is plotted in Fig. 7.9. The SAW E, with the smallest thickness, showed the smallest frequency shift (12.1 Hz for 0.06% H_2). It is observed that for gas concentrations below 0.5%, the frequency shifts increase as the thicknesses increase. Although for compact and non-porous structures,

thinner films with thicknesses comparable to Debye length provide better sensitivity than thicker films [59], it is apparently the opposite for porous structures. Large shifts in the operating frequency of the nanostructured SAW sensors are attributed to the high surface to volume ratio of porous polyaniline nanofibers sensitive films. The deposition time contributes to the surface roughness of the sensitive layer as well. The longer deposition contributes to the elongation of the polyaniline nanofibers perpendicular to the nucleation sites. Hence, the higher surface to volume ratio which increases the adsorption of H_2 molecules. However, for 1% H_2 gas, SAW B with the thickness of 3.5 μm produced the highest frequency shift of 9.46 kHz than the other SAW sensors.

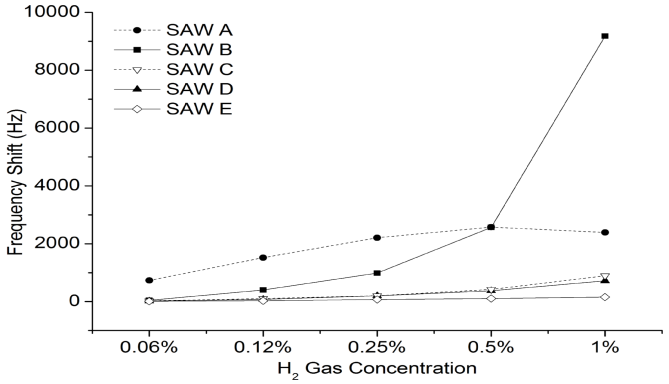

Figure 7.8: Frequency shift of dedoped polyaniline nanofibers based SAW gas sensors with different thin film thicknesses.

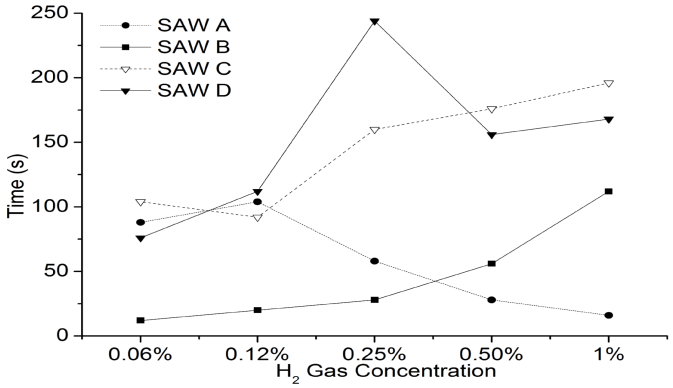

Figure 7.9: Response time of polyaniline nanofibers based SAW sensors versus gas concentrations.

In Fig. 7.9, the graph compares the response time of the thick (SAW A & B) and thin layers of polyaniline nanofibers (SAW C & D). SAW B showed the fast response towards 0.06% and 0.12% H_2. For concentrations higher than 0.25%, it was observed that the response time of the thick layer polyaniline devices were smaller than that of the thin layer devices which showed that thick layer provided large surface area for H_2 adsorption.

Effect of Different Acid Concentrations

Five different sensors were developed. Polyaniline nanofibers were electropolymerized on these sensors using different concentrations of electrolyte with details presented in chapter 5. The electropolymerized polyaniline nanofibers based $LiTaO_3$ SAW sensors were then dedoped in NaOH (pH 12.5) for approximately 10 s. To investigate the gas sensing performance, the dedoped polyaniline nanofibers/$LiTaO_3$ SAW sensors were placed in the gas chamber and exposed to H_2 gas.

Fig. 7.10 shows the frequency shifts of the developed sensors towards five different concentrations of H_2 gas. However, only three of fabricated sensors responded to H_2 gas. Therefore, the results for sensors deposited using 0.5M, 1.0M and 1.5M of HCl are shown in Fig. 7.10.

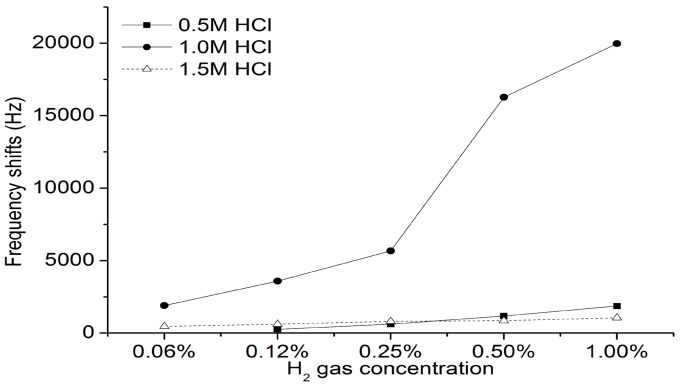

Figure 7.10: Frequency shift of dedoped polyaniline nanofibers based SAW sensors, polymerized in different acid concentrations.

Polyaniline nanofibers/$LiTaO_3$ SAW sensors that were deposited in 0.1M and 0.3M HCl did not respond as SAW sensor. Referring to the SEM images in Fig.

6.9, it can be observed that nanoparticles and nanofibers were grown sparsely on 0.1M and 0.3M devices. This contributes to the inability of the devices to respond as SAW gas sensors. To enable the polyaniline to function as a sensitive layer for gas sensing, it requires to transport charge carriers along the polymer backbone and for the carriers to hop between the polymer chains. Besides there is a possibility that these low acid concentrations form another state of polyaniline. In the insulating form of polyaniline, the H_2 cannot dissociate, therefore no reversible interaction of H_2 with the polymer chain can occur. Subsequently there was no response to hydrogen from these two devices [130].

Fig. 7.11 shows the dynamic responses of polyaniline nanofibers based SAW sensors which were electropolymerized using 0.5M, 1.0M and 1.5M HCl in electrolyte. It is observed that the one that deposited in 1.0M HCl electrolyte has the most stable baseline. Baseline for the 0.5M sensor appeared to be drifted slightly upwards in time, whereas for the 1.5M sensors, it is drifted downwards. Measured responses were approximately 1.863, 19.980 and 1.055 kHz towards 1% H_2 for 0.5M, 1.0M and 1.5M sensors, respectively. The 90% response time for 0.5M, 1.0M and 1.5M sensors were 24, 28 and 164 s towards 1% H_2, respectively.

Both SEM images of polyaniline nanofibers electropolymerized using 1.0M and 0.5M HCl show highly dense nanofibers. However, the frequency shifts of 0.5M sensors were lower than that of 1.0M sensors. As mentioned previously, H_2 gas may form a bridge between nitrogen atoms on two adjacent chains or there may be partial protonation of some of the nitrogens in imine group [130]. The amount of H^+ in 0.5M HCl is lesser than in 1.0M HCl. During the electropolymerization, this may affect the amount of amine and imine in the nanofibers. Hence only few of them may be available to react with H_2 gas.

If very high acid concentration is used, the amount of monomer is decreased consequently. Therefore, for the 1.5M HCl device, the amount of polyaniline produced during electropolymerization was low [248]. As a result, only small amount of the deposited polyaniline is able to react with H_2, causing small frequency shift upon exposure to H_2 gas.

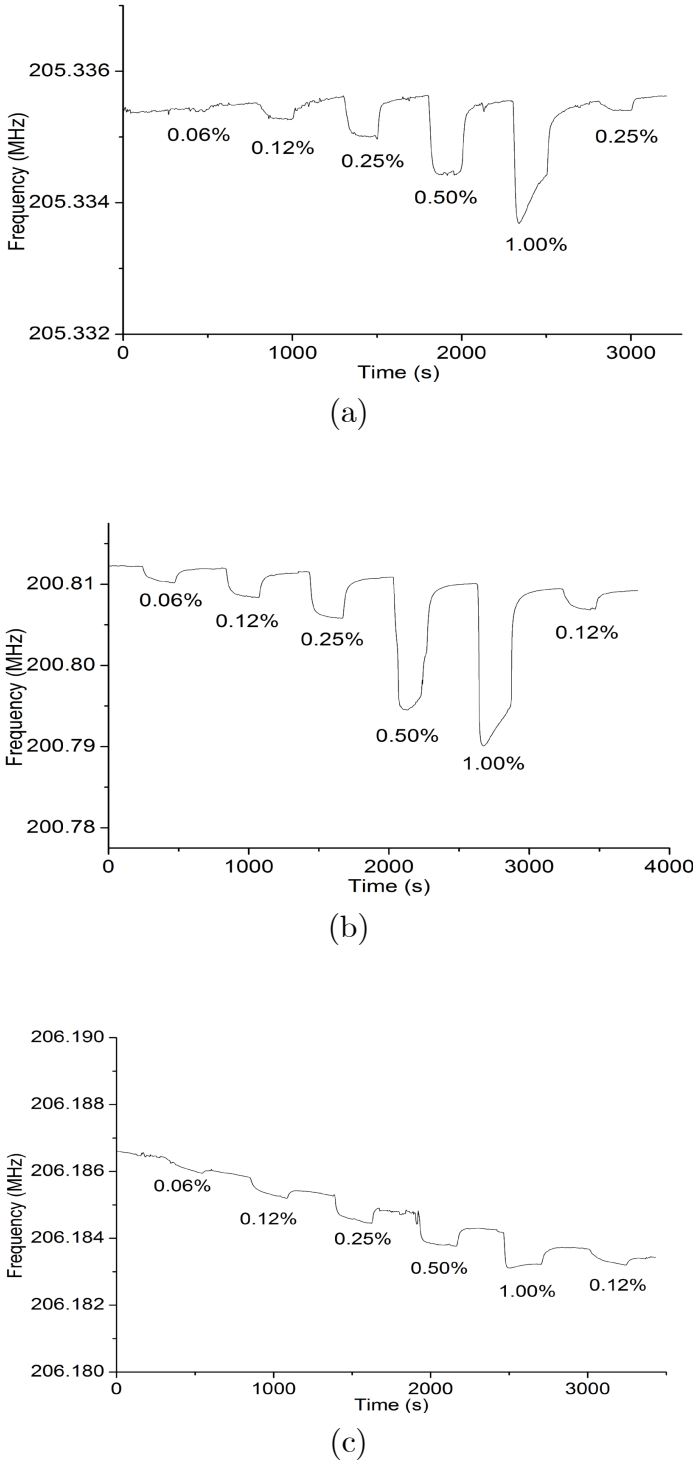

Figure 7.11: Dynamic responses of dedoped polyaniline nanofibers/SAW sensors, polymerized in different HCl concentrations: (a) 0.5M, (b) 1M, and (c) 1.5M.

Effect of Different Type of Acids -HNO_3

Although polyaniline synthesized in HCl and HNO_3 media have already been investigated by other authors [234,249-250], no literature was found that contains the study of their effect on gas sensing performances. HCl media deposited polyaniline nanofibers has higher conductivity than the HNO_3 media deposited polyaniline. This result agrees with findings presented by Gaikwad et al. [250] and Catedral et al. [249].

Dynamic response of HNO_3 doped polyaniline nanofibers based $LiTaO_3$ SAW sensor to different H_2 concentrations is shown in Fig. 7.12. H_2 gas exposure time was set at 4 and 5 mins for HNO_3 doped and HCl doped polyaniline nanofibers based SAW gas sensors, respectively. Then the gas chamber was purged with synthetic air for 5 min for HNO_3 doped and 6 min for HCl doped polyaniline nanofibers based $LiTaO_3$ SAW sensors. The synthetic air was supplied between each pulses of H_2 gas to allow the surface of sensors to recover to the baseline. Both types of sensors were exposed to hydrogen pulse sequences of 0.06%, 0.12%, 0.25%, 0.50%, 1.00% and 0.12% concentrations in synthetic air at room temperature. The experimental set-up and testing procedures had been outlined in details in section 7.2.1.

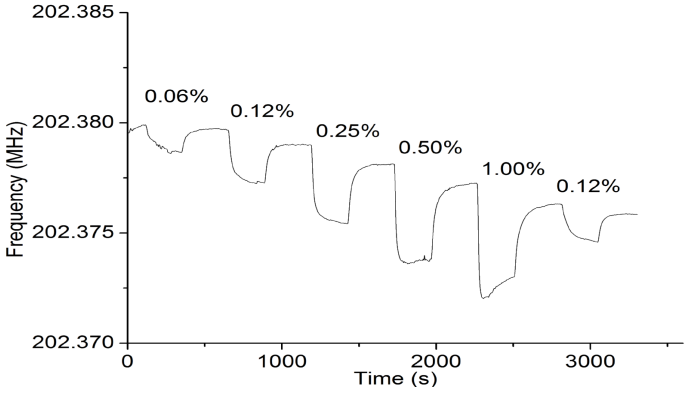

Figure 7.12: Dynamic response of polyaniline nanofibers based SAW sensor (polymerized in HNO_3 medium).

The introduction of H_2 gas to the sensor surface causes the reduction of the device's resonant frequency for both types of sensors. Similar to the results

which were obtained by Sadek et al. [67] for their conductometric measurements, the author was also found that the conductivity of the dedepod polyaniline nanofibers increases which results in a decrease in the acoustic wave velocity.

The measured responses were 5.168 and 19.98 kHz towards 1% of H_2 gas concentration for the HNO_3 and HCl doped polyaniline nanofibers based SAW gas sensors, respectively. Fig. 7.13 shows the plots of the frequency shift of the measured responses for both sensors versus H_2 gas concentrations. The frequency shift for HNO_3 doped polyaniline nanofibers increases linearly with the increase of H_2 gas concentrations. The trend is similar to HCl doped polyaniline nanofibers, but only for H_2 gas concentrations of up to 0.25%. Then the shift increases approximately three and four times for 0.5% and 1% H_2 gas, respectively. Referring to the SEM images of HCl doped and HNO_3 doped polyaniline in Fig. 6.6 and 6.11 respectively, both show almost similar average nanofiber dimensions. However, the HCl doped polyaniline nanofibers were more ordered compared to the HNO_3 doped sample. This contributes to the porosity of the deposited polyaniline nanofibers thin film which enhances the sensitivity.

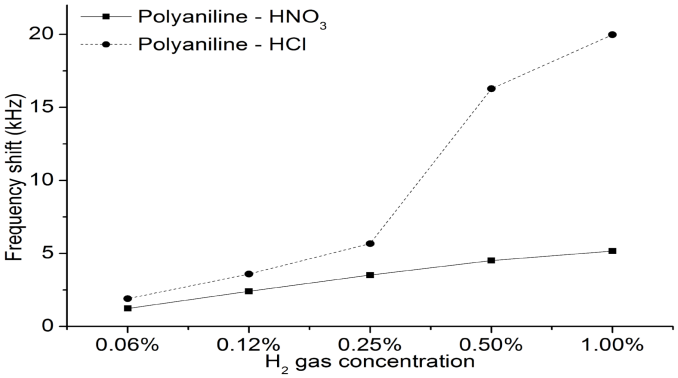

Figure 7.13: Frequency shift of polyaniline nanofibers based SAW sensors, comparison of polyaniline nanofibers which were polymerized in HNO_3 and HCl electrolytes.

The 90% response time of the measured sensors are shown in Fig. 7.14. It is observed than except for response towards 0.12% H_2, HNO_3 doped polyaniline sensor possessed faster response than that of HCl doped polyaniline nanofibers based sensor. Upon exposure to 1% H_2 gas, the reponse time for HNO_3 doped

polyaniline nanofibers based SAW sensor was 20 s. This response was slightly faster than the HCl doped polyaniline nanofibers based SAW sensor (28 s).

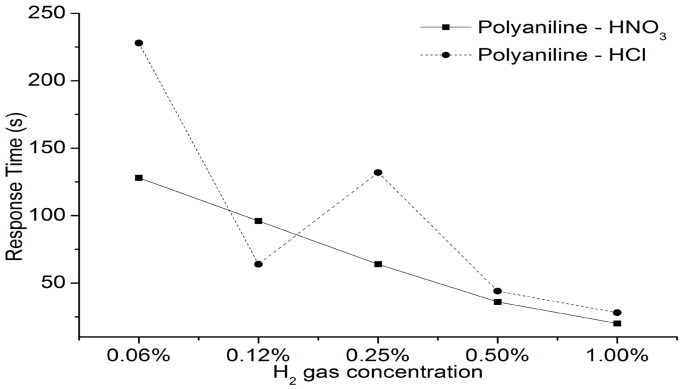

Figure 7.14: Response time for polyaniline-HNO_3 and polyaniline-HCl based $LiTaO_3$ SAW sensors.

Doping Effect on Conductometric Sensitivity

The plotted graph in Fig. 7.15 shows the devices' sensitivities of the electropolymerized doped and dedoped polyaniline nanofibers based conductometric sensors. From the plotted curves, it is observed that dedoped polyaniline sensor shows higher sensitivity of 1.16 than that of the doped polyaniline sensor. It is also observed that the sensitivity of the doped polyaniline device was almost plateau between 0.06% to 1% H_2 gas concentrations. Whereas the sensitivity of dedoped polyaniline sensor increased as the concentration of H_2 gas increased. Fast responses of 36 s for 0.5% and 1% H_2 gas concentrations at room temperature were also observed for dedoped and doped devices, respectively. However, these conductometric sensors exhibited slow recovery time. The response and recovery time versus concentration for both devices are plotted in Fig. 7.16. Doped polyaniline based conductometric sensor required approximately 4 min to fully recover to the original baseline after exposure to 1% H_2, whereas dedoped polyaniline based conductometric sensor required 38 min to recover at the same gas concentration. At elevated temperature, the probability of desorption increases [251]. Thus, the slow recovery was expected as the experiments were conducted at room temperature.

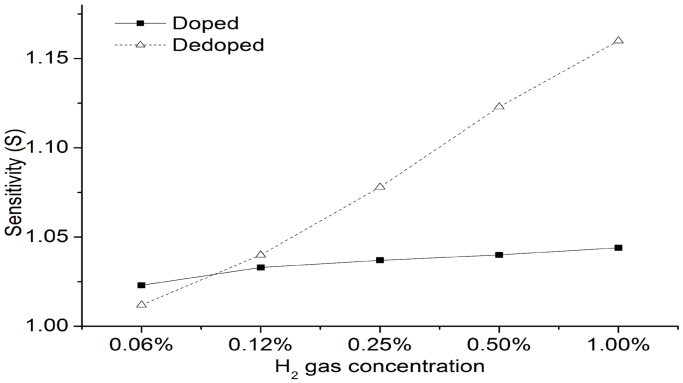

Figure 7.15: Sensitivity of doped and dedoped polyaniline nanofibers based SAW sensors for different concentrations of H_2 at room temperature.

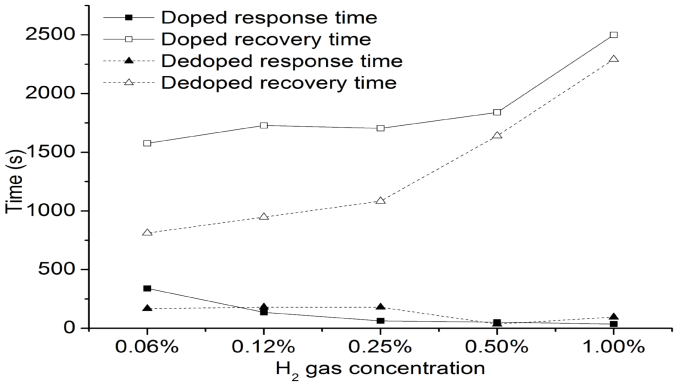

Figure 7.16: Response and recovery time versus H_2 gas concentrations.

During the interaction between H_2 and polyaniline, a proportion of the analyte gas (H_2) is probably catalytically oxidised forming water. The presence of water molecules in the polyaniline backbone leading to an increase in polymer's conductivity [252-253]. Therefore, it was observed that the resistance of both doped and dedoped polyaniline based sensors decreased upon exposure to H_2 gas. This observation is similar to that of Sadek et al. [67] who obtained doped and dedoped polyaniline via chemical polymerization.

Furthermore, McDiarmid et al. suggested that the H_2 may form a bridge between nitrogen atoms on two adjacent chains, or there may be partial protonation of some amine nitrogen atoms [130]. These reactions lead to the protonation of polyaniline nitrogen atoms which result in more delocalized charge carriers on

the polymer's backbone and an increase of film conductivity.

Dedoped Polyaniline/MWNTs Nanocomposite Based SAW Sensors - Electropolymerization

In chapter 5 and 6, the author presented the synthesis and characterization of polyaniline/MWNTs based $LiTaO_3$ SAW sensors via electropolymerization technique. The developed sensors then were placed in the gas chamber for assessing their gas sensing performance. Fig. 7.17 shows the dynamic response of the dedoped polyaniline/MWNTs nanocomposite based $LiTaO_3$ SAW gas sensors. Similar to other polyaniline nanofibers based $LiTaO_3$ SAW sensors, the introduction of H_2 gas to the sensor's surface causes a decrease in device's resonant frequency. The measured response was approximately 4.3 kHz towards 1% H_2 gas at room operating temperature. The 90% response and recovery time of 28 and 240 s were observed for 1% and 0.25% H_2 gas concentrations, respectively. It was also observed that the baseline frequency slightly drifted downwards. Exposing sensor to subsequent pulses of H_2 gas increased the stability of the baseline.

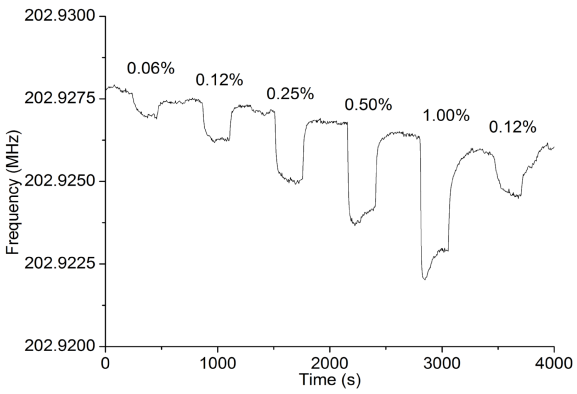

Figure 7.17: The dynamic response of polyaniline/MWNTs nanocomposite based SAW sensor to different H_2 gas concentrations in synthetic air at room temperature.

The response magnitude variation for the sensor to different H_2 gas concentrations is shown in Fig. 7.18. Frequency shift increases almost linearly with the increase of H_2 concentration. Whereas in Fig. 7.19, it is observed that the response became shorter as the H_2 gas concentration increased.

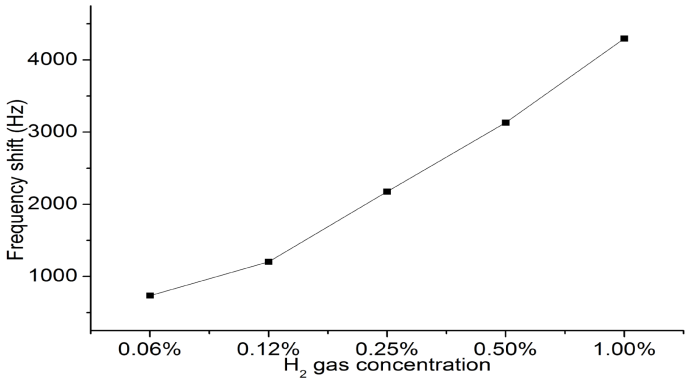

Figure 7.18: Frequency shiff (Hz) versus H_2 gas concentration (%) in synthetic air at room temperature.

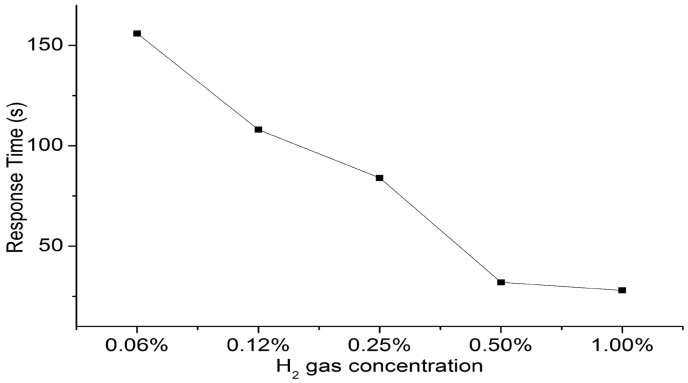

Figure 7.19: Response time (s) versus H_2 gas concentration (%) in synthetic air at room temperature.

It is known that upon exposure to H_2, the sensing mechanism of polyaniline/MWNTs could be complex [83], which includes doping, dedoping, reduction, swelling, conformational changes of polymer chain and so on. From the dynamic response which is seen in Fig. 7.17, it is observed that no change in resonant frequency of polyaniline occur upon exposure to synthetic air. This evidently shows that the dedoped polyaniline/MWNTs has a stable operational frequency upon exposure to synthetic air atmosphere. The frequency response of the dedoped polyaniline/MWNTs based $LiTaO_3$ SAW sensors immediately decreased once the H_2 gas was introduced in the chamber. The sensors show good recovery after purging out the H_2 and introducing the synthetic air again. As the recovery of the polyaniline/MWNTs based $LiTaO_3$ SAW sensors to the baseline take less

than 4 min for 0.25% H_2 gas, it is assumed that weak interaction occurs between the H_2 gas and the surface of the composite [83].

Polyaniline/Diamond Nanocomposite Based SAW Sensors - Chemical Polymerization

Fig. 7.20 exhibits the dynamic response to a sequence of different H_2 gas concentrations in synthetic air. The sensor was initially flushed with 200 sccm of synthetic air until the baseline frequency became stable. Due to polyaniline's ability to react with chemical species at low temperatures, the sensor was tested at room temperature. H_2 gas, with various concentrations, was then introduced in the chamber. It can be seen that the frequency of the polyaniline/diamond nanostructure thin film sensor decreased when exposed to H_2 gas. The frequency then increased to the baseline after synthetic air was purged. However, the polyaniline/diamond sensor exhibited a response overshoot for high H_2 concentration of 1%. Ippolito [173] suggested that this is due to the hydrogen molecules penetrating through the sensing layer and interacting directly with the underneath layers.

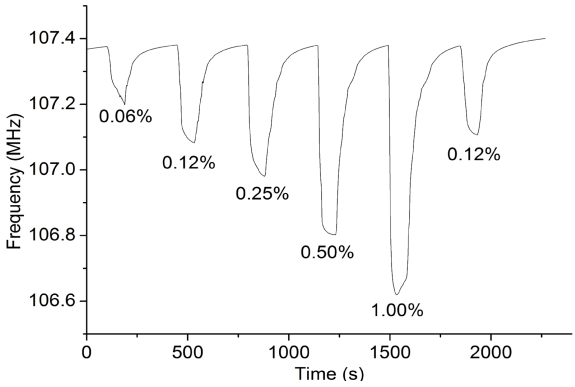

Figure 7.20: Dynamic response of different hydrogen gas concentrations in synthetic air at room temperature.

Fig.7.21 depicts the frequency shifts of different H_2 gas concentrations. From the plotted graph, measured response was more than 750 kHz towards 1% of H_2 gas. It is inferred that frequency shift increases almost linearly with H_2 concentration. Fast response and recovery of 16 s and 180 s towards 1% and 0.06% H_2 gas concentrations at room temperature were observed. The sequence of response

and recovery time for different H_2 gas concentrations is shown in Fig. 7.22. As can be observed in Fig. 6.14 the surface morphology of polyaniline/diamond nanofibers composite consisted of nanometer dimension structures. Its high porosity, which gave very large surface to volume ratio, seems to contribute to the fast response. The porosity enhances the gas diffusion, thus the reaction between gas molecules and the thin film occurs quickly [254]. The enhancement of gas diffusion therefore improves the sensor response of the polyaniline/diamond nanofibers based sensor.

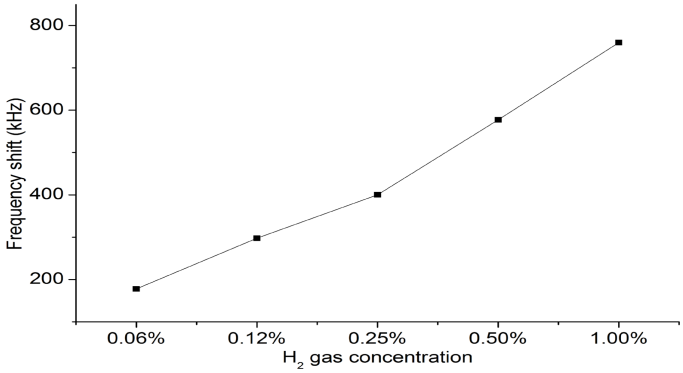

Figure 7.21: Frequency shift versus H_2 gas concentration.

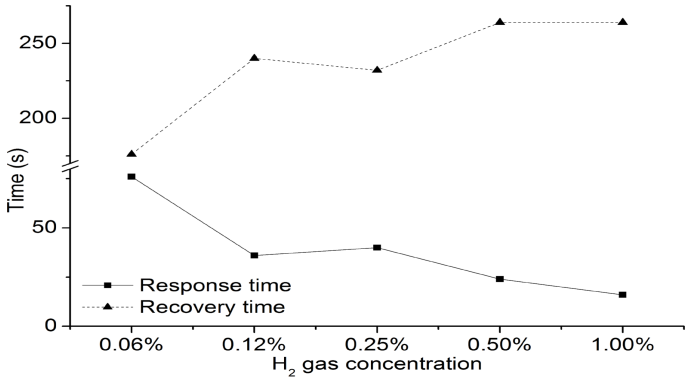

Figure 7.22: Response and recovery time versus H_2 gas concentration.

Previously in the study of doped polyaniline based SAW sensor, it was shown that the conductivity of polyaniline nanofibers is increased upon exposure towards H_2 gas. It is suggested that the H_2 may form a bridge between nitrogen

atoms on two adjacent chains. Besides, the presence of water molecules in polymer chain can also lead to the conductivity change. The sensing mechanism for diamond towards different gases has been suggested by a few researchers [92,255-256]. Referring to the analysis of the steady state reaction kinetics conducted by Gurbuz's group [92,255], it is confirmed that the hydrogen sensitivity of the device is attributed to the adsorption of hydrogen dipoles at the Pd/i-diamond interface.

The mechanism for the polyaniline and diamond composite interaction with hydrogen is still not fully understood. It has been suggested that for the polyaniline/inorganic material composites, there is an interaction with the polyaniline backbone which may induce dissociation of the hydrogen. The dissociation then leads to either a doping type response or chain alignment. This interaction possibly is facilitated by inorganic materials [61,77-78]. In addition, the dissociation of H_2 can also probably be stimulated by interaction with free spin of adjacent polyaniline chains which are contributed by the closer packing of polyaniline backbone.

7.3.2 PVP Based SAW Sensors

Frequency and Phase Responses

Fig. 7.23 shows the measured S_{21} transmission parameters of the electrospin coated PVP fibres based 36° YX $LiTaO_3$ SAW gas sensors before and after the deposition of the PVP fibres. The fabricated 36° YX $LiTaO_3$ SAW transducer has a resonant centre frequency peak of 203.5 MHz. Whereas the insertion loss is approximately -12 dB. After the deposition of PVP fibres, the resonant centre frequency peak and insertion loss have shifted to approximately 203 MHz and -8 dB. The stability of the phase response was still good after the deposition of the layer.

Gas Sensing Results

Testing for the PVP fibres based SAW gas sensors were carried out in a gas chamber. The details of the gas chamber set-up and testing procedures were outlined in section 7.2.1. The response of the PVP/SAW sensors towards H_2 gas was monitored using a frequency counter (Fluke PM6680B). The device was

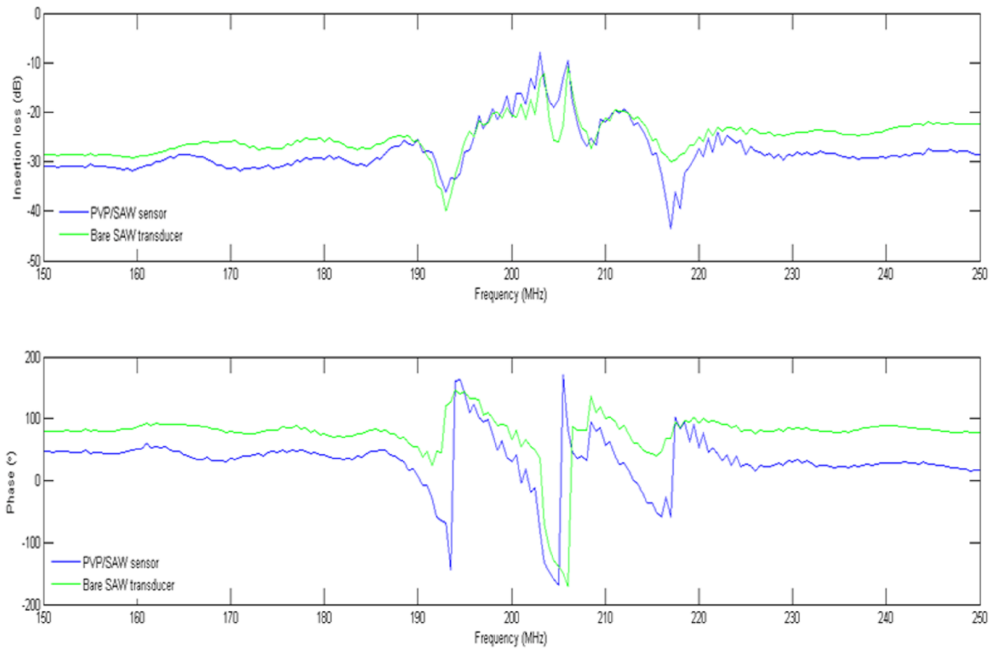

Figure 7.23: Frequency and phase response of the bare $LiTaO_3$ SAW and the PVP deposited on $LiTaO_3$ SAW devices in ambient condition.

exposed to different concentrations of H_2 gas in synthetic air at room temperature. The dynamic response of the sensor is shown in Fig. 7.24. The PVP fibres were deposited on the SAW transducers using electrospinning. The different concentrations for the PVP were used for electrospin PVP fibres. For the shown graph, 48% PVP concentration was used during electrospinning. The details of the synthesis of PVP were presented in chapter 5.

The introduction of H_2 gas to the PVP based $LiTaO_3$ SAW sensor caused reduction of the device's resonant frequency. This results in a decrease in the acoustic wave velocity. The measured responses were 2.10, 4.24, 7.27, 10.58 and 13.06 kHz towards 0.06%, 0.12%, 0.25%, 0.50% and 1.00% of H_2 gas concentrations, respectively. Fast response and recovery of 12 and 61 s towards 1% and 0.06% H_2 gas concentrations at room temperature were observed. Although the diameter of the 48% PVP particles and fibres is in micrometer range, it still provides large surface to volume ratio. The large surface to volume enhances the gas diffusion causes the reaction between gas molecules and PVP occurs quickly and contributes to the fast response.

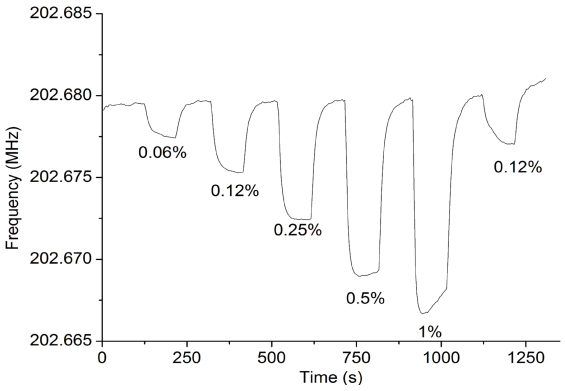

Figure 7.24: Dynamic response of PVP fibres based SAW gas sensor towards H_2 gas (PVP concentration of 48%).

In chapter 2, the author presented the gas sensing mechanism between H_2 gas and PVP molecules which is mainly based on hydrogen-bond based interactions. The carbonyl group in the PVP structure makes it a strong hydrogen bond acceptor. The following reactions may occur between PVP molecules and H_2 gas:

$$H_2 \rightleftarrows 2H^+ + 2e^- \tag{7.8}$$

$$\begin{array}{ccccccccccc} & & O & & & & O & & & & \\ & & \| & & & & \| & & & & \\ - & C & - & N^- & + & H^+ & \rightleftarrows & - & C & - & N & - & H \end{array} \tag{7.9}$$

Effect of PVP with Different Concentrations

In chapter 5, the author presented the preparation of the PVP solution with different PVP concentrations to be electrospun on the whole area of SAW transducers. To investigate the gas sensing performance, the author prepared four different SAW transducers by electrospin coating PVP fibres with 48%, 52%, 56% and 58% PVP concentrations. The details of the preparation of PVP was presented in Table 5.4. Fig. 7.25 plots the frequency shifts of the PVP based SAW sensors upon exposure to different H_2 gas concentrations. The 48% PVP SAW sensor shows the largest frequency shift of 13.1 kHz for 1.00% H_2.

The 90% response and recovery time of electrospun PVP based SAW sensors are plotted in Fig. 7.26 and 7.27, respectively. In Fig. 7.26, it is observed that the response time at 1% H_2 concentrations is almost equal for all measured devices, which was ∼12 s. Whereas in Fig. 7.27, the plotted graph shows that SAW sensor with higher PVP concentrations required more time to desorb H_2 molecules from the surface.

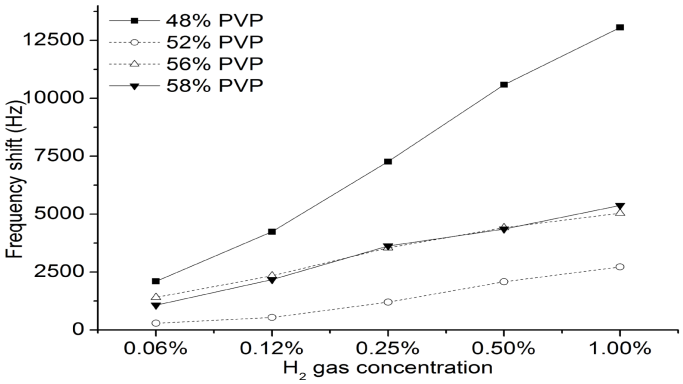

Figure 7.25: Frequency shift of PVP based $LiTaO_3$ SAW sensors, electrospun with different PVP concentrations.

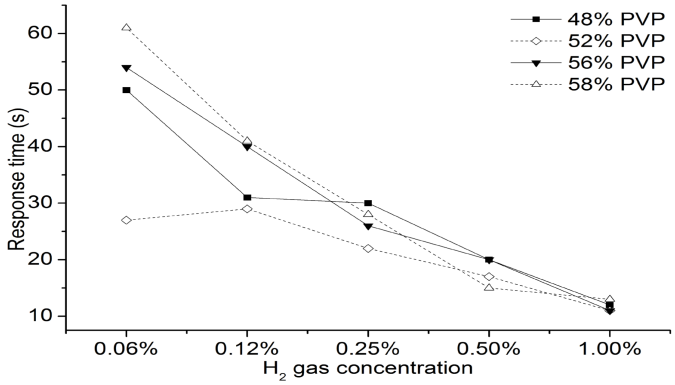

Figure 7.26: Response time of PVP based SAW sensors, electrospin coated with different PVP concentration.

The best explanation for the difference in frequency shift is the morphology difference of the electrospun PVP. Referring to Fig. 6.19, although fibres and beads were started to appear for 48% PVP, the whole surface of the electrospun

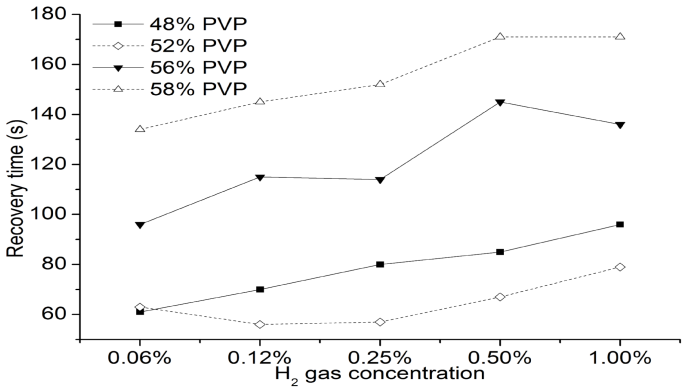

Figure 7.27: Recovery time of PVP based SAW sensors, electrospin coated with different PVP concentration.

device was still dominated by particles. The images evidently show that 48% PVP is denser than the other electrospun PVP which were used for gas sensing applications. Therefore, the large frequency shift was contributed to the high surface to volume ratio of 48% PVP. Among the 52%, 56% and 58% PVP devices, 52% PVP device had the lowest frequency shift for all H_2 gas concentrations. The diameter distributions of the mixture which is presented in Fig. 6.18 reveals that 52% PVP has the largest beads and fibres among all samples. This therefore effected the frequency shift of the gas SAW sensors upon H_2 exposure.

Electrospin Coated PVP/Polyaniline Composite Based SAW Sensors

From Fig. 7.28, it is observed that the electrical conductivity of the PVP/polyaniline (ES) and PVP/polyaniline (EB) based SAW sensors were increased upon exposure to H_2 gas. Both types of sensors show that the H_2 gas was readily desorbed to the surface of the sensing layer. For the PVP/polyaniline (EB) based SAW sensor, the frequency shift for 0.06% and 0.12% H_2 were small and insignificant. However, for high concentrations of H_2 (0.05% and 1.00%), this sensor showed large frequency shifts. From this result, it is obvious that PVP/polyaniline (EB) composite based SAW sensor was not suitable to measure H_2 concentrations lower than 0.25%.

The frequency shift versus different concentrations of H_2 gas is curve shown in Fig. 7.29. It can be seen that frequency shift for both devices increases almost linearly with H_2 concentrations. Fast response of 24 s towards 1% H_2 concen-

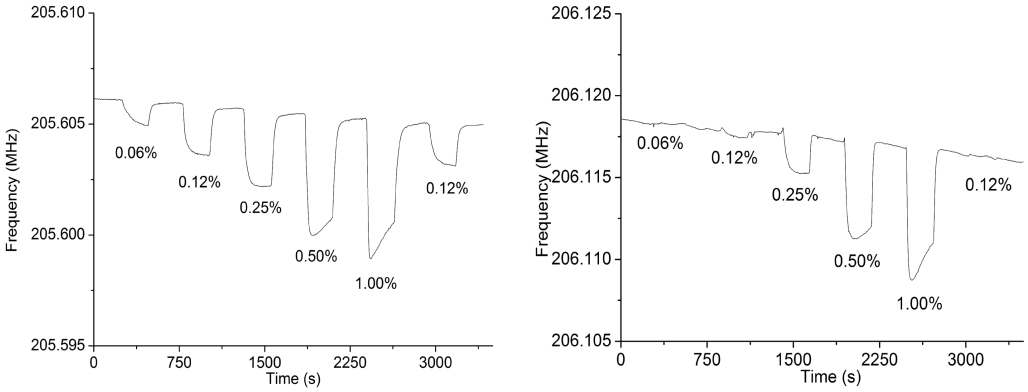

Figure 7.28: Dynamic responses of (a)PVP/polyaniline (ES) based SAW sensor, and (b) PVP/polyaniline (EB) based SAW sensor at room temperature.

tration was observed for both PVP/polyaniline (ES) and PVP/polyaniline (EB) based SAW gas sensors. Fig. 7.30 plotted a reponse sequence for different H_2 gas concentrations. It is also observed that the baseline of the PVP/polyaniline (ES) based SAW gas sensor is more stable than that of the PVP/polyaniline (EB) based SAW gas sensor.

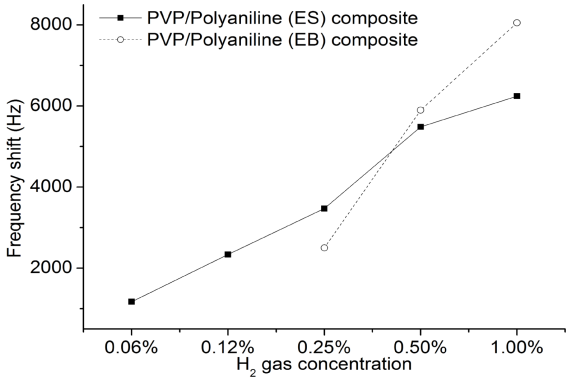

Figure 7.29: Frequency shift of the PVP/polyaniline (ES) and PVP/polyaniline (EB) based SAW gas sensors versus H_2 gas concentration in synthetic air at room temperature.

For the PVP/polyaniline (ES), it is believed that the conductivity of the composite increases upon exposure to H_2 gas. This results in a decrease in

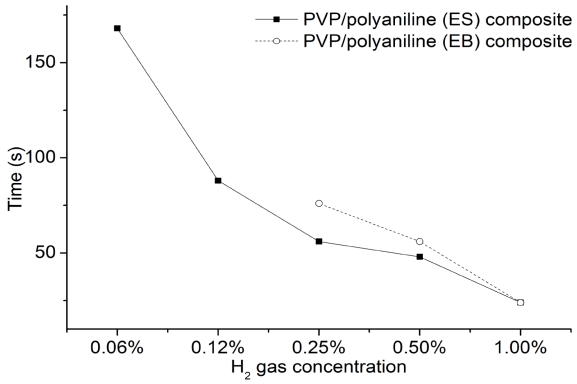

Figure 7.30: Response time of the PVP/polyaniline (ES) and PVP/polyaniline (EB) based SAW gas sensors versus H_2 gas concentration.

the acoustic wave velocity and: therefore a decrease at the resonant frequency. However for the PVP/polyaniline (EB), it is believed the adsorption of H_2 gas causes the mass of the sensing film to change, which contributes to the decrease in acoustic wave velocity and subsequently the resonant frequency. The adsorption of H_2 gas into the PVP/polyaniline (ES) and PVP/polyaniline (EB) appeared to involve the penetration of the gas into the polymer accompanied by swelling of the polymer [257].

Electrospin Coated PVP/MWNTs Composite Based SAW Sensors

Similar to other PVP based SAW gas sensors, the sensing performance of the PVP/MWNTs composite based SAW sensors were investigated by placing the sensors in the gas chamber. The details of the SAW gas sensing set-up were presented in section 7.2.1. Both types of sensors were exposed to hydrogen pulse sequences of 0.06%, 0.12%, 0.25%, 0.50%, 1.00% and 0.12% concentrations in synthetic air at room temperature.

Dynamic responses to a sequence of different H_2 gas concentrations are shown in Fig. 7.31(a) and (b), for which one device contains smaller amount of PVP (1.025 g) than the other one (1.525 g of PVP). The details of the preparation and characterizations of the composites were presented in chapters 5 and 6. It is observed that the introduction of the H_2 gas to the chamber causes reduction of the devices' resonant frequencies. In Fig. 7.31(a), the measured response was 530 Hz towards 1% H_2 gas concentration in synthetic air. Whereas, the

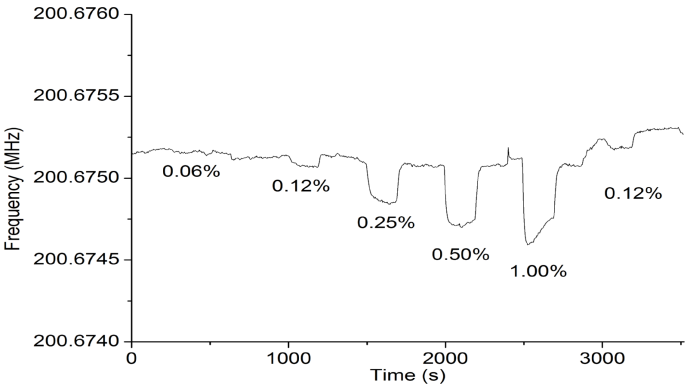

(a) 1.525 g PVP.

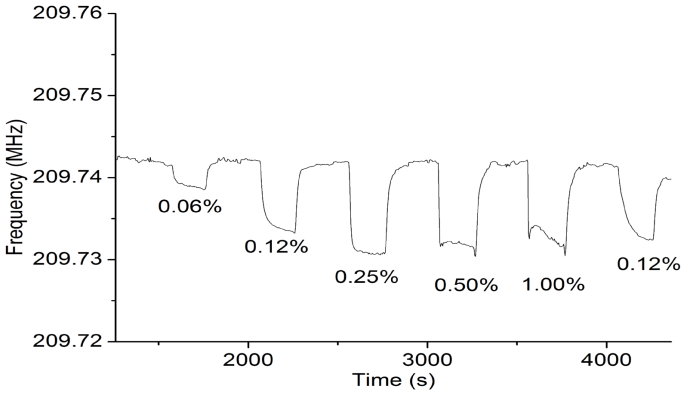

(b) 1.025 g PVP.

Figure 7.31: Dynamic responses of PVP/MWNTs based SAW gas sensors towards H_2 gas.

measured response for the sensor with small amount of PVP was 11.322 kHz towards 0.25% H_2 gas concentration in synthetic air. The 90% response time of 32 and 36 s towards 1.00% and 0.25% H_2 gas concentrations were observed at room temperature.

The response magnitude variation for the sensors for different H_2 concentrations at room temperature is shown in Fig. 7.32. The plotted figure shows that the frequency shift for the composite of 1.525 g PVP and 5% MWNTs based SAW sensor increases linearly with the increase of H_2 gas concentrations. However, this sensor is not able to measure H_2 gas concentration of 0.06%. For the device electrospun with a solution of 1.025 g PVP and 5% MWNTs, the frequency shift increases almost linearly for H_2 concentrations up to 0.25%. From Fig. 7.31, it can be seen that the sensor response magnitudes for 0.50% and 1.00% H_2 concentrations were lower than that of 0.25%. It is believed that high concentrations of H_2 saturates the composite film. The results show that the sensor is best useful for low concentrations of H_2.

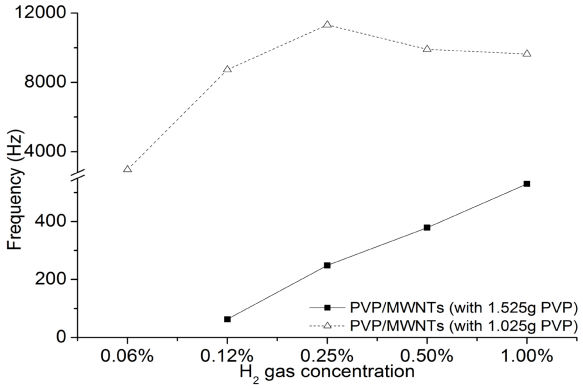

Figure 7.32: Frequency shift of PVP/MWNTs based SAW sensors versus H_2 gas concentration.

For these sensors, the introduction of H_2 caused the decrease in acoustic wave velocity, and subsequently decreased in the resonant frequency. To explain the difference in frequency shifts for both devices, it is suggested that for the device with 1.525 g PVP the interaction with H_2 molecules was governed by the PVP itself. PVP molecules outweight the MWNTs in adsorbing the H_2 gas molecules. Upon H_2 exposure, the mass of the PVP/MWNTs increased

resulting in a decrease in the acoustic wave velocity, which decreased the resonant frequency. However, high freqency shift was observed for the device with less PVP concentration. It is known that SAW sensors respond to both mass change and the change in conductivity. For the device with 1.025 g PVP, there is a possibility that both changes occured upon exposure to H_2 gas. In addition to the mass change that caused by the PVP, the author believes that the conductivity of the MWNTs in the PVP/MWNTs composite layer increases. Subsequently the acoustic wave velocity decreases, thereby decreasing the resonant frequency.

7.3.3 Graphene NanoSheets Based SAW Sensors

Frequency and Phase Responses

Fig. 7.33 shows the transmission responses (S_{21}) of the graphene-like nanosheets based SAW sensor before and after the deposition of graphene layers.

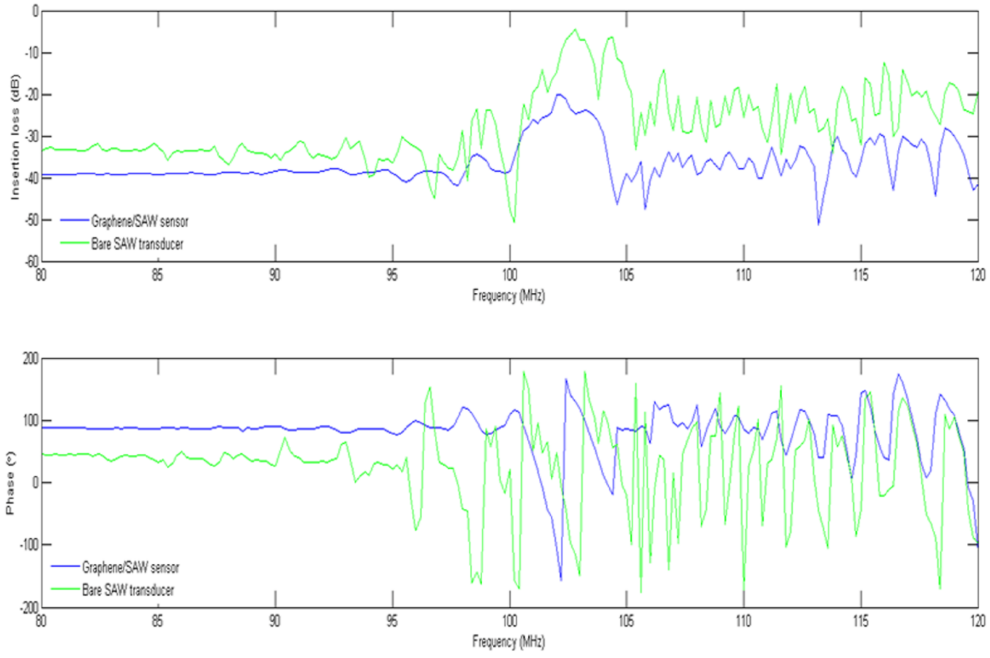

Figure 7.33: Frequency and phase responses of bare $LiTaO_3$ SAW and graphene layer on $LiTaO_3$ SAW devices in ambient conditions.

In Fig. 7.33, it is observed that resonant centre frequency and insertion loss of bare SAW transducer was approximately 102.8 MHz and -5 dB, respectively.

However, after the deposition of graphene layers, the resonant centre frequency and insertion loss were shifted to 102.2 MHz and -20 dB, respectively. The stability of the phase and frequency responses after the deposition of the layer was as good as the bare devices. As it is observed that the deposition of graphene layer increased the insertion loss, it is suggested that the increase in the insertion loss result in the scattering and dampening of the surface waves [245].

Gas Sensing Results

H_2

Employing the experimental set-up and procedure outlined earlier in this chapter, the sensor was tested repeatedly towards sequential pulses of 0.06%, 0.125%, 0.25%, 0.5% and 1% of H_2 gas in air. The exposure and purge time were 200 and 480 s, respectively. Fig. 7.34(a) and 7.34(b) show the dynamic response of the graphene-like nano-sheets/SAW sensor to a sequence of different H_2 gas concentrations in synthetic air at room temperature and 40 °C, respectively. The measured response at room temperature (25 °C) was 5.8 kHz towards 1% H_2. At operating temperature of 40 °C, the frequency shift was lower (1.7 kHz) when exposed to the same concentration of H_2. These low operational temperatures are favorable in many applications, especially those involving low power operations and inflammable environments.

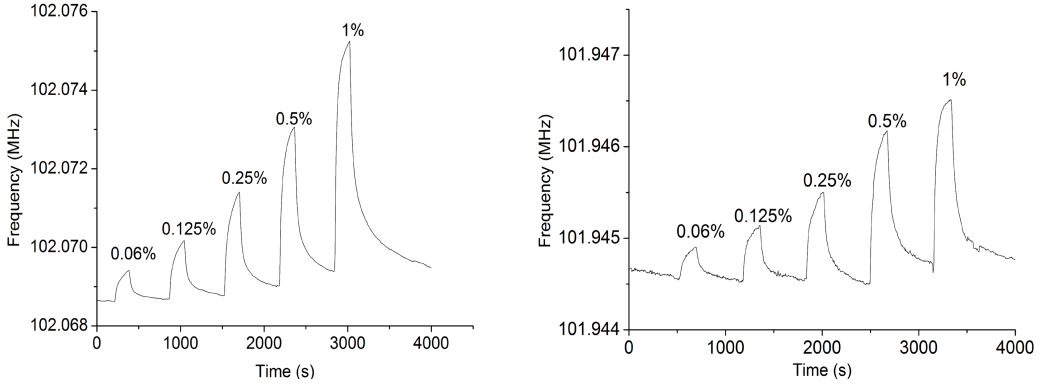

(a) (b)

Figure 7.34: Dynamic responses of graphene-like nano-sheet/$LiTaO_3$ SAW sensors towards H_2 gas at (a) room temperature, and (b) 40^{o}C.

The sensor responses at room temperature and 40 °C operation versus H_2 concentration curves are shown in Fig. 7.35. It is observed that the frequency shift of H_2 at room temperature increases almost linearly with the increase in H_2 concentration. Frequency shifts for 1% H_2 at 40 °C shows a non-linear behaviour which begins to plateau at concentration of 1%. The plotted graph in Fig. 7.36 shows the response and recovery time of measured SAW sensor towards H_2 gas at two different operating temperatures. Exposed to 0.125% H_2 at 40 °C, a fast response of 12 s and recovery of 58 s was observed. It is also observed that the response and recovery time for the high operating temperature was smaller than the room temperature, however the frequency shift was lower. It is known that at elevated temperatures, the probability of desorption increases [251]. Therefore, the slow recovery (∼9 min) for 1% H_2 at room temperature was expected.

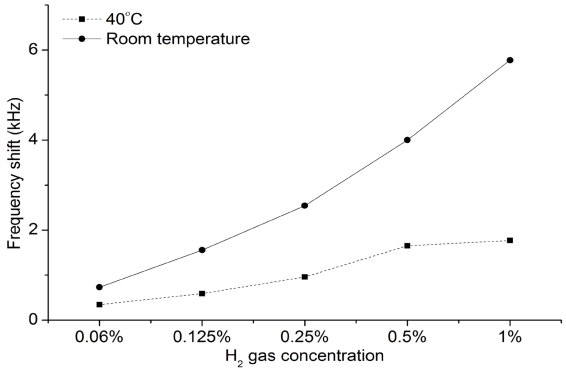

Figure 7.35: Oscillation frequency shift vs H_2 gas concentration of graphene-like nano-sheet/$LiTaO_3$ SAW sensors.

Arellano et al. [133] has investigated the adsorption of molecular hydrogen (H_2) onto a graphene sheet at 0 K via density functional theory (DFT). Four unique orientations and positions of physisorbed H_2 were identified, with the hydrogen molecule lying perpendicular or parallel to the plane of the graphene sheet. The adsorption of H_2 onto graphene is very weak, being physisorbed onto graphene with binding energies of <0.1 eV and adsorbate surface distances between 5.07 Å and 5.50 Å. The hydrogen molecule was found to align itself perpendicular to plane of the graphene sheet above 163 K.

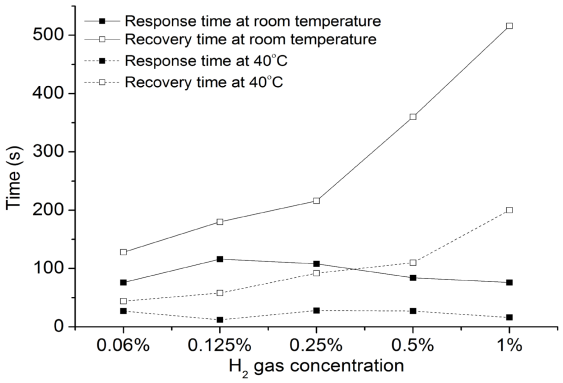

Figure 7.36: Response and recovery time (s) vs H_2 gas concentration (%).

NO_2

The graphene-like nano-sheet/$LiTaO_3$ SAW sensors were tested repeatedly towards sequential pulses of 0.51ppm, 1.0625ppm, 2.125ppm, 4.25ppm and 8.5ppm of NO_2 gas in dry synthetic air. Unlike hydrogen, NO_2 increases the conductivity of the graphene sensitive layer by donating electrons to the conduction band. Fig. 7.37(a) and Fig. 7.37(b) show the dynamic response of the sensors to NO_2 gas at two operating temperatures, which are room temperature and 40 °C. It can be seen the frequency decreased when exposed to the analyte gas. After purging out the NO_2 gas through the introduction of dry synthetic air, the operational frequency of the SAW sensor increased and returned to the baseline, which occurred at both operating temperatures. However, drifting of both baselines was observed. By exposing sensors to subsequent pulses of NO_2 the baseline became stable.

The associated frequency shifts for 0.51 - 8.5 ppm concentrations of NO_2 mixed with synthetic air are plotted in Fig. 7.38. It is observed that the trends of the frequency shifts were almost the same for both temperatures. Both show linear changes as the NO_2 concentration increases. The measured response at 40 °C was 18.7 kHz towards 8.5 ppm NO_2. At room temperature, the frequency shift was smaller (14.9 kHz) when exposed to the same concentration of NO_2. The plotted graph in Fig. 7.39 shows the relation of response time versus NO_2 gas concentrations. At the higher operating temperature, slow response was observed for 0.51 and 1.0625ppm NO_2 concentrations. The response time improves at higher gas concentrations. As for room operating temperature, the fastest

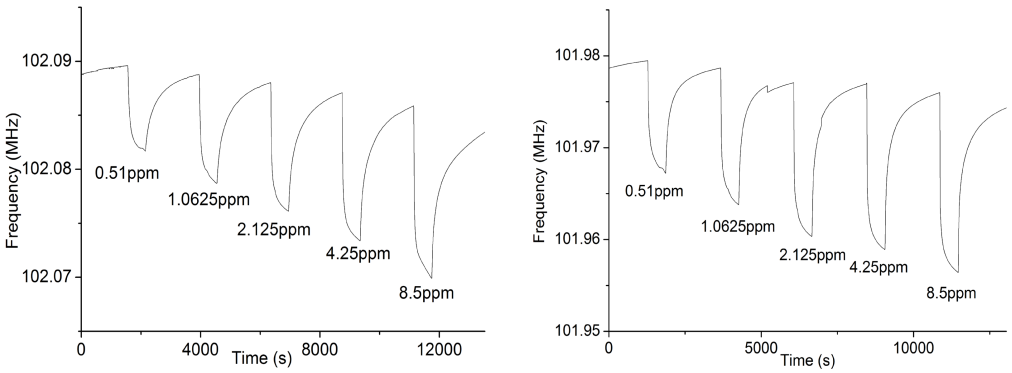

Figure 7.37: Dynamic response of graphene-like nano-sheet/$LiTaO_3$ SAW sensors towards NO_2 gas at (a) room temperature, and (b) 40°C.

response was observed at 8.5 ppm (152 s).

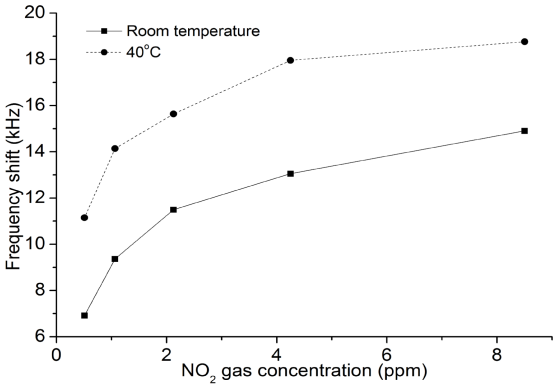

Figure 7.38: Oscillation frequency shift vs NO_2 gas concentration of graphene-like nano-sheet/$LiTaO_3$ SAW sensors.

Utilising DFT, Leenaerts et al [132] have reported the adsorption of NO_2 onto graphene at 0 K. It was found that NO_2 adsorbs between 3.61 Å and 3.93 Å above the surface of the graphene sheet with binding energies ranging between 0.05 and 0.07 eV. The large spacing between the adsorbate and the graphene surface combined with the small binding energies reported, suggest that NO_2 is physisorbing onto the surface of the graphene sheet. The charge transfer calculations indicate that NO_2 can withdraw charges from the graphene sheet

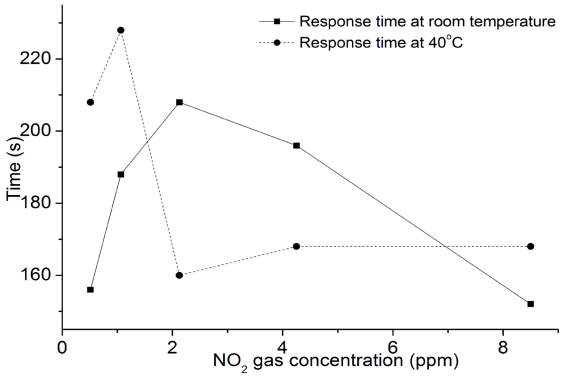

Figure 7.39: Response time (s) vs NO_2 gas concentration (ppm).

and act as an acceptor of charges, accepting a maximum of 0.1 eV. This is in agreement with the experimental data presented in this thesis, which shows that of H_2 and NO_2 adsorption induce a p-type response in graphene. This is further supported by the Hall measurements which reveal that NO_2 is an acceptor [115].

CO

The author extended the gas testing of graphene-like nano-sheet/$LiTaO_3$ SAW sensors towards another reducing gas; CO. Similar to the previous experiments, sensor was exposed to different CO gas concentrations. The experiments were conducted at two different operating temperatures; room temperature and 40 °C. Fig 7.40(a) and 7.40(b) show the dynamic response of the graphene-like nano-sheets/$LiTaO_3$ SAW sensors to a sequence of different concentrations of CO gas in dry synthetic air.

Measured sensor responses were approximately 8.5 and 7.0 kHz to 1000ppm CO at room temperature and 40 °C, respectively. For the low concentrations of CO (60 ppm), the frequency changes were small and almost insignificant, however, the changes increased dramatically at 1000 ppm. Although CO is a reducing gas, frequency decreased upon exposure to CO, which was similar to NO_2, which is an oxidizing gas. The frequency shifts for 125 - 1000 ppm concentrations of CO at these two operating temperatures are plotted in Fig. 7.41. For the concentrations below 500ppm, the frequency shift at both temperatures were almost the same. However, at higher CO concentrations frequency shift of

the sensor operating at room temperature was larger than at 40 °C. This may be due to the instability of graphene material at higher temperature as explained in the previous chapter.

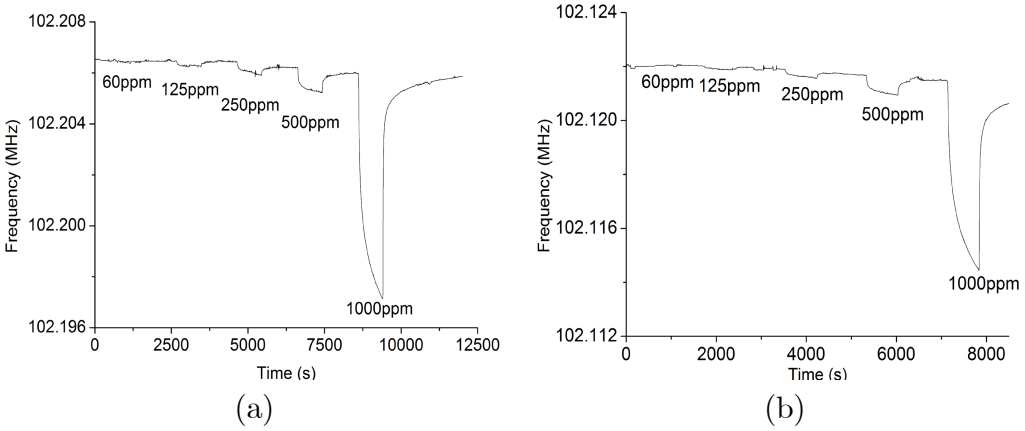

Figure 7.40: Dynamic response of graphene-like nano-sheet/$LiTaO_3$ SAW sensors towards CO gas at (a) room temperature, and (b) 40°C.

The plotted Fig 7.42 shows the response and recovery time which were recorded for the measured CO. The 90% response time was approximately 500 s to 1000 ppm CO at both operating temperatures. It was also observed that for CO, the recovery time took almost 30 and 20 min at room temperature and 40 °C, respectively.

The DFT studies of CO adsorption on graphene [132] suggested that three different orientations of the CO molecule can physisorb onto the graphene surface. The binding energies and adsorbate surface distances were calculated to range between 0.008 - 0.02 eV and 3.70 – 3.75 Å, respectively.

Considering that CO is a reducing gas, one might expect a similar direction for the frequency shift as for H_2 which would be consistent with the Hall measurements reported by Schedin et al [10]. However, the dynamic response of CO does not show such a response. This probably is the result of incomplete reduction of GO with hydrazine. SAW sensors respond to both mass change and the change of surface conductivity. When mass increases, frequency decreases as the adsorbed molecules reduce the acoustic wave velocity. It should be noted that

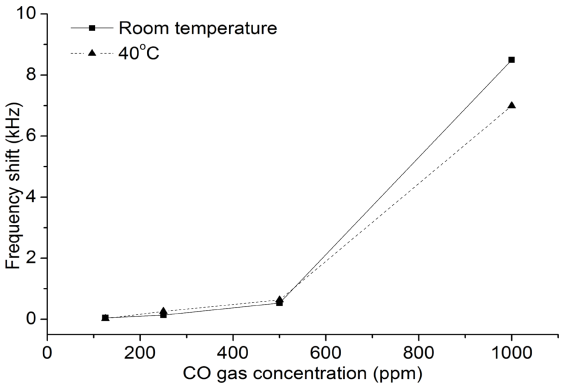

Figure 7.41: Oscillation frequency shift vs CO gas concentration of graphene-like nano-sheet/$LiTaO_3$ SAW sensors.

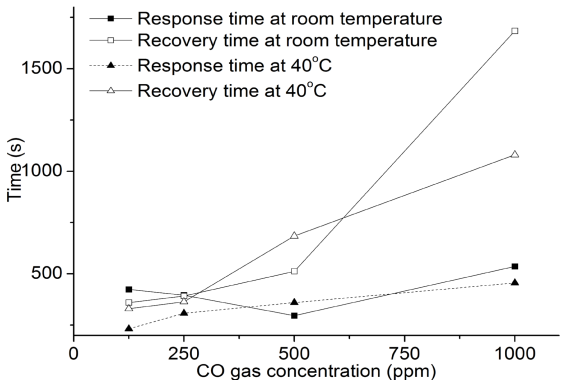

Figure 7.42: Response and recovery times (s) vs CO gas concentration (ppm).

when conductivity of the SAW device surface decreases, the velocity increases. Assuming that the change of conductivity is the dominant factor and considering that both gases are reducing reagents, the direction of the frequency shifts should have been the same. However, in response to H_2, operational frequency increased and upon exposure to CO it decreased. The molecular weight of H_2 molecules is 14 times smaller than CO molecules. As a result, it is suggested that the dominant factor in H_2 response was the change of conductivity of the graphene. Whereas, the dominant sensing mechanism of CO adsorption the mass increase. Upon adsorption of the CO molecules, acoustic wave velocity of the sensing layer is reduced, therefore the operational frequency is also reduced.

The incomplete reduction of GO populates the surface of graphene with epox-

ide, carbonyl, hydroxyl, and other functional groups. These functional groups, even at low coverages, can compete for the adsorption sites on the graphene that would otherwise be occupied by adsorbate gas molecules. Furthermore, these functional groups may passivate the graphene surface, potentially reducing the affinity of the surface with adsorbate molecules. As such, it is hypothesized that a single-layered graphene-based SAW sensor may offer more favorable sensing characteristics than an incomplete reduced GO based sensor.

7.3.4 Antimony Oxide Nanostructured Based Conductometric Sensors

In this subsection, the author will present H_2 gas sensing results of antimony oxide nanostructured based conductometric sensors. The experimental set-up and testing procedures were outlined in details in section 7.2.2. The sensors were exposed to H_2 gas pulse sequence of 0.06%, 0.12%, 0.25%, 0.50%, 1.00% and 0.12% concentrations in dry synthetic air. A thermocouple was used to obtain a real-time temperature reading of the sensor surface as the sensor was tested at elevated temperatures. Fig. 7.43 to 7.45 show the H_2 gas sensing responses and their analysis. All the tests were carried out after the LGS conductometric devices were flushed with 200sccm of synthetic air at the desired operating temperatures until no further changes in resistance was observable. H_2 was only introduced to the system after complete stabilization. Once the H_2 gas with different concentrations were introduced, the resistance dropped rapidly from the baseline and then slowly reached saturation before the flow changed back to the synthetic air.

Fig. 7.43 shows the dynamic response of the Sb_xO_y nanostructured based conductometric sensor tested at different H_2 concentrations at 180 °C. Similar to other metal oxides, Sb_2O_3 has a wide band gap (∼3.3 eV) [125] and it has a very high resistance at room temperature [128]. Response time for every concentration at every operating temperatures was measured. For the hydrogen concentration of 1%, the fastest response was 11 s at 291 °C operating temperature. This operating temperature also gave the fastest response for other H_2 concentrations.

The change in resistance of the Sb_xO_y based LGS conductometric sensor was

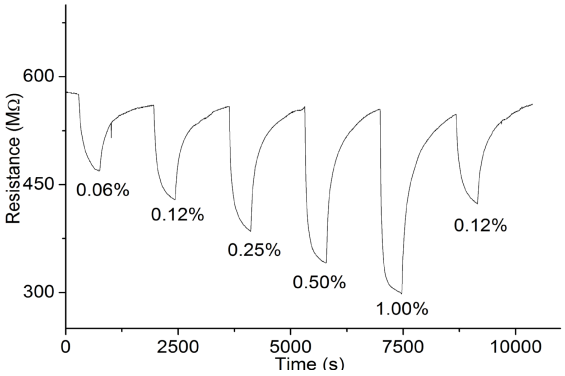

Figure 7.43: Dynamic response of Sb_2O_3 nanostructures based LGS conductometric gas sensor exposed to different H_2 concentrations at 180 °C.

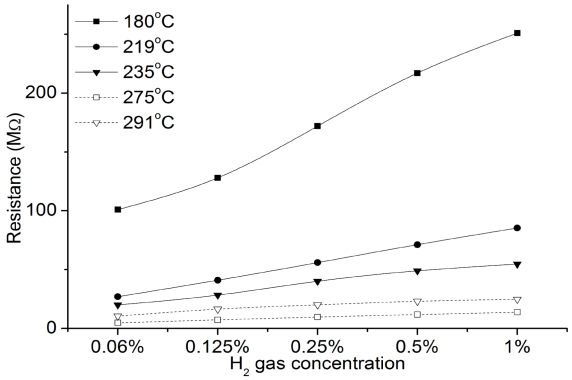

Figure 7.44: Changes in resistance for each operating temperature vs different gas concentration.

monitored for different H_2 gas concentrations at temperature ranges between 180 °C to 291 °C. From the plotted graph in Fig. 7.44, it can be seen that the changes in resistance for the device operating at 180 °C were about 21 and 18 times higher than the changes at 275 °C for 0.06% and 1% of H_2 concentrations, respectively.

Device sensitivity denoted as S and defined as the ratio of resistance for exposed to synthetic air to the resistance when exposed the test gas, $S = R_{air}/R_{gas}$. Fig. 7.45 is the plot of sensitivity of the Sb_xO_y based LGS conductometric sensor with respects to the operating temperature. This graph shows an increase in sensitivity when the temperature is increased. The highest sensitivity for 1%

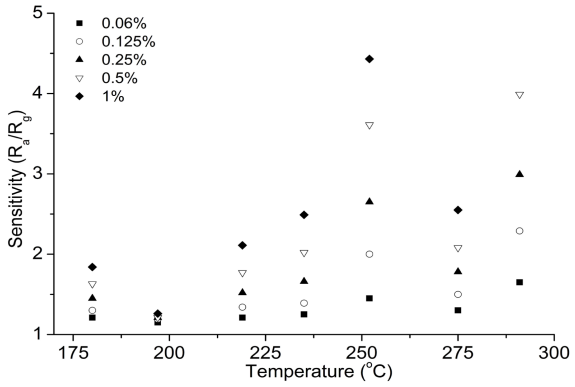

Figure 7.45: Comparison of device sensitivity for various gas concentrations.

hydrogen was 5.21 at 291 °C while the least sensitivity for this concentration was 1.26 which was obtained at 197 °C.

It is widely accepted that the conductivity of semiconducting oxides in air is determined by the trapping of electrons in surface states associated with surface absorbed oxygen [127]. In air, the oxygen molecules can adsorb onto the surface of the Sb_xO_y in several forms such as; O_2^-, O^- and O^{2-}, depending on the operational temperature. However, if the oxygen vacancies are immobile in the lattice, the behaviour may be described by electron distribution between bulk and surface states. H_2 gas reacts with the catalytic surface, causing a change in the surface coverage of the oxygen atoms near the surface. When the Sb_xO_y based conductometric sensors are exposed to H_2 gas, the following reactions may occur:

$$H_{2,gas} \rightleftarrows H_{2,ads} \tag{7.10}$$

$$H_{2,ads} + O^-_{ads} \rightleftarrows H_2O + e^- \tag{7.11}$$

From these equations, it is evident that the electrons trapped by the oxygen adsorbates can be transferred to the oxide surface. The overall effective change in the density of the ionosorbed hydrogens can be sensed by an increase in sensor's conductivity. The deposited Sb_xO_y contains nanorods of approximately 30 to 50 nm diameter. Therefore the adsorbed hydrogen can easily penetrate through the bulk of the nanorod.

The antimony oxide conductometric device showed an n-type behaviour in response to H_2 gas. This agrees well with previous researchers' report who performed several investigations on antimony oxide thin films [127,258]. It is believed that, surface oxygen anion, O^{2-} can be adsorbed on n-type semiconductor oxide, act as a surface acceptor at elevated temperatures. As measurements were conducted for H_2 in synthetic air (21% O_2), the oxygen adsorption of the present O_2 molecules decreases the charge carrier density at the surface, this is balanced by the charged carried on the ionised donors. At this temperature, the activation energy for chemical reaction between H_2 and surface acceptor is higher. Electrons from hydrogen gas are excited to the device surface. As more electrons are being excited to the surface, the device becomes more conductive. Thus resistivity of the sensor is reduced [259-260].

The morphology of the sensing layer influences the sensor's performance. In previous chapter, the SEM shows that the deposited Sb_xO_y is porous and in nanometer scale. Therefore, H_2 gas can access all of the volume of the sensing layer, not confined to the surface of the sensing layer. For the porous layer, the gas sensing reactions can take place on the surface of the individual nanostructures, at grain-grain boundaries and interface between grain and electrodes.

7.4 Summary

This chapter highlighted the gas sensing set-up and techniques employed by the author at RMIT University for testing of the nanostructured materials based SAW and conductometric sensors. The gas sensing performance of these sensors were investigated which was presented in this chapter. This research has led to many outcomes and contributions to the body of knowledge, especially in the field of nanostructured materials and gas sensors. These outcomes are as follow:

1. In this research, doped and dedoped polyaniline based SAW devices were successfully fabricated for gas sensing applications. Measured sensor responses for doped and dedoped polyaniline nanofibers based SAW gas sensors were approximately 0.48 and 9.46 kHz towards 1% H_2 concentration. To the best of author's knowledge, this was the first reports on the testing of a dedoped polyaniline SAW sensor upon exposure to H_2.

2. The dedoped polyaniline nanofibers based SAW sensors with different thin film thickness were investigated for H_2 gas sensing. The results showed that the frequency shift increases as the thickness of the films increase for sensing H_2 concentrations. For 1% H_2 concentration, the SAW sensor with dedoped polyaniline nanofibers thin film thickness of $\sim$3.5 μm exhibited the largest frequency shift. Thick films of porous polyaniline nanofibers provide more surface for H_2 adsorbtion than the thin films, therefore the diffusion of the analyte gas was faster. Hence, the response time of thick films was smaller than the counterparts towards high H_2 concentrations. To the best of author's knowledge, the author was the first researcher who investigated the effect of different thicknesses of electropolymerized polyaniline fo gas sensing.

3. The electropolymerization of dedoped polyaniline nanofibers based SAW sensors using different acid concentrations in electrolyte showed different gas sensing performance upon exposure towards H_2 gas. Dedoped polyaniline based SAW sensor electropolymerized in 1.0M HCl electrolyte possessed the largest frequency shift and the most stable baseline when compared with 0.5M and 1.5M HCl devices. This study provides valuable insight for other researchers to investigate the effect of other acid concentrations to find the optimum conditions.

4. To the best of author's knowledge, this is the first novel studies for the application of different acids in electropolymerized polyaniline sensors were conducted for gas sensing applications. The average diameter of HNO_3 doped polyaniline nanofibers were in the range of 30-50 nm. The measured sensor response of dedoped polyaniline nanofibers (deposited in HNO_3) based SAW sensor was 5.168 kHz. It was observed that the frequency shift was $\sim$4 times lower than that of deposited in HCl electrolyte. Upon exposure to 1% H_2 gas, the response for this sensor was 20 s, which was slightly faster than than HCl polyaniline nanofibers.

5. The gas sensing results of the doped and dedoped polyaniline nanofibers based conductometric sensors towards H_2 gas showed that dedoped polyaniline nanofibers based sensor was more sensitive than that of doped polyaniline nanofibers one. However, doped polyaniline nanofibers based sensor

possessed better baseline stability than the dedoped polyaniline nanofibers sensor.

6. Electropolymerized polyaniline/MWNTs nanofibers composite showed more compact and denser morphology than that of polyaniline nanofibers. The measured sensor response of dedoped polyaniline/MWNTs nanofibers based SAW sensor was approximately 4.3 kHz towards 1% H_2 gas at room temperature. The 90% response and recovery time of 28 and 240 s were observed towards 1% and 0.25% H_2 gas concentrations, respectively. To the best of author's knowledge, this was the first study regarding such a comparison.

7. Chemically polymerization of CSA doped polyaniline/diamond nanocomposite based SAW sensors were formed using nanofibers and clusters of coral-like structures. The measured sensor response was more than 750 kHz towards 1% H_2 gas. Fast response and recovery of 16 and 180 s towards 1% and 0.06% H_2 gas concentrations at room temperature were observed. The author showed that CSA doped polyaniline/diamond nanocomposite based SAW sensors showed a superior performance in comparison to other polyaniline based sensors.

8. PVP fibres were successfully deposited on SAW transducers via the electrospinning method. Upon exposure to 1% H_2 gas, the frequency shift of 13.06 kHz was measured. Fast response and recovery of 12 and 61 s towards 1% and 0.06% H_2 gas concentrations at room temperature was observed.

9. The morphology of the electrospun PVP were found to affect the gas sensing performances. The device electrospun with 48% PVP showed the highest frequency shift upon exposure to H_2 gas. The author attributed this to the high surface to volume ratio of the electrospun particles of 48% PVP. Whereas the device that coated with beads and fibres of 52% PVP had the lowest frequency shift. This 52% PVP device showed the fastest response and recovery towards H_2 gas compared to the other prepared electrospun PVP devices.

10. To the best of author's knowledge, this is the first investigation on the effect of the addition of polyaniline to PVP in the electrospinning process for gas sensing applications. Electrospun of PVP in the presence of polyaniline ES and EB were employed to synthesize PVP/polyaniline composites on

SAW transducers. The gas sensing results for both SAW sensors were investigated. PVP/polyaniline (EB) sensor was observed to show high sensitivity, however the device detection limit of H_2 at room temperature was 0.25%. Whereas for PVP/polyaniline (ES) based SAW sensors, the device was able to measure as low as 0.06% H_2 gas concentrations with good baseline stability.

11. PVP in the presence of MWNTs were electrospun on SAW transducers with two different concentrations of PVP. PVP/MWNTs based SAW sensor with lower concentration of PVP showed higher frequency shift of 11.322 kHz. The author believes that the shift probably caused by the change in both mass and conductivity of the composite materials.

12. To the best of author's knowledge, the graphene-like nanosheets were successfully deposited on SAW transducers and tested towards H_2, NO_2 and CO for the first time by the author. The highest sensitivity for this device was observed at room temperature for NO_2 and 40 °C for H_2 and CO with frequency shifts of 18.7, 5.8, and 8.5 kHz towards 8.5ppm NO_2, 1% H_2 and 1000ppm CO, respectively.

13. To the best of author's knowledge, nanostructured Sb_xO_y based LGS conductometric sensors were developed by the author and tested towards H_2 gas for the first time. The average diameter of the thermally evaporated Sb_xO_y nanorods were in the range of 30-50 nm. The highest sensitivity of 5.21 for these nanorods based conductometric sensor was observed at 291 °C. Whereas the lowest sensitivity of 1.26 was observed at 197 °C.

Chapter 8

Conclusions and Future Works

This research program commenced with aim of investigating novel nanostructured materials based SAW and conductometric for gas sensing applications. To accomplish this, the author developed and deposited nanostructured materials onto the whole area of SAW and conductometric transducers. The structures developed by the author were shown to exhibit excellent static and dynamic performance towards H_2 concentrations below 1% in synthetic air.

The gas sensing performance of the investigated SAW and conductometric structures were achieved by depositing the nanostructured polyaniline and its composites, PVP and its composites, graphene and Sb_2O_3 onto the fabricated transducers to develop novel sensors. The characterizations of such nanostructured materials were performed using SEM, AFM, XRD, EDX, Raman spectroscopy and XPS techniques. Via these techniques, surface morphologies and crystallinity as well as chemical bonds of the deposited materials were obtained. The next stage of these research was dedicated to expose the developed sensors to different concentrations of H_2, NO_2 and CO gases. From these measurements, sensors' static and dynamic parameters such as sensitivity, baseline stability, response and recovery time as well as optimum operating temperatures were obtained. In addition to that, the author also studied and determined the gas interaction mechanism of the developed sensors.

This thesis presented the evolution of the author's research, which can be summarised by the following points:

1. Synthesis and deposition of the nanostructured materials; electropolymerization of polyaniline and polyaniline nanocomposites, electrospinning of

PVP and PVP composites, formation of chemically reduced graphene, and thermal evaporation of Sb_2O_3.

2. Fabrication of the nanostructured materials based 36° YX $LiTaO_3$, 64° YX $LiNbO_3$ SAW and LGS conductometric structures.
3. Charaterization of the deposited nanostructured materials.
4. Electrical characterization of the above mentioned SAW and conductometric structures towards target gases.

In the following sections, the author will present a summary of the major findings of this research program and present her recommendations for future research.

8.1 Conclusions

The author successfully fulfilled research objectives by developing novel nanostructured material/SAW and nanostructured material based conductometric gas sensors. Consequently, this research has resulted in a number of significant contributions to the field of nanostructured conducting polymer, non-conducting polymer, graphene and semiconductive metal oxide based sensors. From these accomplishments, the author summarized and listed the outcomes and contributions.

1. Polyaniline Based SAW and Conductometric Gas Sensors

To the best of author's knowledge, this was the first novel study of dedoped polyaniline nanofibers based $LiTaO_3$ SAW sensors for gas sensing applications. This study provides valuable insight for other researchers to investigate the effect of varying the electropolymerization parameters to find the optimum deposition conditions for gas sensing applications. The author also successfully deposited dedoped polyaniline/MWNTs nanofibers and CSA doped polyaniline/diamond nanocomposite based SAW sensors. From the obtained results, it was observed that CSA doped polyaniline/diamond nanocomposite based SAW sensors showed a superior performance in comparison with other polyaniline based SAW sensors. The outcomes from the investigation of polyaniline nanofibers based SAW sensors are as follows:

- To the best of author's knowledge, novel dedoped polyaniline nanofibers based SAW sensors were successfully fabricated for the first time. Via electropolymerization, the average thickness of the polyaniline nanofibers in the range of 40-50 nm were obtained. It was found that no morphology change occurs on polyaniline nanofibers before and after dedoping with a base. The measured response was approximately 9.46 kHz towards 1% H_2 for dedoped polyaniline sensor. The highest sensitivity was observed at room temperature for H_2 with response time of 12 s for this sensor.

- The deposition time of the electropolymerization were varied to obtain different thicknesses of polyaniline nanofibers thin films. The results show that for dedoped polyaniline nanofibers, the frequency shift increases as the thickness increases for the H_2 concentration below 0.5%. Dedoped polyaniline nanofibers based SAW sensors with a thin film thickness of $\sim$3.5 μm exhibited the largest frequency shift for 1% H_2. Thick films of porous polyaniline nanofibers provides more surface for H_2 adsorbtion than the other thin films so the diffusion of the analyte gas is faster. Hence the response time of thick films were smaller than their thinner counterparts towards high H_2 concentrations.

- The concentrations of HCl acid in electrolyte were varied between 0.1M to 1.5M. To the best of author's knowledge, this has been the first time the effect of acid concentrations towards gas sensing performance was investigated. The SEM images were observed to investigate different density and uniformity which may affect the gas sensing performance. The electrical characterization showed that dedoped polyaniline nanofibers based SAW sensors, electropolymerized in acid concentration lower than 0.5M did not respond to any gas. Dedoped polyaniline nanofibers based SAW sensor electropolymerized in 1.0M HCl exhibited a more stable baseline than 0.5M and 1.0M HCl devices, with frequency shift of 19.98 kHz.

- 1.0M HNO_3 was used in electrolyte for electropolymerization polyaniline nanofibers, replacing 1.0M HCl. The average thickness of HNO_3 doped polyaniline nanofibers was in the range of 30-50 nm. The measured sensor response of dedoped polyaniline nanofibers (deposited in HNO_3) based SAW sensor was 5.168 kHz. It was observed that the frequency shift was $\sim$4 times less than that of deposited in HCl electrolyte. Upon the exposure

to 1% H_2 gas, the response time for this sensor was 20 s, which was slightly higher than for the HCl polyaniline nanofibers based SAW sensors.

- The gas sensing results of electropolymerized doped and dedoped based conductometric sensors towards H_2 gas showed that conductivity change also occurs in SAW device response mechanism. The dynamic response showed that doped polyaniline based conductometric sensors exhibited better baseline stability than that of dedoped polyaniline. However, dedoped polyaniline nanofibers based conductometric sensors showed higher sensitivity than the doped counterparts.

- Dedoped polyaniline/MWNTs nanocomposite was deposited onto the IDTs of SAW devices using electropolymerization method. To the best of author's knowledge, this is the first time dedoped polyaniline/MWNTs nanocomposite based SAW sensors were investigated and applied for gas sensing. The SEM images showed more compact and denser morphology than that of electropolymerized polyaniline nanofibers. The measured sensor response of dedoped polyaniline/MWNTs nanofibers based SAW sensor was approximately 4.3 kHz towards 1% H_2 gas at room temperature. The 90% response and recovery time of 28 and 240 s were observed towards 1% and 0.25% H_2 gas concentrations, respectively.

- To the best of author's knowledge, for the first time the CSA doped polyaniline/diamond nanocomposite based SAW gas sensor has been investigated. Via chemical polymerization, polyaniline and diamond nanocomposite formed nanofibers and clusters of coral-like structures, respectively. Upon exposure to 1% H_2 gas, the frequency change of larger than 750 kHz was observed. Fast response and recovery of 16 and 180 s towards 1% and 0.06% H_2 gas concentrations at room temperature were observed.

2. PVP Based SAW Gas Sensors

To the best of author's knowledge, this is the first investigation of PVP fibres based SAW gas sensors. Via electrospinning, PVP fibres and its composites were deposited on $LiTaO_3$ SAW transducers and exposed to different H_2 gas concentrations. The author also studied the variation of several parameters during electrospinning, which will provide valuable insight for future research

in gas sensing applications. The outcomes from the investigation of PVP based SAW sensors are as follows:

- Novel PVP fibres based $LiTaO_3$ SAW sensors were successfully deposited. By exposing the sensor surface to H_2, the measured sensor response for 48% concentration of PVP was 13.06 kHz at room temperature. The 90% response and recovery time were 12 and 61 s towards 1% and 0.06% H_2 gas concentrations.

- The distribution of the electrospun PVP was investigated by varying the collection distances between 5.5 to 11.5 cm. For the 58% PVP concentration, the shortest distance revealed that the denser morphology of fibres had the highest deposition rate than that of the other distances. The density of fibres decreased as the distance increased. A similar impact also occured for other PVP concentrations. However for closer collection distances, the electrospun of 42% PVP could not be evaporated thoroughly before reaching the target, therefore the collected particles re-dissolved and conglutinated.

- The PVP concentrations were varied from 48% to 58% to obtain different morphologies of the electrospun PVP and investigated their effect for gas sensing. Using SEM, three different morphologies were observed which were particles, beads and fibres. The devices with 48% PVP showed the largest frequency shift upon exposure to H_2 gas. This probably attributed to the high surface to volume ratio of the electrospun particles of 48% PVP. Whereas the devices that were coated with beads and fibres of 52% PVP gave the smallest frequency shift. However, this 52% PVP device showed the fastest response and recovery for the adsorption and desorption of H_2 gas compared to the other devices.

- Electrospin coated PVP in the presence of polyaniline (emeraldine salt and emeraldine base states) and MWNTs (composite with 1.025 and 1.525 g of PVP) were employed to synthesize the PVP composite. For PVP/polyaniline based $LiTaO_3$ SAW sensors, it was observed that PVP/polyaniline (EB) sensor exhibited higher sensitivity than that of PVP/polyaniline (ES). However, this device was unable to measure H_2 concentrations lower than 0.25%. Whereas, PVP/polyaniline (ES) sensor showed good baseline

stability and able to measure H_2 gas concentration as low as 0.06%. For the PVP/MWNTs based $LiTaO_3$ SAW sensor, it was observed that the device with a lower concentration of PVP had the frequency shift of 11.322 kHz which was larger than that of higher concentration of PVP. The change in resonant frequency probably caused by the change in both mass and conductivity of the composite materials. These subsequently decreased the acoustic wave velocity, thereby decreased the resonant frequency.

3. Graphene Based SAW Gas Sensors

- To the best of author's knowledge, graphene-like nanosheets/$LiTaO_3$ SAW gas sensors were investigated for the first time. At first the graphite oxide was spin coated on the SAW transducer. Then, the coated SAW transducer was exposed to hydrazine vapor to reduce the GO to graphene. The sensors were then exposed to different concentrations of H_2, NO_2 and CO gases. The highest sensitivities of the these devices were observed at room temperature for NO_2 and 40 °C for H_2 and CO with frequency shift of 18.7, 5.8, and 8.5 kHz towards 8.5ppm NO_2, 1% H_2 and 1000ppm CO, respectively.

4. Sb_xO_y Based Conductometric Gas Sensors

- To the best of author's knowledge, nanostructured Sb_xO_y based LGS conductometric sensors were developed for the first time by the author. In this research, Sb_xO_y non-homogenous nanostructures and nanorods were successfully synthesized by the thermal evaporation technique. The morphologies of the prepared 1-D nanoscale structures were characterized using SEM, XRD and EDX. Nanorods with diameters of 30 – 50 nm and length up to 750 nm were observed. Meanwhile, 150 – 200 nm in width, height of 50 – 140 nm and the length of up to 300 nm for the non-homogenous nanostructures were found as a result of the deposition. With the assistance of a catalyst, the formation of these 1-D Sb_xO_y structures were according to vapor-liquid-solid growth mechanism. From the experiments, it was concluded that LGS is a well-suited substrate to grow these nano-sized structures. Moreover, the substrate's location in the furnace and the deposition temperature were found to affect the structures density. This device was successfully used as H_2 gas sensor showing the fastest response

at an operating temperature of 291 °C. The highest sensitivity for this device was 5.21.

8.2 Future Works

Throughout the course of this research, several areas of interest, which have tremendous research potential have been identified by the author. These areas of interest can be divided as follows:

1. Polyaniline Based Gas Sensors

    - In this research, the author has deposited polyaniline/MWNTs on SAW transducers with a very low concentration of MWNTs. It was observed that the gas sensing performance of polyaniline/MWNTs based SAW sensors was not much different from that of polyaniline based SAW sensors. This was supported by the Raman spectra which showed that polyaniline was the dominant material in this composite. The author believes that adding higher concentrations of MWNTs (>10%), can improve the polyaniline gas sensing performance.
    - The investigation on electropolymerization of other conducting polymers (eg: polypyrrole and polythiophene): the author believes that by varying the electropolymerization parameters and investigating their effect for gas sensing performance can help in obtaining the desired parameters for the highest sensitivity for polymers other than polyaniline.

2. PVP Based Gas Sensors

    - The investigation of nanostructured PVP with electrospinning method, which can result in sensitive layers with high porosity and surface area.
    - The further investigation of the PVP/inorganic materials composites. For example, the composite of PVP with metal oxides such as SnO and In_2O_3 may improve the gas sensing performance.

3. Graphene Based Gas Sensors

   - The investigation of single layered graphene and graphene/inorganic material composites as sensing layers deposited on SAW transducers. In this research, the investigation towards graphene-like have shown promising results for sensing H_2, NO_2 and CO gases. Therefore, the author believes that single layered graphene can show excellent gas sensing performance.

4. Sb_2O_3 Based Gas Sensors

   - The investigation of nanostructured Sb_2O_3 which are doped with other materials which may improve the dissociation of H_2 gas; therefore, increasing the sensitivity, response and recovery of the films towards H_2 gas.

It is the author's opinion that if the nanostructured materials based SAW and conductometric sensors which are presented in this thesis are further optimised, their gas sensing will be improved which make them highly suitable for commercialisation purposes.

Appendix A

List of Author's Publications

A.1 Refereed Manuscripts

1. **R. Arsat**, J. Tan, W. Wlodarski and K. Kalantar-zadeh, " Hydrogen gas sensor based on Sb_xO_y nanostructures with a langasite substrate," *Sensor Letters*, 4, pp. 419-425, 2006.

2. **R. Arsat**, J. Tan, A. Z. Sadek, K. Shin, D. S. Ahn, C. S. Yoon, K. Kalantar-zadeh and W. Wlodarski, "Camphor sulfonic acid doped polyaniline/diamond nanofibers based ZnO/64° YX $LiNbO_3$ surface acoustic wave H_2 gas sensor," *Sensor Letters, Selected papers from the 7th East Asian Conference on Chemical Sensors (EACCS '07)*, 6, pp. 1-4, 2008

3. **R. Arsat**, M. Breedon, M. Shafiei, P. G Spizziri, K. Kalantar-zadeh, S. Gilje, R. B. Kaner and W. Wlodarski, "Graphene-like Nano-Sheets for Surface Acoustic Wave Gas Sensor Applications," *Chemical Physics Letter*, 467, pp. 344-347, 2009.

4. **R. Arsat**, X. F. Yu, Y. X. Li, W. Wlodarski and K. Kalantar-zadeh, "Hydrogen Gas Sensor Based on Highly Ordered Polyaniline Nanofibers," *Sensors and Actuators B: Chemical, Selected papers from The 12th International Meeting on Chemical Sensors Conference*, 137, pp. 529-532, 2009

A.2 Conference Papers

1. H. Qasim, A. Z. Sadek, **R. Arsat**, W. Wlodarski, I. Belski, R. B. Kaner and K. Kalantar-zadeh, "Optical and conductivity dependence on doping concentrations of polyaniline nanofibers," in *Proc. Device and Process Technologies for Microelectronics, MEMS, Photonics, and Nanotechnology*, SPIE, Canberra, Australia, 6800, pp. 680012, 2007.

2. **R. Arsat**, X. F Yu, Y. X. Li, K. Kalantar-zadeh and W. Wlodarski, "Hydrogen gas sensor based on highly ordered polyaniline nanofibers," in *The 12th International Meeting on Chemical Sensors (IMCS),* Ohio, USA 2008.

3. **R. Arsat**, M. Breedon, M. Shafiei, K. Kalantar-zadeh, S. Gilje, R. B. Kaner and W. Wlodarski, "Graphene-like nano-sheets based $LiTaO_3$ surface acoustic wave NO_2 gas sensor," *Eurosensors XXII,* Dresden, Germany, pp. 1132-1135,.2008.

4. **R. Arsat**, M. Breedon, M. Shafiei, K. Kalantar-zadeh, S. Gilje, R. B. Kaner and W. Wlodarski, " Graphene-like nano-sheets/36 ° $LiTaO_3$ surface acoustic wave hydrogen gas sensor," *The Seventh IEEE Conference on Sensors (IEEE Sensors),* Lecce, Italy, pp. 188-191, 2008.

5. L. Al-Mashat, H. D. Tran, R. B. Kaner, **R. Arsat**, K. Kalantar-zadeh and W. Wlodarski, "A hydrogen gas sensor fabricated from plythiophene nanofibers deposited on a 36 YX LiTaO3 layered surface acoustic wave transducer," in *Proc. Device and Process Technologies for Microelectronics, MEMS, Photonics, and Nanotechnology*, SPIE, Melbourne, Australia, 72680M, 2008.

6. M. Shafiei, A. Z. Sadek, J. Yu, **R. Arsat**, K. Kalantar-zadeh, X. F. Yu, J. G. Patridge, W. Wlodarski, "Pt/anodized TiO2/SiC-based MOS device for hydrocarbon sensing," in *Proc. Device and Process Technologies for Microelectronics, MEMS, Photonics, and Nanotechnology*, SPIE, Melbourne, Australia, 72680K, 2008

7. M. Shafiei, J. Yu, **R. Arsat**, K. Kalantar-zadeh, E. Comini, M. Ferroni, G. Sberveglieri and W. Wlodarski, "Reverse biased Schottky contact hydrogen

sensors based on Pt/nanostructured/ZnO/SiC,"Proceeding of American Institute of Physics (ISOEN conference 2009), Brescia, Italy, pp. 353-356, 2009.

Bibliography

[1] T. Grandke and J. Hesse, "Introduction," in *Sensors, A comprehensive survey* (W. Gopel, J. Hesse, and J. N. Zemel, eds.), vol. 1, pp. 1–16, Weinheim, Germany: VCH Publisher, 1989.

[2] X.-J. Huang and Y.-K. Choi, "Chemical sensors based on nanostructured materials," *Sensors and Actuator B: Chemical*, vol. 122, pp. 659–671, 2007.

[3] H. Y. Dang, J. Wang, and S. S. Fan, "The synthesis of metal oxide nanowires by directly heating metal samples in appropriate oxygen atmospheres," *Nanotechnology*, vol. 14, pp. 738–741, 2003.

[4] I.-S. Park, S.-R. Jang, J. S. Hong, R. Vittal, and K.-J. Kim, "Preparation of composite anatase TiO_2 nanostructure by precipitation from hydrolyzed $TiCl_4$ solution using anodic alumina membrane," *Chemistry of Materials*, vol. 15, pp. 4633–4636, 2003.

[5] H. Qiu, Y.-F. Lu, and Z.-H. Mai, "Nanostructure formation on amorphous WO_3 thin films in air by scanning tunneling microscopy," *Japanese Journal of Applied Physics*, vol. 40, pp. 290–294, 2000.

[6] X. Yu, Y. Li, W. Ge, Q. Yang, N. Zhu, and K. Kalantar-zadeh, "Formation of nanoporous titanium oxide films on silicon substrates using an anodization process," *Nanotechnology*, vol. 17, pp. 808–814, 2006.

[7] A. Errachid, D. Caballero, E. Crespo, F. Bessueille, M. Pla-Roca, C. A. Mills, F. Teixidor, and J. Samitier, "Electropolymerization of nanodimensional polypyrrole micro-ring arrays on gold substrates prepared using submerged micro-contact printing," *Nanotechnology*, vol. 18, p. 485301, 2007.

[8] D. Li, A. Babel, S. A. Jenekhe, and Y. Xia, "Nanofibers of conjugated polymers prepared by electrospinning with two-capillary spinneret," *Advanced Materials*, vol. 16, no. 22, pp. 2062–2066, 2004.

[9] D. H. Reneker and I. Chun, "Nanometre diameter fibres of polymer, produced by electrospinning," *Nanotechnology*, vol. 7, pp. 216–223, 1996.

[10] S. Fan, M. G. Chapline, N. R. Franklin, T. W. Tombler, A. M. Cassell, and H. Dai, "Self-oriented regular arrays of carbon nanotubes and their field emission properties," *Science*, vol. 283, pp. 512–514, 1999.

[11] M. Zhang, S. Fang, A. A. Zakhidoz, S. B. Lee, A. E. Aliev, C. D. Williams, K. R. Atkinson, and R. H. Baughman, "Strong, transparent, multifunctional, carbon nanotube sheets," *Science*, vol. 309, pp. 1215–1219, 2005.

[12] J. Huang, S. Virgi, B. H. Weiller, and R. Kaner, "Nanostructured polyaniline sensors," *Chemistry - A European Journal*, vol. 10, pp. 1314–1319, 2004.

[13] L. F. Dong, Z. L. Cui, and Z. K. Zhang, "Gas sensing properties of nano-ZnO prepared by arc plasma method," *NanoStructured Material*, vol. 8, pp. 815–823, 1997.

[14] R. Afroz, M. N. Hassan, and N. A. Ibrahim, "Review of air pollution and health impacts in Malaysia," *Environmental Research*, vol. 92, no. 2, p. 7, 2003.

[15] N. Yamazoe and N. Miura, "New approaches in the design of gas sensors," in *Gas Sensors* (G. Sberveglieri, ed.), Netherlands: Kluwer Academic Publishers, 1992.

[16] C. M. Gosden, "The 1988 chemical weapon attack on Halabja, Iraq," in *Super Terrorism: Biological, Chemical and Nuclear* (Y. Alexander and M. Hoenig, eds.), Transnational Publishers, Inc., 2001.

[17] A. Trinchi, *Investigation of metal reactive insulator silicon carbide (MRISiC) devices and semiconducting metal oxide thin film for gas sensing applications*. PhD thesis, RMIT University, 2004.

[18] A. Mandelis and C. Christofides, *Physics, chemistry, and technology of solid state gas sensor devices*. New York : Wiley, 1993.

[19] L. C. Cadwallader and J. S. Herring, "Safety issues with hydrogen as a vehicle fuel," tech. rep., Idaho National Engineering and Environmental Laboratory, Lockheed Martin Idaho Technologies Company, 1999.

[20] M. Heisel, "Industrial gases in the chemical industry," tech. rep., Linde Gas Pte Ltd, 2008.

[21] G. Hunter, P. Neudeck, C. Liu, B. Ward, Q. Wu, P. Dutta, M. Frank, J. Trimbol, M. Fulkerson, B. Patton, D. Makel, and V. Thomas, "Development of chemical sensor arrays for harsh environments and aerospace applications," in *Sensors, 2002. Proceedings of IEEE*, vol. 2, pp. 1126–1133, 2002.

[22] *Nitrogen Oxides (nitric oxide, nitrogen dioxide, etc)*. US Department of Health and Human Services, Public Health Service, Agency for Toxic Substances and Disease Registry, 2002.

[23] *Basic information: Nitrogen dioxide (NO_2)*. US Environmental Protection Agency, 1997.

[24] L. Ferrari and J. Salisbury, "National environmental health forum monographs air series no. 3: Nitrogen dioxide," 1997.

[25] S. T. Omaye, "Metabolic modulation of carbon monoxide toxicity," *Toxicology*, vol. 180, no. 2, pp. 139–150, 2002.

[26] N. Cobb and R. Etzel, "Unintentional carbon monoxide-related deaths in the United States, 1979-1988," *Journal of the American Medical Association*, vol. 266, pp. 659–663, 1991.

[27] T. Meredith and A. Vale, "Carbon monoxide poisoning," *British Medical Journal*, vol. 296, pp. 77–78, 1988.

[28] J. A. Raub and V. A. Benignus, "Carbon monoxide and the nervous system," *Neuroscience and Biobehavioral Reviews*, vol. 26, no. 8, pp. 925–940, 2002.

[29] R. W. Kelsall, I. W. Hamley, and M. Geoghegan, eds., *Generic methodologies for nanotechnology: Classification and fabrication*. Nanoscale Science and Technology, John Wiley & Sons, Ltd, 2005.

[30] G. Gao, *Nanostructures and nanomaterials: Synthesis, properties and applications*. London, UK: Imperial College Press, 2004.

[31] A. Z. Sadek, *Investigation of nanostructured semiconducting metal oxide and conducting polymer thin films for gas sensing applications*. PhD thesis, RMIT University, 2008.

[32] A. S. Edelstein and R. C. Cammarata, *Nanomaterials: synthesis, properties, and applications*. Philadelphia: PA: Institute of Physics, 1996.

[33] K. Kalantar-zadeh and B. Fry, *Nanotechnology-enabled sensors*. Berlin Springer, 2007.

[34] G. Inzelt, M. Pineri, J. W. Schultze, and M. A. Vorotyntsev, "Electron and proton conducting polymers: recent developments and prospects," *Electrochimica Acta*, vol. 45, pp. 2403–2421, 2000.

[35] N. Agbor, M. Petty, and A. P. Monkman, "Polyaniline thin film for gas sensing," *Sensors and Actuators B: Chemical*, vol. 28, pp. 173–179, 1995.

[36] S. D. George, S. Saravanan, M. Anantharaman, S. Venkatachalam, P. Radhakrishnan, V. P. N. Nampoori, and C. P. G. Vallabhan, "Thermal characterization of doped polyaniline and its composites with CoPc," *Physical Review B*, vol. 69, p. 235201, 2004.

[37] X. Yu, Y. Li, N. Zhu, Q. Yang, and K. Kalantar-zadeh, "A polyaniline nanofibre electrode and its application in a self-powered photoelectrochromic cell," *Nanotechnology*, vol. 18, no. 1, 2007.

[38] J. Janata and Josowicz, "Conducting polymers in electronic chemical sensors," *Nature Materials*, vol. 2, pp. 19–24, 2003.

[39] K.-h. Li, D. C. Diaz, Y. He, J. C. Campbell, and C. Tsai, "Electroluminescence from porous silicon with conducting polymer film contacts," *Applied Physics Letters*, vol. 64, no. 18, p. 2394, 1994.

[40] S. Virgi, J. Huang, R. Kaner, and B. H. Weiller, "Polyaniline nanofibers gas sensors: Examination of response mechanisms," *Nano Letters*, vol. 4, pp. 491–496, 2004.

[41] U. Kang and K. D. Wise, "A high-speed capasitive humidity sensor with on-chip thermal reset," *IEEE Transactions on Electron Devices*, vol. 47, pp. 702–710, 2000.

[42] M. Yuqing, C. Jianrong, and W. Xiaohua, "Using electropolymerized non-conducting polymers to develop enzyme amperometric biosensors," *TRENDS in Biotechnology*, vol. 22, no. 5, pp. 227–231, 2004.

[43] Y. He, B. Zhu, and Y. Inoue, "Hydrogen bonds in polymer blends," *Progress in Polymer Science*, vol. 29, pp. 1021–1051, 2004.

[44] A. Mirmohseni and A. Oladegaragoze, "Construction of a sensor for determination of ammonia and aliphatic amines using polyvinylpyrrolidone coated quartz crystal microbalance," *Sensors and Actuator B: Chemical*, vol. 89, pp. 164–172, 2003.

[45] H. Tang, M. Yan, X. Ma, H. Zhang, M. Wang, and D. Yang, "Gas sensor behaviour of polyvinylpyrrolidone-modified ZnO nanoparticles for trimethylamine," *Sensors and Actuator B: Chemical*, vol. 113, no. 1, pp. 324–328, 2005.

[46] C. Srinivasan, "Graphene - Mother of all graphitic materials," *Current Science*, vol. 92, no. 10, pp. 1338–1339, 2007.

[47] H.-B. Lin and S. Jeng-Shong, "Fullerene C_{60}-cryptand coated surface acoustic wave quartz crystal sensor for organic vapors," *Sensors and Actuator B: Chemical*, vol. 92, pp. 243–254, 2003.

[48] Y. Gurbuz, W. P. Kang, J. L. Davidson, and D. V. Kerns, "Diamond microelectronic gas sensor for detection of benzene and toluene," *Sensors and Actuator B: Chemical*, vol. 99, pp. 207–215, 2004.

[49] Y. M. Wong, W. Kang, J. Davidson, A. Wisitsora-at, and K. L. Soh, "A novel microelectronic gas sensor utilizing carbon nanotubes for hydrogen gas detection," *Sensors and Actuator B: Chemical*, vol. 93, pp. 327–332, 2003.

[50] K. S. Novoselov, A. K. Geim, S. V. Morozov, D. Jiang, Y. Zhang, S. V. Dubonos, I. V. Grigorieva, and A. A. Firsov, "Electric field effect in atomically thin carbon films," *Science*, vol. 306, pp. 666–669, 2004.

[51] T. Zhang, S. Mubeen, N. V. Myung, and M. A. Deshusses, "Recent progress in carbon nanotube-based gas sensors," *Nanotechnology*, vol. 19, p. 332001, 2008.

[52] G. Mansoori, *Principles of Nanotechnology: Molecular-Based Study of Condensed Matter in Small Systems.* USA: World Scientific Publishing Co. Pte. Ltd, 2005.

[53] D. K. Ashwal and S. K. Gupta, *Science and technology of chemiresistor gas sensors.* New York: Nova Publishers, 2006.

[54] A. G. MacDiarmid, J.-C. Chiang, W. Huang, B. D. Humphrey, and N. L. D. Somasiri, "Polyaniline: Protonic acid doping to the metallic regime," *Molecular Crystals and Liquid Crystals*, vol. 125, pp. 309–318, 1985.

[55] A. Baba, S. Tian, F. Stefani, C. Xia, Z. Wang, R. C. Advincula, D. Johannsman, and W. Knoll, "Electropolymerization and doping/dedoping properties of polyaniline thin films as studied by electrochemical-surface plasmon spectroscopy and by the quartz crystal microbalance," *Journal of Electroanalytical Chemistry*, vol. 562, pp. 95–103, 2004.

[56] G. G. Wallace, G. M. Spinks, and P. R. Teasdale, *Conductive Electroactive Polymers: Intelligent Materials Systems.* Pennsyvania, USA: Technomic Publishing Company, Inc, 1997.

[57] D. Dutta, T. K. Sarma, D. Chowdhury, and A. Chattopadhyay, "A polyaniline-containing filter paper that acts as a sensor, acid, base and endpoint indicator and also filters acids and bases," *Journal of Colloid and Interface Science*, vol. 283, pp. 153–159, 2005.

[58] D. Li, Y. Jiang, Z. Wu, X. Chen, and Y. Li, "Self-assembly of polyaniline ultrathin films based on doping-induced deposition effect and applications for chemical sensors," *Sensors and Actuator B: Chemical*, vol. 66, pp. 125–127, 2000.

[59] D. Xie, Y. Jiang, W. Pan, D. Li, Z. Wu, and Y. Li, "Fabrication and characterization of polyaniline-based gas sensor by ultra-thin film technology," *Sensors and Actuator B: Chemical*, vol. 81, pp. 158–164, 2002.

[60] A. G. Shrivas, R. G. Bavane, and A. M. Mahajan, "Electronic nose: A toxic gas sensor by polyaniline thin film conducting polymer," in *XIV International Workshop on the Physics of Semiconductor Devices (IWPSD) 2007*, (Mumbai), pp. 621–623, 2007.

[61] A. Z. Sadek, W. Wlodarski, K. Shin, R. Kaner, and K. Kalantar-zadeh, "A room temperature polyaniline/SnO_2 nanofibers composite based layered ZnO/64^o YX $LiNbO_3$ SAW hydrogen gas sensor," in *Conf. on Optoelectronic and Microelectronic Materials and Devices (COMMAD)*, pp. 208–211, 2006.

[62] D. Aussawasathien, J.-H. Dong, and L. Dai, "Electrospun polymer nanofiber sensors," *Synthetic Metals*, vol. 154, pp. 37–40, 2005.

[63] E. T. Kang, Z. F. Li, K. G. Neoh, Y. Q. Dong, and K. L. Tan, "Protonation and deprotonation of polyaniline films and powders: Effects of acid and base concentrations on the surface intrinsic oxidation states," *Synthetic Metals*, vol. 92, pp. 167–171, 1998.

[64] J. Huang, "Syntheses and applications of conducting polymer polyaniline nanofibers," *Pure and Applied Chemistry*, vol. 28, no. 1, pp. 15–27, 2006.

[65] C. Conn, S. Sestak, A. T. Baker, and J. Unsworth, "A polyaniline-based selective hydrogen sensor," *Electroanalysis*, vol. 10, no. 16, pp. 1137–1141, 1998.

[66] A. Sadek, K. Kalantar-Zadeh, W. Wlodarski, C. Baker, and R. Kaner, "PSSA doped polyaniline nanofiber based ZnO/64^o YX $LiNbO_3$ SAW H_2 gas sensor," in *Nanoscience and Nanotechnology, 2006. ICONN '06. International Conference on*, (Brisbane, Australia), pp. 717–720, 2006.

[67] A. Sadek, W. Wlodarski, K. Kalantar-Zadeh, C. Baker, and R. Kaner, "Doped and dedoped polyaniline nanofiber based conductometric hydrogen gas sensors," *Sensors and Actuators A: Physical Selected Papers From the Asia-Pacific Conference of Transducers and Micro-Nano Technology*

(APCOT 2006), Asia-Pacific Conference of Transducers and Micro-Nano technology, vol. 139, no. 1-2, pp. 53–57, 2007.

[68] A. Sadek, A. Trinchi, W. Wlodarski, K. Kalantar-zadeh, K. Galatsis, C. Baker, and R. Kaner, "A room temperature polyaniline nanofiber hydrogen gas sensor," in *Sensors, 2005 IEEE*, (Irvine, California, US), pp. 207–210, 2005.

[69] A. Z. Sadek, C. O. Baker, D. A. Powell, W. Wlodarski, R. Kaner, and K. Kalantar-zadeh, "Polyaniline nanofiber based Surface Acoustic Wave gas sensors - effect of nanofiber diameter on H_2 response," *Sensors Journal, IEEE*, vol. 7, no. 2, pp. 213–218, 2007.

[70] D.-J. Yao and Y.-R. Yang, "Bio-chemical sensor using polyaniline nanofibers for sensing amino-group type of gas," in *2005 IEEE International Conference on Robotics and Biomimetics*, (Hong Kong), pp. 763–767, 2005.

[71] W. Wlodarski, A. Z. Sadek, C. Baker, K. Kalantar-zadeh, R. Kaner, and D. Mulcahy, "Camphor sulfonic acid doped polyaniline nanofiber based 64^o YX $LiNbO_3$ SAW hydrogen gas sensor," in *SPIE Smart Materials, Nano & Micro-Smart Systems Proceeding* (S. F. Al-Sarawi, ed.), vol. 6414, (Adelaide, Australia), p. 64141Q, 2007.

[72] Y.-T. Shen, C.-L. Huang, and L. Wu, "Using shear horizontal Surface Acoustic Wave with polyaniline film as ammonia sensor," *Japanese Journal of Applied Physics*, vol. 44, no. 4A, pp. 1844–1846, 2005.

[73] J. Huang and R. B. Kaner, "A general chemical route to polyaniline nanofibers," *Journal of American Chemical Society*, vol. 126, pp. 851–855, 2004.

[74] S. Sadki, P. Schottland, N. Brodie, and G. Sabouraud, "The mechanisms of pyrrole electropolymerization," *Chemical Society Reviews*, vol. 29, pp. 283–293, 2000.

[75] K. Kalantar-zadeh, A. Z. Sadek, W. Wlodarski, Y. Li, and X. Yu, "SAW hydrogen sensor with electropolymerized polyaniline nanofibers," in *International Frequency Control Symposium and Exposition, 2006 IEEE*, (Mi-

ami, Florida, US), pp. 428–431, Institute of Electrical and Electronics Engineers, 2006.

[76] C.-Y. Shen, C.-L. Hsu, and D.-L. Wang, "Shear horizontal surface Acoustic Wave Sensors based on polyaniline for ammonia gas sensing," in *7th Int. Conf. on Thermal, Mechanical and Multiphysics Simulation and Experiments in Micro-Electronics and Micro-systems (EuroSimE-2006)*, (Italy), p. 3, 2006.

[77] A. Z. Sadek, W. Wlodarski, K. Shin, R. Kaner, and K. Kalantar-zadeh, "A layered surface acoustic wave gas sensor based on a polyaniline/In_2O_3 nanofibre composite," *Nanotechnology*, vol. 17, pp. 4488–4492, 2006.

[78] A. Z. Sadek, W. Wlodarski, K. Shin, R. Kaner, and K. Kalantar-zadeh, "A polyaniline/WO_3 nanofiber composite-based ZnO/64^o YX $LiNbO_3$ SAW hydrogen gas sensor," *Synthetic Metals*, vol. 158, pp. 29–32, 2008.

[79] L. Geng, Y. Zhao, X. Huang, S. Wang, S. Zhang, and S. Wu, "Characterization and gas sensitivity study of polyaniline/SnO_2 hybrid material prepared by hydrothermal route," *Sensors and Actuator B: Chemical*, vol. 120, pp. 568–572, 2007.

[80] M. K. Ram, O. Yavuz, V. Lahsangah, and M. Aldissi, "CO gas sensing from ultrathin nano-composite conducting polymer film," *Sensors and Actuators B: Chemical*, vol. 106, no. 2, pp. 750–757, 2005.

[81] S.-J. Su and N. Kuramoto, "Processable polyaniline-titanium dioxide nanocomposites: Effect of the titanium dioxide on the conductivity," *Synthetic Metals*, vol. 114, pp. 147–153, 2000.

[82] H. Tai, Y. Jiang, G. Xie, J. Yu, and X. Chen, "Fabrication and gas sensitivity of polyaniline-titanium dioxide nanocomposite thin film," *Sensors and Actuators B: Chemical*, vol. 125, no. 2, pp. 644–650, 2007.

[83] X. Ma, X. Zhang, Y. Li, G. Li, M. Wang, H. Chen, and Y. Mi, "Preparation of nano-structured polyaniline composite film via 'carbon nanotubes seeding' approach and its gas-response studies," *Macromolecular Materials and Engineering*, vol. 291, no. 1, pp. 75–82, 2006.

[84] Y. Wanna, S. Pratontep, A. Wisitsoraat, and A. Tuarantranont, "Developement of nanofibers composite polyaniline/CNT fabricated by electro spinning technique for co gas sensor.," in *IEEE Sensors*, (Daegu , Korea), pp. 342–345, 2006.

[85] Y. Wanna, N. Srisukhumbowornchai, A. Tuantranont, A. Wisitsoraat, N. Thavarungkul, and P. Singjai, "The effect of carbon nanotube dispersion on co gas sensing characteristics of polyaniline gas sensor.," *Journal of Nanoscience and Nanotechnology*, vol. 6, pp. 1–4, 2006.

[86] Q. Chang, K. Zhao, X. Chen, M. Li, and J. Liu, "Preparation of gold/polyaniline/multiwall carbon nanotube nanocomposites and application in ammonia gas detection.," *Journal of Material Science*, vol. 43, pp. 5861–5866, 2008.

[87] R. Sainz, A. M. Benito, M. T. Martinez, J. F. Galindo, J. Sotres, A. M. Baro, B. Corraze, O. Chauvet, A. B. Dalton, R. H. Baughman, and W. K. Maser, "A soluble and highly functional polyaniline-carbon nanotube composite," *Nanotechnology*, vol. 16, pp. S150–S154, 2005.

[88] D.-j. Guo and H.-l. Li, "Well-dispersed multi-walled carbon nanotube/polyaniline composite films," *Journal of Solid State Electrochemistry*, vol. 9, pp. 445–449, 2005.

[89] J.-E. Huang, X.-H. Li, J.-C. Xu, and H.-L. Li, "Well-dispersed single-walled carbon nanotube/polyaniline composite films," *Carbon*, vol. 41, no. 14, pp. 2731–2736, 2003.

[90] A. Denisenko, A. Aleksov, and E. Kohn, "PH sensing by surface-doped diamond and effect of the diamond surface termination," *Diamond and Related Materials*, vol. 10, pp. 667–672, 2001.

[91] T. Shibata, Y. Kitamoto, K. Unno, and E. Makino, "Micromachining of diamond film for MEMS applications," *Journal of Microelectromechanical Systems*, vol. 9, no. 1, pp. 47–51, 2000.

[92] Y. Gurbuz, W. P. Kang, J. Davidson, D. L. Kinser, and D. Kerns, "Diamond microelectronic gas sensors," in *The 8th International Conference*

on Solid-State Sensors and Actuators, and Eurosensors IX, (Stockholm, Sweden), pp. 745–748, 1995.

[93] Y. Gurbuz, W. P. Kang, J. L. Davidson, and D. V. Kerns, "Current conduction mechanism and gas adsorption effects on device parameters of the Pt/SnO_x/Diamond gas sensor," *IEEE Transactions on Electron Devices*, vol. 46, no. 5, pp. 914–920, 1999.

[94] F. Haaf, A. Sanner, and F. Straub, "Polymer of N-Vynilpyrrolidone: Synthesis, characterization and uses," *Polymer Journal*, vol. 17, no. 1, pp. 143–152, 1985.

[95] M. Sastry, V. Patil, K. S. Mayya, D. V. Paranjape, P. Singh, and S. R. Sainkar, "Organization of polymer-capped platinum colloidal particles at the air-water interface," *Thin Solid Films*, vol. 324, pp. 239–244, 1998.

[96] Y. Zhang and J. Lu, "A mild and efficient biomimetic synthesis of rodlike hydroxyapatite particles with a high aspect ratio using polyvinylpyrrolidone as capping agent," *Crystal Growth and Design*, vol. 8, no. 7, pp. 2101–2107, 2008.

[97] T. Tsuji, D.-H. Thang, Y. Okazaki, M. Nakanishi, Y. Tsuboi, and M. Tsuji, "Preparation on silver nanoparticles by laser ablation in polyvinylpyrrolidone solutions," *Applied Surface Science*, vol. 254, pp. 5224–5230, 2008.

[98] Z. Wang, J. Liu, T. Ren, and L. Liu, "Fabrication of organic PVP doping-based $Ba_{0.5}Sr_0.5TiO_3$ thick films on silicon substrates for MEMs applications," *Sensors and Actuators A: Physical*, vol. 117, pp. 293–300, 2005.

[99] C. Lu, S. S. Dimov, and R. H. Lipson, "Poly(vinyl pyrrolidone) - assisted sol-gel deposition of quality b-barium borate thin films for photonic applications," *Chemistry of Materials*, vol. 19, pp. 5018–5022, 2007.

[100] T.-C. Wei, C.-C. Wan, Y.-y. Wang, C.-m. Chen, and H.-s. Shiu, "Immobolization of poly(N-vinyl-2-pyrrolidone)-capped platinum nanoclusters on indium-tin oxide glass and its application in dye-sensitized solar cells," *Journal of Physical Chemistry C*, vol. 111, pp. 4847–4853, 2007.

[101] M. Tsuji, P. Jiang, S. Hikino, S. Lim, R. Yano, S.-M. Jang, S.-H. Yoon, N. Ishigami, X. Tang, and K. S. Nor Kamarudding, "Toward

to branched platinum nanoparticles by polyol reduction: A role of poly(vinylpyrrolidone) molecules," *Colloids and Surfaces A: Physicochem. Eng. Aspects*, vol. 317, pp. 23–31, 2008.

[102] J. Zhang, H. Liu, Z. Wang, and N. Ming, "Au-induced polyvinylpyrrolidone aggregates with bound water for the highly shape-selective synthesis of silica nanostructures," *Chemistry - A European Journal*, vol. 14, pp. 4374–4380, 2008.

[103] X. Du and J. He, "Facile size-controllable syntheses of highly monodisperse polystyrene nano- and microspheres by polyvinylpyrrolidone-mediatiated emulsifier-free emulsion polymerization," *Journal of Applied Polymer Science*, vol. 108, pp. 1755–1760, 2008.

[104] J. Lee, J. U. Ha, S. Choe, C.-S. Lee, and S. E. Shim, "Synthesis of highly monodisperse polystyrene microspheres via diapersion polymerization using an amphoteric initiator," *Journal of Colloid and Interface Science*, vol. 289, no. 2, pp. 663–671, 2006.

[105] A. J. Paine, W. Luymes, and J. McNulty, "Dispersion polymerization of styrene in polar solvents 6: Influence of reaction parameters on particle size and molecular weight in poly(n-vinylpyrrolidone)-stabilized reactions," *Macromolecules*, vol. 23, pp. 3104–3109, 1990.

[106] T. Du, H. Song, and O. J. Ilegbusi, "Sol-gel derived ZnO/PVP nanocomposite thin film for superoxide radical sensor," *Materials Science and Engineering C*, vol. 27, pp. 414–420, 2007.

[107] A. A. A. De Queiroz, D. A. W. Soares, P. Trzesniak, and G. A. Abraham, "Resistive-type humidity sensors based on $PVP - Co$ and PVP-I_2 complexes," *Journal of Polymer Science: Part B: Polymer Physics*, vol. 39, pp. 459–469, 2001.

[108] M. Yang, Y. Li, X. Zhan, and M. Ling, "A novel resistive-type humidity sensor based on poly(p-diethynylbenzene)," *Journal of Applied Polymer Science*, vol. 74, pp. 2010–2015, 1999.

[109] T. Iwaki, J. Covington, and J. W. Gardner, "Identification of vapours using carbon black/polymer composite sensor and a novel modulation

technique," in *IEEE Sensors 2007 Conference*, (Atlanta, Georgia, US), pp. 1229–1232, IEEE Computer Society, 2007.

[110] K. S. Novoselov, "Graphene: Mind the gap," *Nature Materials*, vol. 6, pp. 720–721, 2007.

[111] E. H. Hwang, S. Adam, S. Das Sarma, and A. K. Geim, "Transport in chemically doped graphene in the presence of adsorbed molecules," *Physical Review B*, vol. 79, no. 19, p. 195421, 2007.

[112] K. S. Novoselov, Z. Jiang, Y. Zhang, S. V. Morozov, H. L. Stormer, U. Zeitler, J. C. Maan, G. S. Boebinger, P. Kim, and A. K. Geim, "Room-temperature quantum hall effect in graphene," *Science*, vol. 315, p. 1379, 2007.

[113] K. S. Subrahmanyam, S. R. C. Vivekchand, A. Govindaraj, and C. N. R. Rao, "A study of graphenes prepared by different methods: characterization, properties and solubilization," *Journal of Material Chemistry*, vol. 18, pp. 1517–1523, 2008.

[114] P. Joshi, A. Gupta, P. C. Eklund, and S. A. Tadigadapa, "On the possibility of a graphene based chemical sensors," in *The 14th International Conference on Solid-State Sensors, Actuators and Microsystems*, (Lyon ,France), pp. 2325–2328, IEEE, 2007.

[115] F. Schedin, A. K. Geim, S. V. Morozov, E. W. Hill, P. Blake, M. I. Katsnelson, and K. S. Novoselov, "Detection of individual gas molecules adsorbed on graphene," *Nature Materials*, vol. 6, pp. 652–655, 2007.

[116] D. W. Zeng, C. S. Xie, B. L. Zhu, and W. L. Song, "Characteristics of Sb_2O_3 nanoparticles synthesized from antimony by vapor condensation method," *Materials Letters*, vol. 58, no. 3-4, pp. 312–315, 2004.

[117] C. Ye, G. Meng, L. Zhang, G. Wang, and Y. Wang, "A facile vapor-solid synthetic route to Sb_2O_3 fibrils and tubules," *Chemical Physics Letters*, vol. 363, no. 1-2, pp. 34–38, 2002.

[118] C. Ye, G. Wang, M. Kong, and L. Zhang, "Controlled synthesis of Sb_2O_3 nanoparticles, nanowires, and nanoribbons," *Journal of Nanomaterials*, vol. 2006, pp. 1–5, 2006.

[119] Y. Liu, Y. Zhang, M. Zhang, W. Zhang, Y. Qian, L. Yang, C. Wang, and Z. Chen, "Preparation of nanocrystalline antimony oxide powders by use of [gamma]-ray radiation – oxidization route," *Materials Science and Engineering B*, vol. 49, no. 1, pp. 42–45, 1997.

[120] L. Guo, Z. Wu, T. Liu, W. Wang, and H. Zhu, "Synthesis of novel Sb_2O_3 and Sb_2O_5 nanorods," *Chemical Physics Letters*, vol. 318, no. 1-3, pp. 49–52, 2000.

[121] Z. Zhang, L. Guo, and W. Wang, "Synthesis and characterisation of antimony oxide nanoparticles," *Journal of Material Research*, vol. 16, no. 3, pp. 803–805, 2001.

[122] A. Laachachi, M. Cochez, M. Ferriol, E. Leroy, J. M. Lopez Cuesta, and N. Oget, "Influence of Sb_2O_3 particles as filler on the thermal stability and flammability properties of poly(methyl methacrylate) (pmma)," *Polymer Degradation and Stability*, vol. 85, no. 1, pp. 641–646, 2004.

[123] Y. Zhang, G. Li, J. Zhang, and L. Zhang, "Shape-controlled growth of one-dimensional Sb_2O_3 nanomaterials," *Nanotechnology*, vol. 15, pp. 762–765, 2004.

[124] B. Pillep, P. Behrens, U.-A. Schubert, J. Spengler, and H. Knozinger, "Mechanical and thermal spreading of antimony oxides on the TiO_2 surface: Dispersion and properties of surface antimony oxide species," *Journal of Physic Chemical B*, vol. 103, pp. 9595–9603, 1999.

[125] Z. Deng, F. Tang, D. Chen, X. Meng, L. Cao, and B. Zou, "A simple solution route to single crystalline Sb_2O_3 nanowires with rectangular cross sections," *Journal of Physic Chemical B*, 2006.

[126] K. Ozawa, Y. Sakka, and M. Amano, "Preparation and electrical conductivity of three types of antimonic acid films," *Journal of Material Research*, vol. 13, no. 4, pp. 830–833, 1998.

[127] R. Binions, C. J. Carmalt, and I. P. Parkin, "Antimony oxide thin films from the atmospheric pressure chemical vapour deposition reaction of antimony pentachloride and ethyl acetate," *Polyhedron*, vol. 25, pp. 3032–3038, 2006.

[128] P. Haycock, G. Horley, K. Molloy, C. Myers, and S. Rushworth, "MOCVD of antimony oxide for gas sensor application," *Journal de Physique IV - Proceedings*, vol. 11, Part 3, pp. 1045–1050, 2001.

[129] C. Myers, P. Haycock, G. Horley, K. Molloy, S. Rushworth, and L. Smith, "Antimony oxide based gas sensors," in *Ceramic Engineering And Science Proceedings*, vol. 24, pp. 107–114, American Ceramic Society, 1998.

[130] S. Virgi, R. Kaner, and B. H. Weiller, "Hydrogen sensors based on conductivity changes in polyaniline nanofibers," *Journal of Physic Chemical B*, vol. 110, pp. 22266–22270, 2006.

[131] J. W. Grate, "Acoustic wave microsensor arrays for vapor sensing," *Chemical Review*, vol. 100, pp. 2627–2648, 2000.

[132] O. Leenaerts, B. Partoens, and F. M. Peeters, "Adsorption of H_2O, NH_3, CO, NO_2, and NO on graphene: A first-principles study," *Condensed Matter*, vol. 1, pp. 1757–1762, 2007.

[133] J. S. Arellano, L. M. Molina, A. Rubio, and J. A. Alonso, "Density functional study of adsorption of molecular hydrogen on graphene layers," *Journal of Chemical Physics*, vol. 112, no. 18, pp. 8114–8119, 2000.

[134] E. Comini, "Metal oxide nano-crystals for gas sensing," *Analytica Chimica Acta*, vol. 568, pp. 28–40, 2006.

[135] Y. Osada and D. E. De Rossi, *Polymer Sensors and Actuators*. Germany: Springer-Verlag Berlin Heidelberg, 2000.

[136] S. Brady, K. T. Lau, W. Megill, G. G. Wallace, and D. Diamond, "The development and characterisation of conducting polymeric-based sensing devices," *Synthetic Metals*, vol. 154, pp. 25–28, 2005.

[137] J. Reemts, J. Parisi, and D. Schlettwein, "Electrochemical growth of gas-sensitive polyaniline thin films across an insulating gap," *Thin Solid Films*, vol. 466, no. 1-2, pp. 320–325, 2004.

[138] D. Nicolas-Debarnot and F. Poncin-Epaillard, "Review: Polyaniline as a new sensitive layer for gas sensors," *Analytica Chimica Acta*, vol. 475, pp. 1–15, 2003.

[139] D. Zhang and Y. Wang, "Synthesis and applications of one-dimensional nanostructured polyaniline: An overview," *Materials Science and Engineering B*, vol. 134, pp. 9–19, 2006.

[140] T. Alizadeh and S. Zeynali, "Electronic nose based on the polymer coated saw sensors array for the warfare agent simulants classification," *Sensors and Actuator B: Chemical*, vol. 129, pp. 412–423, 2008.

[141] N. Levit, D. Pestov, and G. Tepper, "High surface area polymer coatings for SAW-based chemical sensor applications," *Sensors and Actuator B: Chemical*, vol. 82, pp. 241–249, 2002.

[142] Z. Ying, Y. Jiang, X. Du, G. Xie, J. Yu, and H. Tai, "Polymer coated sensor array based on quartz crystal microbalance for chemical agent analysis," *European Polymer Journal*, vol. 44, pp. 1157–1164, 2008.

[143] D. S. J. Ballantine, S. L. Rose, J. W. Grate, and H. Wohltjen, "Correlation of surfaces acoustic wave device coating responses with solubility properties and chemical structure using pattern recognition," *Analytical Chemistry*, vol. 58, pp. 3058–3066, 1986.

[144] J. R. Hanson, *Organic Synthetic Methods*. Royal Society of Chemistry, 2002.

[145] A. K. Geim and K. S. Novoselov, "The rise of graphene," *Nature Materials*, vol. 6, pp. 183–191, 2007.

[146] T. Seiyama, A. Kato, K. Fujiishi, and M. Nagatani, "A new detector for gaseous components using semiconductive thin films," *Analytical Chemistry*, vol. 34, pp. 1502–1503, 1962.

[147] Y. Xu, X. Zhou, and O. T. Sorensen, "Oxygen sensors based on semiconducting metal oxides: An overview," *Sensors and Actuator B: Chemical*, vol. 65, pp. 2–4, 2000.

[148] G. Korotcenkov, "Gas response control through structural and chemical modification of metal oxide films: state of the art and approaches," *Sensors and Actuator B: Chemical*, vol. 107, pp. 209–232, 2005.

[149] G. Korotcenkov, V. Macsanov, V. Tolstoy, V. Brinzari, J. Schwank, and G. Faglia, "Structural and gas response characterization of nano-size sno2 films deposited by sild method," *Sensors and Actuator B: Chemical*, vol. 96, pp. 602–609, 2003.

[150] N. Barsan and U. Weimar, "Conduction model of metal oxide gas sensors," *Journal of Electroceramics*, vol. 7, pp. 143–167, 2001.

[151] F. Lu, Y. Liu, M. Dong, and X. Wang, "Nanosized tin oxide as the novel material with simultaneous detection towards CO, H_2 and CH_4," *Sensors and Actuator B: Chemical*, vol. 66, pp. 225–227, 2000.

[152] M. E. Franke, T. J. Koplin, and U. Simon, "Metal and metal oxide nanoparticles in chemiresistors: Does the nanoscale matter?," *Small*, vol. 2, no. 1, pp. 36–50, 2006.

[153] Y. Shimizu and M. Egashira, "Basic aspects and challenges of semiconductor gas sensor," *MRS Bulletin*, vol. 6, pp. 18–24, 1999.

[154] W. Gopel, T. A. Jones, M. Kleitz, I. Lundstrom, and T. Seiyama, "Chemical and biochemical sensors: Part 1," in *Sensors: A comprehensive survey* (W. Gopel, J. Hesse, and J. N. Zemel, eds.), vol. 2, Weinheim: Wiley-VCH, 1991.

[155] A. Hulanicki, S. Glab, and F. Ingman, "Chemical sensors definition and classification," *Pure and Applied Chemistry*, vol. 63, no. 9, pp. 1247–1250, 1991.

[156] C. Nylander, "Chemical and biological sensors," *Journal of Physics E: Scientific Instruments*, vol. 18, pp. 736–750, 1985.

[157] G. Jimenez-Cadena, J. Riu, and F. X. Rius, "Gas sensors based on nanostructured materials," *Analyst*, vol. 132, pp. 1083–1099, 2007.

[158] D. S. Ballantine, R. M. White, S. J. Martin, A. J. Ricco, E. T. Zeller, G. C. Frye, and H. Wohltjen, *Acoustic wave sensors: Theory, design and physico-chemical applications*. San Diego: Academic Press, 1997.

[159] G. Sauerbrey, "The use of quartz oscillators for weighting thin layers and for microweighting," *Z Phys*, vol. 155, pp. 206–222, 1959.

[160] B. Drafts, "Acoustic wave technology sensors," *Sensors Magazine*, vol. 17, no. 10, p. 4 pages, 2000.

[161] R. M. White and F. W. Voltmer, "Direct piezoelectric coupling to surface elastic waves," *Applied Physics Letters*, vol. 17, pp. 314–316, 1965.

[162] H. Wohltjen and R. Dessy, "Surface acoustic wave probe for chemical analysis, I: Introduction and instrument description," *Analytical Chemistry*, vol. 51, no. 9, pp. 1458–1464, 1979.

[163] M.-A. Dubois, "Thin film bulk acoustic wave resonators: a technology overview," in *MEMSWAVE*, (Toulouse, France), p. 4 pages, 2003.

[164] H. P. Loebl, M. Klee, C. Metzmacher, W. Brand, R. Milsom, and P. Lok, "Piezoelectric thin AlN films for bulk acoustic wave (BAW) resonators," *Materials Chemistry and Physics*, vol. 79, no. 2, pp. 143–146, 2003.

[165] L. Rayleigh, "On waves propagated along the plane surface of an elastic solid," *Proceeding of the London Mathematical Society*, vol. 17, pp. 4–11, 1885.

[166] R. M. White, "Surface elastic waves," *Proceeding of the IEEE*, vol. 58, no. 8, pp. 1238–1276, 1970.

[167] A. Ballato, "Piezoelectricity: History and new thrusts," *IEEE Ultrasonics Symposium*, vol. 1, pp. 575–583, 1996.

[168] C. K. Campbell, *Surface acoustic waves devices for mobile and wireless communications*. London, UK: Academic Press, 1998.

[169] D. P. Morgan, *Surface-wave devices for signal processing*. Elsevier, The Netherland, 1978.

[170] B. A. Auld, *Acoustic fields and waves in solids*. New York: John Wiley and Sons, 1973.

[171] A. A. Oliner, *Acoustic Surface Waves*. New York: Springer-Verlag Berlin Heidelberg, 1978.

[172] J. J. Campbell and W. R. Jones, "A method for estimating optimal crystal cuts and propagation directions for excitation of piezoelectric surface waves," *IEEE Transactions on Ultrasonics*, vol. 15, no. 4, pp. 209–217, 1968.

[173] S. J. Ippolito, *Investigation of Multilayered Surface Acoustic Wave Devices for Gas Sensing Applications: Employing Piezoelectric Intermediate and Nanocrystalline Metal Oxide Sensitive Layers.* Phd thesis, RMIT University, 2006.

[174] D. W. Galipeau, P. R. Story, K. A. Vetelino, and R. D. Mileham, "Surface acoustic wave microsensors and applications," in *Smart Material Structure*, vol. 6, pp. 658–667, Brookings, SD 57006 USA: IOP Publishing Ltd, 1997.

[175] A. J. Ricco and S. J. Martin, "Thin metal film characterization and chemical sensors: Monitoring electronic conductivity, mass loading and mechanical properties with surface acoustic wave devices," *Thin Solid Films*, vol. 206, pp. 94–101, 1991.

[176] H. Becker, M. von Schickfus, and S. Hunklinger, "A new sensor principle based on reflection of surface acoustic waves," *Sensors and Actuators A: Physical*, vol. 54, pp. 618–621, 1996.

[177] A. Rugemer, S. Reiss, A. Geyer, M. von Schickfus, and S. Hunklinger, "Surface acoustic wave NO_2 sensing using attenuation as the measured quantitiy," *Sensors and Actuator B: Chemical*, vol. 56, pp. 45–49, 1999.

[178] S. J. Martin and A. J. Ricco, "Effective utilization of acoustic wave sensor responses: simultaneous measurements of velocity and attenuation," *Proceedings of the IEEE Ultrasonics Symposium*, pp. 621–625, 1989.

[179] H. Wohltjen and R. Dessy, "Surface acoustic wave probes for chemical analysis, II: Gas chromatography," *Analytical Chemistry*, vol. 51, no. 9, pp. 1465–1470, 1979.

[180] A. D'Amico, A. Palma, and E. Verona, "Surface acoustic wave hydrogen sensor," *Sensors and Actuators*, vol. 3, pp. 31–39, 1982.

[181] A. D'Amico, A. Palma, and E. Verona, "Hydrogen sensor using a palladium coated surface acoustic wave delay-line," *Proceedings of the IEEE Ultrasonics Symposium*, pp. 308–311, 1982.

[182] M. Rapp, R. Stanzel, M. von Schickfus, S. Hunklinger, H. Fuchs, W. Screpp, H. Keller, and B. Fleischmann, "Gas detection in the ppb-range with a high frequency, high sensitivity surface acoustic wave device," *Thin Solid Films*, vol. 210-211, pp. 474–476, 1992.

[183] J. D. Galipeau, R. S. Falconer, J. F. Vetelino, J. J. Caron, E. L. Wittman, M. G. Schweyer, and J. C. Andle, "Theory, design and operation of a surface acoustic wave hydrogen sulfide microsensor," *Sensors and Actuator B: Chemical*, vol. 24-25, pp. 49–53, 1995.

[184] M. S. Nieuwenhuizen and A. J. Nederlof, "A SAW gas sensor for carbon dioxide and water. preliminary experiments," *Sensors and Actuators*, vol. B2, pp. 97–101, 1990.

[185] D. Rebiere, C. Dejous, J. Pistre, J.-F. Lipskier, and R. Planade, "Synthesis and evaluation of floropolyol isomers as SAW microsensor coating: Role of humidity and temperature," *Sensors and Actuator B: Chemical*, vol. 49, pp. 139–145, 1998.

[186] A. D'Amico and E. Verona, "SAW sensors," *Sensors and Actuators*, vol. 17, pp. 55–66, 1989.

[187] D. S. Ballantine and H. Wohltjen, "Surface acoustic wave devices for chemical analysis," *Analytical Chemistry*, vol. 61, pp. 704A–715A, 1989.

[188] J. W. Grate, S. J. Martin, and R. M. White, "Acoustic wave microsensors," *Analytical Chemistry*, vol. 65, pp. 940A–948A, 1993.

[189] J. W. Grate, S. J. Martin, and R. M. White, "Acoustic wave microsensors. part ii," *Analytical Chemistry*, vol. 65, pp. 987A–996A, 1993.

[190] S. J. Martin, G. C. Frye, J. J. Spates, and M. A. Butler, "Gas sensing with acoustic devices," *Proceedings of the IEEE Ultrasonics Symposium*, pp. 423–433, 1996.

[191] J. D. N. Cheeke and Z. Wang, "Acoustic wave gas sensors," *Sensors and Actuator B: Chemical*, vol. 59, pp. 146–153, 1999.

[192] M. J. Vellekoop, "Acoustic wave sensors and their technology," *Proceedings of the IEEE Ultrasonics Symposium*, vol. 36, pp. 7–14, 1998.

[193] B. Drafts, "Acoustic wave technology sensors," *IEEE Transactions on Microwave Theory and Techniques*, vol. 49, pp. 795–802, 2001.

[194] V. I. Anisimkin, V. Gulyaev, and I. V. Anisimkin, "Surface acoustic waves method: New analytical capabilities," *Surface Investigation*, vol. 16, pp. 1213–1224, 2001.

[195] D. A. Powell, K. Kalantar-zadeh, W. Wlodarski, and S. Ippolito, "Layered surface acoustic wave chemical and bio-sensors," 2006.

[196] M. Hoummady, A. P. Campitelli, and W. Wlodarski, "Acoustic wave sensors: design, sensing mechanisms and applications," *Smart Material Structure*, vol. 6, pp. 647–657, 1997.

[197] Z. Wang, J. D. N. Cheeke, and C. K. Jen, "Perturbation for analysing mass sensitivity of planar multilayer acoustic sensors," *IEEE Transactions on Ultrasonics, Ferroelectrics, and Frequency Control*, vol. 43, pp. 844–851, 1996.

[198] D. A. Powell, *Modelling of Layered Surface Acoustic Wave Resonators for Liquid Media Sensing Applications*. PhD thesis, RMIT University, 2006.

[199] A. J. Ricco, S. J. Martin, and T. E. Zipperian, "Surface acoustic wave gas sensors based on film conductivity changes," *Sensors and Actuator B: Chemical*, vol. 8, no. 4, pp. 319–333, 1985.

[200] S. J. Martin, G. C. Frye, and S. D. Senturia, "Dynamics and response of polymer-coated surface acoustic wave devices: Effect of viscoelastic properties and film resonance," *Analytical Chemistry*, vol. 66, p. 2201, 1994.

[201] A. Ahuja, D. L. James, and R. Narayan, "Dynamic behaviour of ultra-thin polymer films deposited on surface acoustical wave devices," *Sensors and Actuators A: Physical*, vol. 72, pp. 234–241, 1999.

[202] C. E. Rogers, "Permeation of gases and vapours in polymers," in *Polymer Permeability* (J. Comyn, ed.), London: Elsevier Appled Science, 1985.

[203] G. L. Harding, "Mass sensitivity of Love-mode acoustic sensors incorporating silicon dioxide and silicon-oxy-flouride guiding layers," *Sensors and Actuators A: Physical*, vol. 88, pp. 20–28, 2001.

[204] J. Tamaki, T. Maekawa, S. Matsushima, N. Miura, and N. Yamazoe, "Ethanol gas sensing properties of $Pd-La_2O_3$-In_2O_3 thick film element," *Chemical Letters*, vol. 19, no. 3, p. 477, 1990.

[205] G. Cao, *Nanostructures and nanomaterials: Synthesis, properties and applications*. London: Imperial College Press, 2004.

[206] Y. T. Zhu and T. G. Langdon, "The fundamentals of nanostructured materials processed by severe plastic deformation," *JOM*, vol. 56, no. 10, pp. 58–63, 2004.

[207] J. Stejskal, I. Sapurina, J. Prokes, and J. Zemek, "In-situ polymerization polyaniline films," *Synthetic Metals*, vol. 105, pp. 195–202, 1999.

[208] H. Qiu, H. Li, K. Fang, J. Li, W. Mao, and S. Luo, "Micromorphology and conductivity of the vacuum-deposited polyaniline films," *Synthetic Metals*, vol. 148, pp. 71–74, 2005.

[209] L. K. Werake, J. G. Story, M. F. Bertino, S. K. Pillalamarri, and F. D. Blum, "Photolithograpic synthesis of polyaniline nanofibres," *Nanotechnology*, vol. 16, pp. 2833–2837, 2005.

[210] A. Eftekhari and P. Jafarkhani, "Polymerization of aniline through simultaneous chemical and electrochemical routes," *Polymer Journal*, vol. 38, no. 7, pp. 651–658, 2006.

[211] J. Liu, Y. Lin, L. Liang, J. A. Voigt, D. L. Huber, Z. R. Tian, E. Coker, B. McKenzie, and M. J. McDermott, "Templateless assembly of molecularly aligned conductive polymer nanowires: A new approach for oriented nanostructures," *Chemistry - A European Journal*, vol. 9, no. 3, pp. 604–611, 2003.

[212] L. Liang, J. Liu, C. F. J. Windisch, G. J. Exarhos, and Y. Lin, "Direct assembly of large arrays of oriented conducting polymers nanowires," *Angewandte Chemie International Edition*, vol. 114, no. 19, pp. 3817–3820, 2002.

[213] D. M. Mohilner, R. N. Adams, and W. J. J. Argersinger, "Investigation of the kinetics and mechanism of the anodic oxidation of aniline in aqueous sulfuric acid solution at a platinum electrode," *Journal of the American Chemical Society*, vol. 84, pp. 3618–3622, 1962.

[214] H. Zengin, W. Zhou, J. Jin, R. Czerw, D. W. J. Smith, L. Echegoyan, D. L. Carroll, S. H. Foulger, and J. Ballato, "Carbon nanotube doped polyaniline," *Advanced Materials*, vol. 14, no. 20, pp. 1480–1483, 2002.

[215] C. Berger, Z. Song, T. Li, X. Li, A. Y. Ogbazghi, R. Feng, Z. Dai, A. N. Marchenkov, E. H. Conrad, P. N. First, and W. A. de Heer, "Ultrathin epitaxial graphite: 2D electron gas properties and a route toward graphene based nanoelectronics," *Journal of Physic Chemical B*, vol. 108, pp. 19912–19916, 2004.

[216] H. C. Schniepp, J.-L. Li, M. J. McAllister, H. Sai, M. Herrera-Alonso, D. H. Adamson, R. K. Prud'homme, R. Car, D. A. Saville, and I. A. Aksay, "Functionalized single graphene sheets derived from splitting graphite oxide," *The Journal of Physical Chemistry B: Letters*, vol. 110, pp. 8535–8539, 2006.

[217] S. Gilje, S. Han, M. Wang, K. L. Wang, and R. B. Kaner, "A chemical route to graphene for device applications," *Nano Letters*, vol. 7, no. 11, p. 3394, 2007.

[218] R. Neidlein, T.-V. Dao, A. Gieren, M. Kokkinidis, R. Wilcken, H. P. Geserich, and W. Ruppel, "Synthesis, structures, x-ray structure analysis, and eletrical properties of di- and polychalcogen diimides," *Chemishe Berichte*, vol. 115, pp. 2898–2904, 1982.

[219] P. Wharton and D. Bohlen, "Hydrazine reduction of a,B-epoxy ketones to allylic alcohols," *The Journal of Organic Chemistry*, vol. 26, pp. 3615–3616, 1961.

[220] S. Stankovich, D. A. Dikin, R. D. Piner, K. A. Kohlhaas, A. Kleinhammes, Y. Jia, Y. Wu, S. T. Nguyen, and R. S. Ruoff, "Synthesis of graphene-based nanosheets via chemical reduction of exfoliated graphite oxide," *Carbon*, vol. 45, pp. 1558–1565, 2007.

[221] Y. Hu, H. Zhang, and H. Yang, "Direct synthesis of Sb_2O_3 nanoparticles via hydrolysis-precipitation method," *Journal of Alloys and Compounds*, vol. 428, no. 1-2, pp. 327–331, 2007.

[222] C. Xu, S. Shi, and Q. Tang, "Synthesis of antimony oxide nano-particles by thermal oxidation," *NSTI-Nanotech 2005*, vol. 2, pp. 54–57, 2005.

[223] X. Chen, X. Wang, C. An, J. Liu, and Y. Qian, "Synthesis of Sb_2O_3 nanorods under hydrothermal conditions," *Materials Research Bulletin*, vol. 40, no. 3, pp. 469–474, 2005.

[224] S. Friedrichs, R. Meyer, J. Sloan, A. Kirkland, J. Hutchison, and M. Green, "Complete characterisation of a Sb_2O_3/(21,-8)SWNT inclusion composite," *Chemical Communication*, pp. 929–930, 2001.

[225] R. S. Wagner and W. C. Ellis, "Vapor-liquid-solid mechanism of single crystal growth," *Applied Physics Letters*, vol. 4, pp. 89–91, 1964.

[226] M. Haruta, "Gold as a novel catalyst in 21st century: Preparation, working mechanism and applications," *Gold 2003*, p. 13, 2003.

[227] G. J. Hutchings and M. Haruta, "A golden age of catalysis: A perspective," *Applied Catalysis A: General*, vol. 291, pp. 2–5, 2005.

[228] G. Binnig, C. F. Quate, and C. Gerber, "Atomic force microscope," *Physical Review Letters*, vol. 56, pp. 930–933, 1986.

[229] I. De Wolf, C. Jian, and W. M. van Spengen, "The investigation of the microsystems using raman spectroscopy," *Optics and Lasers in Engineering*, vol. 36, pp. 213–223, 2001.

[230] J. Yano, K.-i. Yoshikawa, and A. Kitani, "Kinetic study of the electropolymerization of aniline using chronoamperometric techniques," *Analytical Sciences*, vol. 13, pp. 741–746, 1997.

[231] J.-H. Jeong, S.-H. Kim, Y. Choi, and S.-S. Kim, "Microstructure of nanopores in AAO templates favoring the growth of nickel nanowires by electrodeposition," *Physica Status Solidi (c)*, vol. 4, no. 12, pp. 4429–4432, 2007.

[232] P. Ingleby, J. W. Gardner, and P. N. Bartlett, "Effect of micro-electrode geometry on response of thin-film poly(pyrrole) and poly(aniline) chemoresistive sensors," *Sensors and Actuators B: Chemical*, vol. 57, no. 1-3, pp. 17–27, 1999.

[233] M. H. Pournaghi-Azar and B. Habibi, "Electropolymerization of aniline in acid media on the bare and chemically pre-treated aluminum electrodes: A comparative characterization of the polyaniline deposited electrodes," *Electrochimica Acta*, vol. 52, pp. 4222–4230, 2007.

[234] L. Duic, Z. Mandic, and F. Kovacicek, "The effect of supporting electrolyte on the electrochemical synthesis, morphology, and conductivity of polyaniline," *Journal of Polymer Science: Part A: Polymer Chemistry*, vol. 32, pp. 105–111, 1994.

[235] P. C. Ramamurthy, A. M. Malshe, W. R. Harrell, R. V. Gregory, K. McGuire, and A. M. Rao, "Polyaniline/single-walled carbon nanotube composite electronic devices," *Solid-State Electronics International Semiconductor Device Research Symposium 2003*, vol. 48, no. 10-11, pp. 2019–2024, 2004.

[236] C. Su, G. Wang, and F. Huang, "Preparation and characterization of composites of polyaniline nanorods and multiwall carbon nanotubes coated with polyaniline," *Journal of Applied Polymer Science*, vol. 106, pp. 4241–4247, 2007.

[237] H. Fong, I. Chun, and D. H. Reneker, "Beaded nanofibers formed during electrospinning," *Polymer*, vol. 40, pp. 4585–4592, 1999.

[238] A. C. Ferrari, "Raman spectroscopy of graphene and graphite: Disorder, electron-phonon coupling, doping and nonadiabatic effects," *Solid-State Communications*, vol. 143, pp. 45–57, 2007.

[239] D. Graf, F. Molitor, K. Ensslin, C. Stampfer, A. Jungen, C. Hierold, and L. Wirtz, "Spatially resolved raman spectroscopy of single- and few-layer graphene," *Nano Letters*, vol. 7, no. 2, pp. 238–242, 2007.

[240] F. Tuinstra and J. L. Koenig, "Raman spectrum of graphite," *The Journal of Chemical Physics*, vol. 53, no. 3, pp. 1126–1130, 1970.

[241] M. A. Pimenta, G. Dresselhaus, M. S. Dresselhaus, L. G. Cancado, A. Jario, and R. Saito, "Studying disorder in graphite-based systems by Raman spectroscopy," *Physical Chemistry Chemical Physics*, vol. 9, no. 11, pp. 1276–1291, 2007.

[242] A. Bryant, M. Poirier, G. Riley, D. L. Lee, and J. F. Vetelino, "Gas detection using surface acoustic wave delay lines," *Sensors and Actuator B: Chemical*, vol. 4, pp. 105–111, 1983.

[243] M. F. Lewis, "Surface acoustic wave devices and applications: Oscillators - the next successful surface acoustic wave device," *Ultrasonics*, pp. 115–123, 1974.

[244] G. K. Montress, T. E. Parker, and D. Andres, "Review of saw oscillator performance," *Ultrasonics Symposium*, pp. 43–45, 1994.

[245] Y. Rao and G. Zhang, "3D modeling of a Surface-Acoustic-Wave based sensor," in *COMSOL Conference 2007*, (Boston), 2007.

[246] S. Ippolito, S. Kandasamy, K. Kalantar-zadeh, and W. Wlodarski, "Hydrogen sensing characteristics of WO_3 thin film conductometric sensors activated by Pt and Au catalysts," *Sensors and Actuators B: Chemical Proceedings of the Tenth International Meeting on Chemical Sensors*, vol. 108, no. 1-2, pp. 154–158, 2005.

[247] S. Ippolito, S. Kandasamy, K. Kalantar-zadeh, and W. Wlodarski, "Layered SAW hydrogen sensor with modified tungsten trioxide selective layer," *Sensors and Actuator B: Chemical*, vol. 108, no. 1-2, pp. 553–557, 2005.

[248] S. Bhadra, N. K. Singha, and D. Khastgir, "Electrochemical synthesis of polyaniline and its comparison with chemically synthesized polyaniline," *Journal of Applied Polymer Science*, vol. 104, pp. 1900–1904, 2007.

[249] M. D. Catedral, A. K. G. Tapia, R. V. Sarmago, J. Tamayo, and E. J. del Rosario, "Effect of dopant ions on the electrical conductivity and microstructure of polyaniline (emeraldine salt)," *Science Diliman*, vol. 16, pp. 41–46, 2004.

[250] P. D. Gaikwad, D. J. Shirale, V. K. Gade, P. A. Savale, H. J. Kharat, K. P. Kakde, S. S. Hussaini, N. R. Dhumane, and M. D. Shirsat, "Synthesis of H_2SO_4 doped polyaniline film by potentiometric method," *Bulletin of Materials Science*, vol. 29, no. 2, pp. 169–172, 2005.

[251] G. Liang, J. Huot, S. Boily, and R. Schulz, "Hydrogen desorption kinetics of a mechanically milled MgH2+5at.V nanocomposite," *Journal of Alloys and Compounds*, vol. 305, no. 1-2, pp. 239–245, 2000.

[252] H. H. S. Javadi, M. Angelopolous, A. G. MacDiarmid, and A. J. Epstein, "Conduction mechanism of polyaniline: Effect of moisture," *Synthetic Metals*, vol. 26, pp. 1–8, 1988.

[253] M. Nechtschein, C. Santier, J. P. Travers, J. Chroboczek, A. Alix, and M. Ripert, "Water effect in polyaniline: NMR and transport properties," *Synthetic Metals*, vol. 18, p. 311, 1987.

[254] L. Jiang, H.-K. Jun, Y.-S. Hoh, J.-O. Lim, D.-D. Lee, and J.-S. Huh, "Sensing characteristics of polypyrrole-poly(vinyl alcohol) methanol sensors prepared by in situ vapor state polymerization," *Sensors and Actuator B: Chemical*, vol. 105, pp. 132–137, 2005.

[255] W. Kang, Y. Gurbuz, J. Davidson, and D. Kerns, "A polycrystalline diamond thin-film-based hydrogen sensor," *Sensors and Actuator B: Chemical*, vol. 24-25, pp. 421–425, 1995.

[256] R. S. Gi, T. Ishikawa, S. Tanaka, T. Kimura, Y. Akiba, and M. Iida, "Possibility of realizing a gas sensor using surface conductive layer on diamond films," *Japanese Journal of Applied Physics*, vol. 36, pp. 2057–2060, 1997.

[257] S. H. Hosseini and A. A. Entezami, "Preparation and characterization of polyaniline blends with polyvinylacetate, polystyrene and polyvinylchloride for toxic gas sensors," *Polymers for Advanced Technologies*, vol. 12, pp. 482–493, 2001.

[258] W. Badawy, "Preparation and electrochemical behaviour of Sb_2O_5 films," *Thin Solid Films*, vol. 186, pp. 59–72, 1990.

[259] S. Shukla, S. Seal, L. Ludwig, and C. Parish, "Nanocrystalline indium oxide-doped tin oxide thin film as low temperature hydrogen sensor," *Sensors and Actuators B: Chemical*, vol. 97, pp. 256–265, 2004.

[260] W. F. Smith and J. Hashemi, *Foundations of Materials Science and Engineering*. New York: McGraw-Hill, 4th ed., 2006.